

Nanomaterials for Cancer Diagnosis and Therapy

Guest Editors: Huisheng Peng and Chao Lin





Nanomaterials for Cancer Diagnosis and Therapy

Journal of Nanomaterials

**Nanomaterials for Cancer
Diagnosis and Therapy**

Guest Editors: Huisheng Peng and Chao Lin



Copyright © 2010 Hindawi Publishing Corporation. All rights reserved.

This is a special issue published in volume 2010 of “Journal of Nanomaterials.” All articles are open access articles distributed under the Creative Commons Attribution License, which permits unrestricted use, distribution, and reproduction in any medium, provided the original work is properly cited.

Editor-in-Chief

Michael Z. Hu, Oak Ridge National Laboratory, USA

Advisory Board

James H. Adair, USA
C. Jeffrey Brinker, USA
T. Hyeon, Republic of Korea
Nathan Lewis, USA

Ed Ma, USA
Alon V. McCormick, USA
Gary L. Messing, USA
Zhonglin Wang, USA

Enge Wang, China
Ching P. Wong, USA
N. Xu, China
Jackie Y. Ying, Singapore

Associate Editors

Alan K. T. Lau, Hong Kong
Xuedong Bai, China
Donald A. Bansleben, USA
Theodorian Borca-Tasciuc, USA
Christian Brosseau, France
Sang-Hee Cho, Republic of Korea
Chun Xiang Cui, China
Ali Eftekhari, USA
Claude Estournes, France
Alan Fuchs, USA
Lian Gao, China
Hong cheng Gu, China
Michael Harris, USA
Justin D. Holmes, Ireland

David Hui, USA
Wanqin Jin, China
Rakesh K. Joshi, USA
Do K. Kim, Republic of Korea
Burtrand Lee, USA
Jun Li, Singapore
Shijun Liao, China
Gong-Ru Lin, Taiwan
J. -Y. Liu, USA
Jun Liu, USA
Songwei Lu, USA
Daniel Lu, China
Sanjay R. Mathur, Germany
Nobuhiro Matsushita, Japan

Sherine Obare, USA
P. Panine, France
Edward Andrew Payzant, USA
Donglu Shi, USA
Bohua Sun, South Africa
Maryam Tabrizian, Canada
Theodore Tsotsis, USA
Yong Wang, China
Xiaogong Wang, China
Michael S. Wong, USA
Ping Xiao, UK
Zhi-Li Xiao, USA
Doron Yadlovker, Israel
Kui Yu, Canada

Contents

Nanomaterials for Cancer Diagnosis and Therapy, Huisheng Peng, and Chao Lin
Volume 2010, Article ID 592901, 1 pages

Application of Quantum Dots-Based Biotechnology in Cancer Diagnosis: Current Status and Future Perspectives, Chun-Wei Peng and Yan Li
Volume 2010, Article ID 676839, 11 pages

Development of Near Infrared-Fluorescent Nanophosphors and Applications for Cancer Diagnosis and Therapy, Tamotsu Zako, Hiroshi Hyodo, Kosuke Tsuji, Kimikazu Tokuzen, Hidehiro Kishimoto, Masaaki Ito, Kazuhiro Kaneko, Mizuo Maeda, and Kohei Soga
Volume 2010, Article ID 491471, 7 pages

Cancer Therapy Based on Nanomaterials and Nanocarrier Systems, Weili Qiao, Bochu Wang, Yazhou Wang, Lichun Yang, Yiqiong Zhang, and Pengyu Shao
Volume 2010, Article ID 796303, 9 pages

Detection of Thyroid Carcinoma Antigen with Quantum Dots and Monoclonal IgM Antibody (JT-95) System, Fujioka, Noriyoshi Manabe, Mayumi Nomura, Michiko Watanabe, Hiroshi Takeyama, Akiyoshi Hoshino, Sanshiro Hanada, Kenji Yamamoto, and Yoshinobu Manome
Volume 2010, Article ID 937684, 7 pages

Protein Viability on Au Nanoparticles during an Electrospray and Electrostatic-Force-Directed Assembly Process, Shun Mao, Ganhua Lu, Kehan Yu, and Junhong Chen
Volume 2010, Article ID 196393, 6 pages

Surfactant-Templated Mesoporous Metal Oxide Nanowires, Hongmei Luo, Qianglu Lin, Stacy Baber, and Mahesh Naalla
Volume 2010, Article ID 750960, 6 pages

Suppression of Proinflammatory Cytokines in Functionalized Fullerene-Exposed Dermal Keratinocytes, Jun Gao, Hsing-Lin Wang, and Rashi Iyer
Volume 2010, Article ID 416408, 9 pages

Nanoprodugs of NSAIDs Inhibit the Growth of U87-MG Glioma Cells, Bong-Seop Lee, Xiangpeng Yuan, Qijin Xu, Minhee K. Ko, Aruna K. Nalla, Ilana Frankiel, Talia Shear, Keith L. Black, and John S. Yu
Volume 2010, Article ID 583970, 10 pages

Nanoconjugate Platforms Development Based in Poly(β ,L-Malic Acid) Methyl Esters for Tumor Drug Delivery, José Portilla-Arias, Rameshwar Patil, Jinwei Hu, Hui Ding, Keith L. Black, Montserrat Garcíá-Alvarez, Sebastián Muñoz-Guerra, Julia Y. Ljubimova, and Eggehard Holler
Volume 2010, Article ID 825363, 8 pages

Controlled Release of Doxorubicin from Doxorubicin/ γ -Polyglutamic Acid Ionic Complex, Bhavik Manocha and Argyrios Margaritis
Volume 2010, Article ID 780171, 9 pages

Preparation, Mechanical, and Thermal Properties of Biodegradable Polyesters/Poly(Lactic Acid) Blends, Peng Zhao, Wanqiang Liu, Qingsheng Wu, and Jie Ren
Volume 2010, Article ID 287082, 8 pages



Electrospun Poly(L-Lactide-co- ϵ -Caprolactone)/Polyethylene Oxide/Hydroxyapatite Nanofibrous Membrane for Guided Bone Regeneration, Gang Wang, Tianbin Ren, Chunhong Cao, Weizhong Yuan, Ying Song, and Jiansheng Su
Volume 2010, Article ID 232017, 8 pages

Uptake and Cytotoxicity of Ce(IV) Doped TiO₂ Nanoparticles in Human Hepatocyte Cell Line L02, Jian Mao, Long Wang, Zhiyong Qian, and Mingjing Tu
Volume 2010, Article ID 910434, 8 pages

Editorial

Nanomaterials for Cancer Diagnosis and Therapy

Huisheng Peng^{1,2} and Chao Lin²

¹ Key Laboratory of Molecular Engineering of Polymers of Ministry of Education, Department of Macromolecular Science and Laboratory of Advanced Materials, Fudan University, Shanghai 200438, China

² The Institute for Advanced Materials and Nano Biomedicine, Tongji University, Tongji University, Shanghai 200092, China

Correspondence should be addressed to Huisheng Peng, penghs2004@yahoo.com

Received 31 March 2010; Accepted 31 March 2010

Copyright © 2010 H. Peng and C. Lin. This is an open access article distributed under the Creative Commons Attribution License, which permits unrestricted use, distribution, and reproduction in any medium, provided the original work is properly cited.

The early diagnosis of cancer, that is, prior to the visibility of anatomic anomalies, has been universally accepted to be essential for the success of cancer treatment. However, it remains challenging to detect tumors at a very early stage. For instance, traditional medical imaging may require more than a million cells for accurate clinical diagnosis. By contrast, an ideal molecular imaging is expected to correctly diagnose early-stage tumor of approximately 100–1000 cells. On the other hand, in the clinical cancer therapy process, anticancer drugs are simply employed to kill cancer cells. Unfortunately, nontargeted drugs may be rapidly and widely distributed in healthy organs and tissues. As a result, a high dose of anticancer drugs is normally needed to obtain favorable therapy efficacy. Moreover, the patients have to suffer from severe side effects or even from the drug toxicity far earlier than the tumor burden. Presently, these clinical difficulties have largely impeded successful cancer therapy.

Nanomaterials are anticipated to revolutionize the cancer diagnosis and therapy. Nanoscale particles decorated with multiple functionalities are able to target and, subsequently, visualize tumor site via an imaging technology, thereby allowing for the early detection of cancers. Furthermore, intelligent nanosystems can be constructed as controlled delivery vehicles for improved therapy efficacy; that is, such vehicles are capable of delivering anticancer drugs to a predetermined site and then releasing them with a programmed rate. These nanomaterials are composed of natural or synthetic materials, such as, polymer, carbon nanotube, quantum dot, superparamagnetic iron oxide, and their composites. They represent new directions for accurate diagnosis and effective administration in cancer.

We organize this special issue of *Journal of Nanomaterials* to give state-of-the-art findings in nanomaterials for cancer

diagnosis and therapy. In this special issue, three review articles firstly shed light on some important topics on the design, preparation, and integration of nanomaterials aiming at cancer diagnosis and therapy. The following ten research articles focus on a broad spectrum of nanomaterials with diagnosis and/or therapy functionalities. Toxicity of nanomaterials has been also included in some studies. All of the authors in this special have extensive research experience in nanomaterials and biomedical sciences. We are indebted to them for their important contributions and believe that readers will benefit considerably.

*Huisheng Peng
Chao Lin*

Review Article

Application of Quantum Dots-Based Biotechnology in Cancer Diagnosis: Current Status and Future Perspectives

Chun-Wei Peng¹ and Yan Li^{1,2}

¹Department of Oncology, Zhongnan Hospital of Wuhan University, No 169 Donghu Road, Wuchang District, Wuhan 430071, China

²Hubei Key Laboratory of Tumor Biological Behaviors, Hubei Cancer Clinical Study Center, No 169 Donghu Road, Wuchang District, Wuhan 430071, China

Correspondence should be addressed to Yan Li, liyansd2@163.com

Received 1 October 2009; Revised 15 December 2009; Accepted 20 January 2010

Academic Editor: Huisheng Peng

Copyright © 2010 C.-W. Peng and Y. Li. This is an open access article distributed under the Creative Commons Attribution License, which permits unrestricted use, distribution, and reproduction in any medium, provided the original work is properly cited.

The semiconductor nanocrystal quantum dots (QDs) have excellent photo-physical properties, and the QDs-based probes have achieved encouraging developments in cellular and in vivo molecular imaging. More and more researches showed that QDs-based technology may become a promising approach in cancer research. In this review, we focus on recent application of QDs in cancer diagnosis and treatment, including early detection of primary tumor such as ovarian cancer, breast cancer, prostate cancer and pancreatic cancer, as well as regional lymph nodes and distant metastases. With the development of QDs synthesis and modification, the effect of QDs on tumor metastasis investigation will become more and more important in the future.

1. Introduction

Cancer is a major public health problem in the world, and one in four deaths in the United States is due to cancer, with an estimated 1479350 new cancer cases and 562340 deaths from cancer expected in 2009 [1]. Although progress has been made in reducing incidence and mortality rates and improving survival, cancer still accounts for more deaths than heart disease in persons younger than 85 years of age [1]. One major challenge is how to diagnose cancer in early stage when curative treatment is possible. New technologies are required to dramatically improve the early detection and treatment of cancer, and fluorescent molecules can play a big role in this field [2, 3].

Nanotechnology is an emerging field that may have potentials to make paradigm changes in the detection, treatment, and prevention of cancer [4]. The development of biocompatible nanoparticles for molecular targeted diagnosis and treatment is an area of considerable interest. The basic rationale is that nanoparticles have unique structural and functional properties different from those of discrete molecules or bulk materials [5, 6]. One of the most exciting advances in label technology is the development of quantum

dots (QDs), a heterogeneous class of engineered nanoparticles with unique optical and chemical properties making them important nanoparticles with numerous potential applications ranging from medicine to energy [7, 8]. Used as in vitro and in vivo fluorophores, QDs are intensely studied in molecular, cellular, and in vivo imaging due to their novel optical and electronic properties [9–11]. To be different from those reviews focusing on the basic mechanisms and development of QDs, this review focuses on recent application of QDs in cancer diagnosis, including early detection of primary tumor such as ovarian cancer, breast cancer, prostate cancer, and pancreatic cancer, as well as regional lymph nodes and distant metastases.

2. QDs Properties

QDs are nanocrystals composed of a semiconductor core including group II-VI or group III-V elements encased within a shell comprised of a second semiconductor material. A typical QD has a diameter ranging from 2 to 10 nm containing roughly 200 to 10,000 atoms, with size comparable to a large protein. In comparison with organic dyes and fluorescent proteins, QDs have unique optical and

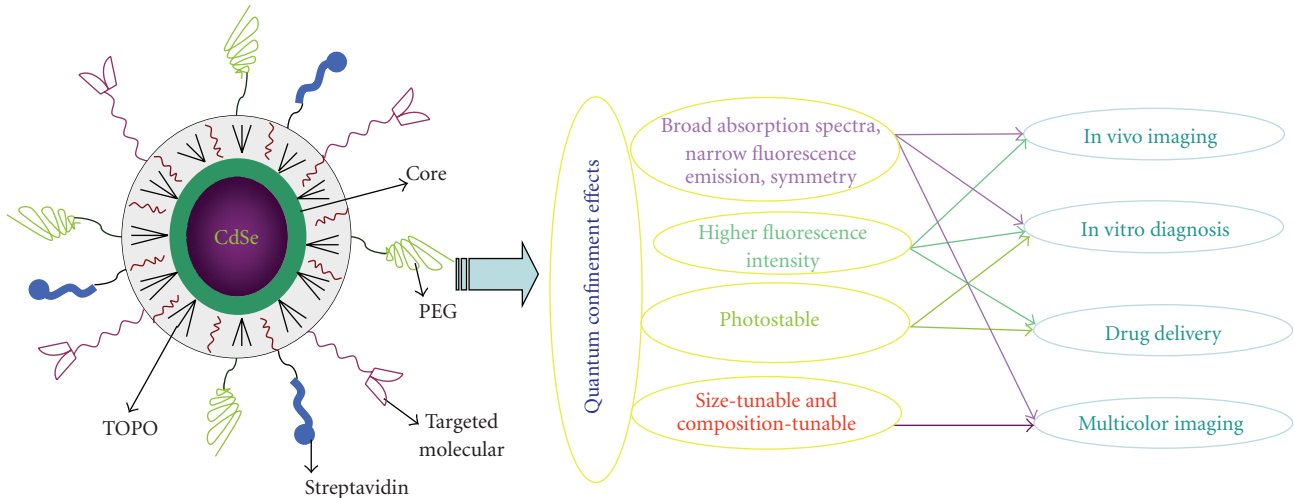


FIGURE 1: *Properties of QDs.* QDs are characterized with broad absorption spectra, size- and composition-tunable, narrow fluorescence emission, high levels of brightness and photostability. QDs can be used in in vitro and in vivo multicolor imaging and targeted drug delivery.

electronic properties such as size- and composition-tunable light emission, improved signal brightness, resistance to photobleaching and simultaneous excitation of multiple fluorescence colors. In addition, different colors of QDs can be simultaneously excited with a single light source, with minimal spectral overlapping, which provides significant advantages for multiplexed detection of target molecules [10, 12–15] (Figure 1). However, as QDs are hydrophobic by nature, it is necessary to solubilize QDs before application by surface modification with biofunctional molecules [16], because QDs have large surface areas for the attachment of such molecules. When conjugated with diagnostic (e.g., optical) and therapeutic (e.g., anticancer) agents, QDs can be used for cancer diagnosis and therapy with high specificity [17–19]. Significant research efforts have been focused on cancer early diagnosis with QDs [20]. As early as 2002, after overcoming the limitation in obtaining biocompatible nanocrystals, Dubertret [21] showed the potential to revolutionize biological imaging. In case of imaging probes, active targeting of cancer antigens (molecular imaging) has become an area of tremendous interest because of the potential to detect early stage cancers and their metastases [22–24]. Major recent developments in this regard are summarized in Table 1.

3. QDs-Based Detection of Primary Tumor

3.1. Ovarian Cancer. Ovarian cancer is the second most-common malignancy of the female genital tract and the leading cause of death from gynecological malignancies [33]. Carbohydrate antigen 125 (CA 125) is an epithelial antigen and a useful tumor marker in the detection and therapy of ovarian cancer [34–36]. The ability to visualize native processes occurring in living organisms is invaluable for clinical diagnostic applications, yet it remains elusive in practice due to conventional imaging limitations and the availability of suitable fluorescence markers. Because of

their unique photophysical properties, QDs are promising fluorophores for in vivo fluorescence imaging and can overcome many shortcomings of conventional dyes. Wang et al. [37] used QDs with maximum emission wavelength 605 nm (QD605) to detect CA125 in ovarian cancer specimens of different types (fixed cells, tissue sections, and xenograft tumor) with high specificity and sensitivity. Comparison between QDs and fluorescein isothiocyanate (FITC) showed that QDs labeling signals were brighter, more specific and stable than those of FITC. In another study, Nathwani [38] synthesized biocompatible QDs coated with a natural protein silk fibroin (SF) and used such QDs conjugates as a fluorescent label for successful bioimaging HEYA8 ovarian cancer cells. The properties of QDs have opened new possibilities for advanced molecular and cellular imaging as well as for ultrasensitive bioassays and diagnostics of ovarian cancer.

3.2. Breast Cancer. Wu et al. [39] explored a new technology to label HER2 (human epidermal growth factor receptor 2, HER2) on breast cancer cell membrane, which is known as c-erbB-2 or HER2/neu and overexpressed in approximately 25–30% invasive breast cancer [40, 41] and plays an important role in breast cancer prognosis and treatment selection [42–45]. After that, several studies on the detection of HER2 for breast cancer diagnosis with QDs have completed [46, 47]. Yezhlyev et al. [25] reported the use of multicolor QDs for quantitative and simultaneous profiling of multiple biomarkers using intact breast cancer cells and clinical specimens and the comparison between the new QDs-based molecular profiling technology with standard western blotting and fluorescence in situ hybridization (FISH). The multicolor bioconjugates were used for simultaneous detection of the five clinically significant tumor markers, including HER2 (QD-HER2), ER (QD-ER), PR (QD-PR), EGFR (QD-EGFR), and mTOR (QD-mTOR), in breast cancer cells MCF-7 and BT474. A quantitative correlation

TABLE 1: Application of QDs in molecular, cell, tissue, animal model cancer imaging (since 2007).

Authors	QDs used	Major findings	Advantages	Problems
Molecular imaging				
Yezhelyev et al. [25], 2007	QD-HER2 (525 nm), QD-ER (565 nm), QD-PR (605 nm), QD-EGFR (655 nm), QD-mTOR (705 nm)	QDs can be used for multiplexed and quantitative detection of tumor biomarkers.	High sensitivity; Increased resolution; Decreased autofluorescence.	Better conjugation chemistry for well-controlled bio-ligand are needed;
Mulder et al. [26], 2009	RGD-conjugated QDs	QDs readily reveal the angiogenic tumor vasculature, with the highest angiogenic activity occurring in the periphery of the tumor.		The number of bio-ligands per nanoparticle needs to be characterized
Cancer cell imaging				
Tada et al. [27], 2007	Trastuzumab-QDs (800 nm)	Single breast cancer cell can be observed with QDs.	High brightness; Resistance to photobleachings;	The methods current used for delivery into cells are not highly efficient.
Shah et al. [28], 2007	Bio-conjugated QDs	Stem cells can be effectively labeled by QDs during both proliferation and multilineage differentiation for long term.	InP/ZnS QDs are nontoxic.	It is difficult to prepare InP/ZnS QDs because of the sensitivity of precursors and surfactants toward the reaction environment in obtaining good InP QDs
Yong et al. [29], 2009	Bio-conjugated InP/ZnS QDs	InP/ZnS QDs can be used as non-cadmium-based safe and efficient optical imaging nanoprobles.		
Cancer tissue imaging				
Chen et al. [30], 2009	HER2-QDs	The expression of Her2 of human breast cancer tissue was detected.	Highly efficient, nontoxic, quantitative, sensitive, convenient.	Data from clinical trials about QDs comparing with "Gold standard" is required.
Animal model imaging				
Smith et al. [31], 2008	RGD-QDs	For the first time, authors have demonstrated the ability to directly follow the specific binding of nanoparticles to biomolecules expressed on tumor neovascular endothelium in mouse model.	Portends the promise of studying nanoscale structures interacting with microscale entities in living subjects at the cellular-to-subcellular level.	The kinetic and toxicity of QDs in animal model are still controversial limiting the clinical use of QDs.
Parungo et al. [32], 2007	NIR QDs (840 nm)	The purpose was to determin whether the peritoneal space has a predictable lymph node drainage pattern. Bowel lymphatics are a key determinant of peritoneal lymph flow, because bowel resection shifts lymph flow directly to the intrathoracic lymph nodes via chest wall lymphatics.	QDs can be excellently visualized in vivo using IVM.	

QDs: quantum dots; Her2: human epidermal growth factor receptor 2; ER: estrogen receptor, PR: progesterone receptor; EGFR: epithelial growth factor receptor; mTOR: mammalian target of rapamycin; RGD: arginine-glycine-aspartic acid; NIR: near infrared; IVM: in vivo metric systems.

between the HER2 gene amplification and HER2 protein expression was detected using QD-Abs profiling. This study suggests the possibility of using conjugated QDs to detect low levels of HER2 protein expression, but the clinical relevance of that finding deserves further investigation. To overcome the limitation in the clinical application of those studies aforementioned, we recently used QDs conjugated with antibody for assessment of HER2 status in breast cancer [30].

In our study, 700 patients with invasive breast cancer were enrolled, including 3 males and 697 females. The expression of HER2 in breast cancer was detected in an automated, quantitative, sensitive, and convenient way using our QDs-immunohistochemistry (QDs-IHC) analysis system. Compared with conventional IHC, the QDs-based approach is more sensitive, accurate, and economic, especially for cases of IHC (2+), which indicates that this new method may have

potentials for clinical application, especially in developing countries (Figure 2).

3.3. Prostate Cancer. Adenocarcinoma of the prostate is the most common cancer for males in the West, with approximately 192,280 new cases and 27,360 deaths from this disease in 2009 in USA alone [1]. Early diagnosis of prostate cancer is based on the prostate-specific antigen (PSA), and the introduction of PSA-based screening has revolutionized prostate cancer detection and ushered in the PSA era in which prostate cancer was detected at an earlier stage and in greater numbers than ever before [48, 49]. PSA is also an important prognostic marker of prostate cancer [50]. Fluorescent probe conjugated with PSA provides a specific and sensitive tool for early prostate cancer imaging *in vivo*. With QDs probes conjugated to a PSMA monoclonal antibody (Ab), another marker for prostate cancer diagnosis and therapy, Gao et al. [51] have achieved sensitive and multicolor fluorescence imaging of cancer cells under *in vivo* conditions. Shi [52] showed the superior quality of QDs, in comparison to IHC, for the detection of androgen receptor (AR) and PSA in prostate cancer cells. Both of those two studies, showing the potential ability of QDs as a diagnosis technology, are good examples to demonstrate why QDs are promising nanoparticles for diagnostic applications [53]. In another study, Gao et al. [54] demonstrated the potential of QDs as a new diagnosis technology for metastasis prostate cancer. Usually, antibodies conjugated to QDs are full-length antibody, which leads to dramatically reduced binding activities. Recently a study demonstrated that the use of single-chain antibody fragments (scFvs) conjugated with QDs appears to have a number of advantages, in terms of solubility, activity, ease of preparation and ease of structure-based genetic engineering, which were approved by detecting prostate cancer cells [55]. Barua Rege [56] also developed a new method to identify prostate cancer cells with different phenotype by unconjugated QDs whose trafficking is cancer-cell-phenotype-dependent.

3.4. Pancreatic Cancer. The mean survival of pancreatic cancer is around 6 months, and less than 5% of all patients diagnosed with pancreatic cancer survive beyond 5 years [57, 58]. This dismal scenario is primarily due to the fact that most patients are diagnosed at advanced stage, due to the lack of specific symptoms and limitations in diagnostics [59]. QDs can target the purpose of early diagnosis of pancreatic cancer [60], even at an early stage of development, with the help of proteins/peptides directed against overexpressed surface receptors on the cancer cells/tissues such as the transferring receptor, the antigen claudin-4 and urokinase plasminogen activator receptor (uPAR) [61].

Qian [62] used CdSe/CdS/ZnS QDs with improved photoluminescence efficiency and stability as optical agent for imaging pancreatic cancer cells using transferring and anti-Claudin-4. Pancreatic cancer specific uptake is also demonstrated using the monoclonal antibody anti-Claudin-4. This targeted QDs platform will be further modified to develop early detection imaging tool for pancreatic cancer.

Yong et al. [29] used non-cadmium-based QDs as highly efficient and nontoxic optical probes for imaging live pancreatic cancer cells. Further bioconjugation with pancreatic cancer specific monoclonal antibodies, such as anticlaudin 4, to the functionalized InP/ZnS QDs, allowed specific *in vitro* targeting of pancreatic cancer cell lines. The receptor-mediated delivery of the bioconjugates was further confirmed by the observation of poor *in vitro* targeting in nonpancreatic cancer cell lines without claudin-4-receptor. These observations suggest the immense potential of InP/ZnS QDs as non-cadmium-based safe and efficient optical imaging nanoprobe in diagnostic imaging.

4. QDs-Based Detection of Cancer Metastasis

Metastasis is a complex, multistep process by which primary tumor cells invade adjacent tissue, enter the systemic circulation (intravasate), translocate through the vasculature, arrest in distant capillaries, extravasate into the surrounding tissue parenchyma, and finally proliferate from microscopic growths (micrometastases) into macroscopic secondary tumors [63]. Over the past 30 years, the study of cancer metastasis has grown exponentially, and a thorough historical review of the field by the late Leonard Weiss has been published [64], but the process of metastasis is still invisible. The vast majority of patients present with locally advanced or distant metastatic disease, rendering their malignancy surgically inoperable [65]. As the origins of the invasive and metastatic phenotypes of carcinoma cells have been the subjects of intense investigation [66], a new model for visualizing the metastasis is needed. QDs-based technology shows advantages in detecting metastasis [67].

4.1. Blood-Born Metastasis to the Lungs. Most of the studies published in literature are focused on breast cancer and prostate cancer, and there is almost no report on the molecular imaging of hepatocellular carcinoma (HCC), especially HCC lung metastasis. HCC is the sixth most common cancer worldwide in terms of numbers of cases (626,000 or 5.7% of new cancer cases), but the number of deaths is almost the same (598,000) due to the very poor prognosis [68]. Disease that is diagnosed at an advanced stage or with progression after locoregional therapy has a dismal prognosis, owing to the underlying liver disease, lack of effective treatment options and metastasis at early stage [69, 70]. It is documented that 82% of cases (and deaths) are in developing countries (55% in china alone) [57], but the incidence is also increasing in developed regions including Japan, West Europe, and the United States [71]. Alpha-fetoprotein (AFP) is an important tumor marker for HCC [72–74]. In our prior study, we used CdSe/ZnS QDs with emission wavelength of 590 nm (QDs 590) linked to AFP monoclonal antibody (Ab) as a probe for fluorescence spectral analysis of HCC [75, 76]. In another study [77], we tested the biocompatibility, hemodynamics, tissues distribution of the QDs-AFP-Ab probes, and studied the imaging of HCC and its metastasis *in vitro* and *in vivo*. Our results indicate that such QDs-based probes have good

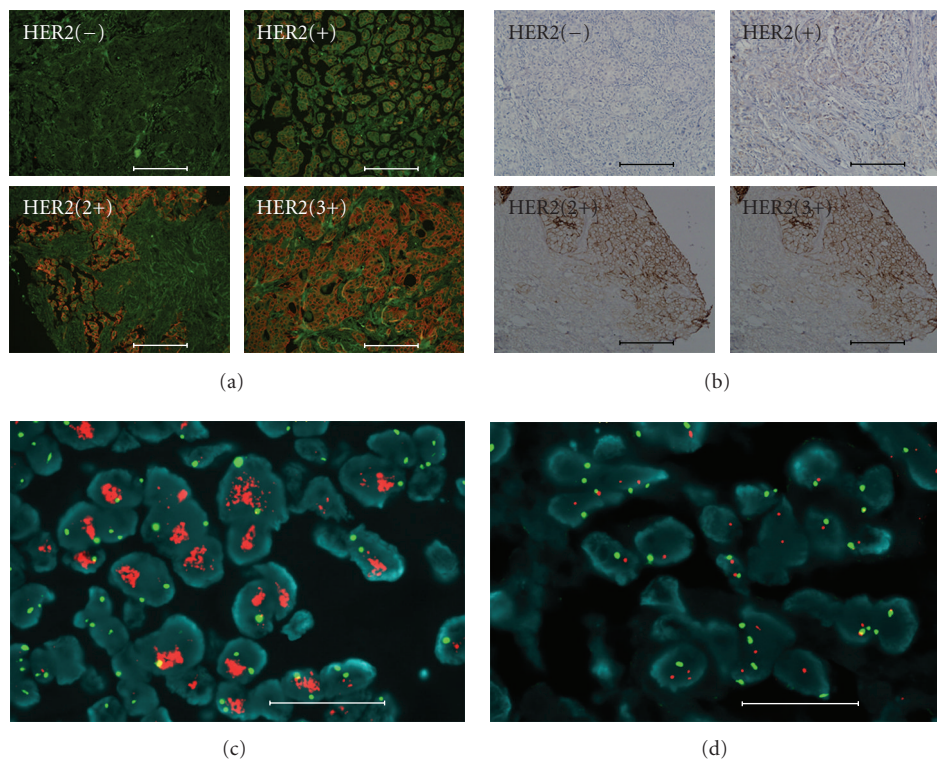


FIGURE 2: Accurate HER2 testing by QDs-IHC. (a) Specimens with difference HER2 IHC cores detected by QDs-IHC. (b) Control for (a) by conventional IHC (c) and (d) FISH positive (c) and negative (d). Scale bar, 100 μm for (a) and (b), 20 μm for (c) and (d). (Work from [30].)

stability, specificity and biocompatibility for ultrasensitive fluorescence imaging of molecular targets in our liver cancer model system (Figure 3).

4.2. Lymph Node Metastasis. Lymph metastasis is a major route of cancer progression. The state of lymph node draining from the tumor is essential for the diagnosis and therapy of cancer and has major prognostic implications [78, 79]. Sentinel lymph node (SLN) is much more likely to contain metastatic tumor cells than other lymph nodes in the same region. Among the various methods for SLN diagnosis, QDs have received increasing attention as lymph node delivery agents [80], and Kim [81] was the first to detect animal model SLN as deep as 1 cm subcutaneously. Near-infrared QDs are characterized by good tissue penetration and lower background, which are suitable for lymph node metastasis diagnosis [82, 83]. Ballou et al. [84] demonstrated that the QDs injected into two model tumors rapidly migrate to sentinel lymph nodes. Passage from the tumor through lymphatics to adjacent nodes could be visualized dynamically through the skin, and at least two nodes could be defined. Imaging during necropsy confirmed confinement of the QDs to the lymphatic system and demonstrated easy tagging of sentinel lymph nodes for pathology. In addition, examination of the sentinel nodes showed that at least some contained metastatic tumor foci.

The axillary nodal status is the most powerful prognostic factor for early stage breast cancer [85, 86]. Breast cancer patients routinely undergo surgical staging of the axilla

because other primary tumor features are inadequate in predicting the presence versus absence of nodal positivity [87, 88]. Besides identifying the SLN of breast cancer [89], the state of lymph node draining from esophageal cancer was diagnosed successfully with near-infrared QDs, too [90]. Kobayashi [91] visualized migration of QD-labeled melanoma cells within draining lymphatics. This technique could enable better understanding of lymph node metastasis.

5. Metabolism and Toxicity

QDs are promising novel nanoparticles for in vivo biomedical application. To assess their usefulness, it is important to characterize their behavior in vivo, rather than rely on ex vivo measurements and theoretical considerations alone [92]. One obstacle to the in vivo study of QDs is the nonspecific uptake by reticuloendothelial system (RES) including the liver, spleen and lymph system. Particle size, surface coating and PEG-ylation influence the biodistribution of QDs. Nonspecific uptake can be decreased significantly by modifying the surface of QDs with appropriate coat/polymer, which results to prolonged plasma half-life [93–95]. In another way, Jayagopal and his colleagues [96] increased the in vivo circulation time and targeting efficiency by synthesizing QDs incorporating PEG crosslinkers and Fc-shielding mAb fragments. Comparison of the timecourse of fluorescence from Fc-shielded and non-Fc-shielded bioconjugates indicated nonspecific uptake and increased clearance of the non-Fc-shielded QD-mAb. This combination of QD

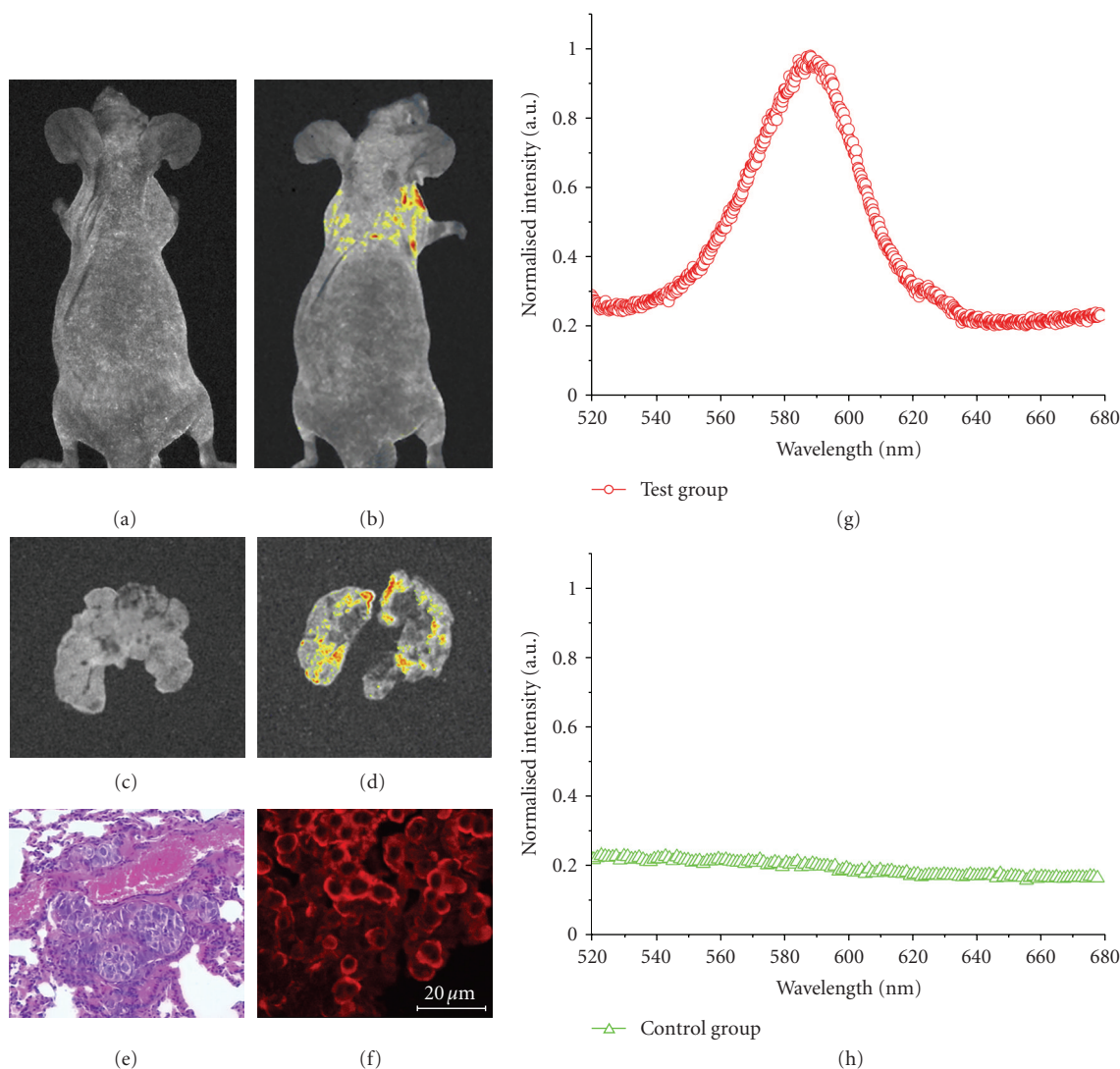


FIGURE 3: In vivo targeting and imaging of lung metastasis model with QD-AFP-Ab probes. (a) and (b) As compared with the control group (a), the whole body imaging showed that the QD fluorescence was localized in the lung metastases of the model (b). (c, d) As compared with the control group (c), the lung-imaging also showed that there was bright fluorescence in the lung metastases (d). (e) Microphotography of tumor metastasis to lungs, replacing the normal lung tissue with massive tumor cells obviously (HE stain, 200). (f) The confocal microscopic imaging of tumor metastasis to lungs, which showed the specific binding of QD-AFP-Ab probes to tumor cells. Scale bar: 20 μm. (g) and (h) The spectra analysis of the test group (g) and the control group (h) showed that the fluorescence spectra of metastases in the test group were the same with those of QD-AFP-Ab probes, but there was no characteristic 590 nm peak of the QD at those in the control group. (Work from [77].)

surface design elements offers a promising new in vivo approach to specifically label vascular cell and biomolecules of interest. The in vivo distribution and metabolism of QDs have been studied in some researches, which showed that QDs were generally localized in liver, kidney, spleen, and lung [97–101]. However, there was no universal conclusion about the pathway of QDs clearance and its influence factors. Chen et al. [102] demonstrated that the metabolic pathway of QDs were closely correlated to their aggregation states, and three metabolic pathways were disclosed after intravenous injection: (1) the QDs that maintained their original nanosize without binding in vivo can be rapidly excreted via the kidney; (2) some QDs binding to proteins

were translocated to the liver and excreted with feces; (3) an even smaller fraction of the QDs aggregated to larger particles and were retained in liver tissue for long time.

The most obvious challenge to QDs clinical use is the toxicity as most QDs contained heavy metal such as Cd²⁺. Release of Cd²⁺ from QDs will result to heavy metal toxicity, which limited the use of QDs. But it is still a controversy. Cho et al. [103] assessed the intracellular Cd²⁺ concentration in human breast cancer MCF-7 cells treated with cadmium telluride (CdTe) and core/shell cadmium selenide/zinc sulfide (CdSe/ZnS) nanoparticles capped with mercaptopropionic acid (MPA), cysteamine (Cys), or N-acetylcysteine (NAC) conjugated to cysteamine. In cells incubated with CdTe QDs,

the Cd²⁺ concentration determined by a Cd²⁺ specific cellular assay ranged from 30 to 150 nm, depending on the capping molecule. A cell viability assay revealed that CdSe/ZnS QDs were nontoxic, where the CdTe QDs were cytotoxic. However, for the various CdTe QDs samples, there was no dose-dependent correlation between cell viability and intracellular [Cd²⁺], implying that their cytotoxicity cannot be attributed solely to the toxic effect of free Cd²⁺. CdTe QDs capped with small organic ligands are cytotoxic, core shell CdSe/ZnS QDs present little damaging effects to cells. Those findings conform to with the consensus that the toxicity of QDs is not only Cd-dependent, but affected by many other factors including the size, surface charge, concentration, coat, oxidation, photo-degradation of QDs [104–107]. When injected into *Xenopus* embryos, the QDs were stable, and embryos displayed an unaltered phenotype and their health was similar to that of uninjected embryos (2×10^9 QDs/cell). At higher injection concentration (5×10^9 QDs/cell), abnormalities became apparent which may result from changes in the osmotic equilibrium of the cell [21]. Lovric et al. [108] founded out that the size of QDs contributes to their subcellular distribution and pretreatment of cells with the antioxidant N-acetylcysteine and with bovine serum albumin, but not Trolox, significantly reduced the QD-induced cell death. QDs induce cell death via mechanisms involving both Cd²⁺ and reactive oxygen species (ROS) accompanied by lysosomal enlargement and intracellular redistribution [109]. Other mechanisms of cell death induced by QDs have been revealed. In a study focused on the cellular calcium homeostasis dysregulation caused by QDs [110], it was found that unmodified QDs can induce neuron death dose dependently, via two possible mechanisms: (a) elevated cytoplasmic calcium levels for an extended period by QDs treatment, due to both extracellular calcium influx and internal calcium release from endoplasmic reticulum; and (b) QDs treatment enhanced activation and inactivation of I-Na, prolonged the time course of activation, slowed I-Na recovery, and reduced the fraction of available voltage-gated sodium channel (VGSC). Therefore, although QDs provide potential invaluable benefit, there are still biosafety considerations for in vivo imaging clinically.

6. Future Perspectives

It is clear that as biocompatible QDs are developed they will make powerful basic probes and research tools, and the delivery of QDs/QD bioconjugates is strongly affected by the nature of both the QDs conjugates and the cell types utilized [111]. A lot of techniques about QDs have been improved with the development of new QDs, major issues need to be resolved in the near future. (1) As surface and function modification endue QDs more advantages, QDs become too large for medical imaging with the diameter up to 100 nm; (2) For the stereospecific blockade effect, it is not clear how many functional molecules can conjugate to one QD, which hold back the quantification in molecular detection. (3) FRET is based on individual QDs for QDs deep in aggregation cannot be acting as energy donor, how to avoid the aggregation of QDs in vivo is an important

practical issue; (4) More studies on the toxicity of QDs are needed [53, 112–115]. (5) For the ethics reason, there is no clinical trail of QDs with large samples. Though it is revealed that QDs are stable in animal [98, 102, 116], more research about kinetics and toxicity of QDs in human are needed before extensive application for clinical diagnosis and therapy [103].

Since the first report about the application of QDs in biology in 1998, there has been no doubt about the advantages of QDs for long fluorescence time and photostability [117]. QDs offer a powerful new tool for illuminating the complex labyrinth of signal transduction pathways and uncovering the intricacies of biomolecular interaction within cells. Remarkably, QDs-base intracellular probes have advantages concurrently with superresolution optical imaging techniques, a combination of the two techniques promises to reveal the mysteries of cellular biology in unprecedented detail [17, 118, 119]. As much technologies based on QDs such as FISH, FRET, and BRET will provide an opportunity for optimizing the treatment of cancer. Cancer therapy will be influenced by QDs significantly. The National Institutes Health (NIH) and the National Nanotechnology Initiative (NNI) are investing into nanomedicine in general and resolving QD toxicity issues for medical applications in particular [120–122]. The NIH expects that over half of the biomedical advances by 2010 will be in the nanotechnology sector, and by that time, the projected market growth for molecular imaging is \$45 billion [121]. The most promising applications of QDs in cancer are tumor detection, tissue imaging, intracellular imaging, immunohistochemistry, multiplexed diagnostics, and fluoroimmunoassays. All in all, the potential of QDs is immense and would shed a new light on various medical applications.

In summary, the use of QDs in cancer investigations has increased dramatically due to their unique size-dependent optical properties. Bioconjugated near-infrared QDs probes are highly sensitive molecular imaging tools for in vivo study. Further development of QDs might enable their application in detecting and localizing metastasis, quantitative measurement of molecular targets to facilitate targeted therapy, tracking drug delivery, and monitoring the efficacy of therapeutics noninvasively in real time.

Acknowledgments

This research was supported by the grants from the New-Century Excellent Talents Supporting Program of the Ministry of Education of China (no. NCET-04-0669), the Natural Science Foundation of China (no. 20675058), the Science Fund for Creative Research Groups of the National Natural Science Foundation of China (no. 20621502).

References

- [1] A. Jemal, R. Siegel, E. Ward, Y. Hao, J. Xu, and M. J. Thun, "Cancer statistics, 2009," *CA: A Cancer Journal for Clinicians*, vol. 59, no. 4, pp. 225–249, 2009.
- [2] R. M. Hoffman, "The multiple uses of fluorescent proteins to visualize cancer in vivo," *Nature Reviews Cancer*, vol. 5, no. 10, pp. 796–806, 2005.

- [3] R. M. Hoffman, "Imaging cancer dynamics in vivo at the tumor and cellular level with fluorescent proteins," *Clinical and Experimental Metastasis*, vol. 26, no. 4, pp. 345–355, 2009.
- [4] National Cancer Institute, Cancer Nanotechnology Plan, <http://nano.cancer.gov/about-alliance/cancernanotechnology-plan.asp>.
- [5] P. D. Cozzoli, T. Pellegrino, and L. Manna, "Synthesis, properties and perspectives of hybrid nanocrystal structures," *Chemical Society Reviews*, vol. 35, no. 11, pp. 1195–1208, 2006.
- [6] P. S. Nair, K. P. Fritz, and G. D. Scholes, "Evolutionary shape control during colloidal quantum-dot growth," *Small*, vol. 3, no. 3, pp. 481–487, 2007.
- [7] U. Resch-Genger, M. Grabolle, S. Cavaliere-Jaricot, R. Nitschke, and T. Nann, "Quantum dots versus organic dyes as fluorescent labels," *Nature Methods*, vol. 5, no. 9, pp. 763–775, 2008.
- [8] J. L. Pelley, A. S. Daar, and M. A. Saner, "State of academic knowledge on toxicity and biological fate of quantum dots," *Toxicological Sciences*, vol. 112, no. 2, pp. 276–296, 2009.
- [9] K. Manzoor, S. Johnny, D. Thomas, S. Setua, D. Menon, and S. Nair, "Bio-conjugated luminescent quantum dots of doped ZnS: a cyto-friendly system for targeted cancer imaging," *Nanotechnology*, vol. 20, no. 6, Article ID 065102, 2009.
- [10] X. Michalet, F. F. Pinaud, L. A. Bentolila, et al., "Quantum dots for live cells, in vivo imaging, and diagnostics," *Science*, vol. 307, no. 5709, pp. 538–544, 2005.
- [11] S. M. Reimann and M. Manninen, "Electronic structure of quantum dots," *Reviews of Modern Physics*, vol. 74, no. 4, pp. 1283–1342, 2002.
- [12] A. Gokarna, L.-H. Jin, J. S. Hwang, et al., "Quantum dot-based protein micro- and nanoarrays for detection of prostate cancer biomarkers," *Proteomics*, vol. 8, no. 9, pp. 1809–1818, 2008.
- [13] F. Marchal, E. Pic, T. Pons, B. Dubertret, L. Bolotine, and F. Guillemin, "Quantum dots in oncological surgery: the future for surgical margin status?" *Bulletin du Cancer*, vol. 95, no. 12, pp. 1149–1153, 2008.
- [14] K. C. Weng, C. O. Noble, B. Papahadjopoulos-Sternberg, et al., "Targeted tumor cell internalization and imaging of multifunctional quantum dot-conjugated immunoliposomes in vitro and in vivo," *Nano Letters*, vol. 8, no. 9, pp. 2851–2857, 2008.
- [15] M. Zhou and I. Ghosh, "Quantum dots and peptides: a bright future together," *Biopolymers*, vol. 88, no. 3, pp. 325–339, 2007.
- [16] F. Erogbogbo, K.-T. Yong, I. Roy, G. X. Xu, P. N. Prasad, and M. T. Swihart, "Biocompatible luminescent silicon quantum dots for imaging of cancer cells," *ACS Nano*, vol. 2, no. 5, pp. 873–878, 2008.
- [17] E. T. Ben-Ari, "Nanoscale quantum dots hold promise for cancer applications," *Journal of the National Cancer Institute*, vol. 95, no. 7, pp. 502–504, 2003.
- [18] A. F. E. Hezinger, J. Tessmer, and A. Gopferich, "Polymer coating of quantum dots—a powerful tool toward diagnostics and sensorics," *European Journal of Pharmaceutics and Biopharmaceutics*, vol. 68, no. 1, pp. 138–152, 2008.
- [19] K.-T. Yong, I. Roy, M. T. Swihart, and P. N. Prasad, "Multifunctional nanoparticles as biocompatible targeted probes for human cancer diagnosis and therapy," *Journal of Materials Chemistry*, vol. 19, no. 27, pp. 4655–4672, 2009.
- [20] I. L. Medintz, H. Mattoussi, and A. R. Clapp, "Potential clinical applications of quantum dots," *International Journal of Nanomedicine*, vol. 3, no. 2, pp. 151–167, 2008.
- [21] B. Dubertret, P. Skourides, D. J. Norris, V. Noireaux, A. H. Brivanlou, and A. Libchaber, "In vivo imaging of quantum dots encapsulated in phospholipid micelles," *Science*, vol. 298, no. 5599, pp. 1759–1762, 2002.
- [22] A. M. Smith, S. Dave, S. Nie, L. True, and X. Gao, "Multicolor quantum dots for molecular diagnostics of cancer," *Expert Review of Molecular Diagnostics*, vol. 6, no. 2, pp. 231–244, 2006.
- [23] H. Zhang, D. Yee, and C. Wang, "Quantum dots for cancer diagnosis and therapy: biological and clinical perspectives," *Nanomedicine*, vol. 3, no. 1, pp. 83–91, 2008.
- [24] A. M. Smith, H. Duan, A. M. Mohs, and S. Nie, "Bioconjugated quantum dots for in vivo molecular and cellular imaging," *Advanced Drug Delivery Reviews*, vol. 60, no. 11, pp. 1226–1240, 2008.
- [25] M. V. Yezhelyev, A. Al-Hajj, C. Morris, et al., "In situ molecular profiling of breast cancer biomarkers with multicolor quantum dots," *Advanced Materials*, vol. 19, no. 20, pp. 3146–3151, 2007.
- [26] W. J. M. Mulder, K. Castermans, J. R. van Beijnum, et al., "Molecular imaging of tumor angiogenesis using $\alpha\beta 3$ -integrin targeted multimodal quantum dots," *Angiogenesis*, vol. 12, no. 1, pp. 17–24, 2009.
- [27] H. Tada, H. Higuchi, T. M. Wanatabe, and N. Ohuchi, "In vivo real-time tracking of single quantum dots conjugated with monoclonal anti-HER2 antibody in tumors of mice," *Cancer Research*, vol. 67, no. 3, pp. 1138–1144, 2007.
- [28] B. S. Shah, P. A. Clark, E. K. Moiola, M. A. Stroschio, and J. J. Mao, "Labeling of mesenchymal stem cells by bioconjugated quantum dots," *Nano Letters*, vol. 7, no. 10, pp. 3071–3079, 2007.
- [29] K. T. Yong, H. Ding, I. Roy, et al., "Imaging pancreatic cancer using bioconjugated inq quantum dots," *ACS Nano*, vol. 3, no. 3, pp. 502–510, 2009.
- [30] C. Chen, J. Peng, H.-S. Xia, et al., "Quantum dots-based immunofluorescence technology for the quantitative determination of HER2 expression in breast cancer," *Biomaterials*, vol. 30, no. 15, pp. 2912–2918, 2009.
- [31] B. R. Smith, Z. Cheng, A. De, A. L. Koh, R. Sinclair, and S. S. Gambhir, "Real-time intravital imaging of RGD-quantum dot binding to luminal endothelium in mouse tumor neovasculature," *Nano Letters*, vol. 8, no. 9, pp. 2599–2606, 2008.
- [32] C. P. Parungo, D. I. Soybel, Y. L. Colson, et al., "Lymphatic drainage of the peritoneal space: a pattern dependent on bowel lymphatics," *Annals of Surgical Oncology*, vol. 14, no. 2, pp. 286–298, 2007.
- [33] H. Lu, B. Li, Y. Kang, et al., "Paclitaxel nanoparticle inhibits growth of ovarian cancer xenografts and enhances lymphatic targeting," *Cancer Chemotherapy and Pharmacology*, vol. 59, no. 2, pp. 175–181, 2007.
- [34] E. V. S. Høgdall, L. Christensen, S. K. Kjaer, et al., "CA125 expression pattern, prognosis and correlation with serum CA125 in ovarian tumor patients. From The Danish "MAL-OVA" Ovarian Cancer Study," *Gynecologic Oncology*, vol. 104, no. 3, pp. 508–515, 2007.
- [35] R. W. Tothill, A. V. Tinker, J. George, et al., "Novel molecular subtypes of serous and endometrioid ovarian cancer linked to clinical outcome," *Clinical Cancer Research*, vol. 14, no. 16, pp. 5198–5208, 2008.
- [36] Y. Zheng, D. Katsaros, S. J. C. Shan, et al., "A multiparametric panel for ovarian cancer diagnosis, prognosis, and response to chemotherapy," *Clinical Cancer Research*, vol. 13, no. 23, pp. 6984–6992, 2007.

- [37] H.-Z. Wang, H.-Y. Wang, R.-Q. Liang, and K.-C. Ruan, "Detection of tumor marker CA125 in ovarian carcinoma using quantum dots," *Acta Biochimica et Biophysica Sinica*, vol. 36, no. 10, pp. 681–686, 2004.
- [38] B. B. Nathwani, M. Jaffari, A. R. Juriani, A. B. Mathur, and K. E. Meissner, "Fabrication and characterization of silk-fibroin-coated quantum dots," *IEEE Transactions on Nanobioscience*, vol. 8, no. 1, pp. 72–77, 2009.
- [39] X. Wu, H. Liu, J. Liu, et al., "Immunofluorescent labeling of cancer marker Her2 and other cellular targets with semiconductor quantum dots," *Nature Biotechnology*, vol. 21, no. 1, pp. 41–46, 2003.
- [40] L. Harris, H. Fritsche, R. Mennel, et al., "American society of clinical oncology 2007 update of recommendations for the use of tumor markers in breast cancer," *Journal of Clinical Oncology*, vol. 25, no. 33, pp. 5287–5312, 2007.
- [41] D. J. Slamon, W. Godolphin, L. A. Jones, et al., "Studies of the HER-2/neu proto-oncogene in human breast and ovarian cancer," *Science*, vol. 244, no. 4905, pp. 707–712, 1989.
- [42] A. Goldhirsch, J. H. Glick, R. D. Gelber, A. S. Coates, B. Thurlimann, and H. J. Senn, "Meeting highlights: international expert consensus on the primary therapy of early breast cancer 2005," *Annals of Oncology*, vol. 16, no. 10, pp. 1569–1583, 2005.
- [43] M. M. Moasser, "The oncogene HER2: its signaling and transforming functions and its role in human cancer pathogenesis," *Oncogene*, vol. 26, no. 45, pp. 6469–6487, 2007.
- [44] H. Tsuda, "HER-2 (c-erbB-2) test update: present status and problems," *Breast Cancer*, vol. 13, no. 3, pp. 236–248, 2006.
- [45] A. C. Wolff, M. E. H. Hammond, J. N. Schwartz, et al., "American Society of Clinical Oncology/College of American Pathologists guideline recommendations for human epidermal growth factor receptor 2 testing in breast cancer," *Journal of Clinical Oncology*, vol. 25, no. 1, pp. 118–145, 2007.
- [46] S. Li-Shishido, T. M. Watanabe, H. Tada, H. Higuchi, and N. Ohuchi, "Reduction in nonfluorescence state of quantum dots on an immunofluorescence staining," *Biochemical and Biophysical Research Communications*, vol. 351, no. 1, pp. 7–13, 2006.
- [47] Y. Xiao, X. Gao, G. Gannot, et al., "Quantitation of HER2 and telomerase biomarkers in solid tumors with IgY antibodies and nanocrystal detection," *International Journal of Cancer*, vol. 122, no. 10, pp. 2178–2186, 2008.
- [48] S. J. Freedland, J. M. Hotaling, N. J. Fitzsimons, et al., "PSA in the new millennium: a powerful predictor of prostate cancer prognosis and radical prostatectomy outcomes—results from the SEARCH database," *European Urology*, vol. 53, no. 4, pp. 758–766, 2008.
- [49] M. Noguchi, T. A. Stamey, J. E. McNeal, and C. M. Yemoto, "Preoperative serum prostate specific antigen does not reflect biochemical failure rates after radical prostatectomy in men with large volume cancers," *Journal of Urology*, vol. 164, no. 5, pp. 1596–1600, 2000.
- [50] R. A. Smith, V. Cokkinides, and O. W. Brawley, "Cancer screening in the United States, 2009: a review of current American Cancer Society guidelines and issues in cancer screening," *CA: A Cancer Journal for Clinicians*, vol. 59, no. 1, pp. 27–41, 2009.
- [51] X. Gao, Y. Cui, R. M. Levenson, L. W. K. Chung, and S. Nie, "In vivo cancer targeting and imaging with semiconductor quantum dots," *Nature Biotechnology*, vol. 22, no. 8, pp. 969–976, 2004.
- [52] C. Shi, G. Zhou, Y. Zhu, et al., "Quantum dots-based multiplexed immunohistochemistry of protein expression in human prostate cancer cells," *European Journal of Histochemistry*, vol. 52, no. 2, pp. 127–134, 2008.
- [53] H. M. E. Azzazy, M. M. H. Mansour, and S. C. Kazmierczak, "Nanodiagnostics: a new frontier for clinical laboratory medicine," *Clinical Chemistry*, vol. 52, no. 7, pp. 1238–1246, 2006.
- [54] X. Gao, L. W. K. Chung, and S. Nie, "Quantum dots for in vivo molecular and cellular imaging," *Methods in Molecular Biology*, vol. 374, pp. 135–145, 2007.
- [55] Y. Wang, A. M. Dossey, J. W. Froude II, et al., "PSA fluoroimmunoassays using anti-PSA ScFv and quantum-dot conjugates," *Nanomedicine*, vol. 3, no. 4, pp. 475–483, 2008.
- [56] S. Barua and K. Rege, "Cancer-cell-phenotype-dependent differential intracellular trafficking of unconjugated quantum dots," *Small*, vol. 5, no. 3, pp. 370–376, 2009.
- [57] R. H. Hruban, A. Maitra, S. E. Kern, and M. Goggins, "Precursors to pancreatic cancer," *Gastroenterology Clinics of North America*, vol. 36, no. 4, pp. 831–849, 2007.
- [58] S. L. Swierczynski, A. Maitra, S. C. Abraham, et al., "Analysis of novel tumor markers in pancreatic and biliary carcinomas using tissue microarrays," *Human Pathology*, vol. 35, no. 3, pp. 357–366, 2004.
- [59] X. Montet, R. Weissleder, and L. Josephson, "Imaging pancreatic cancer with a peptide-nanoparticle conjugate targeted to normal pancreas," *Bioconjugate Chemistry*, vol. 17, no. 4, pp. 905–911, 2006.
- [60] L. Yang, H. Mao, Y. A. Wang, et al., "Single chain epidermal growth factor receptor antibody conjugated nanoparticles for in vivo tumor targeting and imaging," *Small*, vol. 5, no. 2, pp. 235–243, 2009.
- [61] L. Yang, H. Mao, Z. Cao, et al., "Molecular imaging of pancreatic cancer in an animal model using targeted multifunctional nanoparticles," *Gastroenterology*, vol. 136, no. 5, pp. 1514–1525, 2009.
- [62] J. Qian, K.-T. Yong, I. Roy, et al., "Imaging pancreatic cancer using surface-functionalized quantum dots," *Journal of Physical Chemistry B*, vol. 111, no. 25, pp. 6969–6972, 2007.
- [63] I. J. Fidler, "The pathogenesis of cancer metastasis: the 'seed and soil' hypothesis revisited," *Nature Reviews Cancer*, vol. 3, no. 6, pp. 453–458, 2003.
- [64] L. Weiss, "Metastasis of cancer: a conceptual history from antiquity to the 1990s," *Cancer and Metastasis Reviews*, vol. 19, no. 3–4, pp. 193–383, 2000.
- [65] K.-T. Yong, "Mn-doped near-infrared quantum dots as multimodal targeted probes for pancreatic cancer imaging," *Nanotechnology*, vol. 20, no. 1, Article ID 015102, 10 pages, 2009.
- [66] A. E. Karnoub, A. B. Dash, A. P. Vo, et al., "Mesenchymal stem cells within tumour stroma promote breast cancer metastasis," *Nature*, vol. 449, no. 7162, pp. 557–563, 2007.
- [67] J. Yoo, T. Kambara, K. Gonda, and H. Higuchi, "Intracellular imaging of targeted proteins labeled with quantum dots," *Experimental Cell Research*, vol. 314, no. 19, pp. 3563–3569, 2008.
- [68] D. M. Parkin, F. Bray, J. Ferlay, and P. Pisani, "Global cancer statistics, 2002," *CA: A Cancer Journal for Clinicians*, vol. 55, no. 2, pp. 74–108, 2005.
- [69] J. Bruix and M. Sherman, "Management of hepatocellular carcinoma," *Hepatology*, vol. 42, no. 5, pp. 1208–1236, 2005.
- [70] J. M. Llovet, A. Burroughs, and J. Bruix, "Hepatocellular carcinoma," *Lancet*, vol. 362, no. 9399, pp. 1907–1917, 2003.
- [71] M. B. Thomas and A. X. Zhu, "Hepatocellular carcinoma: the need for progress," *Journal of Clinical Oncology*, vol. 23, no. 13, pp. 2892–2899, 2005.

- [72] T. Morinaga, M. Sakai, T. G. Wegmann, and T. Tamaoki, "Primary structures of human α -fetoprotein and its mRNA," *Proceedings of the National Academy of Sciences of the United States of America*, vol. 80, no. 15, pp. 4604–4608, 1983.
- [73] C. J. P. Smith and P. C. Kelleher, "Alpha-fetoprotein molecular heterogeneity. Physiological correlations with normal growth, carcinogenesis and tumor growth," *Biochimica et Biophysica Acta*, vol. 605, no. 1, pp. 1–32, 1980.
- [74] F. Trevisani, P. E. D'Intino, A. M. Morselli-Labate, et al., "Serum α -fetoprotein for diagnosis of hepatocellular carcinoma in patients with chronic liver disease: influence of HBsAg and anti-HCV status," *Journal of Hepatology*, vol. 34, no. 4, pp. 570–575, 2001.
- [75] X. Yu, L. Chen, Y. Deng, et al., "Fluorescence analysis with quantum dot probes for hepatoma under one- and two-photon excitation," *Journal of Fluorescence*, vol. 17, no. 2, pp. 243–247, 2007.
- [76] X. Yu, L. Chen, K. Li, et al., "Immunofluorescence detection with quantum dot bioconjugates for hepatoma in vivo," *Journal of Biomedical Optics*, vol. 12, no. 1, Article ID 014008, 2007.
- [77] L.-D. Chen, J. Liu, X.-F. Yu, et al., "The biocompatibility of quantum dot probes used for the targeted imaging of hepatocellular carcinoma metastasis," *Biomaterials*, vol. 29, no. 31, pp. 4170–4176, 2008.
- [78] K. Dowlatshahi, M. Fan, H. C. Snider, and F. A. Habib, "Lymph node micrometastases from breast carcinoma: reviewing the dilemma," *Cancer*, vol. 80, no. 7, pp. 1188–1197, 1997.
- [79] H. Kobayashi, S. Kawamoto, M. Bernardo, M. W. Brechbiel, M. V. Knopp, and P. L. Choyke, "Delivery of gadolinium-labeled nanoparticles to the sentinel lymph node: comparison of the sentinel node visualization and estimations of intra-nodal gadolinium concentration by the magnetic resonance imaging," *Journal of Controlled Release*, vol. 111, no. 3, pp. 343–351, 2006.
- [80] R. Jain, P. Dandekar, and V. Patravale, "Diagnostic nanocarriers for sentinel lymph node imaging," *Journal of Controlled Release*, vol. 138, no. 2, pp. 90–102, 2009.
- [81] S. Kim, Y. T. Lim, E. G. Soltesz, et al., "Near-infrared fluorescent type II quantum dots for sentinel lymph node mapping," *Nature Biotechnology*, vol. 22, no. 1, pp. 93–97, 2004.
- [82] L. A. Bentolila, Y. Ebenstein, and S. Weiss, "Quantum dots for in vivo small-animal imaging," *Journal of Nuclear Medicine*, vol. 50, no. 4, pp. 493–496, 2009.
- [83] K.-T. Yong, I. Roy, H. Ding, E. J. Bergey, and P. N. Prasad, "Biocompatible near-infrared quantum dots as ultrasensitive probes for long-term in vivo imaging applications," *Small*, vol. 5, no. 17, pp. 1997–2004, 2009.
- [84] B. Ballou, L. A. Ernst, S. Andreko, et al., "Sentinel lymph node imaging using quantum dots in mouse tumor models," *Bioconjugate Chemistry*, vol. 18, no. 2, pp. 389–396, 2007.
- [85] A. D. Purushotham, S. Upponi, M. B. Klevesath, et al., "Morbidity after sentinel lymph node biopsy in primary breast cancer: results from a randomized controlled trial," *Journal of Clinical Oncology*, vol. 23, no. 19, pp. 4312–4321, 2005.
- [86] U. Veronesi, G. Paganelli, G. Viale, et al., "Sentinel lymph node biopsy and axillary dissection in breast cancer: results in a large series," *Journal of the National Cancer Institute*, vol. 91, no. 4, pp. 368–373, 1999.
- [87] R. Crane-Okada, R. A. Wascher, D. Elashoff, and A. E. Giuliano, "Long-term morbidity of sentinel node biopsy versus complete axillary dissection for unilateral breast cancer," *Annals of Surgical Oncology*, vol. 15, no. 7, pp. 1996–2005, 2008.
- [88] G. H. Lyman, A. E. Giuliano, M. R. Somerfield, et al., "American Society of Clinical Oncology guideline recommendations for sentinel lymph node biopsy in early-stage breast cancer," *Journal of Clinical Oncology*, vol. 23, no. 30, pp. 7703–7720, 2005.
- [89] Y. Hama, Y. Koyama, Y. Urano, P. L. Choyke, and H. Kobayashi, "Simultaneous two-color spectral fluorescence lymphangiography with near infrared quantum dots to map two lymphatic flows from the breast and the upper extremity," *Breast Cancer Research and Treatment*, vol. 103, no. 1, pp. 23–28, 2007.
- [90] C. P. Parungo, S. Ohnishi, S.-W. Kim, et al., "Intraoperative identification of esophageal sentinel lymph nodes with near-infrared fluorescence imaging," *Journal of Thoracic and Cardiovascular Surgery*, vol. 129, no. 4, pp. 844–850, 2005.
- [91] H. Kobayashi, M. Ogawa, N. Kosaka, P. L. Choyke, and Y. Urano, "Multicolor imaging of lymphatic function with two nanomaterials: quantum dot-labeled cancer cells and dendrimer-based optical agents," *Nanomedicine*, vol. 4, no. 4, pp. 411–419, 2009.
- [92] A. M. Mohs, H. W. Duan, B. A. Kairdolf, A. M. Smith, and S. M. Nie, "Proton-resistant quantum dots: stability in gastrointestinal fluids and implications for oral delivery of nanoparticle agents," *Nano Research*, vol. 2, no. 6, pp. 500–508, 2009.
- [93] B. Ballou, B. C. Lagerholm, L. A. Ernst, M. P. Bruchez, and A. S. Waggoner, "Noninvasive imaging of quantum dots in mice," *Bioconjugate Chemistry*, vol. 15, no. 1, pp. 79–86, 2004.
- [94] X. Gao, L. Yang, J. A. Petros, F. F. Marshall, J. W. Simons, and S. Nie, "In vivo molecular and cellular imaging with quantum dots," *Current Opinion in Biotechnology*, vol. 16, no. 1, pp. 63–72, 2005.
- [95] M. L. Schipper, G. Iyer, A. L. Koh, et al., "Particle size, surface coating, and PEGylation influence the biodistribution of quantum dots in living mice," *Small*, vol. 5, no. 1, pp. 126–134, 2009.
- [96] A. Jayagopal, P. K. Russ, and F. R. Haselton, "Surface engineering of quantum dots for in vivo vascular imaging," *Bioconjugate Chemistry*, vol. 18, no. 5, pp. 1424–1433, 2007.
- [97] H. S. Choi, B. I. Ipe, P. Misra, J. H. Lee, M. G. Bawendi, and J. V. Frangioni, "Tissue- and organ-selective biodistribution of NIR fluorescent quantum dots," *Nano Letters*, vol. 9, no. 6, pp. 2354–2359, 2009.
- [98] H. S. Choi, W. Liu, P. Misra, et al., "Renal clearance of quantum dots," *Nature Biotechnology*, vol. 25, no. 10, pp. 1165–1170, 2007.
- [99] Y. Inoue, K. Izawa, K. Yoshikawa, H. Yamada, A. Tojo, and K. Ohtomo, "In vivo fluorescence imaging of the reticuloendothelial system using quantum dots in combination with bioluminescent tumour monitoring," *European Journal of Nuclear Medicine and Molecular Imaging*, vol. 34, no. 12, pp. 2048–2056, 2007.
- [100] V. Karabanovas, E. Zakarevicius, A. Sukackaite, G. Streckyte, and R. Rotomskis, "Examination of the stability of hydrophobic (CdSe)ZnS quantum dots in the digestive tract of rats," *Photochemical and Photobiological Sciences*, vol. 7, no. 6, pp. 725–729, 2008.
- [101] W. Liu, H. S. Choi, J. P. Zimmer, E. Tanaka, J. V. Frangioni, and M. Bawendi, "Compact cysteine-coated CdSe(ZnCdS)

- quantum dots for in vivo applications,” *Journal of the American Chemical Society*, vol. 129, no. 47, pp. 14530–14531, 2007.
- [102] Z. Chen, H. Chen, H. Meng, et al., “Bio-distribution and metabolic paths of silica coated CdSeS quantum dots,” *Toxicology and Applied Pharmacology*, vol. 230, no. 3, pp. 364–371, 2008.
- [103] S. J. Cho, D. Maysinger, M. Jain, B. Roder, S. Hackbarth, and F. M. Winnik, “Long-term exposure to CdTe quantum dots causes functional impairments in live cells,” *Langmuir*, vol. 23, no. 4, pp. 1974–1980, 2007.
- [104] W.-H. Chan, N.-H. Shiao, and P.-Z. Lu, “CdSe quantum dots induce apoptosis in human neuroblastoma cells via mitochondrial-dependent pathways and inhibition of survival signals,” *Toxicology Letters*, vol. 167, no. 3, pp. 191–200, 2006.
- [105] R. Hardman, “A toxicologic review of quantum dots: toxicity depends on physicochemical and environmental factors,” *Environmental Health Perspectives*, vol. 114, no. 2, pp. 165–172, 2006.
- [106] H. Li, Q. Zhou, W. Liu, B. Yan, Y. Zhao, and G. Jiang, “Progress in the toxicological researches for quantum dots,” *Science in China, Series B*, vol. 51, no. 5, pp. 393–400, 2008.
- [107] A. Anas, H. Akita, H. Harashima, T. Itoh, M. Ishikawa, and V. Biju, “Photosensitized breakage and damage of DNA by CdSe-ZnS quantum dots,” *Journal of Physical Chemistry B*, vol. 112, no. 32, pp. 10005–10011, 2008.
- [108] J. Lovric, H. S. Bazzi, Y. Cuie, G. R. A. Fortin, F. M. Winnik, and D. Maysinger, “Differences in subcellular distribution and toxicity of green and red emitting CdTe quantum dots,” *Journal of Molecular Medicine*, vol. 83, no. 5, pp. 377–385, 2005.
- [109] M. C. Mancini, B. A. Kairdolf, A. M. Smith, and S. Nie, “Oxidative quenching and degradation of polymer-encapsulated quantum dots: new insights into the long-term fate and toxicity of nanocrystals in vivo,” *Journal of the American Chemical Society*, vol. 130, no. 33, pp. 10836–10837, 2008.
- [110] M. Tang, T. Xing, J. Zeng, et al., “Unmodified CdSe quantum dots induce elevation of cytoplasmic calcium levels and impairment of functional properties of sodium channels in rat primary cultured hippocampal neurons,” *Environmental Health Perspectives*, vol. 116, no. 7, pp. 915–922, 2008.
- [111] J. B. Delehanty, H. Mattoussi, and I. L. Medintz, “Delivering quantum dots into cells: strategies, progress and remaining issues,” *Analytical and Bioanalytical Chemistry*, vol. 393, no. 4, pp. 1091–1105, 2009.
- [112] J. Drbohlavova, V. Adam, R. Kizek, and J. Hubalek, “Quantum dots—characterization, preparation and usage in biological systems,” *International Journal of Molecular Sciences*, vol. 10, no. 2, pp. 656–673, 2009.
- [113] W. A. Hild, M. Breunig, and A. Goepferich, “Quantum dots—nano-sized probes for the exploration of cellular and intracellular targeting,” *European Journal of Pharmaceutics and Biopharmaceutics*, vol. 68, no. 2, pp. 153–168, 2008.
- [114] B.-K. Pong, B. L. Trout, and J.-Y. Lee, “Modified ligand-exchange for efficient solubilization of CdSe/ZnS quantum dots in water: a procedure guided by computational studies,” *Langmuir*, vol. 24, no. 10, pp. 5270–5276, 2008.
- [115] M. A. Walling, J. A. Novak, and J. R. E. Shepard, “Quantum dots for live cell and in vivo imaging,” *International Journal of Molecular Sciences*, vol. 10, no. 2, pp. 441–491, 2009.
- [116] Y. Higuchi, M. Oka, S. Kawakami, and M. Hashida, “Mannosylated semiconductor quantum dots for the labeling of macrophages,” *Journal of Controlled Release*, vol. 125, no. 2, pp. 131–136, 2008.
- [117] D. J. Bharali, D. W. Lucey, H. Jayakumar, H. E. Pudavar, and P. N. Prasad, “Folate-receptor-mediated delivery of InP quantum dots for bioimaging using confocal and two-photon microscopy,” *Journal of the American Chemical Society*, vol. 127, no. 32, pp. 11364–11371, 2005.
- [118] A. M. Smith, A. M. Mohs, and S. Nie, “Tuning the optical and electronic properties of colloidal nanocrystals by lattice strain,” *Nature Nanotechnology*, vol. 4, no. 1, pp. 56–63, 2009.
- [119] A. M. Smith and S. Nie, “Next-generation quantum dots,” *Nature Biotechnology*, vol. 27, no. 8, pp. 732–733, 2009.
- [120] R. Bawa, “Will the nanomedicine ‘patent land grab’ thwart commercialization?” *Nanomedicine: Nanotechnology, Biology, and Medicine*, vol. 1, no. 4, pp. 346–350, 2005.
- [121] T. Flynn and C. Wei, “The pathway to commercialization for nanomedicine,” *Nanomedicine: Nanotechnology, Biology, and Medicine*, vol. 1, no. 1, pp. 47–51, 2005.
- [122] National Nanotechnology Initiative (NNI), <http://www.nano.gov>.

Research Article

Development of Near Infrared-Fluorescent Nanophosphors and Applications for Cancer Diagnosis and Therapy

**Tamotsu Zako,^{1,2} Hiroshi Hyodo,^{3,4,5} Kosuke Tsuji,³ Kimikazu Tokuzen,³
Hidehiro Kishimoto,^{5,6} Masaaki Ito,⁷ Kazuhiro Kaneko,⁸ Mizuo Maeda,^{1,2}
and Kohei Soga^{3,4,5}**

¹ Bioengineering Laboratory, RIKEN Institute, 2-1 Hirosawa, Wako, Saitama 351-0198, Japan

² Nano-Scale Science & Technology Research Group, RIKEN Institute, 2-1 Hirosawa, Wako, Saitama 351-0198, Japan

³ Department of Material Science and Technology, Tokyo University of Science, 2641 Yamazaki, Noda, Chiba 278-8510, Japan

⁴ Polyscale Technology Research Center, Tokyo University of Science, 2641 Yamazaki, Noda, Chiba 278-8510, Japan

⁵ Center for Technologies against Cancer, Tokyo University of Science, 2641 Yamazaki, Noda, Chiba 278-8510, Japan

⁶ Research Institute for Biological Sciences, Tokyo University of Science, 2669 Yamazaki, Noda, Chiba 278-0022, Japan

⁷ Department of Colorectal and Pelvic Surgery, National Cancer Center Hospital East, Kashiwanoha 6-5-1, Kashiwa, Chiba 277-8577, Japan

⁸ Division of Digestive Endoscopy and Gastrointestinal Oncology, National Cancer Center Hospital East, Kashiwanoha 6-5-1, Kashiwa, Chiba 277-8577, Japan

Correspondence should be addressed to Tamotsu Zako, zako@riken.jp and Kohei Soga, mail@ksoga.com

Received 1 November 2009; Revised 25 December 2009; Accepted 5 March 2010

Academic Editor: Huisheng Peng

Copyright © 2010 Tamotsu Zako et al. This is an open access article distributed under the Creative Commons Attribution License, which permits unrestricted use, distribution, and reproduction in any medium, provided the original work is properly cited.

The use of near infrared (NIR) light for biomedical photonics in the wavelength region between 800 and 2000 nm, which is called “biological window”, has received particular attention since water and biological tissues have minimal optical loss due to scattering and absorption as well as autofluorescence in this region. Recent development of InGaAs CCD enables observations in this wavelength region. In the present paper, we report development of Yb and Er-doped yttrium oxide nanoparticles ($Y_2O_3:YbEr$ -NP) which show strong NIR emission under NIR excitation (NIR-NIR emission). We also demonstrate that NIR emission can be observed through swine colon wall. Based on these results, we propose a possible application of $Y_2O_3:YbEr$ -NP for cancer diagnosis and therapy using NIR-NIR imaging system. Our results also suggest potential applications of $Y_2O_3:YbEr$ -NP for noninvasive detection of various diseases.

1. Introduction

Bioimaging technique has received particular attention as an essential tool in the field of biomedical research through the observation of biological phenomena both in vivo and in vitro. The use of near infrared (NIR) light in the wavelength region between 800 and 2000 nm for biomedical photonics attracts great interest because this region is a so-called “biological window”, where water and biological tissues have minimal absorbance and autofluorescence. As shown in the loss spectrum of human skin [1] (see Figure 1 of Supplementary Material available online at [doi:10.1155/2010/491471](https://doi.org/10.1155/2010/491471)), one can expect the lowest loss of the spectrum within the above region.

Recently, upconverting (UC) phosphors (UCPs) have been used for bioimaging (Figure 1) [2–8]. UCPs are ceramic materials containing rare earth ions. The materials can absorb IR radiation and upconvert it to emit visible light by stepwise excitation among discrete energy levels of the rare earth ions (NIR-VIS imaging) [9]. For example, yttrium oxide (Y_2O_3) matrix containing several atomic % of erbium (Er) exhibits upconversion emission at 550 nm (green) and 660 nm (red) following excitation at 980 nm. The advantage of NIR-VIS bioimaging is that NIR light can penetrate deeper into tissues due its lower scattering.

The wavelength for biomedical photonics has been limited due to the use of the silicon-based CCD. The observation wavelength is limited to at most 1100 nm due to the band

gap of silicon. In recent years, however, the InGaAs CCD which can cover wavelength between 800 and 2200 nm has become available. Considering various advantages of the NIR window, the time is ideal for the development of phosphors to emit fluorescence in this region.

Rare-earth doped ceramics can be a good candidate, since these are known to emit efficient fluorescence in the NIR wavelength region by NIR excitation. For example, the most representative solid state laser material Nd:YAG (Nd-doped yttrium aluminum garnet) can emit light with a wavelength of 1064-nm with 800-nm excitation [10]. Er-doped silicate glass fibers are used to amplify the signal of long-distance fiber optical communication by emitting 1550-nm fluorescence with 980-nm excitation [11]. The authors have previously reported that Er-doped yttrium oxide nanoparticles ($Y_2O_3:Er$ -NP) showed NIR fluorescence (1550 nm) with NIR excitation [12]. The advantage of this NIR-NIR imaging is that both excitation and emission light can penetrate deep into/from tissues, which enables imaging of the target inside the tissues (Figure 1).

In this study, we report a development of Yb and Er-doped yttrium oxide nanoparticles ($Y_2O_3:YbEr$ -NP), which possess higher NIR emission than $Y_2O_3:Er$ -NP. Yb^{3+} was added as a so-called “sensitizer” to increase the NIR emission. Since Yb^{3+} has much larger absorption efficiency and the excitation energy can be efficiently transferred to Er^{3+} in case of upconversion phosphors [9], we added the Yb^{3+} codopant as a sensitizer expecting the same effect for the 1550 nm NIR emission of Er^{3+} . We also demonstrated for the first time that NIR emission could be observed even through the swine colon wall. Based on this observation, we propose possible new NIR-NIR biophotonics applications for cancer diagnosis and therapy using $Y_2O_3:YbEr$ -NP, especially for resection surgery of colon cancer.

2. Material and Methods

2.1. Materials. $Y(NO_3)_3 \cdot 6H_2O$ (99.99% purity) and Urea (99.0% purity) were purchased from Kanto Chemicals (Tokyo, Japan). $Er(NO_3)_3 \cdot 5H_2O$ (>99% purity), $Yb(NO_3)_3 \cdot 5H_2O$ (99.9% purity) and Na_2CO_3 (99% purity) were obtained from Kojundo Chemical Laboratory (Saitama, Japan).

2.2. Preparation of NIR Biophotonic Nanoparticles. $Y_2O_3:YbEr$ -NP were prepared by the homogeneous precipitation method as used for preparation of upconversion nanoparticles [13]. Twenty mmol/L $Y(NO_3)_3$, 0.2 mmol/L $Yb(NO_3)_3$, and 0.2 mmol/L $Er(NO_3)_3$ were dissolved in 200 mL purified water, mixed with 100 mL of 4 mol/L Urea solution, and stirred for 1 hour at 100°C. The obtained precipitates were separated by centrifugation, and dried at 80°C for 12 hours. The hydroxide or hydroxyl carbonated precursors were calcinated at 1200°C for 60 minutes in an electric furnace to convert them into anhydrous crystalline Y_2O_3 nanoparticles doped with Yb and Er.

2.3. Characterization of NIR Biophotonic Nanoparticles. The prepared $Y_2O_3:YbEr$ -NP were provided for characterization

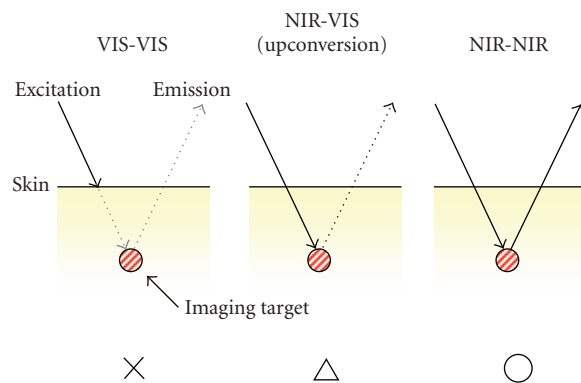


FIGURE 1: Advantage of NIR-NIR imaging system. Near infrared (NIR) emission by NIR excitation is observed using a NIR-NIR system. Due to weaker scattering and absorption, NIR light can penetrate deeper into/from tissues. In contrast, excitation light in the visible (VIS) region cannot reach the imaging target in tissues in the conventional VIS-VIS imaging. In upconversion (NIR-VIS) imaging, although NIR excitation light can reach its target in tissues, only a weak VIS emission can be obtained.

using FE-SEM (S-4200, Hitachi Ltd., Tokyo, Japan) and XRD (XRD-6100, Shimadzu, Kyoto, Japan) with $CuK\alpha$ radiation.

Optical absorption spectra were observed using a spectrometer (U-4000, Hitachi Ltd., Tokyo, Japan) equipped with an integrating sphere. The loss spectrum of the swine colon was also observed using the same equipment and sandwiching a slice of the colon (thickness: 250–330 μm) between two glass slides. The loss spectra were measured in a normal mode without using the integrating sphere.

Fluorescence spectra of $Y_2O_3:YbEr$ -NP and $Y_2O_3:Er$ -NP were recorded using a spectrometer (AvaSpec-NIR256-1.7, Avantes, Eerbeek, Netherlands) under an excitation of 980-nm and a laser diode (LD, SLI-CW-9MM-C1-980-1M-PD, Semiconductor Laser International Corp., USA).

2.4. NIR Imaging System. NIR-NIR imaging was carried out using the NIR imaging system, consisting of a fiber pigtail laser diode at 980 nm with 2 W power (LU0975T050, Lumics, Berlin, Germany), a laser scanner (VM500+, GSI Group, Massachusetts, USA) for planer irradiation of the excitation light, and InGaAs CCD camera (NIR-300PGE, VDS Vosskühler, Osnabrück, Germany) for detection of the NIR fluorescence between 1100 and 1600 nm.

2.5. NIR Imaging Inside Swine Colon. In order to demonstrate that NIR light under NIR excitation can be observed through the colon wall, a tablet of $Y_2O_3:YbEr$ -NP with a diameter of 3 mm and a length of 6 mm was formed by mixing $Y_2O_3:YbEr$ -NP with a conventional dental composite resin (Fuji I, GC, Tokyo, Japan). An endoscopic clip [14] (Olympus, Tokyo, Japan) painted with $Y_2O_3:YbEr$ -NP-containing paint (NIR clip) was also prepared in order to demonstrate that NIR light from the clip can also be observed through colon wall. After fixing the NIR clip in the mucosal side (inside) of a piece of the tubular swine colon, we observed the colon using the NIR-NIR imaging system. It is

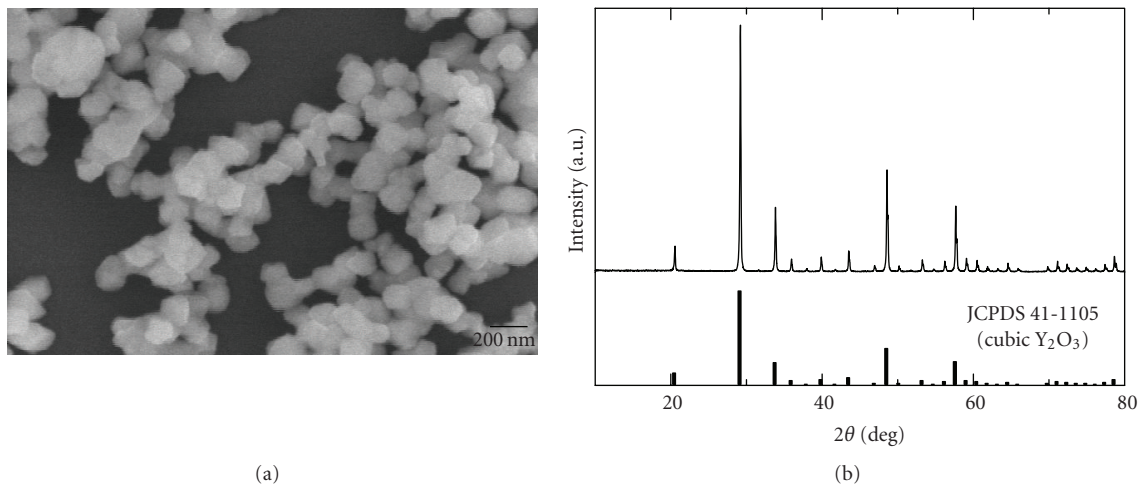


FIGURE 2: Characterization of NIR biophotonic nanoparticles (a) FE-SEM images of $\text{Y}_2\text{O}_3:\text{YbEr}$ -NP synthesized by homogeneous precipitation and calcination at 1200°C for 60 minutes. The particle size was approximately 130 ± 25 nm. The scale bar represents 200 nm. (b) XRD patterns of $\text{Y}_2\text{O}_3:\text{YbEr}$ -NP.

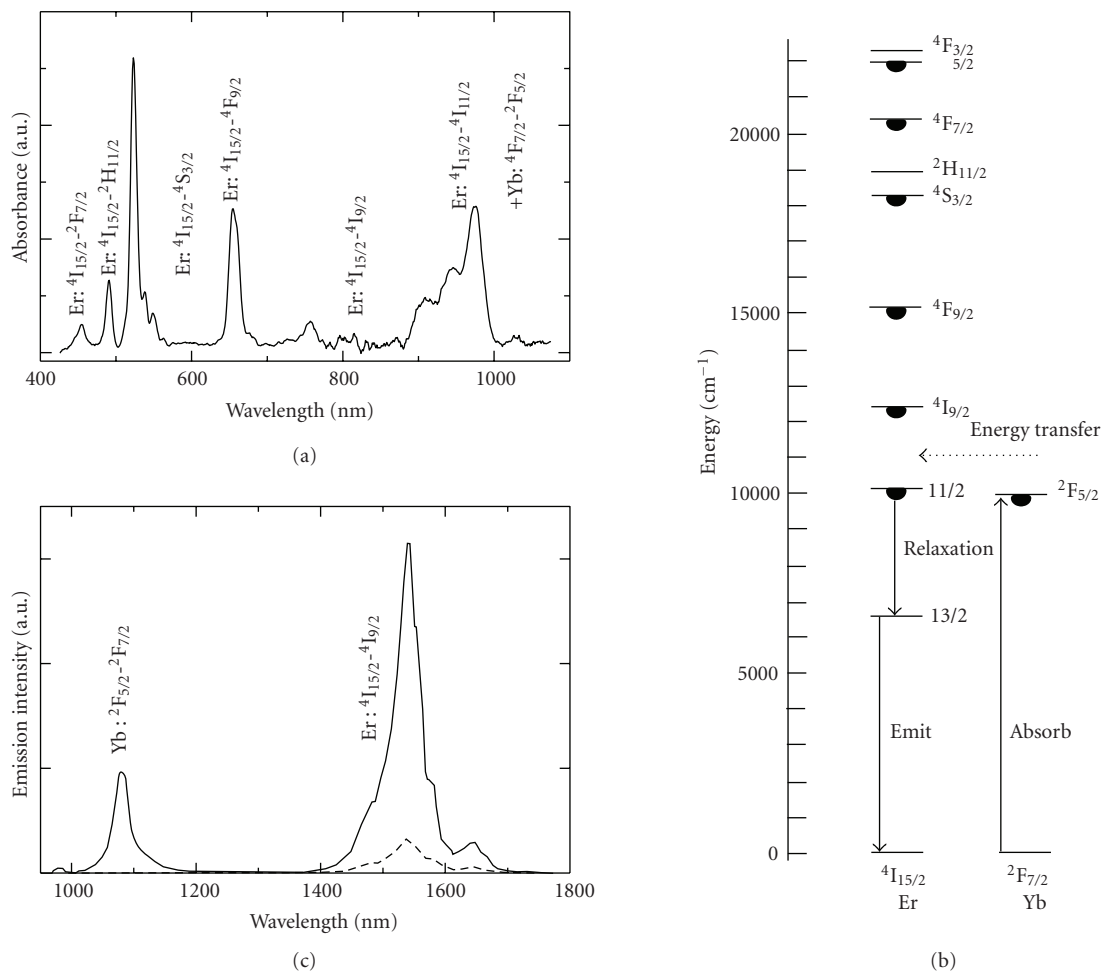


FIGURE 3: (a) Absorption spectrum of $\text{Y}_2\text{O}_3:\text{YbEr}$ -NP. (b) Energy level diagram of $\text{Y}_2\text{O}_3:\text{YbEr}$ -NP. (c) Fluorescence spectra of $\text{Y}_2\text{O}_3:\text{YbEr}$ -NP (solid line) and $\text{Y}_2\text{O}_3:\text{Er}$ -NP (dot line). The fluorescence was measured under an excitation wavelength of 980 nm.

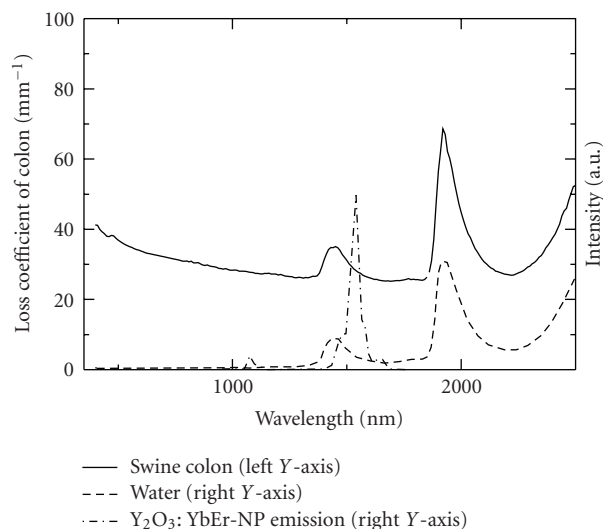


FIGURE 4: Loss spectrum of a sliced sample of swine colon (solid line). The absorption peak at 1420 nm corresponds to the second harmonic of the infrared absorption of water and depends on the water content. The water absorption spectrum is inserted with a dashed line. The emission spectrum of $Y_2O_3:YbEr-NP$ is also incorporated with a chain line.

expected that the painted portion of these endoscopic clips will be observed through the colon wall from the serosal side (outside) of the colon.

3. Results and Discussion

3.1. Characterization of NIR Biophotonic Nanoparticles. Figure 2(a) shows FE-SEM images of $Y_2O_3:YbEr-NP$ synthesized by homogeneous precipitation and calcination at 1200°C for 60 minutes. The particle size was approximately 130 ± 25 nm. Figure 2(b) shows the XRD pattern of $Y_2O_3:YbEr-NP$. The sample was confirmed to be single-phase Y_2O_3 since all of the peaks were identified as those of cubic Y_2O_3 (JCPDS 41-1105).

3.2. Absorption and Fluorescence Spectra. Absorption and fluorescence spectra of $Y_2O_3:YbEr-NP$ are shown in Figure 3. Yb^{3+} was added as a so-called “sensitizer” for increasing the absorption efficiency of the excitation light at 980 nm in this study. In the absorption spectrum (Figure 3(a)), a strong absorption band of Yb^{3+} was observed. The absorbed excitation light at 980 nm was mainly absorbed by Yb^{3+} and the excitation energy transfers to Er^{3+} to emit the NIR fluorescence at 1550 nm, as shown in Figure 3(b). The absorption and fluorescence schemes are well known in the field of optical communication and the phenomenon has been well understood [10, 11]. Figure 3(c) shows that the NIR emission of $Y_2O_3:YbEr-NP$ is much higher than that of $Y_2O_3:Er-NP$, indicating that codoping of Yb^{3+} is also effective to enhance NIR emission.

Figure 4 shows the loss spectrum of the slice of swine colon. The spectrum was obtained by deducting the spectrum due to a thickness of 250 μm from that of 330 μm to yield the net loss due to a swine colon thickness of 110 μm . The spectrum is divided by the corresponding thickness to make it a coefficient spectrum. A water absorption spectrum as well as the emission spectrum of $Y_2O_3:YbEr-NP$, were also coplotted. There are absorption band peaks at 1420 nm, which are due to the second harmonic absorption of the O-H stretching vibration in water molecules. In the spectrum, the fluorescence spectrum is super imposed. Although the fluorescence and the absorption bands overlap, the tail of the fluorescence is still out of the absorption band and one can expect observation of the fluorescence through the colon wall. It appeared better to select phosphors which could emit fluorescence avoiding the water absorption at 1420 nm. The development of the phosphors that can emit NIR light at different wavelength by doping different rare-earth ions such as Nd, Pr or Tm is now in progress.

3.3. NIR Imaging. Figure 5(a) shows images of the $Y_2O_3:YbEr-NP$ tablet set in a tubular swine colon. The tablet emission could be clearly observed even through the colon wall. This result indicates that the NIR excitation light and the NIR emission from $Y_2O_3:YbEr-NP$ is strong enough to penetrate the colon wall.

In an effort to show the applicability of $Y_2O_3:YbEr-NP$ in cancer therapy, NIR imaging of $Y_2O_3:YbEr-NP$ -coated medical clips and $Y_2O_3:YbEr-NP$ solution injected from the mucosal side (inside) of the colon were carried out. The clips used in this experiment are commercially available for endoscopic therapy and can be easily employed to mark the part of cancer using a conventional endoscopy system. The coating was applied onto the plastic part of the clip. Figure 5(b) shows the NIR imaging $Y_2O_3:YbEr-NP$ -coated clips and those set inside of the swine colon under NIR excitation. Although the coating was as thin as several tens of μm , the NIR fluorescence was clearly observed and was comparable to the case of the tablets.

NIR imaging of $Y_2O_3:YbEr-NP$ solution injected inside the colon was also carried out. As shown in Figure 5(c), NIR emission from $Y_2O_3:YbEr-NP$ injected in the other side of the colon wall was clearly observed. This result suggests that $Y_2O_3:YbEr-NP$ can be used as a substitution for tattoo (black ink) solution which is usually used in cancer therapy as described below. Since tattoo solution is usually injected at both ends of tumor region before laparoscopic surgery, $Y_2O_3:YbEr-NP$ solution was also injected at two points.

3.4. Possible Applications of NIR Photonic Nanomaterials for Cancer Diagnosis and Therapy. The spectroscopic properties of swine colon and the development and demonstrative work using $Y_2O_3:YbEr-NP$ suggest a great potential of NIR-NIR photonic nanomaterials for cancer therapy. For example, this technology can be applied to the intraoperative recognition of the tumor site in laparoscopic surgery for the gastrointestinal cancer (Figures 6(a) and 6(b)). Tattooing

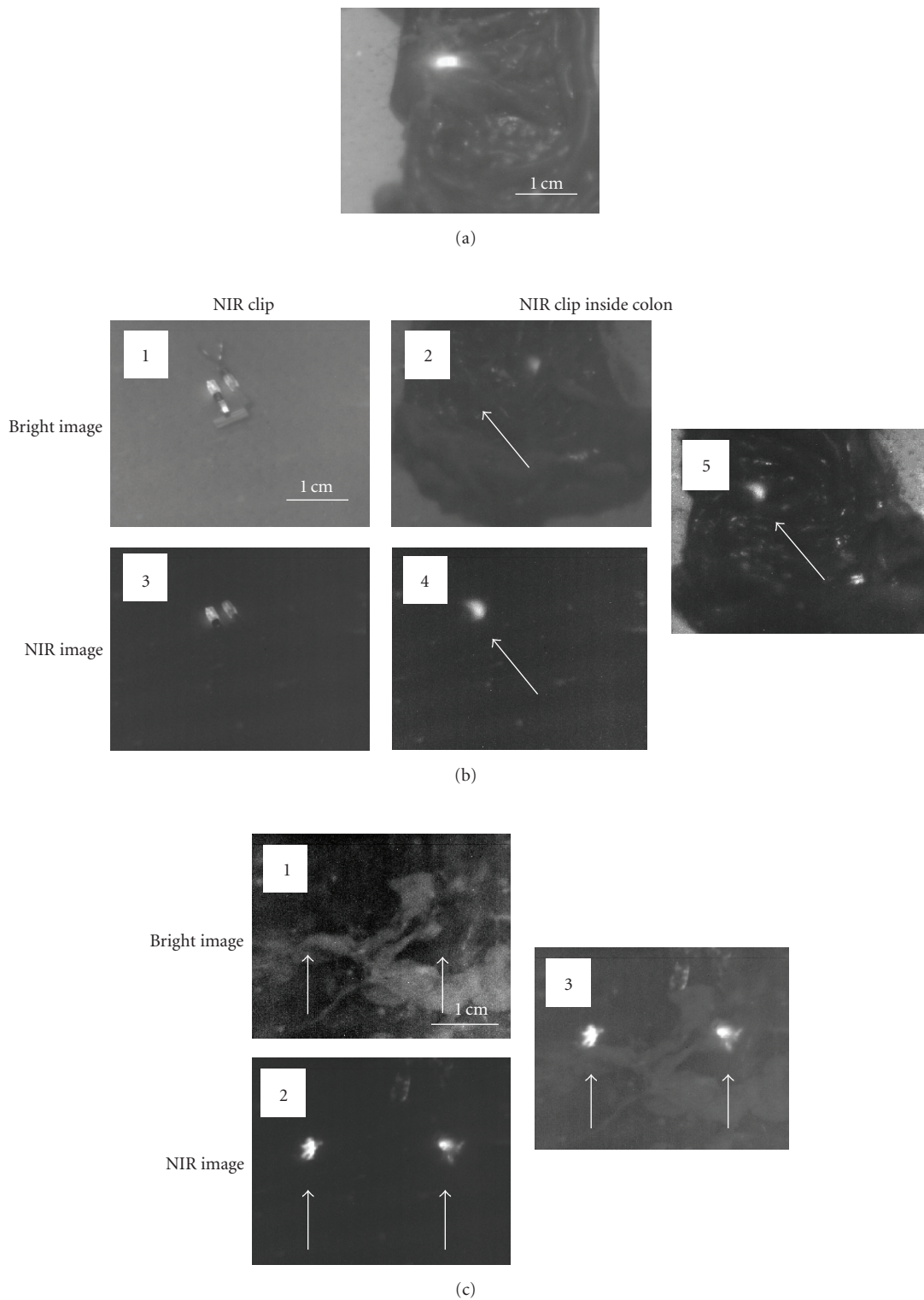


FIGURE 5: NIR imaging (a) $\text{Y}_2\text{O}_3:\text{YbEr}$ -NP tablet set in the tubular sample of swine colon. Hybrid image of bright-field and NIR fluorescence is shown. (b) Bright-field (1, 2) and NIR fluorescence (3, 4) images of $\text{Y}_2\text{O}_3:\text{YbEr}$ -NP-coated clips (1, 3) and those set inside the swine colon (2, 4). Observations of (2) and (4) are from outside of the colon. Hybrid image of the $\text{Y}_2\text{O}_3:\text{YbEr}$ -NP-coated clips set in the swine colon (5) are shown. Arrows in (2), (4), and (5) show the position of the clip inside swine colon. (c) $\text{Y}_2\text{O}_3:\text{YbEr}$ -NP solution (10 mg/mL) injected from the reverse side of the swine colon. Bright-field (1), NIR fluorescence (2) and hybrid (3) images are shown. Observations are from outside of the colon. Arrows show the injection position of $\text{Y}_2\text{O}_3:\text{YbEr}$ -NP solution inside swine colon.

arginine-glycine-aspartic acid (RGD) peptide as a specific probe for tumor cell detection [7]. The RGD peptide strongly binds to integrin $\alpha_v\beta_3$, whose expression is significantly upregulated in invasive tumor cells of certain cancer types (glioblastoma, melanoma, breast, ovarian, and prostate cancers, and in almost all tumor vasculature), but not in quiescent endothelium and normal tissues [16, 17]. Thus, modification of $Y_2O_3:YbEr$ -NP with cyclic RGD peptide will also be useful for the development of a tumor cell-targeted NIR-NIR imaging probe. Successful observation of NIR emission from $Y_2O_3:YbEr$ -NP solution injected inside the colon (Figure 5(c)) supports the idea that targeting and detection of cancer sites in colon using $Y_2O_3:YbEr$ -NP are possible. Research along this line is currently in progress. Our results also suggest that probe-modified $Y_2O_3:YbEr$ -NP could be used for noninvasive detection of various diseases.

Cell toxicity is another important issue when considering probes for use in bioimaging. Previous studies showed that Y_2O_3 and Er^{3+} -doped Y_2O_3 nanoparticles were nontoxic to cultured cell [6, 18]. Since the chemical properties of Yb^{3+} are similar to those of Er^{3+} [19], it is plausible that Yb^{3+} and Er^{3+} -doped Y_2O_3 nanoparticles also are nontoxic. However, further studies on biocompatibility such as inflammation assays and long-term toxicity assays using animal models are important for their medical application.

4. Conclusion

The use of near infrared (NIR) light in the wavelength region between 800 and 2000 nm for biomedical photonics attracts great interest. This region is a so-called “biological window”, where water and biological tissues have minimal absorbance and autofluorescence. In the present study, we report high NIR emission under NIR excitation (NIR-NIR emission) of Yb and Er-doped yttrium oxide nanoparticles ($Y_2O_3:YbEr$ -NP), and propose a possible NIR-NIR biophotonic application using $Y_2O_3:YbEr$ -NP for cancer diagnosis and therapy based on demonstrative experiments. Observations of NIR emission through swine colon wall support our idea that NIR-NIR biophotonic nanomaterials can be used for cancer diagnosis and therapy.

Acknowledgments

The authors thank Professor Atsuo Yasumori for the XRD measurement and Dr. Karin Sörgjerd for helpful comments. This work is financially supported by Industrial Technology Research Grant Program from New Energy and Industrial Technology Development Organization (NEDO) of Japan (Tamotsu Zako).

References

- [1] R. R. Anderson and J. A. Parrish, “The optics of human skin,” *Journal of Investigative Dermatology*, vol. 77, no. 1, pp. 13–19, 1981.
- [2] M. Kamimura, D. Miyamoto, Y. Saito, K. Soga, and Y. Nagasaki, “Design of poly(ethylene glycol)/streptavidin coimmobilized upconversion nanophosphors and their application to fluorescence biolabeling,” *Langmuir*, vol. 24, no. 16, pp. 8864–8870, 2008.
- [3] S. F. Lim, R. Riehn, W. S. Ryu, et al., “In vivo and scanning electron microscopy imaging of upconverting nanophosphors in *Caenorhabditis elegans*,” *Nano Letters*, vol. 6, no. 2, pp. 169–174, 2006.
- [4] P. N. Prasad, “Emerging opportunities at the interface of photonics, nanotechnology and biotechnology,” *Molecular Crystals and Liquid Crystals*, vol. 415, pp. 1–7, 2004.
- [5] S. Sivakumar, P. R. Diamente, and F. C. van Veggel, “Silica-coated Ln^{3+} -Doped LaF_3 nanoparticles as robust down- and upconverting biolabels,” *Chemistry: A European Journal*, vol. 12, no. 22, pp. 5878–5884, 2006.
- [6] T. Zako, H. Nagata, N. Terada, M. Sakono, K. Soga, and M. Maeda, “Improvement of dispersion stability and characterization of upconversion nanophosphors covalently modified with PEG as a fluorescence bioimaging probe,” *Journal of Materials Science*, vol. 43, no. 15, pp. 5325–5330, 2008.
- [7] T. Zako, H. Nagata, N. Terada, et al., “Cyclic RGD peptide-labeled upconversion nanophosphors for tumor cell-targeted imaging,” *Biochemical and Biophysical Research Communications*, vol. 381, no. 1, pp. 54–58, 2009.
- [8] H. J. Zijlmans, J. Bonnet, J. Burton, et al., “Detection of cell and tissue surface antigens using up-converting phosphors: a new reporter technology,” *Analytical Biochemistry*, vol. 267, no. 1, pp. 30–36, 1999.
- [9] F. Auzel, “Upconversion and anti-stokes processes with f and d ions in solids,” *Chemical Reviews*, vol. 104, no. 1, pp. 139–173, 2004.
- [10] R. C. Powell, *Physics of Solid State Laser Materials*, Springer, New York, NY, USA, 1998.
- [11] S. Sudo, *Optical Fiber Amplifiers: Materials, Devices, and Applications*, Artech House, Norwood, Mass, USA, 1997.
- [12] N. Venkatachalam, Y. Okumura, K. Soga, R. Fukuda, and T. Tsuji, “Bioimaging of M1 cells using ceramic nanophosphors: synthesis and toxicity assay of Y_2O_3 nanoparticles,” *Journal of Physics: Conference Series*, vol. 191, Article ID 012002, 2009.
- [13] N. Venkatachalam, Y. Saito, and K. Soga, “Synthesis of Er^{3+} -doped Y_2O_3 nanophosphors,” *Journal of the American Ceramic Society*, vol. 92, no. 5, pp. 1006–1010, 2009.
- [14] G. S. Raju and L. Gajula, “Endoclips for GI endoscopy,” *Gastrointestinal Endoscopy*, vol. 59, no. 2, pp. 267–279, 2004.
- [15] K. L. Lane, R. Vallera, K. Washington, and M. R. Gottfried, “Endoscopic tattoo agents in the colon: tissue responses and clinical implications,” *American Journal of Surgical Pathology*, vol. 20, no. 10, pp. 1266–1270, 1996.
- [16] J. D. Hood and D. A. Cheresh, “Role of integrins in cell invasion and migration,” *Nature Reviews Cancer*, vol. 2, no. 2, pp. 91–100, 2002.
- [17] H. Jin and J. Varner, “Integrins: roles in cancer development and as treatment targets,” *British Journal of Cancer*, vol. 90, no. 3, pp. 561–565, 2004.
- [18] D. Schubert, R. Dargusch, J. Raitano, and S.-W. Chan, “Cerium and yttrium oxide nanoparticles are neuroprotective,” *Biochemical and Biophysical Research Communications*, vol. 342, no. 1, pp. 86–91, 2006.
- [19] K. A. Gschneidner Jr., L. Eyring, and G. H. Lander, *Handbook on the Physics and Chemistry of Rare Earths*, Elsevier, Amsterdam, The Netherlands, 1978.

Review Article

Cancer Therapy Based on Nanomaterials and Nanocarrier Systems

Weili Qiao, Bochu Wang, Yazhou Wang, Lichun Yang, Yiqiong Zhang, and Pengyu Shao

College of Bioengineering, Chongqing University, Chongqing 400030, China

Correspondence should be addressed to Bochu Wang, wangbc2000@126.com

Received 30 September 2009; Revised 1 December 2009; Accepted 21 January 2010

Academic Editor: Chao Lin

Copyright © 2010 Weili Qiao et al. This is an open access article distributed under the Creative Commons Attribution License, which permits unrestricted use, distribution, and reproduction in any medium, provided the original work is properly cited.

Targeted delivery of drug molecules to tumor tissue is one of the most interesting and challenging endeavors faced in pharmaceutical field, due to the critical and pharmacokinetically specific environment that exists in tumor. Over these years, cancer targeting treatment has been greatly improved by new tools and approaches based on nanotechnology. The review firstly introduces the specific physical and chemical properties of a serial of nanomaterials, such as nanoparticles, micelles, dendrimers, carbon nanotubes, quantum dots, and nanofibers. It then places great emphasis on their application in the field of cancer therapy when they are used as nanocarrier systems. Based on the current status, the paper further discusses the unsolved problems and makes a perspective for the future prospects of the nanocarrier systems.

1. Introduction

Cancer occurs at a molecular level when multiple subsets of genes undergo genetic alterations, either activation of oncogenes or inactivation of tumor suppressor genes. Then malignant proliferation of cancer cells, tissue infiltration, and dysfunction of organs will appear [1]. Tumor tissues are characterized with active angiogenesis and high vascular density which keep blood supply for their growth, but with a defective vascular architecture. Combined with poor lymphatic drainage, they contribute to what is known as the enhanced permeation and retention (EPR) effect [2, 3]. Tumor genes are not stable with their development and often show genovariation. The inherent complexity of tumor microenvironment and the existence of P-glycoprotein (P-gp) usually act as barriers to traditional chemotherapy by preventing drug from reaching the tumor mass. Meanwhile, delivery of the therapeutic agents in vivo shares physiological barriers, including hepatic and renal clearance, enzymolysis and hydrolysis, as well as endosomal/lysosomal degradation [4, 5]. In addition, the efficiency of anticancer drugs is limited by their unsatisfactory properties, such as poor solubility, narrow therapeutic window, and intensive cytotoxicity to normal tissues, which may be the causes of treatment failure in cancer [6].

Accordingly, there is a great need for new therapeutic strategies capable of delivering chemical agents and other therapeutic materials specifically to tumor locations [7]. With the development of nanotechnology, the integration of nanomaterials into cancer therapeutics is one of the rapidly advancing fields. It can revolutionize the treatment of cancer. Nanotechnology is the creation and utilization of materials, devices, and systems through the control of matter on the nanometer (1 billionth of a meter) scale [8]. Nanocarrier systems can be designed to interact with target cells and tissues or respond to stimuli in well-controlled ways to induce desired physiological responses. They represent new directions for more effective diagnosis and therapy of cancer [9]. Therefore, this paper discusses the characteristics of various nanotechnology-based drug delivery systems in details, including nanoparticles, micelles, carbon nanotubes, dendrimers, quantum dots, and nanofibers, and with more emphasis on their applications in cancer therapy.

2. Different Nanotechnology-Based Nanocarrier Systems

Based on nanotechnology, nanocarriers synthesized from organic and inorganic materials have been developed, such

as nanoparticles, micelles, carbon nanotubes, dendrimers, quantum dots, and nanofibers [10, 11] (Figure 1). They have shown great potential in cancer therapy by enhancing the performance of medicines and reducing systemic side effect in order to gain therapeutic efficiency.

2.1. Polymeric Nanoparticles. Polymeric nanoparticles are particles of less than $1\ \mu\text{m}$ diameter that are prepared from natural or synthetic polymers. Depending on the methods of preparation, nanoparticles can be obtained with different properties and different release characteristics by forming matrix-type or reservoir-type structure, named nanospheres or nanocapsules [12]. They have been considered as the promising carriers for drug delivery because they can improve the specificity of action of drugs by changing their tissue distribution and pharmacokinetics [13]. Polymeric nanoparticles have played pivotal roles in delivering anti-tumor drugs in a targeted manner to the malignant tumor cells, thereby reducing the systemic toxicity and increasing their therapeutic efficacy. Due to the reticulo-endothelial system (RES) and the effect of enhanced permeation and retention (EPR), nanoparticles can be formulated for passive delivery to the lymphatic system, brain, arterial walls, lungs, liver, spleen, or made for long-term systemic circulation [2, 13, 14]. Importantly, the critical feature of polymeric nanoparticles as drug carriers is that they are amenable to surface functionalization for active targeting to tumor tissues or cells and for stimulus-responsive controlled release of drug [15]. Active targeting of nanoparticles to action sites is based on the pathological state of tumor tissues, such as the angiogenesis and the overexpressed receptors. Thus, varieties of researchers have focused on formulating multifunctional nanoparticles to improve the effectiveness of drug delivery and therapy [15].

The receptor-mediated endocytosis (RME) reveals the selective recognition, high-affinity binding, and immediate internalization for the ligands at a cellular level [16]. For this reason, various targeting moieties can be attached to the polymer backbone, which will act as a secondary uptake mechanism following EPR-based primary accumulation [3, 17] (Figure 2). Liang et al. developed paclitaxel-loaded nanoparticles with galactosamine conjugated on for targeting to liver cancer cells. The prepared nanoparticles appeared most efficient in reducing the size of the tumor when injected into hepatoma-tumor-bearing nude mice, through the specific interaction between galactosamine and asialoglycoprotein receptors [18]. Thermosensitive magnetoliposomes (TMs) encapsulated with methotrexate (MTX) prepared by reverse-phase evaporation can achieve a good magnetic targeting effect and rapid drug release in response to hyperthermia, which implies their great potential in cancer therapy [19].

2.2. Micelles. Polymeric micelles are usually formed into core-shell structures by spontaneous assembly when its concentration is above critical micelle concentration (CMC). They have a number of unique features, including nanosize, easy manipulation of surface chemistry, core functionalities,

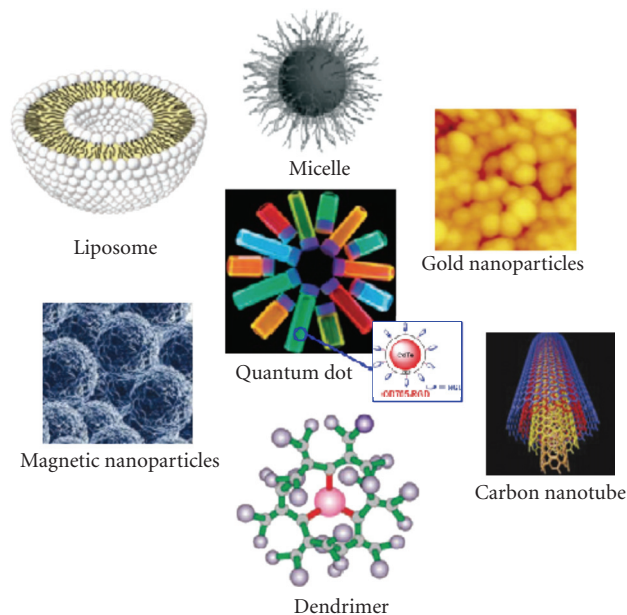


FIGURE 1: Examples of nanomaterials and nanocarrier systems (adapted from [11, 15]).

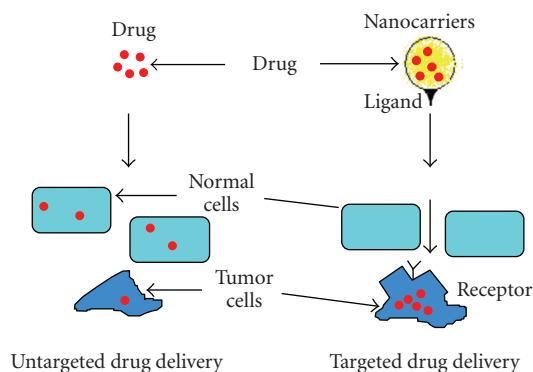


FIGURE 2: Schematic of nanocarrier systems for site-targeted drug delivery (cited from [16]).

as well as ease of fabrication, making them suitable as carriers for encapsulation, and delivery of water insoluble agents [4]. The micelles have a solid-like inner core, which serves as a potent nanocontainer of hydrophobic compounds for solubilization of chemotherapeutics, including docetaxel (DOC) [20], paclitaxel (PTX) [21], camptothecin [22], and dequalinium (DQA) [23]. While polyionic complex (PIC) micelles and cationic polymer micelles can incorporate and protect anionic gene or protein with low rate of cellular uptake and low physiological environment stability, such as vascular endothelial growth factor (VEGF), siRNA [24], and luciferase reporter gene [25]. Thanks to their hydrophilic shell, polymeric micelles play an important part in escaping the recognition of RES and prolonging the blood circulation of drugs. The small size ($<100\ \text{nm}$) allows micelles for efficient accumulation in pathological tissues with permeabilized vasculature via the enhanced permeability and retention (EPR)

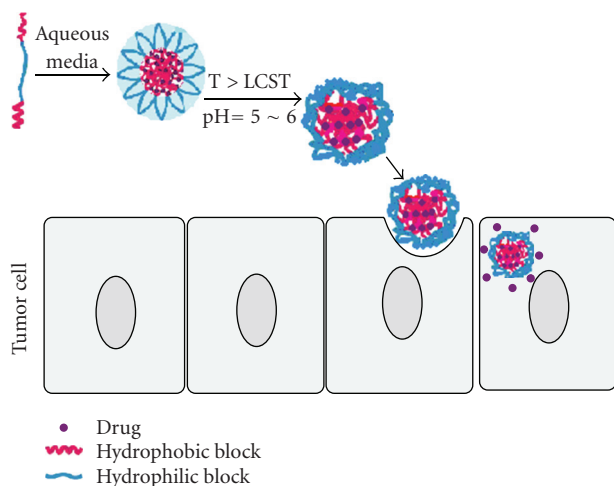


FIGURE 3: Schematic of drug release from micelles with temperature or pH trigger when they are uptaken by tumor cells (adapted from [35]).

effect [26]. However, the physiological factors, such as the density and heterogeneity of the vasculature at tumor sites, interstitial fluid pressure, and transport of macromolecules in the tumor interstitium, are responsible for the extent of micelles extravasations. Mikhail contributed a detailed review in this perspective [27].

Stimuli-responsive polymeric micelles are often designed for controlled release of drug into tumor tissue with external stimuli trigger, like temperature, pH, ultrasound, and special enzymes [28, 29] (Table 1). Among these stimuli, pH and temperature are of representativeness, because the external pH of cancerous tissue tends to be lower and the temperature is higher compared to the surrounding normal tissue, which are caused by abnormal metabolism of cancer tissues [4]. Lower critical solution temperature (LCST) polymers, such as poly (N-isopropylacrylamide) (PNIPAAm) with a cloud point around 32°C or some other poly (N-alkylacrylamide) compounds, were investigated as components of temperature-responsive copolymer micelles [29]. The micelles exhibited rapid and temperature-responsive drug release in cancer cells, which was caused by the destruction of the hydrophobic-hydrophilic balance with the increase of temperature (Figure 3). Licciardi et al. synthesized novel folic acid- (FA-) functionalized diblock copolymer micelles for target delivery of antitumor drugs. The micelles could be directly targeted delivery via folic acid and rapidly release of drug could be triggered by lowering the solution pH to 5. This strategy combined the targeted delivery of therapeutics and pH-controlled drug release together, providing a tumor-selective nanocarrier for the efficient delivery of anticancer drugs [30].

2.3. Dendrimers. Dendrimers are artificial macromolecules with tree-like structures in which the atoms are arranged in many branches and subbranches radiate out from a central core [36, 37]. They are synthesized from branched monomer units in a stepwise manner (Figure 4). Thus it

is possible to control their molecular properties, such as size, shape, dimension, and polarity, which depend on the branched monomer units [37]. These highly branched architectures offer unique interfacial and functional performance advantages due to their empty internal cavities and surface functional groups [38]. So they have an enormous capacity for solubilization of hydrophobic drugs and can be modified or conjugated with various interesting guest molecules [37]. Based on the specific properties, the dendrimers have shown great promise in the development of anticancer drug delivery systems [39].

To achieve active targeting drugs to tumor tissues, the well-defined multivalency of dendrimers are widely exploited for covalent attachment of special targeting moieties, such as sugar [40], folic acid [30], antibody [41], biotin [37], and epidermal growth factors [42]. At the same time, therapeutic drugs can be encapsulated into or conjugated with dendrimers. For example, Choi and coworkers have prepared generation 5 polyamidoamine (G5 PAMAM) dendrimers conjugated to fluorescein and folic acid, and then linked them together using complementary DNA oligonucleotides to produce clustered molecules for targeting cancer cells that overexpress the high-affinity folate receptor. In vitro studies indicated the DNA-linked dendrimer clusters could specifically bind to KB cells and may be used as imaging agents and therapeutics for cancer therapy [43].

2.4. Carbon Nanotubes. Carbon nanotubes are cylinders of one several coaxial graphite layers with a diameter in the order of nanometers, and they serve as instructive examples of the Janus-like properties of nanomaterials [44]. They can be classified into two general categories based on their structure: single-walled carbon nanotubes (SWCNTs) with a single cylindrical carbon wall and multiwalled carbon nanotubes (MWCNTs) with multiple walls—cylinders nested within other cylinders [45] (Figure 5). Thanks to their unique electronic, thermal, and structural characteristics, they can offer a promising approach for gene and drug delivery for cancer therapy [16, 45].

Heating of organs and tissues by placing multifunctional nanomaterials at tumor sites is emerging as an art of tumor treatment by “nanothermal therapy” [46]. Carbon nanotubes have become candidates to kill cancer cells via local hyperthermia, due to their thermal conductivity and optical properties. A research showed that oligonucleotides could be translocated into cell nucleus by nanotubes and cause cell death with continuous near-infrared radiation (NIR) because of excessive local heating of SWCNT in vitro [47]. It can afford carbon nanotubes an opportunity to be uptaken only by cancerous cells via functionalization of them with tumor-specific ligands and antibody, like folic acid and monoclonal antibody which can act as targeting agents for many tumors [48]. Accordingly, a highly effective drug delivery system triggered by pH change has been developed via firstly coated with a polysaccharide material and then modified with folic acid [48]. The encapsulated doxorubicin was only released from the modified nanotubes at a low pH, resulting in nuclear DNA damage and the HeLa

TABLE 1: Stimuli that can be utilized to control the behavior and properties of micelles.

Stimuli	Stimuli origin	Examples	References
pH	Decreased pH in cancer site caused by hypoxia and massive cell death	Tumoral acidic extracellular pH targeting of pH-responsive micelles encapsulated doxorubicin for cancer therapy	[31]
Temperature	Increased temperature in cancerous tissues owing to their high metabolic activities. External applied heating	Self-assembled, thermosensitive micelles for controlled doxorubicin delivery	[32]
Magnetic field	Locally applied magnetic field	Folate-encoded and Fe ₃ O ₄ -loaded polymeric micelles for dual targeting of cancer cells	[33]
Ultrasound	Locally applied ultrasound	Ultrasonic release of doxorubicin from pluronic P105 micelles	[28]
Redox potential	Increased concentration of glutathione inside many cancerous cells	Poly(ethylene glycol)-modied thiolated gelatin nanoparticles for glutathione-responsive intracellular DNA delivery	[34]

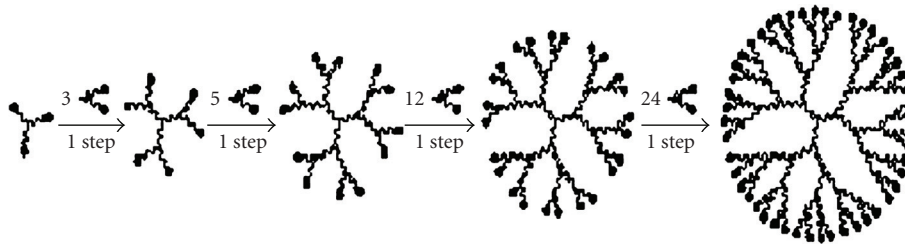


FIGURE 4: Dendrimers synthesized in a stepwise manner (cited from [38]).

cell proliferation inhibition. However, the pharmacokinetics, biodistribution, toxicity, and activity of novel functional carbon nanotubes in vivo should be further investigated to ensure their future applications [46].

2.5. Quantum Dots (QDs). Quantum dots are inorganic fluorescent semiconductor nanoparticles composed of 10–50 atoms with a diameter ranging from 2 to 10 nm [11, 49]. Their sizes and shapes which determine their absorption and emission properties can be controlled precisely [36]. They are widely studied for optical image application in living systems and are stable for months without degradation and alteration [11]. Targeted ligands have been attached to QDs in order to achieve specific targeting for tumor cell labeling [49]. Thus, they are assured to be chosen as long-term, high-sensitivity and multicontrast imaging agents applied for the detection and diagnosis of cancer in vivo [36].

Now, many researchers focus on using quantum dots as carriers for genes delivery to overcome the obstacles of cell membranes. Klein and coworkers have developed functionalized silicon quantum dots (SiQDs) to serve as self-tracking transfection tool for ABCB1 siRNA [50]. Li et al. investigated glutathione-mediated release of functional plasmid DNA from positively charged CdTe quantum dots, which suggested potential applications of these QDs in selective unpacking of payload in living cells in a visible

manner [51]. The applicability of quantum dots for cancer therapies based on the mechanisms of photosensitization and radiosensitization has also been investigated. Possessing electronic energy levels in the range of 1–5 eV, quantum dots can perform as photosensitizers applied in photodynamic therapy (PDT), which has recently become an approved treatment modality for some type of cancer. Due to high atom and electron density, quantum dots could absorb high-energy photons acting as radiosensitizers to cause localized and targeted damages to cancer cells, which was reviewed in details by Juzenas [52].

With the help of near-infrared (NIR) optical imaging devices, QDs-based tumor imaging and treatment could allow for application in deeper tissues and may offer optical guide for surgery on organs. However, the toxicity of QDs cannot be ignored for their applications in vivo, because they are composed of hazardous heavy metals. Accordingly, it is necessary to investigate their toxicity systematically to ensure their security for further applications to human.

2.6. Nanofibers. Electrospinning has gained widespread interest as a potential polymer processing technique to produce ultrafine polymer fibers for drug delivery applications. It has been proven to be a relatively simple and versatile method for producing polymeric fibers with diameters ranging from tens of nanometers to microns [53].

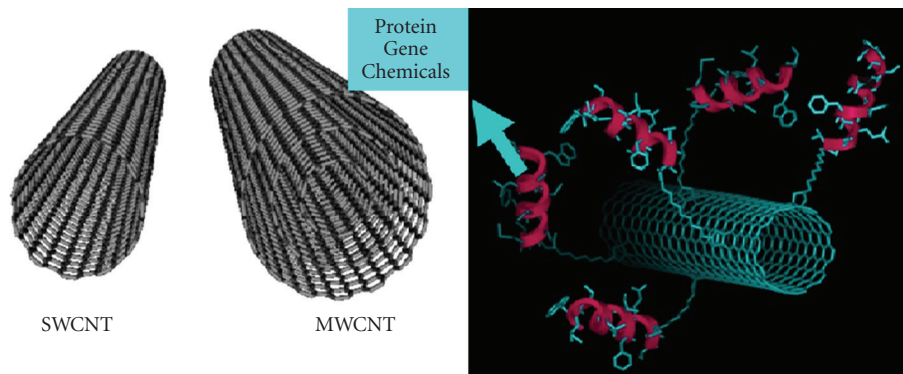


FIGURE 5: Structure of single-walled carbon nanotubes (SWCNTs) and multiwalled carbon nanotubes (MWCNTs), as well as drug loaded carbon nanotubes (adapted from http://www-ibmc.u-strasbg.fr/ict/vectorisation/nanotubes_eng.shtml and http://www-ibmc.u-strasbg.fr/ict/vectorisation/vectorisation_eng.shtml).

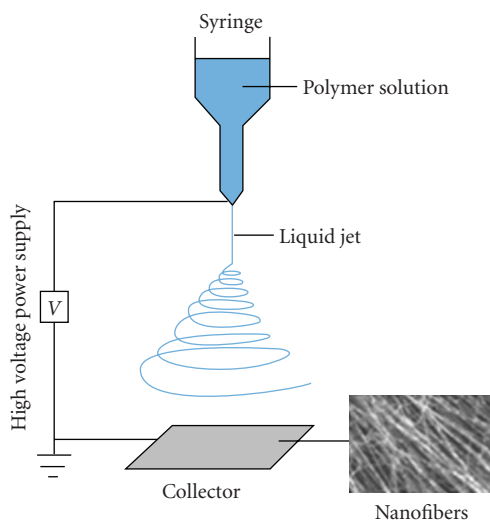


FIGURE 6: Schematic of electrospinning process (adapted from [56]).

Electrospinning process can be briefly described as follows. A polymer solution is ejected from the capillary outlet of a syringe by strong enough electrostatic forces, and finally deposits as a nonwoven fabric mat on a grounded metal screen (counter electrode). As this jet travels through the air, the solvent evaporates, leaving behind ultrafine polymer fibers [54, 55] (Figure 6). Accordingly, the properties of nanofibers can be controlled easily by a number of processing parameters, such as applied voltage, polymer flow rate, capillary-collector distance, as well as the surface tension and viscoelasticity of solution [53].

As a fibrous scaffold, nanofibers are able to entrap drugs with a high loading capacity and high encapsulation efficiency because of their low weight and inherent high surface-to-volume ratio. They have been designed as promising carriers for delivering anticancer drugs, especially in post-operative local chemotherapy via surgical implantation of the scaffold [57]. Xie and Wang develop electrospun PLGA-based micro- and nanofibers as implants for the sustained

delivery of paclitaxel to treat C6 glioma *in vitro*. With an increased drug loading and prolonged release period, the antitumor efficiency was comparable to commercial paclitaxel formulation Taxol [58]. Xu et al. developed implantable BCNU-loaded poly (ethylene glycol)-poly (L-lactic acid) (PEG-PLLA) diblock copolymer fibers for the controlled release of 1, 3-bis (2-chloroethyl)-1-nitrosourea (BCNU) for postoperative chemotherapy of cancers. Compared with pristine BCUN, the BCNU released from the fiber retained its efficacy for prolonged period and increased antitumor activity against rat Glioma C6 cells [59]. Recently, they prepared nanofibers entrapped both paclitaxel (PTX) and doxorubicin hydrochloride (DOX) by means of “emulsion-electrospinning,” providing a new approach for multidrug delivery on combination therapy [60]. Although electrospun nanofibers have been investigated greatly and show effective antitumor activity as drug carriers for postoperative local chemotherapy *in vitro*, further researches on the destiny and antitumor activity of the nanofibers *in vivo* should be investigated.

2.7. Others. Current nanotechnology platforms for cancer therapeutics also include other nanomaterials. In addition to polymeric nanoparticles, gold nanoparticles (GNPs) and magnetic nanoparticles are being paid more attention because their unique physical, chemical, and biological properties are quite different from the bulk of their counterparts [7]. They can act as active medicine or drug additives for detection and hyperthermia treatment of cancer after laser irradiation [65, 66]. Nanoshells which consist of a silica core and a thin gold shell are designed to apply in cancer imaging and therapy. Because of the silica core and gold shell, the most useful nanoshells can strongly absorb NIR light and create intense heat that is lethal to cells for thermal ablation therapy [67]. Recombinant adenovirus (Ad) can produce a linear, double-stranded viral genome that does not integrate with the genome of the host cell during the replication but induces a DNA double-strand break repair response in the host cell. There are many studies on the

TABLE 2: Advantages of nanotechnology-based on drug delivery systems in cancer therapy.

Features	Examples	References
Solubilization effect	Self-assembled polymeric micelles with hydrophobic core can serve as a potent nanocontainer for increasing the solubility of hydrophobic drugs.	[20]
Protective effect	Entrapment or conjugation of a drug to polymeric systems may protect the drug from inactivation and help to store its activity for prolonged duration.	[61]
Passive targeting	The enhanced permeability and retention (EPR) effect allows for the accumulation of drug carriers in the interstitial fluid of the diseased tissue. The drug entrapped or conjugated to the carriers can be retained in the tumor tissue for a longer time, whereas free drug with low-molecular weight easily diffuse back out.	[62]
Active targeting	Active targeting can be achieved via specific recognition processes, including ligand-receptor and antibody-antigen recognition by the surface modification with various ligands, such as folate, mannose, and galactose.	[27, 63, 64]
Controlled release of drugs	The drug can be controlled release at diseased site when an appropriate signal is offered, such as pH, temperature, ultrasound, or special enzymes.	[28, 29]

use of recombinant adenovirus particles as carriers for sensitizers to enhance noninvasive cancer therapeutics, such as radiation therapy, photodynamic therapy, and photothermal therapy. They can also be fabricated to combine multiple functions of targeting, imaging, and drug delivery together to increase the sensitivity and specificity of cancer therapy [68].

3. Summary

Nanotechnology-based drug carriers and materials have yielded more medical benefits in the recent years, especially the field of cancer therapy. Compared to conventional formations, nanocarrier systems have many advantages. For example, they can improve the solubility of poorly soluble drugs [20], protect the recombinant of protein and genes [61], circulate in blood stream for longer time without being recognized by macrophages, as well as controlled release of drugs at an expected rate in the desired area [28] (Table 2). Due to their various advantages, the nanocarrier systems and nanomaterials have demonstrated comparable or superior anticancer efficiency to commercial formations and provided new strategies to fight against cancer.

4. Problems and Future Perspective

The nanoscale platforms have made significant progress in formulation preparations and achieved more precise treatment at a molecular level. There are already novel formations for cancer therapy available commercially, such as Abraxane, Doxil, and Embosphere, et al. [69–71], and they may offer great opportunities for personalized medicine. Although drug delivery systems and nanomaterials are mostly investigated in preclinical animal models, too few studies are carried out to examine the cellular uptake of delivery systems in human body, because (a) the data from pre-clinical animals cannot exactly reflect its effect on human body because of the complexity of tumor biology and the differences between animal and human physiology, (b) the development of new drug delivery systems is based

on the advancement of the carrier materials, but there are only few types of materials approved by Food and Drug Administration (FDA), and (c) the security and the long-term effects of nanotechnology are unknown, which need research strategies to evaluate the specific risks when used in human body. With the development of cancer biology and polymer chemistry, new nanotechnology-based tools and therapeutic strategies will be designed and applied in the fields of cancer precaution diagnosis and treatment. Besides, nanotechnology also plays an important part in delivery of drugs for ocular therapy and in generation of scaffolds for tissue engineering. However, the other major developments will have to take place for them to be permanently established not only in academia but also in industry. The basic theories of drug release from nanocarriers and pharmacokinetic models need to be developed and improved. The cytotoxicity of nanomedicine or their degradation products remains a serious problem, so more attention should be paid to improve the biocompatibility in future investigations. Their toxicity, long-term stability, and degradation pathways may also influence the integrity of the environment. It will not be of great benefit to clinical application and industrial production of nanomedicine unless the problems are solved.

Acknowledgment

The authors would like to thank Dr. Gurinder K. Singh for her critical evaluation and helpful suggestions to the paper.

References

- [1] F. H. Sarkar, S. Banerjee, and Y. W. Li, "Pancreatic cancer: pathogenesis, prevention and treatment," *Toxicology and Applied Pharmacology*, vol. 224, no. 3, pp. 326–336, 2007.
- [2] J. D. Byrne, T. Betancourt, and L. Brannon-Peppas, "Active targeting schemes for nanoparticle systems in cancer therapeutics," *Advanced Drug Delivery Reviews*, vol. 60, no. 15, pp. 1615–1626, 2008.

- [3] A. K. Iyer, G. Khaled, J. Fang, and H. Maeda, "Exploiting the enhanced permeability and retention effect for tumor targeting," *Drug Discovery Today*, vol. 11, no. 17-18, pp. 812–818, 2006.
- [4] N. Wiradharma, Y. Zhang, S. Venkataraman, J. L. Hedrick, and Y. Y. Yang, "Self-assembled polymer nanostructures for delivery of anticancer therapeutics," *Nano Today*, vol. 4, no. 4, pp. 302–317, 2009.
- [5] L. Jabr-Milane, L. V. Vlerken, H. Devalapally, et al., "Multi-functional nanocarriers for targeted delivery of drugs and genes," *Journal of Controlled Release*, vol. 130, no. 2, pp. 121–128, 2008.
- [6] M. Pulkkinen, J. Pikkariainen, T. Wirth, et al., "Three-step tumor targeting of paclitaxel using biotinylated PLA-PEG nanoparticles and avidin-biotin technology: formulation development and in vitro anticancer activity," *European Journal of Pharmaceutics and Biopharmaceutics*, vol. 70, no. 1, pp. 66–74, 2008.
- [7] N. R. Panyala, E. M. Peña-Méndez, and J. Havel, "Gold and nano-gold in medicine: overview, toxicology and perspectives," *Journal of Applied Biomedicine*, vol. 7, no. 2, pp. 75–91, 2009.
- [8] K. K. Jain, "Nanotechnology in clinical laboratory diagnostics," *Clinica Chimica Acta*, vol. 358, no. 1-2, pp. 37–54, 2005.
- [9] G. Linazasoro, "Potential applications of nanotechnologies to Parkinson's disease therapy," *Parkinsonism and Related Disorders*, vol. 14, no. 5, pp. 383–392, 2008.
- [10] W. Cai, A. R. Hsu, Z.-B. Li, and X. Chen, "Are quantum dots ready for in vivo imaging in human subjects?" *Nanoscale Research Letters*, vol. 2, no. 6, pp. 265–281, 2007.
- [11] W. Cai and X. Chen, "Nanoplatforms for targeted molecular imaging in living subjects," *Small*, vol. 3, no. 11, pp. 1840–1854, 2007.
- [12] A. K. Bajpai, S. K. Shukla, S. Bhanu, and S. Kankane, "Responsive polymers in controlled drug delivery," *Progress in Polymer Science*, vol. 33, no. 11, pp. 1088–1118, 2008.
- [13] C. Fonseca, S. Simoes, and R. Gaspar, "Paclitaxel-loaded PLGA nanoparticles: preparation, physicochemical characterization and in vitro anti-tumoral activity," *Journal of Controlled Release*, vol. 83, no. 2, pp. 273–286, 2002.
- [14] M. L. Hans and A. M. Lowman, "Biodegradable nanoparticles for drug delivery and targeting," *Current Opinion in Solid State and Materials Science*, vol. 6, no. 4, pp. 319–327, 2002.
- [15] N. Sanvicens and M. P. Marco, "Multifunctional nanoparticles—properties and prospects for their use in human medicine," *Trends in Biotechnology*, vol. 26, no. 8, pp. 425–433, 2008.
- [16] T. Tanaka, S. Shiramoto, M. Miyashita, Y. Fujishima, and Y. Kaneo, "Tumor targeting based on the effect of enhanced permeability and retention (EPR) and the mechanism of receptor-mediated endocytosis (RME)," *International Journal of Pharmaceutics*, vol. 277, no. 1-2, pp. 39–61, 2004.
- [17] S. Sandhiya, S. A. Dkhar, and A. Surendiran, "Emerging trends of nanomedicine—an overview," *Fundamental and Clinical Pharmacology*, vol. 23, no. 3, pp. 263–269, 2009.
- [18] Y. Fukumori and H. Ichikawa, "Nanoparticles for cancer therapy and diagnosis," *Advanced Powder Technology*, vol. 17, no. 1, pp. 1–28, 2006.
- [19] M. Johannsen, U. Gneveckow, B. Thiesen, et al., "Thermotherapy of prostate cancer using magnetic nanoparticles: feasibility, imaging, and three-dimensional temperature distribution," *European Urology*, vol. 52, no. 6, pp. 1653–1662, 2007.
- [20] B. Liu, M. Yang, R. Li, et al., "The antitumor effect of novel docetaxel-loaded thermosensitive micelles," *European Journal of Pharmaceutics and Biopharmaceutics*, vol. 69, no. 2, pp. 527–534, 2008.
- [21] K. M. Huh, H. S. Min, S. C. Lee, H. J. Lee, S. Kim, and K. Park, "A new hydrotropic block copolymer micelle system for aqueous solubilization of paclitaxel," *Journal of Controlled Release*, vol. 126, no. 2, pp. 122–129, 2008.
- [22] O. M. Koo, I. Rubinstein, and H. Onyuksel, "Camptothecin in sterically stabilized phospholipid micelles: a novel nanomedicine," *Nanomedicine: Nanotechnology, Biology, and Medicine*, vol. 1, no. 1, pp. 77–84, 2005.
- [23] C. Lizano, V. Weissig, V. P. Torchilin, P. Sancho, A. I. García-Pérez, and M. Pinilla, "In vivo biodistribution of erythrocytes and polyethyleneglycol-phosphatidylethanolamine micelles carrying the antitumor agent dequalinium," *European Journal of Pharmaceutics and Biopharmaceutics*, vol. 56, no. 2, pp. 153–157, 2003.
- [24] A. M. Al-Abd, S. H. Lee, S. H. Kim, et al., "Penetration and efficacy of VEGF siRNA using polyelectrolyte complex micelles in a human solid tumor model in-vitro," *Journal of Controlled Release*, vol. 137, no. 2, pp. 130–135, 2009.
- [25] N. Wiradharma, Y. W. Tong, and Y. -Y. Yang, "Self-assembled oligopeptide nanostructures for co-delivery of drug and gene with synergistic therapeutic effect," *Biomaterials*, vol. 30, no. 17, pp. 3100–3109, 2009.
- [26] L. B. Li and Y. B. Tan, "Preparation and properties of mixed micelles made of Pluronic polymer and PEG-PE," *Journal of Colloid and Interface Science*, vol. 317, no. 1, pp. 326–331, 2008.
- [27] A. S. Mikhail and C. Allen, "Block copolymer micelles for delivery of cancer therapy: transport at the whole body, tissue and cellular levels," *Journal of Controlled Release*, vol. 138, no. 3, pp. 214–223, 2009.
- [28] G. A. Hussein, N. Y. Rapoport, D. A. Christensen, J. D. Pruitt, and W. G. Pitt, "Kinetics of ultrasonic release of doxorubicin from pluronic P105 micelles," *Colloids and Surfaces B*, vol. 24, no. 3-4, pp. 253–264, 2002.
- [29] N. Rapoport, "Physical stimuli-responsive polymeric micelles for anti-cancer drug delivery," *Progress in Polymer Science*, vol. 32, no. 8-9, pp. 962–990, 2007.
- [30] M. Licciardi, G. Giammona, J. Du, S. P. Armes, Y. Tang, and A. L. Lewis, "New folate-functionalized biocompatible block copolymer micelles as potential anti-cancer drug delivery systems," *Polymer*, vol. 47, no. 9, pp. 2946–2955, 2006.
- [31] J. Ko, K. Park, Y.-S. Kim, et al., "Tumoral acidic extracellular pH targeting of pH-responsive MPEG-poly(β -amino ester) block copolymer micelles for cancer therapy," *Journal of Controlled Release*, vol. 123, no. 2, pp. 109–115, 2007.
- [32] M. Nakayama, T. Okano, T. Miyazaki, F. Kohori, K. Sakai, and M. Yokoyama, "Molecular design of biodegradable polymeric micelles for temperature-responsive drug release," *Journal of Controlled Release*, vol. 115, no. 1, pp. 46–56, 2006.
- [33] X. Yang, Y. H. Chen, R. Yuan, et al., "Folate-encoded and Fe₃O₄-loaded polymeric micelles for dual targeting of cancer cells," *Polymer*, vol. 49, no. 16, pp. 3477–3485, 2008.
- [34] V. Torchilin, "Multifunctional and stimuli-sensitive pharmaceutical nanocarriers," *European Journal of Pharmaceutics and Biopharmaceutics*, vol. 71, no. 3, pp. 431–444, 2009.
- [35] C. Chang, H. Wei, C.-Y. Quan, et al., "Fabrication of thermosensitive PCL-PNIPAAm-PCL triblock copolymeric micelles for drug delivery," *Journal of Polymer Science A*, vol. 46, no. 9, pp. 3048–3057, 2008.

- [36] K. J. Morrow Jr., R. Bawa, and C. Wei, "Recent advances in basic and clinical nanomedicine," *Medical Clinics of North America*, vol. 91, no. 5, pp. 805–843, 2007.
- [37] W. J. Yang, Y. Y. Cheng, T. W. Xu, X. Y. Wang, and L. P. Wen, "Targeting cancer cells with biotinyne-dendrimer conjugates," *European Journal of Medicinal Chemistry*, vol. 44, no. 2, pp. 862–868, 2009.
- [38] S. Svenson and D. A. Tomalia, "Dendrimers in biomedical applications—reflections on the field," *Advanced Drug Delivery Reviews*, vol. 57, no. 15, pp. 2106–2129, 2005.
- [39] E. R. Gillies and J. M. J. Fréchet, "Dendrimers and dendritic polymers in drug delivery," *Drug Discovery Today*, vol. 10, no. 1, pp. 35–43, 2005.
- [40] D. Bhadra, A. K. Yadav, S. Bhadra, and N. K. Jain, "Glycodendrimeric nanoparticulate carriers of primaquine phosphate for liver targeting," *International Journal of Pharmaceutics*, vol. 295, no. 1–2, pp. 221–233, 2005.
- [41] A. K. Patri, A. Myc, J. Beals, T. P. Thomas, N. H. Bander, and J. R. Baker Jr., "Synthesis and in vitro testing of J591 antibody-dendrimer conjugates for targeted prostate cancer therapy," *Bioconjugate Chemistry*, vol. 15, no. 6, pp. 1174–1181, 2004.
- [42] M. Hussain, M. Shchepinov, M. Sohail, et al., "A novel anionic dendrimer for improved cellular delivery of antisense oligonucleotides," *Journal of Controlled Release*, vol. 99, no. 1, pp. 139–155, 2004.
- [43] Y. Choi, T. Thomas, A. Kotlyar, M. T. Islam, and J. R. Baker Jr., "Synthesis and functional evaluation of DNA-assembled polyamidoamine dendrimer clusters for cancer cell-specific targeting," *Chemistry and Biology*, vol. 12, no. 1, pp. 35–43, 2005.
- [44] A. A. Shvedova, E. R. Kisin, D. Porter, et al., "Mechanisms of pulmonary toxicity and medical applications of carbon nanotubes: two faces of Janus?" *Pharmacology and Therapeutics*, vol. 121, no. 2, pp. 192–204, 2009.
- [45] L. Lacerda, A. Bianco, M. Prato, and K. Kostarelos, "Carbon nanotubes as nanomedicines: from toxicology to pharmacology," *Advanced Drug Delivery Reviews*, vol. 58, no. 14, pp. 1460–1470, 2006.
- [46] R. Sharma and C. J. Chen, "Newer nanoparticles in hyperthermia treatment and thermometry," *Journal of Nanoparticle Research*, vol. 11, no. 3, pp. 671–689, 2009.
- [47] N. W. S. Kam, M. O'Connell, J. A. Wisdom, and H. Dai, "Carbon nanotubes as multifunctional biological transporters and near-infrared agents for selective cancer cell destruction," *Proceedings of the National Academy of Sciences of the United States of America*, vol. 102, no. 33, pp. 11600–11605, 2005.
- [48] X. K. Zhang, L. J. Meng, Q. H. Lu, Z. F. Fei, and P. J. Dyson, "Targeted delivery and controlled release of doxorubicin to cancer cells using modified single wall carbon nanotubes," *Biomaterials*, vol. 30, no. 30, pp. 6041–6047, 2009.
- [49] K. Y. Kim, "Nanotechnology platforms and physiological challenges for cancer therapeutics," *Nanomedicine: Nanotechnology, Biology, and Medicine*, vol. 3, no. 2, pp. 103–110, 2007.
- [50] S. Klein, O. Zolk, M. F. Fromm, F. Schrödl, W. Neuhuber, and C. Kryschi, "Functionalized silicon quantum dots tailored for targeted siRNA delivery," *Biochemical and Biophysical Research Communications*, vol. 387, no. 1, pp. 164–168, 2009.
- [51] D. Li, G. P. Li, W. Guo, P. Li, E. Wang, and J. Wang, "Glutathione-mediated release of functional plasmid DNA from positively charged quantum dots," *Biomaterials*, vol. 29, no. 18, pp. 2776–2782, 2008.
- [52] P. Juzenas, W. Chen, Y.-P. Sun, et al., "Quantum dots and nanoparticles for photodynamic and radiation therapies of cancer," *Advanced Drug Delivery Reviews*, vol. 60, no. 15, pp. 1600–1614, 2008.
- [53] M. Wang, A. J. Hsieh, and G. C. Rutledge, "Electrospinning of poly(MMA-co-MAA) copolymers and their layered silicate nanocomposites for improved thermal properties," *Polymer*, vol. 46, no. 10, pp. 3407–3418, 2005.
- [54] X. L. Xu, X. S. Chen, A. X. Liu, Z. K. Hong, and X. B. Jing, "Electrospun poly(L-lactide)-grafted hydroxyapatite/ poly(L-lactide) nanocomposite fibers," *European Polymer Journal*, vol. 43, no. 8, pp. 3187–3196, 2007.
- [55] M. Wang, H. Singh, T. A. Hatton, and G. C. Rutledge, "Field-responsive superparamagnetic composite nanofibers by electrospinning," *Polymer*, vol. 45, no. 16, pp. 5505–5514, 2004.
- [56] E. Jo, S. Lee, K. T. Kim, et al., "Core-sheath nanofibers containing colloidal arrays in the core for programmable multi-agent delivery," *Advanced Materials*, vol. 20, no. 9, pp. 968–972, 2008.
- [57] X. Xu, X. Chen, P. Ma, X. Wang, and X. Jing, "The release behavior of doxorubicin hydrochloride from medicated fibers prepared by emulsion-electrospinning," *European Journal of Pharmaceutics and Biopharmaceutics*, vol. 70, no. 1, pp. 165–170, 2008.
- [58] J. Xie and C.-H. Wang, "Electrospun micro- and nanofibers for sustained delivery of paclitaxel to treat C6 Glioma in vitro," *Pharmaceutical Research*, vol. 23, no. 8, pp. 1817–1826, 2006.
- [59] X. Xu, X. Chen, X. Xu, et al., "BCNU-loaded PEG-PLLA ultrafine fibers and their in vitro antitumor activity against Glioma C6 cells," *Journal of Controlled Release*, vol. 114, no. 3, pp. 307–316, 2006.
- [60] X. L. Xu, X. S. Chen, Z. F. Wang, and X. B. Jing, "Ultrafine PEG-PLA fibers loaded with both paclitaxel and doxorubicin hydrochloride and their in vitro cytotoxicity," *European Journal of Pharmaceutics and Biopharmaceutics*, vol. 72, no. 1, pp. 18–25, 2009.
- [61] Y. T. Ko, A. Kale, W. C. Hartner, B. Papahadjopoulos-Sternberg, and V. P. Torchilin, "Self-assembling micelle-like nanoparticles based on phospholipid-polyethyleneimine conjugates for systemic gene delivery," *Journal of Controlled Release*, vol. 133, no. 2, pp. 132–138, 2009.
- [62] K. F. Pirolo and E. H. Chang, "Does a targeting ligand influence nanoparticle tumor localization or uptake?" *Trends in Biotechnology*, vol. 26, no. 10, pp. 552–558, 2008.
- [63] D. J. Betting, X. Y. Mu, K. Kaf, et al., "Enhanced immune stimulation by a therapeutic lymphoma tumor antigen vaccine produced in insect cells involves mannose receptor targeting to antigen presenting cells," *Vaccine*, vol. 27, no. 2, pp. 250–259, 2009.
- [64] E. Gabano, M. Ravera, C. Cassino, S. Bonetti, G. Palmisano, and D. Osella, "Stepwise assembly of platinum—folic acid conjugates," *Inorganica Chimica Acta*, vol. 361, no. 5, pp. 1447–1455, 2008.
- [65] H. F. Liang, C. T. Chen, S. C. Chen, et al., "Paclitaxel-loaded poly(g-glutamic acid)-poly(lactide) nanoparticles as a targeted drug delivery system for the treatment of liver cancer," *Biomaterials*, vol. 27, no. 9, pp. 2051–2059, 2006.
- [66] L. Zhu, Z. Huo, L. Wang, X. Tong, Y. Xiao, and K. Ni, "Targeted delivery of methotrexate to skeletal muscular tissue by thermosensitive magnetoliposomes," *International Journal of Pharmaceutics*, vol. 370, no. 1–2, pp. 136–143, 2009.
- [67] K. Y. Kim, "Nanotechnology platforms and physiological challenges for cancer therapeutics," *Nanomedicine: Nanotechnology, Biology, and Medicine*, vol. 3, no. 2, pp. 103–110, 2007.

- [68] R. Singh and K. Kostarelos, "Designer adenoviruses for nanomedicine and nanodiagnostics," *Trends in Biotechnology*, vol. 27, no. 4, pp. 220–229, 2009.
- [69] W. J. Gradishar, S. Tjulandin, N. Davidson, et al., "Phase III trial of nanoparticle albumin-bound paclitaxel compared with polyethylated castor oil-based paclitaxel in women with breast cancer," *Journal of Clinical Oncology*, vol. 23, no. 31, pp. 7794–7803, 2005.
- [70] T. Chidiac, G. T. Budd, R. Pelley, et al., "Phase II trial of liposomal doxorubicin (Doxil®) in advanced soft tissue sarcomas," *Investigational New Drugs*, vol. 18, no. 3, pp. 253–259, 2000.
- [71] S. O. Rodiek, A. Stolze, and C. B. Lumenta, "Preoperative embolization of intracranial meningiomas with Embosphere® microspheres," *Minimally Invasive Neurosurgery*, vol. 47, no. 5, pp. 299–305, 2004.

Research Article

Detection of Thyroid Carcinoma Antigen with Quantum Dots and Monoclonal IgM Antibody (JT-95) System

Kouki Fujioka,^{1,2} Noriyoshi Manabe,² Mayumi Nomura,¹ Michiko Watanabe,¹ Hiroshi Takeyama,³ Akiyoshi Hoshino,^{1,2} Sanshiro Hanada,² Kenji Yamamoto,² and Yoshinobu Manome¹

¹ Department of Molecular Cell Biology, Institute of DNA Medicine, Jikei University School of Medicine, 3-25-8 Nishi-Shinbashi, Minato, Tokyo 105-8461, Japan

² International Clinical Research Center, Research Institute, International Medical Center of Japan, 1-21-1 Toyama, Shinjuku, Tokyo 162-8655, Japan

³ Department of Surgery, Jikei University School of Medicine, 4-11-1 Izumi-Honcho, Komae City, Tokyo 201-8601, Japan

Correspondence should be addressed to Yoshinobu Manome, manome@jikei.ac.jp

Received 1 October 2009; Revised 3 December 2009; Accepted 8 March 2010

Academic Editor: Chao Lin

Copyright © 2010 Kouki Fujioka et al. This is an open access article distributed under the Creative Commons Attribution License, which permits unrestricted use, distribution, and reproduction in any medium, provided the original work is properly cited.

High-intensity fluorescent nanoparticles, quantum dots (QDs), have been applied to a wide range of biological studies and medical studies by taking advantage of their fluorescent properties. On the other hand, we have reported the specificity of JT-95 monoclonal IgM antibody, which recognizes the antigen of thyroid carcinomas. Here we show that the combination of QDs and JT-95 monoclonal antibody was applicable to Western blotting analysis, ELISA-like system, and fluorescent microscopic analysis of SW1736 thyroid carcinoma cell line. We have opened up the possibility that antibodies for higher specific recognition, even IgM, are applicable to the detection system with QDs.

1. Introduction

Diagnosis of thyroid cancer involves methods such as palpation, ultrasonography, fine-needle aspiration cytology (FNAC), scintigraphy, and blood test. To achieve more precise diagnosis and alleviate burdens of both patients and doctors, however, we consider that the following 2 points need to be improved.

The first point is the blood test. Although the blood test is thought to be the simplest method without much burden on patients, blood tests currently performed are not well suited for screening tests to determine the existence or nonexistence of cancer. In the blood tests, thyroglobulin [1, 2] and calcitonin are considered to be most effective [3]. Thyroglobulin is known to exhibit high values with papillary and follicular carcinomas of the classified thyroid cancers as well as with other diseases including inflammation and benign tumors [2]. Although calcitonin is reported to be a marker for medullary carcinoma [3], negative cases are also reported [2]. Hence, the development of a new blood

test method which will replace these ones and increase the precision is required.

The second point is the judgment of the degree of malignancy of neoplasm in FNAC. The FNAC is known to be extremely precise in classifying neoplasm and judging the degree of malignancy [4, 5]. The follicular carcinoma which has the second highest rate of occurrence in Japan [6], within the classified thyroid cancers such as papillary carcinoma, follicular carcinoma, poorly differentiated carcinoma, undifferentiated carcinoma, and medullary carcinoma, however, does not exhibit any nuclear atypicity. This fact makes it difficult to judge from FNAC results whether a tumor is benign or malignant. When such a judgment is found to be difficult before operation, surgical removal of follicular lesions is preferably carried out. Recent studies showed that in patients who had their follicular carcinoma removed only 15–20% of them were malignant, while more than 80% were benign [7, 8]. That is, more than 80% of patients have supposedly undergone an operation to have their benign tumors removed without such a need. Hence, we think the

availability of testing methods of high-precision is highly beneficial.

We hereby propose new detection methods of thyroid carcinoma antigen by combining the high-intensity fluorescent nanoparticles with antibodies for the specific recognition of thyroid cancer. In previous studies, we have been developing monoclonal antibodies for the specific recognition of thyroid cancer (JT-95) [9]. The JT-95 antibody belongs to IgM group. IgM antibodies are often known to have low affinity (dissociation constant (K_d) $> 10^{-5}$ M) and therefore they are usually neglected as tools [10]. However, the result of histological stains using JT-95 and the enzyme-labeled second antibody shows the possibility of distinguishing cancer from benign lesions with precision [9]. Moreover, we have shown using enzyme-linked immunosorbent assay (ELISA) test that these antibodies react to the plasma samples from patients with thyroid carcinoma.

On the other hand, we have been conducting researches on biochemical applications of the quantum dots (QDs) [11–17], which are the high-intensity fluorescent nanoparticles [18]. We have developed a high-intensity detection method for microbial toxins [19] or myeloperoxidase from neutrophil [20] by binding QDs to antibodies, similar as the applications in the report [21].

From these studies, we can expect that the combination of the JT-95 antibody and QDs will further increase the detection sensitivity of thyroid cancer, enabling the detection with blood test and helping judge the degree of malignancy of follicular carcinoma in the future.

In the present study, we tried to detect the antigen of SW1736 thyroid cancer cell line in microscopic analysis, Western blotting analysis, and ELISA-like system with QDs. Moreover, in order to speculate the differences of reactivities between streptavidin-conjugated QDs (streptavidin-QDs) and avidin-conjugated-horseradish peroxidase (avidin-HRP) or between IgM and IgG during the immunoassays, we investigated the size distributions of immunocomplexes.

2. Materials and Methods

2.1. Cell Line. SW1736 human thyroid carcinoma cell line was used in this study. Previous study showed that the JT-95 antibody recognized the sialic-acid-modified fibronectin from the cells [22]. Pancreatic cell lines (10 cell lines: KP4, KP4-1, KP4-2, IC3, 2C6, T3M4, Panc28 Puru, Panc28 DB2M, Panc-1, and MiaPaca2) were used as negative control cells in Western blotting analysis. Green fluorescent protein- (GFP-) expressed U937 human leukemic monocyte lymphoma cell line was used as negative control cells in fluorescent microscopy analysis.

2.2. Purification of JT-95 IgM Antibody and Normal Mouse IgM Antibody. For the preparation of JT-95 antibody, antibody-producing hybridoma was cultured in serum-free medium (Cosmedium-001, CosmoBio Corporation, Tokyo, Japan). Normal mouse IgM was prepared from mouse serum (BALB/cA Jcl, Clea Japan, Tokyo, Japan). The JT-95 antibody

and normal mouse IgM were purified using an affinity IgM column (HiTrap IgM purification HP column, GE Healthcare, Buckinghamshire, UK) and bound; the IgM antibody was eluted with glycine buffer (0.2 M glycine, 0.15 M NaCl, pH 2.8). Eluates were neutralized with a 1/10 volume of 1 M Tris buffer (tris hydroxymethyl aminomethane, pH 8.5), and the IgM concentrations were determined by a spectrophotometer.

2.3. QDs Imaging of Cells and Observation under Microscopy. The 4×10^4 cells of SW1736 cells were cocultured with the 4×10^4 cells of GFP-expressed U937 cells on collagen-coated chamber slides (4-well) for 2 days. The co-cultured cells were fixed with 4% (w/v) paraformaldehyde in Dulbecco's PBS (DPBS) for 20 minutes. The $9 \mu\text{g}$ of JT-95 or normal mouse IgM in $300 \mu\text{L}$ Block Ace (Snow Brand Milk Products Corporation, Tokyo, Japan) was added and incubated for 90 min. Then biotinylated anti-IgM antibody in Vectastain ABC mouse IgM kit (Vector Laboratories, Inc., CA, USA) was added as second antibody and incubated for 60 min. After the incubation, the slides were washed and 20 nM of streptavidin-Qdot 655 (Qdot 655 ITK streptavidin conjugation kit, Invitrogen Corporation, USA) or streptavidin-PE (BioLegend, CA, USA) was added and incubated for 30 min. The cells were observed with BZ-9000 fluorescent microscope (Keyence Corporation, Osaka, Japan). The slides were washed with DPBS 3 times between all procedures.

2.4. Western Blotting Analysis. In order to evaluate the immunoreactivity of the JT-95 with QDs, Western blotting analysis was conducted. SW1736 cells were dispersed in DPBS and lysed with supersonic on ice (3 seconds \times 3 times). The lysates were separated by 7.5% SDS-PAGE and transferred to a membrane (Hybond-P, Amersham Biosciences, Harsham, UK) for 60 min. The membranes were blocked with the Block ace overnight at 4°C . The $7.5 \mu\text{g}$ of JT-95 or normal mouse IgM in 5 mL Block ace was added and incubated for 90 min. Then biotinylated anti-IgM antibody in the Vectastain ABC mouse IgM kit, was added as second antibody and incubated for 60 min. After the incubation, 20 nM of streptavidin-Qdot 655, or complexes of Avidin DH and Biotinylated Horseradish Peroxidase H (HRP) in the kit was added and incubated for 30 min. After washing of the membrane, fluorescence of the Qdot 655 was examined under 365 nm UV light excitation. Antigen-binding activity of JT-95 with Qdot 655 was confirmed by comparison to the HRP reaction with DAB kit (Vector Laboratories, CA, USA). The membranes were washed with PBS containing 0.05% Tween 20 (PBST) 3 times between all procedures.

2.5. ELISA-Like Assay with QDs. In order to evaluate the quantitative reactivity of the JT-95 with QDs, ELISA-like system was conducted. The supernatant of SW1736 cells culture media was plated on high-affinity plastic plates (96-Well Clear Flat Bottom Polystyrene High Bind Microplate: Corning, NY, USA) in $15\text{--}0.015 \mu\text{g}/100 \mu\text{L}$ PBS, and the plates were incubated at 4°C for 16 hours. The plate was blocked with the $200 \mu\text{L}$ of Block ace 1 hour at 37°C .

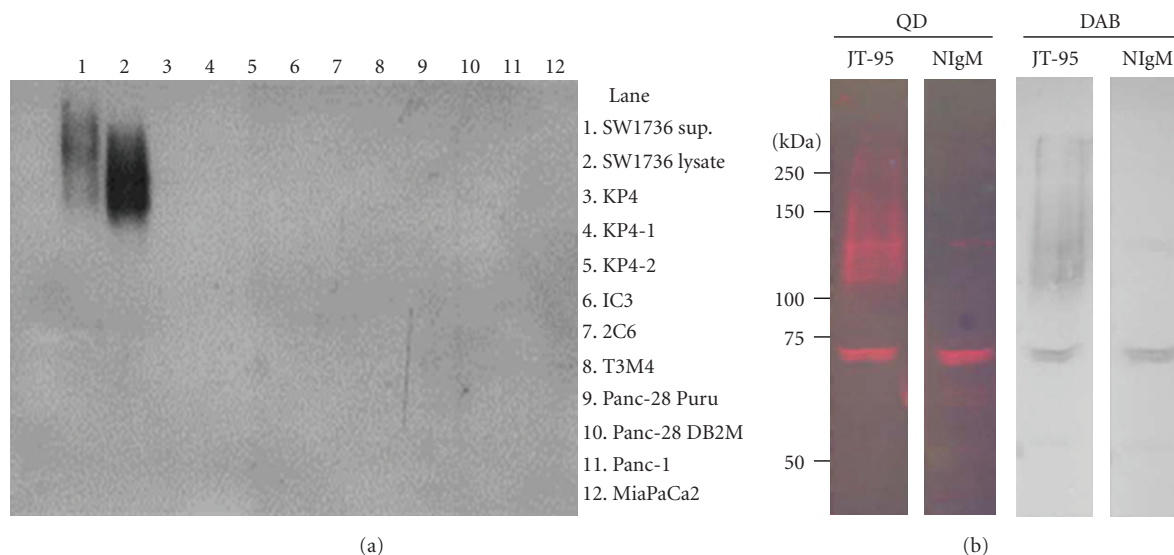


FIGURE 1: Western blotting analysis with JT-95 monoclonal antibody for thyroid carcinoma antigen. (a) Reactivity of JT-95 antibody with HRP-anti-IgM antibody against SW1736 thyroid carcinoma cell lines (lanes 1, 2) and lysates of pancreatic carcinoma cell lines as negative controls (lanes 3-12). This membrane image was developed with ECL Plus Western Blotting Detection System (GE Health Care). Sup.: supernatant in the culture media of SW1736 cells. (b) Reactivity of JT-95 antibody against the lysates of SW1736 cells with streptavidin-Qdot 655 staining (a) and nickel-DAB staining (b) system. The membrane stained with QDs was excited with UV (365 nm). NIgM: normal mouse IgM.

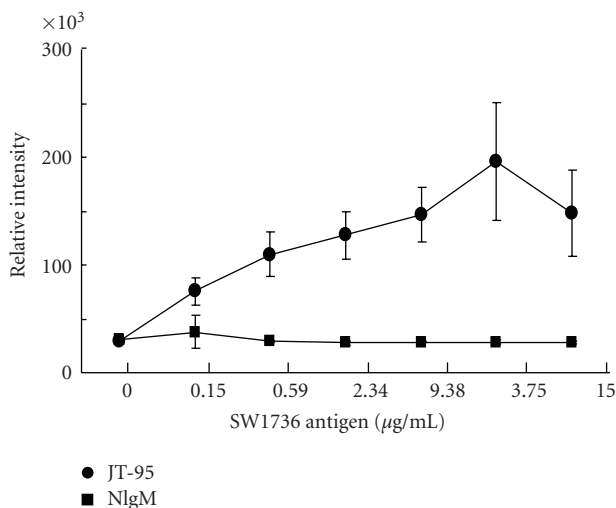


FIGURE 2: ELISA-like assay with QDs for the antigen of SW1736 cells. The SW1736 antigens were serially diluted and reacted with JT-95, biotinylated anti-IgM antibody, and streptavidin-Qdot 655 in immunoreaction enhancer solutions (Can Get Signal: Toyobo, Osaka, Japan).

The 1.13 μg of JT-95 or normal mouse IgM in 50 μL immunoreaction enhancer solution 1 (Can Get Signal: Toyobo, Osaka, Japan) was added and incubated for 2 hours. Then the 1.25 μg of biotinylated anti-IgM antibody in the 50 μL enhancer solution 2 was added and incubated for 60 min. After the incubation, 5 nM of streptavidin-Qdot 655 in the 50 μL enhancer solution 2 was added and incubated for 60 min. After 100 μL of PBS was added, the reacted QDs were detected with a filter set of excitation 360 nm/emission 650 nm in DTX880 plate reader (Beckman Coulter, CA, USA). The plates were washed with PBST 3 times between all procedures.

2.6. Dynamic Light-Scattering Analysis. To investigate the conformation changes of immunoglobulin complexes during the process of immunoassays, we attempted to measure the particle diameter of the complexes by dynamic light scattering (DLS) with Zetasizer Nano (Malvern Instruments, Worcestershire, UK). The 0.5 mg/mL of JT-95 antibody or Mouse IgG₁ antibody (Mouse IgG₁ Isotype Control, R&D Systems, MN, USA) in DPBS was incubated with 20 μL of biotinylated anti-IgM antibody or biotinylated anti-IgG antibody in the Vectastain ABC kit for 60 min, respectively. After the incubation, the streptavidin-Qdot 655 was added to the concentration of 200 nM, or 20 μL of the avidin-HRP

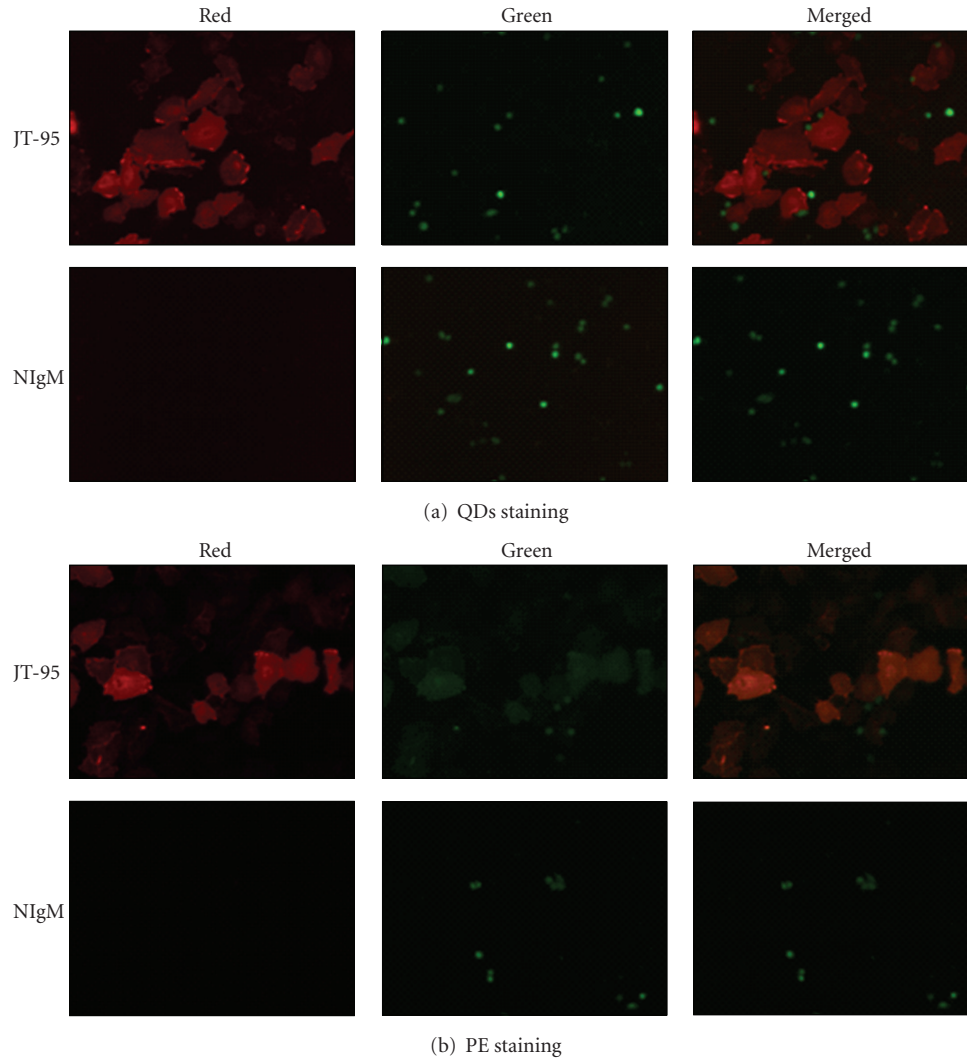


FIGURE 3: Fluorescent microscopic analysis of SW1736 cells with JT-95 monoclonal antibody. (a) Streptavidin-Qdot 655 staining. (b) Streptavidin-PE staining. NIgM: normal mouse IgM (Magnification: $\times 80$).

complexes (Avidin DH and Biotinylated Horseradish Peroxidase) was added.

3. Results and Discussion

In previous study, we showed that the JT-95 antibody recognized antigen from SW1736 thyroid carcinoma cell lines as well as malignant lesions and serum from patients [9]. In order to reaffirm the specificity, we investigated the affinities of JT-95 antibody against several carcinoma cell lines (Figure 1(a)). Western blotting analysis with HRP-enhanced chemiluminescent (ECL) system showed that the JT-95 antibody recognized the supernatant in cultured medium and whole lysate of SW1736, while the JT-95 antibody did not recognize 10 kinds of pancreatic carcinoma cell lines as negative controls.

Although the ECL system has high sensitivity, the system needs development procedure in a dark room. For the usability, we attempted Western blotting analysis using

streptavidin-QDs or nickel-diaminobenzidine (DAB) system as concise methods. The results showed a band in the range of 100–250 kDa was detected in both the detection system using QDs and the system using DAB (Figure 1(b)). In comparison to DAB system, the visibility of the band is higher with QDs. With normal mouse IgM as a negative control, bands were found in 2 places. These can possibly be attributed to nonspecific binds of IgM.

Quantitative reactivity was measured with ELISA-like assay. The JT-95 bound to the SW1736 antigens in a dose-dependent manner in the range of 0.15–3.75 $\mu\text{g}/\text{mL}$ (Figure 2). Previous report using peroxidase ELISA system showed that the JT-95 bound to the membrane fraction of papillary carcinoma in the range of 1–100 $\mu\text{g}/\text{mL}$ [9]. Since the range of QDs assay are sufficiently lower than that of previous ELISA system, our QDs system will be applicable to antigen screening.

In order to investigate the possibility of usage in pathology assessment, we applied QDs and JT-95 antibody to stain

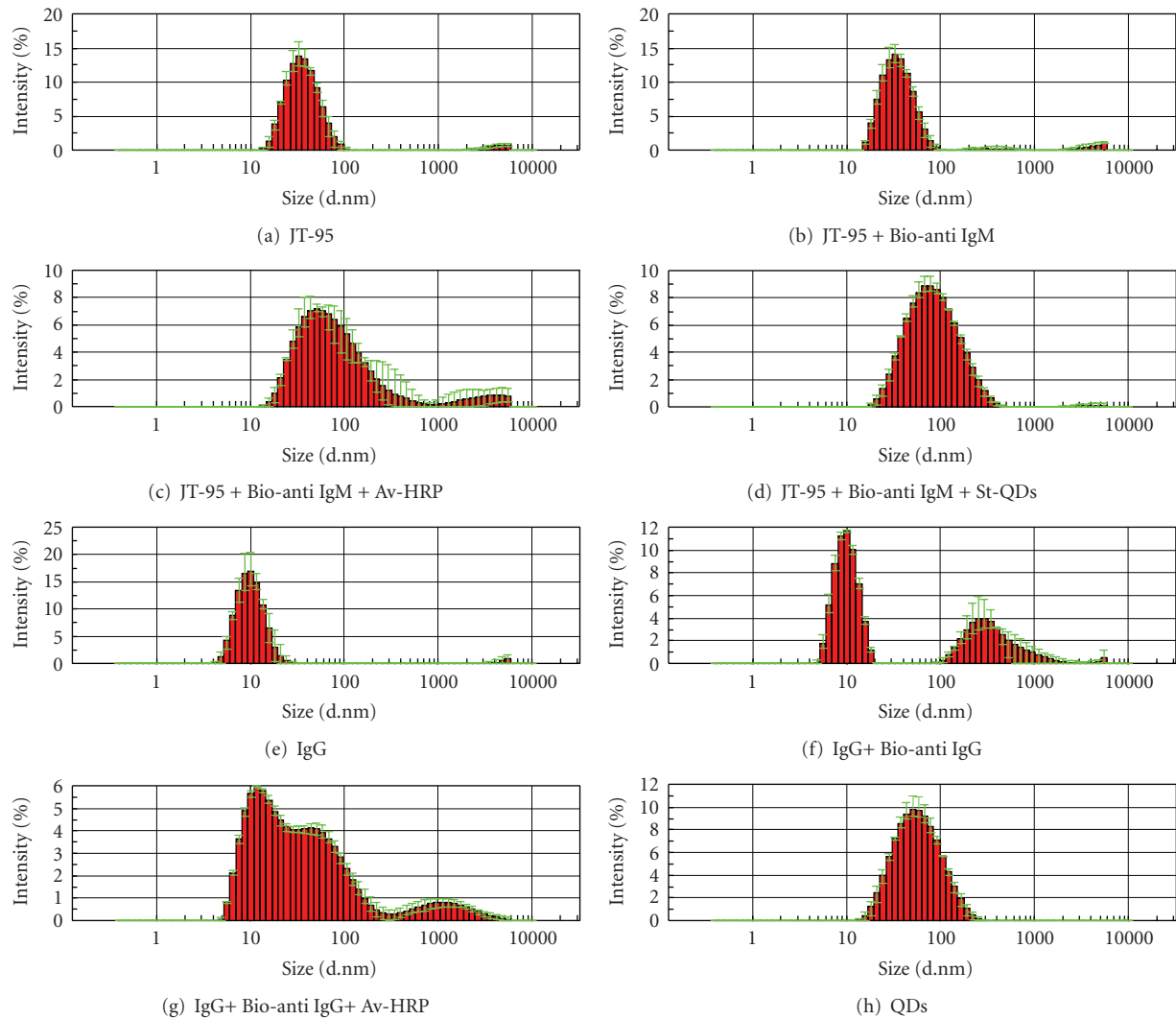


FIGURE 4: Size distributions of immunoglobulin and immunocomplexes in immunoassay procedures. The size distributions during reactions of JT-95 antibody were shown in (a)-(d). JT-95 antibody in DPBS (a) was reacted with biotinylated anti-IgM antibody for 60 min (b). After the reaction, the solution was incubated with avidin-HRP (c) or streptavidin-Qdot 655 (d) for 30 min. As a comparison, the size distributions during reactions of normal mouse IgG₁ were shown in (e)-(g). The IgG₁ (e) was reacted with biotinylated anti-IgG antibody for 60 min (f). After the reaction, the solution was incubated with avidin-HRP (g). On the other hand, aggregation occurred, in the solution which incubated with streptavidin-Qdot 655 (data not shown). The size distribution of only streptavidin-Qdot 655 in DPBS (h).

SW1736 cells. Figure 3(a) shows the images where thyroid cancer cell lines were stained with the combination. The JT-95 antibody is known to recognize the mutant fibronectin on cell membranes, which are also found to be strongly stained in this study. The co-cultured U937 cells expressing GFP are not stained with this system, denoting its specificity of antigen staining. No QDs were detected using normal mouse IgM. As a comparison with a conventional method, we conducted phycoerythrin (PE) staining (Figure 3(b)). The combination of PE and JT-95 antibody also stained the membrane of SW1736 cells. However, the emission from PE was detected not only in the Red channel but also in the Green channel, since the fluorescence of PE has broad emission band. When double staining was conducted in pathological assessment, narrow-emission QDs may be better suited.

There are problems to solve, however. It needed 3 seconds to identify the fluorescence from QDs by a microscopic observation, which is low in sensitivity when compared to conventional detection systems which require less than 1 second. This may be possibly attributed to the high molecular weights or large size of the combination of QDs and IgM.

On the other hand, although we succeeded in constructing an ELISA system with avidin-HRP and JT-95 antibody in PBS, we failed to construct an ELISA-like assay with streptavidin-QDs and JT-95 antibody in PBS. Therefore we conducted the latter assay in immunoreaction enhancer solution (see Materials and Methods section). In order to speculate the difference of reactivity between avidin-HRP and streptavidin-QDs, we measured the size distributions of immunocomplexes in the immunoassay procedures by

dynamic light scattering (Figure 4). The JT-95 antibody showed the peak size of 32.7 nm in DPBS (Figure 4(a)). After adding biotinylated anti-IgM antibody, the peak size was 32.7 nm as same (Figure 4(b)). Additionally, the new slight peak appeared within 100–1,000 nm. When avidin-HRP was added, the peak size moved to 50.7 nm (Figure 4(c)). The complexes within 100–1,000 nm increased drastically and the complexes over 1,000 nm increased slightly. While adding streptavidin-QDs, the peak size moved to 78.7 nm (Figure 4(d)). The complexes in 100–1,000 nm increased similarly. Different from the avidin-HRP complexes, QDs complexes within 2,300–4,800 nm were detected slightly. These results suggested that the dispersed larger size complexes over 1,000 nm, which was supposed to be constructed from several biotin-avidin or -streptavidin complexes, determine the detection abilities.

As a comparison with another immunoglobulin reactivity, we conducted the similar experiment with normal mouse IgG₁ antibody. The IgG₁ antibody showed the peak size of 10.1 nm (Figure 4(e)). After adding biotinylated anti-IgG antibody, the peak size was 10.1 nm as same (Figure 4(f)). Drastically, the new peak of complexes appeared within 100–2,000 nm. When avidin-HRP was added, the peak size moved to 13.4 nm (Figure 4(g)). Different from the final JT-95 antibody complexes with avidin-HRP (Figure 4(c)), the second highest peak of complexes appeared in 43.8 nm. Additionally, complexes at the peak size of 1,110 nm increased. When we added streptavidin-QDs with the IgG antibody and biotinylated-anti-IgG antibody dispersion, the complexes aggregated and precipitated (data not shown).

From these results, we revealed the ratio of IgG and the biotinylated antibody was higher than that of IgM case (Figure 4(b), (f)). For further detection ability, it may require the conformation change from IgM to IgG, or stronger binding ability of biotinylated anti-IgM antibody. Additionally, as a reason for fail in the ELISA-like assay with streptavidin-QDs, high molecular weight or aggregations of QDs may affect an antigen-ELISA plate interaction. The streptavidin-QDs have 5–10 streptavidins per one QD label (manufacturer's protocol). The complexes of JT-95 antibody and the biotinylated antibody were cross-linked with streptavidin-QDs and may become higher-molecular weight complexes or aggregation in near antigen area, since the QDs, which were added with the IgG₁ antibody and biotinylated-anti-IgG antibody dispersion, aggregated and precipitated. For the amelioration in the ELISA-like assay with QDs, the JT-95 antibody may need direct labeling or fragmentation for saving molecular weight.

In this study, we have succeeded in the detection of thyroid carcinoma antigen using the Western blotting analysis, ELISA-like assay, and staining thyroid cancer cell lines with QDs using a microscopy. Thus, we have opened up the possibility that antibodies for higher specific recognition, even IgM, will be applicable to the detection system with QDs.

In our previous study, the JT-95 antibodies in combination with the enzyme-labeled second antibody showed a diagnostic accuracy of 95% in papillary carcinoma and 75% in follicular carcinoma [9], when stained with sections of

thyroid cancer tissues. In the future it will be necessary to compare the accuracies between the enzyme system and the QDs system. Especially in the Western blotting system, the visibility was higher and a stronger band was detected than when stained with DAB in this study. As some cancer cells express different sugar chains in differentiation or organs [23], the higher sensitive detection of bands may be helpful for judging the degree of malignancy.

4. Conclusion

We have succeeded in building new detection systems by the combination QDs and JT-95 antibody for recognition of thyroid carcinoma. These methods involved the use of IgM antibody with QDs and that is academically meaningful in the antibody detection methods where IgG is the mainstream. Although these methods need amelioration for clinical use, we are of the opinion that in the future this can become a complementary technique to the existing methods by applying to pathological assessment and blood test.

Acknowledgments

This research was partly supported by The Jikei University Research Fund and Health and Labour Sciences Research Grants (H19-nano-012: the Ministry of Health, Labour and Welfare of Japan).

References

- [1] A. J. Van Herle, R. P. Uller, N. I. Matthews, and J. Brown, "Radioimmunoassay for measurement of thyroglobulin in human serum," *Journal of Clinical Investigation*, vol. 52, no. 6, pp. 1320–1327, 1973.
- [2] H. Tamaki, "Thyroid carcinoma," *Japanese Journal of Cancer & Chemotherapy*, vol. 32, no. 4, pp. 561–565, 2005.
- [3] H. Takami, J.-I. Shikata, H. Horie, K. Sekine, and K. Ito, "PDN-21: possible tumor marker for medullary thyroid carcinoma," *Journal of Surgical Oncology*, vol. 44, no. 4, pp. 205–207, 1990.
- [4] B. Hamberger, H. Gharib, L. J. Melton III., J. R. Goellner, and A. R. Zinsmeister, "Fine-needle aspiration biopsy of thyroid nodules. Impact on thyroid practice and cost of care," *American Journal of Medicine*, vol. 73, no. 3, pp. 381–384, 1982.
- [5] C. Ravetto, L. Colombo, and M. E. Dottorini, "Usefulness of fine-needle in the diagnosis of thyroid carcinoma: a retrospective study in 37,895 patients," *Cancer*, vol. 90, no. 6, pp. 357–363, 2000.
- [6] W. Kitagawa, K. Shimizu, H. Akasu, and S. Tanaka, "Endocrine surgery the ninth report: the latest data on and clinical characteristics of the epidemiology of thyroid carcinoma," *Journal of Nippon Medical School*, vol. 70, no. 1, pp. 57–61, 2003.
- [7] D. S. Cooper, G. M. Doherty, B. R. Haugen, et al., "Management guidelines for patients with thyroid nodules and differentiated thyroid cancer," *Thyroid*, vol. 16, no. 2, pp. 109–142, 2006.
- [8] F. Pacini, M. Schlumberger, H. Dralle, R. Elisei, J. W. Smit, and W. Wiersinga, "European consensus for the management of patients with differentiated thyroid carcinoma of the follicular

- epithelium," *European Journal of Endocrinology*, vol. 154, no. 6, pp. 787–803, 2006.
- [9] H. Takeyama, T. Hosoya, K. Sakurai, et al., "Production of a novel monoclonal antibody, JT-95, which can detect antigen of thyroid carcinoma," *Cancer Research*, vol. 56, no. 8, pp. 1817–1822, 1996.
- [10] M. Strandh, M. Ohlin, C. A. K. Borrebaeck, and S. Ohlson, "New approach to steroid separation based on a low affinity IgM antibody," *Journal of Immunological Methods*, vol. 214, no. 1-2, pp. 73–79, 1998.
- [11] A. Hoshino, K. Fujioka, T. Oku, et al., "Quantum dots targeted to the assigned organelle in living cells," *Microbiology and Immunology*, vol. 48, no. 12, pp. 985–994, 2004.
- [12] A. Hoshino, K. Fujioka, T. Oku, et al., "Physicochemical properties and cellular toxicity of nanocrystal quantum dots depend on their surface modification," *Nano Letters*, vol. 4, no. 11, pp. 2163–2169, 2004.
- [13] N. Manabe, A. Hoshino, Y.-Q. Liang, T. Goto, N. Kato, and K. Yamamoto, "Quantum dot as a drug tracer in vivo," *IEEE Transactions on Nanobioscience*, vol. 5, no. 4, pp. 263–267, 2006.
- [14] A. Hoshino, N. Manabe, K. Fujioka, K. Suzuki, M. Yasuhara, and K. Yamamoto, "Use of fluorescent quantum dot bioconjugates for cellular imaging of immune cells, cell organelle labeling, and nanomedicine: surface modification regulates biological function, including cytotoxicity," *Journal of Artificial Organs*, vol. 10, no. 3, pp. 149–157, 2007.
- [15] S. Yamamoto, N. Manabe, K. Fujioka, A. Hoshino, and K. Yamamoto, "Visualizing vitreous using quantum dots as imaging agents," *IEEE Transactions on Nanobioscience*, vol. 6, no. 1, pp. 94–98, 2007.
- [16] K. Fujioka, M. Hiruoka, K. Sato, et al., "Luminescent passive-oxidized silicon quantum dots as biological staining labels and their cytotoxicity effects at high concentration," *Nanotechnology*, vol. 19, no. 41, Article ID 415102, 2008.
- [17] A. Hoshino, N. Manabe, K. Fujioka, et al., "GFP expression by intracellular gene delivery of GFP-coding fragments using nanocrystal quantum dots," *Nanotechnology*, vol. 19, no. 49, Article ID 495102, 2008.
- [18] W. C. W. Chan and S. Nie, "Quantum dot bioconjugates for ultrasensitive nonisotopic detection," *Science*, vol. 281, no. 5385, pp. 2016–2018, 1998.
- [19] A. Hoshino, K. Fujioka, N. Manabe, et al., "Simultaneous multicolor detection system of the single-molecular microbial antigen with total internal reflection fluorescence microscopy," *Microbiology and Immunology*, vol. 49, no. 5, pp. 461–470, 2005.
- [20] A. Hoshino, T. Nagao, A. Nakasuga, et al., "Nanocrystal quantum dot-conjugated anti-myeloperoxidase antibody as the detector of activated neutrophils," *IEEE Transactions on Nanobioscience*, vol. 6, no. 4, pp. 341–345, 2007.
- [21] M. Arruebo, M. Valladares, and A. González-Fernández, "Antibody-conjugated nanoparticles for biomedical applications," *Journal of Nanomaterials*, vol. 2009, Article ID 439389, 24 pages, 2009.
- [22] N. Kimura, K. Kurokawa, K.-I. Yamamoto, et al., "Molecular identification of the antigens recognized by monoclonal antibody JT95 specific for thyroid carcinomas," *Biochemical and Biophysical Research Communications*, vol. 251, no. 2, pp. 449–453, 1998.
- [23] K. Maenuma, M. Yim, K. Komatsu, et al., "Use of a library of mutated Maaackia amurensis hemagglutinin for profiling the cell lineage and differentiation," *Proteomics*, vol. 8, no. 16, pp. 3274–3283, 2008.

Research Article

Protein Viability on Au Nanoparticles during an Electrospray and Electrostatic-Force-Directed Assembly Process

Shun Mao,¹ Ganhua Lu,¹ Kehan Yu,¹ and Junhong Chen^{1,2}

¹Department of Mechanical Engineering, University of Wisconsin-Milwaukee, 3200 North Cramer Street, Milwaukee, WI 53211, USA

²State Key Laboratory of Pollution Control and Resource Reuse, College of Environmental Science and Engineering, The Institute for Advanced Materials and Nano Biomedicine, Tongji University, 1239 Siping Road, Shanghai 200092, China

Correspondence should be addressed to Junhong Chen, jhchen@uwm.edu

Received 13 October 2009; Accepted 7 December 2009

Academic Editor: Chao Lin

Copyright © 2010 Shun Mao et al. This is an open access article distributed under the Creative Commons Attribution License, which permits unrestricted use, distribution, and reproduction in any medium, provided the original work is properly cited.

We study the protein viability on Au nanoparticles during an electrospray and electrostatic-force-directed assembly process, through which Au nanoparticle-antibody conjugates are assembled onto the surface of carbon nanotubes (CNTs) to fabricate carbon nanotube field-effect transistor (CNTFET) biosensors. Enzyme-linked immunosorbent assay (ELISA) and field-effect transistor (FET) measurements have been used to investigate the antibody activity after the nanoparticle assembly. Upon the introduction of matching antigens, the colored reaction from the ELISA and the change in the electrical characteristic of the CNTFET device confirm that the antibody activity is preserved during the assembly process.

1. Introduction

The protein viability has always been an issue in the biosensor design and fabrication, and is a key factor for the function of biosensing devices. In the past decade, carbon nanotubes (CNTs) with all atoms on the surface have been demonstrated for biomolecular sensing [1–3]; and in particular, field effect transistors (FETs) based on semiconducting CNTs have been used as biosensors [4–8]. The CNTFET devices are sensitive to variations in the surrounding environment because all the electrical current flows through the outermost layer of the CNT. The electrochemical detection of protein binding [9, 10] and DNA hybridization [11–14] using the CNTFET have been reported and changes in the device characteristics (e.g., drain current amplitude and threshold voltage) are mainly attributed to the charge transfer between proteins and CNTs. In these CNTFET devices [10–12], the CNT surface is often directly or indirectly (e.g., through Au nanoparticles) labeled with probe proteins, which function as binding sites for target proteins in the sensing process. Therefore, the viability of proteins during the assembly or labeling process is critical to the device functionality.

Here we investigate the viability of proteins on Au nanoparticles (Au NPs) during an assembly process for the fabrication of CNTFET biosensors, in which Au NPs labeled with anti-horseradish peroxidase (anti-HRP) were assembled onto the external surface of CNTs by a simple method that combines electrospray with electrostatic force directed assembly (ESFDA) [15–17]. To study the viability of antibodies on Au NPs, we first used the enzyme-linked immunosorbent assay (ELISA) technique, which is mainly used in immunology to detect the presence of antibodies and antigens. For visualization of the antigen-antibody reaction, an enzyme and a related substrate are often introduced, which could offer a colored reaction that can be spectrophotometrically measured. In this study, the antigen-antibody binding reaction was indicated by the color change (diimine terminal oxidation product/yellow end product) from the 3, 3', 5, 5'-tetramethyl benzidine (TMB) substrate in the ELISA, in which horseradish peroxidase (HRP) functions as the antigen and enzyme. To further confirm the viability of antibodies, CNTFET devices containing the antibody-conjugated Au NPs were fabricated and FET measurements were obtained to detect the antigen-antibody binding events. The amplitude change of the drain current was observed

when HRP were introduced in the sensor. The above two independent approaches clearly show that the antibodies on Au NPs are still active after the electro spray and electrostatic force directed assembly process.

2. Experimental

2.1. Materials. Au nanoparticles (18 nm Colloidal Gold) labeled with anti-HRP were purchased from Jackson ImmunoResearch and used without further purification. HRP from human serum were ordered from Sigma-Aldrich. A blocking agent bovine serum albumin (BSA), which was used to block the nonspecific binding of proteins with the sensing element, was purchased from Rockland. PBS (pH 7.4, $\times 1$) (Fisher BioReagents) was used as the solvent for HRP and BSA. TMB and HCL were purchased from Bio-Rad Lab and VWR, respectively. All solutions were prepared with distilled and deionized water (DI water) supplied by Cellgro. Multiwalled CNTs (MWCNTs) with diameter of 20 nm and lengths of several microns were purchased from Alfa Aesar.

2.2. Electro spray and Electrostatic Force Directed Assembly. Figure 1 shows a schematic of Au nanoparticle-antibody conjugates aerosolization by an electro spray process and the subsequent assembly of the conjugates onto CNTs by ESFDA. A commercial electro spray aerosol generator (EAG, TSI Model 3480) was used to spray colloidal Au nanoparticle-antibody conjugates. The colloidal conjugates applied with a high dc voltage were extracted through a capillary tube due to the capillary effect and the capillary inlet/outlet pressure difference. The conjugates ejected from the capillary were atomized to form charged fine droplets due to the electrohydrodynamic break-up. Charged Au NP-antibody conjugates were obtained after the solvent evaporation and subsequently assembled onto the surface of CNTs in an electric field. Since the electric field near the CNT was significantly enhanced due to their small diameters, the charged conjugates were attracted to the external surface of CNTs via electrostatic force. In our case, CNTs on a copper transmission electron microscopy (TEM) grid and Au electrodes were used. The assembly time was on the order of hours.

2.3. ELISA. 96-well polystyrene microplate (Sigma-Aldrich) was used as the reaction chamber in this procedure. At first, MWCNTs were dispersed on a copper TEM grid (400 mesh, Ted Pella, Inc.), and then Au nanoparticle-antibody conjugates were assembled onto the CNTs by electro spray and ESFDA. Three samples with different antibody concentrations on the CNTs were prepared by adjusting the deposition time from one hour to three hours. The samples were placed in a microplate and incubated with 200 μL BSA (0.01 mg/mL) for two hours, and then washed with the PBS buffer. After that, 100 μL of HRP ($1.8E - 6$ M, 0.08 mg/mL) were pipetted into the microplate for the protein binding for one hour, followed by wash and dry. Finally, 100 μL of TMB substrates were pipetted into the microplate for the colored reaction; after 30 minutes, 100 μL of 0.1 M HCL were

pipetted to stop the reaction and to turn the solution into yellow which can be measured through the light absorption using a microplate reader.

2.4. CNTFET Fabrication and Measurement. Gold interdigitated electrodes with both finger width and inter-finger spacing (source-drain separation) of about 1 μm were fabricated using an e-beam lithography process (Raith 150 lithography tool, 30 kV) on a Si wafer with a top layer of thermally-formed SiO_2 (thickness of 200 nm). Firstly, MWCNTs were dispersed onto the electrodes and dried under room temperature. The device was then annealed in argon flow (1 lpm) for one hour at 200°C to remove residue solvents and to improve the contact between CNTs and electrodes. After annealing, we found that the device was very robust. CNTs were immobilized between two metal electrodes and could not be washed away after several cycles of washing and drying, which has been confirmed by the SEM imaging. The device was then incubated with BSA for two hours and washed with the PBS buffer to reduce the possible nonspecific binding of HRP to CNTs and electrodes. After that, 20 μL HRP was pipetted onto the device for protein binding for one hour, followed by wash and dry. FET measurements were carried out using a Keithley 2602 source meter by recording the drain current response ($V_d = 0.01$ V) when ramping the gate voltage V_g from -3.0 to 3.0 V (with a step of 0.01 V). A Hitachi S-4800 UHR FE-SEM was used for scanning electron microscopy (SEM) characterization of the biosensing device at an acceleration voltage of 30 kV.

3. Results and Discussion

For the ELISA technique (Figure 2(a)), three samples with increasing deposition time from one hour to three hours were prepared. All the samples were performed in ELISA with exactly the same procedure as described previously in Experimental. BSA was used to reduce the possible nonspecific binding of HRP to the CNT, TEM grid and the well wall. In our case, the HRP functions as an enzyme, which converts the related substrate (TMB) to produce a yellow product. After adding the TMB substrate and HCL, the color of the solution turned yellow, which confirms the presence of HRP on the sample. Since BSA was introduced to block the non-specific binding, HRP could only bind with anti-HRP on the CNT. Therefore, the color change of the solution indicates that the antibody activity was preserved in the electro spray and ESFDA process.

Figure 2(b) shows the light absorption measurements for the three samples after the colored reaction. The absorption intensity increased with the deposition time. By adjusting the deposition time of electro spray and ESFDA, the concentration of Au NP-anti HRP conjugates on CNTs could be controlled. With more antibodies on CNTs, more HRP can bind on the device, therefore leading to more converted yellow product. The absorption results further confirm that the anti-HRP activity is preserved and antigen-antibody binding events occurred in the ELISA.

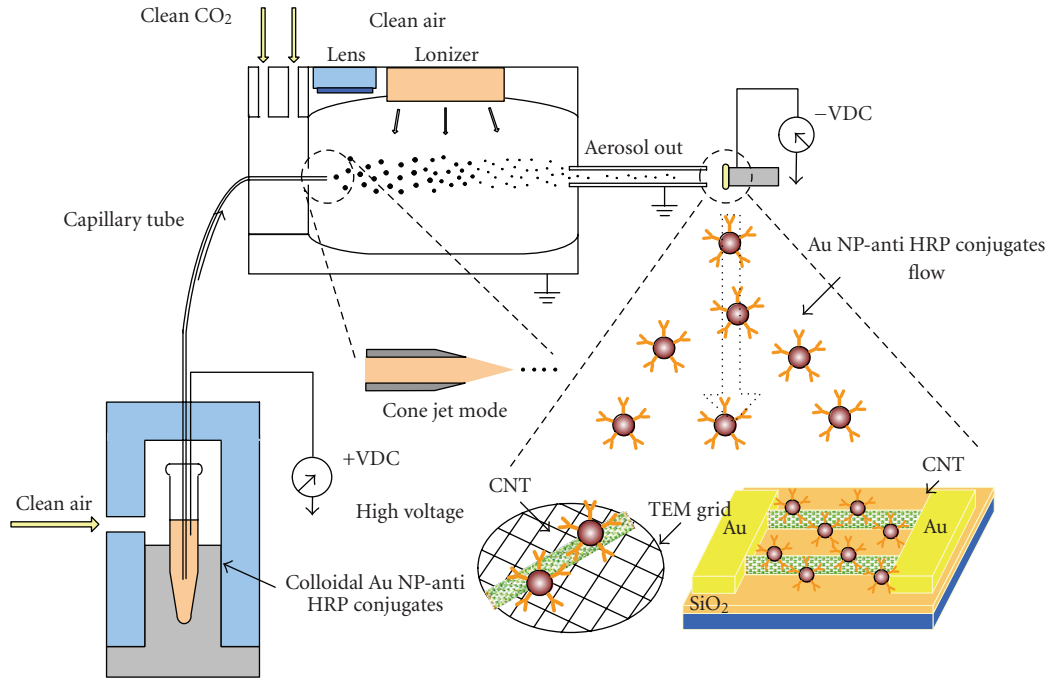


FIGURE 1: Schematic of Au nanoparticle-antibody conjugates aerosolization by an electrospay process and their subsequent assembly onto CNTs by ESFDA.

Au nanoparticle-antibody conjugates assembled on CNTs could be used in a CNTFET biosensor, from which the antibody activity could be studied by FET measurements. To confirm the presence of Au NPs on the surface of the CNT, SEM imaging was used to examine the CNTFET after the electrospay of Au NP-antibody conjugates. Figure 3(a) shows an SEM image of the Au interdigitated electrode [18]. In this configuration, Au electrodes are used as metal contacts for drain and source and the SiO₂ layer is used as the insulating material, through which a gate bias is applied to the back silicon wafer during the FET measurement.

Figure 3(b) shows the SEM image of a single CNT coated with Au NP-anti HRP conjugates and spanning across an electrode gap. After being electrospayed with Au NP-antibody conjugates, many Au NPs (light dots) are uniformly distributed on the surface of the CNT, indicating the presence of Au NPs in the CNTFET. Based on the SEM images, we conclude that Au NPs have been successfully attached to the CNTs likely through noncovalent binding [15, 17]. On the other hand, anti-HRPs are covalently linked to the surface of Au NPs and the bonding between antibody and Au NPs is relatively strong. Therefore, it is reasonable to assume that the antibodies are present in the CNTFET device after the assembly process. From the SEM image, we also found that the surface of the Au NPs was covered with a solvent layer, which is from the colloidal solution. It is known that the antibody is active for months when stored in buffer solution at 2–8°C. In our case, the antibody on the Au NPs are covered with a solvent layer similar to the buffer solution, which prevents the metamorphose of the antibody. We assume that the antibodies are active in the sensor for probing antigens,

which has been confirmed by the sensing results presented as follows.

Figure 4(a) shows the schematic illustration of the fabrication process of the CNTFET biosensor, in which the anti-HRP is anchored to the CNT surface through Au NPs and functions as the specific recognition group for HRP binding. FET measurements of the device were performed to study the antibody viability. Figure 4(b) shows the gate voltage dependence of the normalized drain current I_d (I_d is normalized by the drain current of the device at $V_g = -3.0$ V) after the CNTFET was treated with Au NP-anti-HRP conjugates, BSA and HRP. During the FET measurement, a gate bias V_g ramped from -3.0 V to 3.0 V while a constant bias of 0.01 V was held between the drain and the source. Based on Figure 4(b), the device characteristics resemble those of typical p-type semiconductors, in which holes are the majority carriers and the conductivity of the CNT depends on the mobility and density of holes. No hysteresis was observed in all V_g - I_d measurements. The type of device did not change after the CNTs and Au NP-anti-HRP conjugates were further treated with BSA and HRP; however, the drain current I_d decreased for both processes. The decrease in the drain current I_d after the BSA treatment is possibly because BSA is negatively charged in the PBS buffer and negative charges could transfer to CNTs or electrons could transfer from the electron-rich group such as secondary amine N-H in the BSA to CNTs, both of which could lead to the decrease in the density of holes in CNTs.

After the introduction of HRPs to the device, a significant decrease of I_d (about 36% at $V_g = -3.0$ V) was observed, which is a direct evidence for antigen-antibody binding

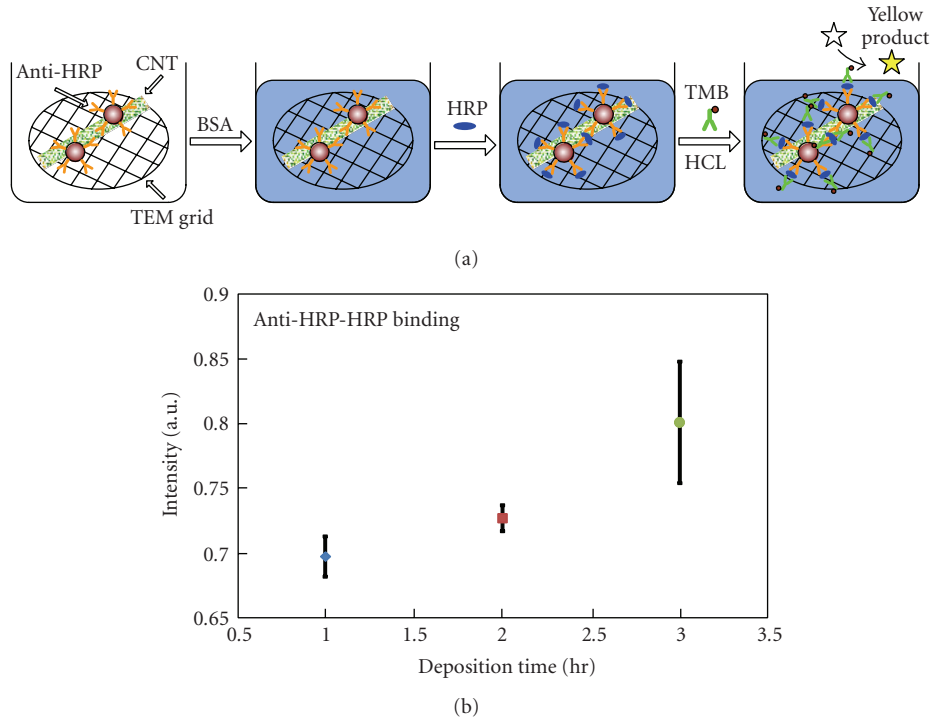


FIGURE 2: (a) Schematic illustration of ELISA. (b) Light absorption measurement from ELISA, in which HRP was added to three samples with different Au NP-anti HRP conjugates deposition time (1 hr, 2 hrs, and 3 hrs) and thus concentrations.

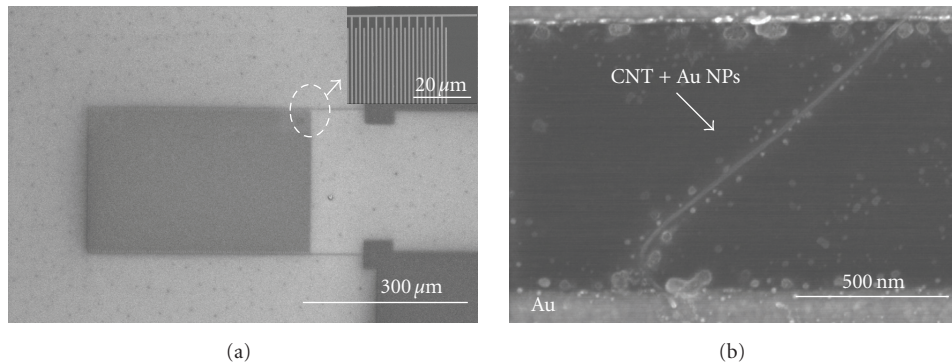


FIGURE 3: (a) SEM image of the Au interdigitated electrode. (b) SEM image of a single CNT coated with Au NP-anti HRP conjugates and spanning across an electrode gap.

events. The antibody-antigen interaction may have two effects on the CNT conductivity [5]. First, the antigen (HRP) triggers various scattering centers across the CNT as a result of binding events. Upon antigen-antibody binding, geometric deformations occur and increase the scattering centers across the tube; thereby reducing the mobility of holes in the CNT and thus leading to the decrease of drain current. As a possible second effect, the decrease of the drain current involves the charge tunneling from HRPs to CNTs. Charge tunneling from α -amino acid groups in HRPs to the CNT through the solvent is possible in the buffer solution, which reduces the carrier density in CNTs and thus leads to the decrease in the drain current. The observed drain current decrease could be the results of both the scattering

mechanism and the charge tunneling [10, 12]. To study the solvent influence to the drain current, a control experiment was performed by introducing only the PBS buffer to the device and a very tiny response (5% decrease in I_d) from the device was observed, indicating that the sensor response is mainly due to the binding of antigen to antibody. Figure 4(c) shows the drain-source voltage dependence of drain current I_d for a CNTFET treated with HRP of concentrations ranging from $4.5E-8$ M to $4.5E-5$ M. From the $I-V$ characteristics, we found that the drain current decreased monotonically with the increase of the HRP concentration, and this could only be explained by more antigens binding with antibodies, more scattering centers created, and more charge tunneling between CNTs and Au NPs.

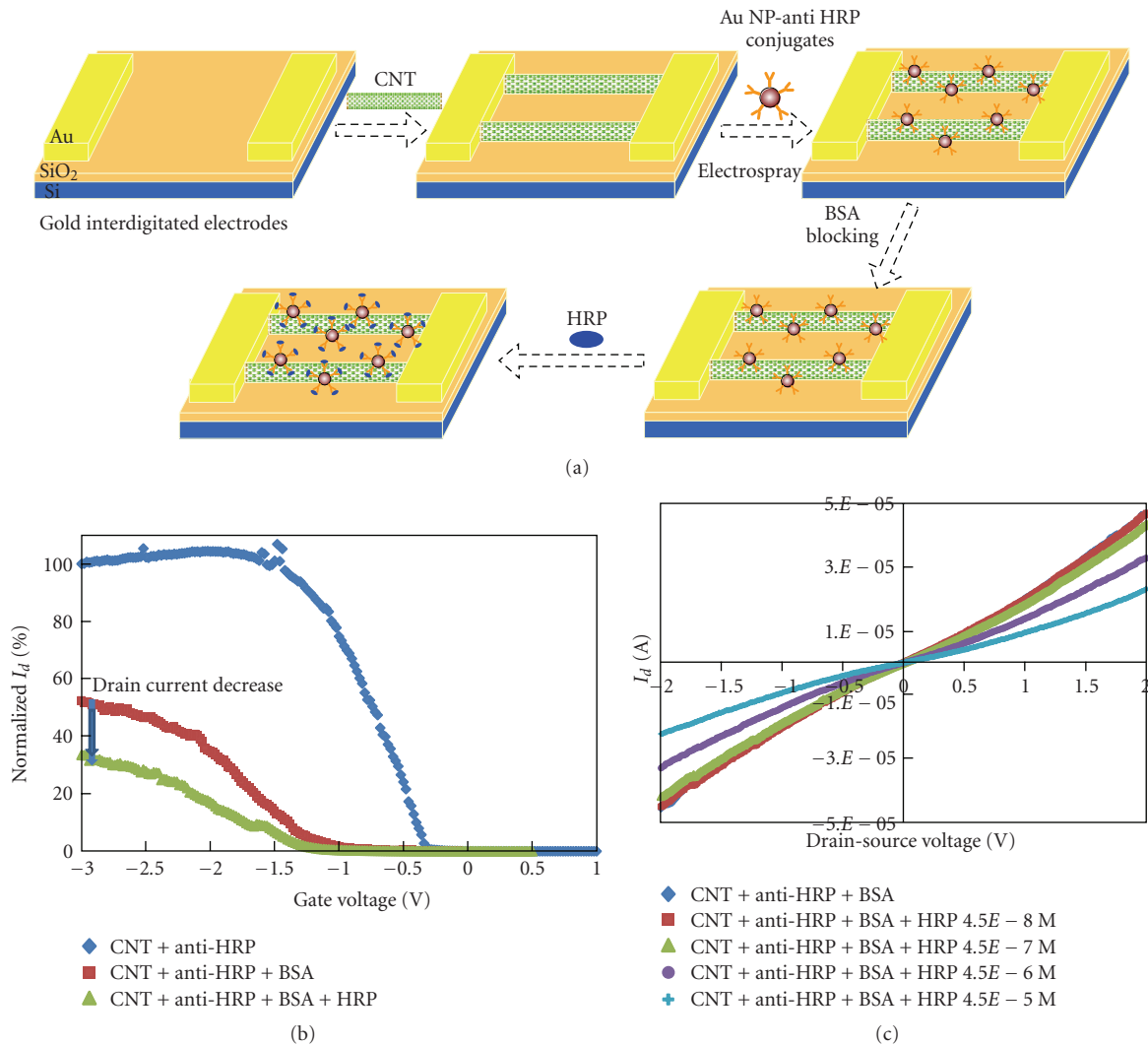


FIGURE 4: (a) Schematic illustration of the CNTFET biosensor fabrication process. (b) Gate voltage dependence of the normalized drain current I_d for a CNTFET treated with Au NP-anti-HRP conjugates, BSA and HRP ($V_d = -0.01$ V, HRP concentration = $4.5E - 5$ M). (c) Drain-source voltage dependence of drain current I_d for a CNTFET treated with HRP of concentrations ranging from $4.5E - 8$ M to $4.5E - 5$ M.

Each antibody preferentially binds to a specific antigen, an interaction similar to that of a lock and key. The antigen (HRP) used in this study can only bind to the corresponding antibody (anti-HRP); therefore, if the structure of the antibody changes during the assembly process, there will be no binding events in the sensing process and no significant change in the drain current would have been observed. Moreover, the drain current change was observed to increase with the increasing HRP concentration. Based on the FET sensing results and the ELISA results, we conclude that the activity of antibodies on Au NPs is preserved during the electrostatic force directed assembly process.

4. Conclusion

The viability of antibodies on Au nanoparticles during an electrostatic force directed assembly process

is studied using ELISA and FET biosensing measurements. The activity of antibodies on Au nanoparticles is preserved in the assembly process as confirmed by the colored reaction in ELISA and the drain current change in FET measurements. Since the same assembly technique could successfully assemble Au nanoparticle-antibody conjugates onto carbon nanotubes and many other nanostructures in a controlled manner, the assembly method could be useful for protein labeling in various biosensor fabrication processes.

Acknowledgments

Financial support for this work was partially provided by the National Science Foundation (CMMI-0900509, CBET-0803142, and ECCS-0708998). The SEM imaging was conducted at the Electron Microscope Laboratory of UWM. The e-beam lithography was performed at the Center for

Nanoscale Materials of Argonne National Laboratory, which is supported by the US Department of Energy, Office of Science, Office of Basic Energy Sciences, under Contract no. DE-AC02-06CH11357. The authors thank Prof. D. P. Klemmer for insightful discussion and helpful comments, Dr. H. A. Owen for technical support with SEM analyses, and Dr. L. E. Ocola for assistance in the electrode fabrication.

References

- [1] R. J. Chen, S. Bangsaruntip, K. A. Drouvalakis, et al., “Non-covalent functionalization of carbon nanotubes for highly specific electronic biosensors,” *Proceedings of the National Academy of Sciences of the United States of America*, vol. 100, no. 9, pp. 4984–4989, 2003.
- [2] J. Li, H. T. Ng, A. Cassell, et al., “Carbon nanotube nanoelectrode array for ultrasensitive DNA detection,” *Nano Letters*, vol. 3, no. 5, pp. 597–602, 2003.
- [3] J. Wang, “Carbon-nanotube based electrochemical biosensors: a review,” *Electroanalysis*, vol. 17, no. 1, pp. 7–14, 2005.
- [4] M. Abe, K. Murata, A. Kojima, et al., “Quantitative detection of protein using a top-gate carbon nanotube field effect transistor,” *Journal of Physical Chemistry C*, vol. 111, no. 24, pp. 8667–8670, 2007.
- [5] B. L. Allen, P. D. Kichambare, and A. Star, “Carbon nanotube field-effect-transistor-based biosensors,” *Advanced Materials*, vol. 19, no. 11, pp. 1439–1451, 2007.
- [6] P. Avouris, “Molecular electronics with carbon nanotubes,” *Accounts of Chemical Research*, vol. 35, no. 12, pp. 1026–1034, 2002.
- [7] J. P. Kim, B. Y. Lee, S. Hong, and S. J. Sim, “Ultrasensitive carbon nanotube-based biosensors using antibody-binding fragments,” *Analytical Biochemistry*, vol. 381, no. 2, pp. 193–198, 2008.
- [8] J. P. Kim, B. Y. Lee, J. Lee, S. Hong, and S. J. Sim, “Enhancement of sensitivity and specificity by surface modification of carbon nanotubes in diagnosis of prostate cancer based on carbon nanotube field effect transistors,” *Biosensors and Bioelectronics*, vol. 24, no. 11, pp. 3372–3378, 2009.
- [9] C. Li, M. Curreli, H. Lin, et al., “Complementary detection of prostate-specific antigen using In_2O_3 nanowires and carbon nanotubes,” *Journal of the American Chemical Society*, vol. 127, no. 36, pp. 12484–12485, 2005.
- [10] A. Star, J.-C. P. Gabriel, K. Bradley, and G. Gruner, “Electronic detection of specific protein binding using nanotube FET devices,” *Nano Letters*, vol. 3, no. 4, pp. 459–463, 2003.
- [11] M. T. Martinez, Y.-C. Tseng, N. Ormategui, I. Loinaz, R. Eritja, and J. Bokor, “Label-free DNA biosensors based on functionalized carbon nanotube field effect transistors,” *Nano Letters*, vol. 9, no. 2, pp. 530–536, 2009.
- [12] X. C. Dong, C. M. Lau, A. Lohani, et al., “Electrical detection of femtomolar DNA via gold-nanoparticle enhancement in carbon-nanotube-network field-effect transistors,” *Advanced Materials*, vol. 20, no. 12, pp. 2389–2393, 2008.
- [13] A. Star, E. Tu, J. Niemann, J.-C. P. Gabriel, C. S. Joiner, and C. Valcke, “Label-free detection of DNA hybridization using carbon nanotube network field-effect transistors,” *Proceedings of the National Academy of Sciences of the United States of America*, vol. 103, no. 4, pp. 921–926, 2006.
- [14] E.-L. Gui, L.-J. Li, P. S. Lee, et al., “Electrical detection of hybridization and threading intercalation of deoxyribonucleic acid using carbon nanotube network field-effect transistors,” *Applied Physics Letters*, vol. 89, no. 23, pp. 232104–232106, 2006.
- [15] J. H. Chen and G. H. Lu, “Controlled decoration of carbon nanotubes with nanoparticles,” *Nanotechnology*, vol. 17, no. 12, pp. 2891–2894, 2006.
- [16] G. H. Lu, L. Y. Zhu, P. X. Wang, et al., “Electrostatic-force-directed assembly of Ag nanocrystals onto vertically aligned carbon nanotubes,” *Journal of Physical Chemistry C*, vol. 111, no. 48, pp. 17919–17922, 2007.
- [17] S. Mao, G. H. Lu, and J. H. Chen, “Coating carbon nanotubes with colloidal nanocrystals by combining an electrospray technique with directed assembly using an electrostatic field,” *Nanotechnology*, vol. 19, no. 45, pp. 455610–455615, 2008.
- [18] G. H. Lu, K. L. Huebner, L. E. Ocola, M. Gajdardziska-Josifovska, and J. Chen, “Gas sensors based on tin oxide nanoparticles synthesized from a mini-arc plasma source,” *Journal of Nanomaterials*, vol. 2006, Article ID 60828, 7 pages, 2006.

Research Article

Surfactant-Templated Mesoporous Metal Oxide Nanowires

Hongmei Luo, Qianglu Lin, Stacy Baber, and Mahesh Naalla

Department of Chemical Engineering, New Mexico State University, Las Cruces, NM 88003, USA

Correspondence should be addressed to Hongmei Luo, hluo@nmsu.edu

Received 29 September 2009; Accepted 6 December 2009

Academic Editor: Chao Lin

Copyright © 2010 Hongmei Luo et al. This is an open access article distributed under the Creative Commons Attribution License, which permits unrestricted use, distribution, and reproduction in any medium, provided the original work is properly cited.

We demonstrate two approaches to prepare mesoporous metal oxide nanowires by surfactant assembly and nanoconfinement via sol-gel or electrochemical deposition. For example, mesoporous Ta₂O₅ and zeolite nanowires are prepared by block copolymer Pluronic 123-templated sol-gel method, and mesoporous ZnO nanowires are prepared by electrodeposition in presence of anionic surfactant sodium dodecyl sulfate (SDS) surfactant, in porous membranes. The morphologies of porous nanowires are studied by scanning electron microscopy (SEM) and transmission electron microscopy (TEM) analyses.

1. Introduction

One-dimensional (1D) nanostructures have become the focus of intensive research owing to their potential applications as building blocks for nanoelectronic and nanophotonic devices [1, 2]. A lot of synthesis strategies have been developed to fabricate 1D nanostructures with various compositions, controlled morphologies, and complex architectures [3]. Template synthesis is one of the well-established strategies where porous anodized aluminum oxide (AAO) membranes are often used as alternative templates for making nanowire arrays [4].

Mesostructured materials with well-defined pore structures and uniform pore sizes attract much attention [5–8]. Surfactant templating strategy through cooperative self-assembly of inorganic species and surfactant is a basic synthetic powerful approach to fabricate ordered mesostructured materials. Recently, by confined self-assembly of surfactant in cylindrical pore channels of AAO membranes, hierarchically mesoporous silica nanowires or nanotubes with different morphologies have been fabricated [9–21]. These hierarchical structures can be further used as hard templates to host and guide the growth of aligned and ordered metal and semiconductor 1D nanostructures [22, 23]. Those mesoporous nanowires are particular attractive for sensor and catalyst applications because of their hierarchically organized structure, tunable pore size, and higher surface area. However, only a few studies have been carried

out to directly confine the nonsilica mesoporous materials in the cylindrical pore channels [24].

In this study, we will report that mesoporous metal oxide nanowires can be prepared by surfactant confined in porous membranes via sol-gel or electrodeposition approach. More specifically, the overall diameter of nanowires is defined by the cylindrical AAO pore channels. Surfactant nanoconfined in AAO is used to generate mesoporosity and to control the texture of nanowires. Here we use mesoporous Ta₂O₅ and zeolite by sol-gel and ZnO nanowires by electrodeposition as examples. Ta₂O₅ is a fascinating functional material that has been used in applications such as dynamic random access memory (DRAM) devices, antireflection coating layers, gas sensors, photocatalysts, and capacitors owing to its high dielectric constant, high refractive index, chemical stability, and high temperature piezoelectric properties [25–27]. Zeolite is commercially used as catalysts and separation media [28–30]. Both of mesoporous Ta₂O₅ and zeolite nanowires have not been reported so far. ZnO is a unique material that exhibits semiconducting and piezoelectric dual properties for wide applications in chemical sensors, laser diodes, solar cell, photocatalyst, and piezoelectric transduction [8, 31–33]. This is the first surfactant templated growth of mesoporous ZnO nanowires.

2. Experimental Procedures

Mesoporous Ta₂O₅ and zeolite nanowires were prepared by surfactant templated sol-gel method. The solution

for mesoporous Ta₂O₅ nanowires is similar to that used for the preparation of mesoporous Ta₂O₅ powder [34]. Typically, 1 g of block copolymer Pluronic P-123 (HO(CH₂CH₂O)₂₀(CH₂CH(CH₃)O)₇₀(CH₂CH₂O)₂₀H, designed EO₂₀PO₇₀EO₂₀) was dissolved in 5 g of ethanol, then 0.5 g of TaCl₅ was added, and the solution was stirred for 0.5 h. For mesoporous zeolite, 0.4 g P-123 was dissolved in 6 mL of H₂O with 2 mL of 0.1 M HCl, followed by 3.5 ml of pure-silica zeolite MFI nanoparticle suspension; the solution was then stirred for 1 hour. A pure-silica zeolite MFI nanoparticle suspension was synthesized by hydrothermal method from TEOS, TPAOH, ethanol, and H₂O (TEOS and TPAOH stand for tetraethylorthosilicate and tetrapropylammonium hydroxide, resp.) as starting materials. The molar composition of the synthesis solution was 1 TPAOH/3 SiO₂/25.1 EtOH/52.4 H₂O [28, 29]. It is noted that complete in situ hydrolysis of TEOS would produce 11.2 mol of EtOH. TEOS, ethanol, and H₂O were first mixed together and stirred for 0.5 hour, TPAOH was then added slowly into the solution. The clear solution thus obtained was aged in a capped plastic vessel for 3 days at room temperature followed by heating at 100°C for another 7 days with stirring. The zeolite nanoparticle suspension after cooling to room temperature was then centrifuged at 5000 rpm for 20 minutes to remove big particles, and then passed through 0.2 μm HT Tuffryn syringe filter. This solution will be used to mix with P-123 to make mesoporous zeolite nanowires.

Commercial AAO membranes with pore diameter of 20 or 100 nm and thickness of 60 μm thickness were immersed in the above P-123 assembly sol-gel solutions for overnight. Then the membranes were dry and calcined at 400°C for 5 hours to remove P-123; nanowires were then dispersed in ethanol after removing AAO membrane by 2 M NaOH and cleaning by DI H₂O.

Mesoporous ZnO nanowires were prepared by surfactant templated electrodeposition. The electrodeposition was performed in a standard three-electrode glass cell, which was immersed in a water bath held at 65°C. 100 nm thick Au-coated porous polycarbonate membrane (50 nm pore size and 6 μm thickness) or AAO (100 nm pore size and 60 μm thickness) was used as the cathode while Pt gauze as the anode and Ag/AgCl electrode as the reference electrode ($U_{eq} = 0.215$ V standard hydrogen electrode, SHE). ZnO was electrodeposited at -0.9 V versus Ag/AgCl from 0.05 M Zn(NO₃)₂. ZnO nanowires were electrodeposited from 0, 0.5, 5, and 20 wt% SDS surfactant in 0.05 M Zn(NO₃)₂ solutions. After electrodeposition, the nanowires were stripped from the membrane templates by first dissolving Au by mercury, then dissolving polycarbonate membrane with chloroform, or AAO membrane with 2 M NaOH, and followed cleaning with distilled water and ethanol by centrifugation with 4000 rpm for several times.

The X-ray diffraction (XRD) patterns were obtained on Siemens D-500 diffractometer using Cu K_α radiation. Scanning electron microscopy (SEM) images were obtained on a HITACHI S4800 field emission microscope (FESEM) at 3 kV equipped with EDX. Transmission electron microscopy (TEM) images and selected area electron diffraction (SAED)

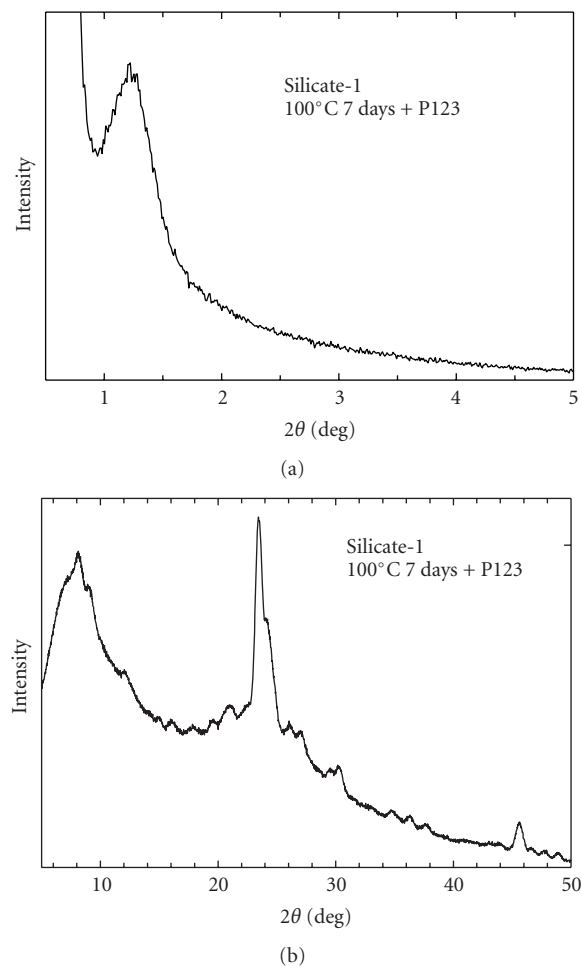


FIGURE 1: Low-angle and wide-angle XRD patterns for porous zeolite films from self-assembly of silicate-1 zeolite MFI at 100°C for 7 days with P-123.

patterns were obtained on a JEOL 2010 TEM microscope equipped with Oxford Link ISIS 6498 spectrometer for energy dispersive X-ray (EDX) analysis and operated at 200 kV to determine the nanowire morphology and structure.

3. Results and Discussion

Before soaking the porous membranes in the solutions, porous zeolite films were prepared from the same solution. Figure 1 shows the low-angle and wide-angle XRD patterns for films from spin-coating P-123 self-assembled zeolite MFI solution on silicon substrates and heating at 400°C for 2 hours. The low-angle shows typical hexagonal structure with a strong (100) diffraction peak of a d-spacing of 7.2 nm, consistent with the surfactant P123 used, indicating mesostructure preserves in the films, however, without long-range order. The wide-angle XRD pattern shows crystalline MFI zeolite formation where the degree of crystallinity can be controlled by the solution aging and heating temperature and time.

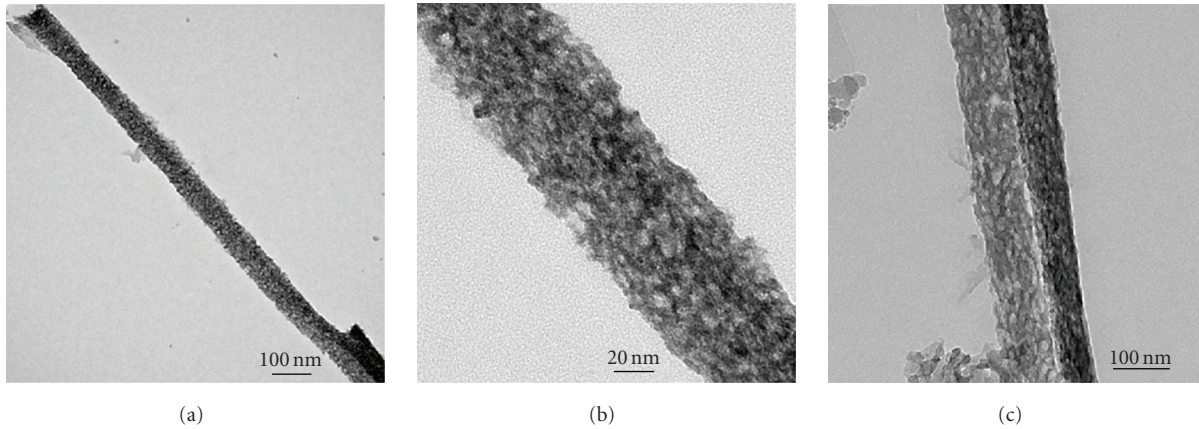


FIGURE 2: TEM images for mesoporous Ta₂O₅ nanowires (a,b) and zeolite nanowires (c).

Mesoporous Ta₂O₅ and zeolite nanowires were obtained by soaking the porous membrane in the surfactant self-assembled sol-gel solution. The isolated nanowires were obtained by removing surfactant P-123 via the calcination and removing AAO membrane through dissolution. Figure 2 shows TEM images for mesoporous Ta₂O₅ and zeolite nanowires. The porous nanowires with diameters of 80–100 nm and lengths of tens of μm were clearly visible. Ta₂O₅ nanowires are amorphous, while zeolite shows crystalline due to the longer heating time for the zeolite nanoparticle suspension. In other words, by controlling the zeolite nanoparticle suspension aging and heating conditions, the amorphous or crystalline zeolite nanowires can be formed. It is reported that amorphous mesoporous Ta₂O₅ powders were obtained from block copolymer templated sol-gel method [34]. With increasing heating temperature and time, the oxides can go from amorphous to semicrystalline to crystalline, however, the pores in oxides may collapse at higher temperature. Here we use surfactant self-assembly nanoconfined in AAO membranes to demonstrate the formation of mesoporous metal oxide nanowires. The nanowire diameter is in consistent with the pore size of the AAO membranes, and the length of nanowires is probably dependent on the soaking time of the membranes in the solution. Surfactant assembled structure nanoconfined within the pores is used to generate porosity and to control the texture of nanowires. Here the pores in the nanowires are from P-123 while the pore size should be around 8–10 nm, in consistent with the surfactant used. However, bigger pores were clearly observed may be due to the merging of the individual pores.

Before making the mesoporous ZnO nanowires, we also prepared mesoporous ZnO films. Figure 3(a) shows the low-angle XRD patterns for the mesoporous ZnO films on ITO-glass electrodeposited from 0.05 M Zn(NO₃)₂ with 0.5 and 5 wt% SDS. Without surfactant, no low-angle peaks were observed. While adding SDS in the solution, low-angle XRD pattern has two sets of evenly spaced *00l* reflections, which are unambiguously indexed as two different lamellar phases, one with $d_{001^*} = 3.18$ nm and the other with

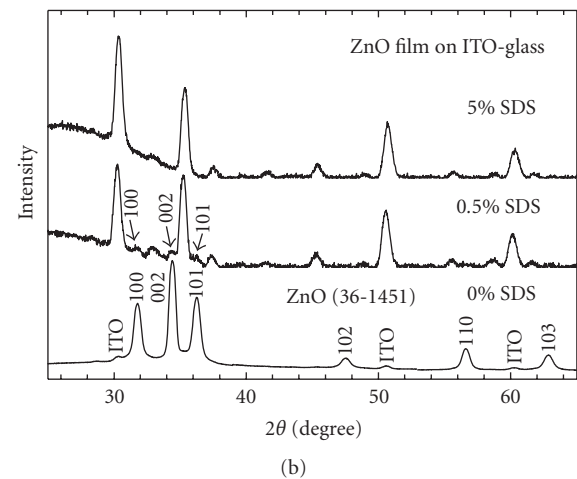
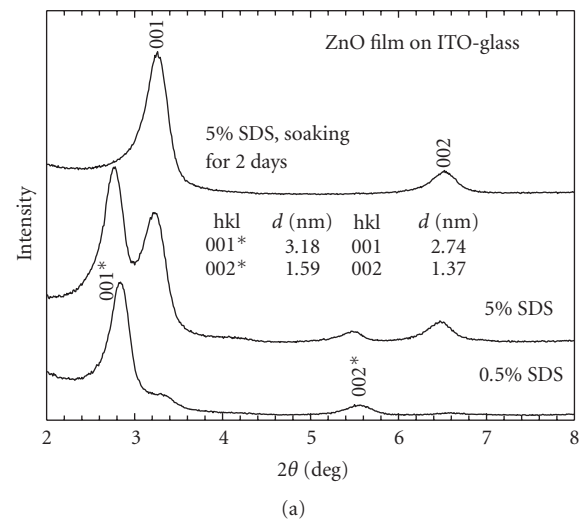


FIGURE 3: Low-angle XRD patterns for porous ZnO film on ITO-glass from 0.05 M Zn(NO₃)₂ with 0.5 and 5 wt% SDS via electrodeposition and after soaking in water and ethanol for 2 days; and (b) Wide-angle XRD patterns for ZnO films on ITO-glass from 0.05 M Zn(NO₃)₂ with 0, 0.5 and 5 wt% SDS surfactants.

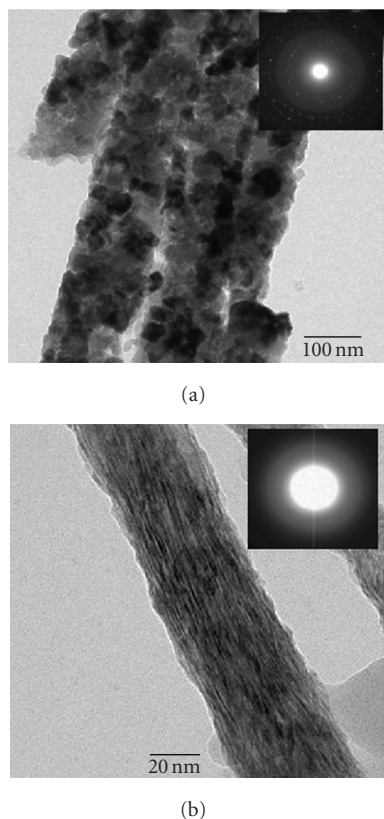


FIGURE 4: TEM images and SAED patterns for ZnO nanowires from 0.05M $\text{Zn}(\text{NO}_3)_2$ without surfactant (a) and 5 wt% SDS in $\text{Zn}(\text{NO}_3)_2$ (b).

$d_{001*} = 2.74$ nm, implying well-defined long-range order nanostructure preserved in the film. Identical d spacing values are obtained by varying the concentration of SDS from 0.5 and 5 wt% SDS in aqueous solutions, indicating that the interfacial assembly pattern of surfactant-inorganic intermediates does not depend on the bulk surfactant concentration. The formation of lamellar bi-phases suggests that two different geometrical orientations of SDS- Zn^{2+} bilayers are formed relative to the electrode surface [8]. After film soaking in water and ethanol for 1 day, the former lamellar structure peaks intensity decreases, after further soaking for 2 days, the low-angle XRD pattern only has one family lamellar mesostructure with $d_{001*} = 2.74$ nm, indicating that the former family lamellar with $d_{001*} = 3.18$ nm may not be stable and change to the latter lamellar phase with stable geometrical orientations. Figure 3(b) shows the wide-angle XRD patterns for ZnO films on ITO-glass from 0.05 M $\text{Zn}(\text{NO}_3)_2$ and mesoporous films from the solution with 0.5 and 5 wt% SDS. For the pure ZnO film without surfactant, wide-angle XRD indicates that highly crystalline wurtzite hexagonal ZnO forms (JCPDS, no. 36-1451). For mesostructured ZnO films, the film with 0.5 wt% SDS still shows weak crystalline. However, with increasing SDS amount to 5 wt%, except the substrate ITO-glass peaks, we no longer see crystalline ZnO peaks, indicating, ZnO is amorphous. This result suggests that under the influence of

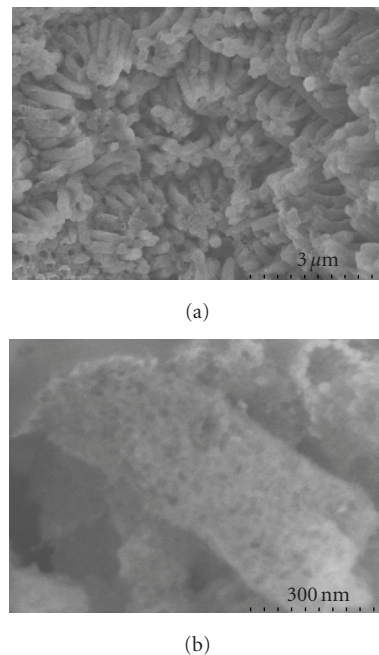


FIGURE 5: FESEM images for mesoporous ZnO nanowires from 0.05 M $\text{Zn}(\text{NO}_3)_2$ with 20 wt% SDS after dissolution of the alumina template membrane.

an electrostatic potential, surfactant-inorganic species self-assembly and electrodeposition occurs on the surface of the ITO-glass cathod, amorphous ZnO films with lamellar mesostructure can be produced.

Mesoporous ZnO nanowires were formed when self-assembly of surfactants confined within cylindrical pore channels via electrodeposition. Figure 4 shows TEM images and SAED patterns for ZnO nanowires electrodeposited from 0.05M $\text{Zn}(\text{NO}_3)_2$ with 0 and 5 wt% SDS surfactant. The images clearly see nanowires formation with diameters of 80–100 nm and lengths of up to 1 μm . It is well known that the nanowire diameter can be tuned by different pore size membrane templates, and the wire length can be easily controlled from nm to μm by electrodeposition time. However, due to semiconducting behavior of ZnO, the nanowires are not easily to grow as long as the porous membrane thickness as metals or other conducting materials. EDX analysis shows that the nanowires contain Zn and O. SDS surfactant can be removed by thoroughly washing with water and ethanol, but the nanowires may be broken by mechanical force such as ultrasonication. Without surfactants in the electrolytes, the crystalline ZnO nanowires can be electrodeposited. SAED pattern shows the crystalline ZnO formation. With further increasing SDS to 5 wt%, SAED pattern indicates that ZnO is amorphous, and the images clearly exhibit the ordered lamellar mesostructure with pore size of 2.5 nm, in consistent with SDS surfactant size [8]. The amorphous nature of the nanowires is in consistent with the amorphous films determined by XRD in Figure 3(b).

Figure 5 shows FESEM images for the mesoporous ZnO nanowires deposited from 20 wt% SDS in $\text{Zn}(\text{NO}_3)_2$ after

dissolving the membranes. Highly ordered mesoporous nanowire arrays were obtained with 200 nm in diameters and 1–2 μm in lengths and one can clearly see the porosity and mesostructure from the nanowires (Figure 5(b)).

Confinement on the lamellar liquid crystal assembly from block copolymers or silica-surfactant nanocomposite in the nanoscale pores has been extensively studied both theoretically and experimentally [9–11]. These lamellar mesostructure with the layers are parallel to the substrates; nanoconfinement in nanoscale pores results in the coaxially concentric multilayered cylindrical mesophase by curling the layered structures to diminish the interfacial curvatures [9–11]. However, different from the above lamellar mesophase, upon the addition of the anionic surfactant SDS into an inorganic electrolyte solutions $\text{Zn}(\text{NO}_3)_2$, the electrostatic interaction results in the formation of an interface ($\text{S}^- \text{I}^+$), comprised of metal cations and anionic headgroups of surfactants. The metal cations adsorb on the electrode surface, when applying a potential between a working and counter electrodes, the interface will stack layer by layer and the surfactants pack parallel to each other, perpendicular to the substrate. Two-dimensional grazing-incidence small-angle X-ray scattering (SAXS) technique proves the mesoporous ZnO films with the layers stacked not parallel to the substrate, different from the sol-gel self-assembly method [8]. Thus mesostructured nanowires (not nanotubes) are electrodeposited when the surface self-assembly is confined in the nanoscale pores.

4. Conclusions

In conclusion, by combination of surfactant self-assembly, nanoconfinement and sol-gel or electrodeposition, mesoporous Ta_2O_5 , zeolites and ZnO nanowires are produced. These novel approaches could be extended to prepare some other metal oxide porous nanowires. The controlled pore size and morphology nanostructured nanowires may have applications in optical and electric nanodevices.

Acknowledgments

The authors gratefully acknowledge the supports from the New Mexico Consortium, Los Alamos Institute for Advanced Studies (IAS), and Center for Integrated Nanotechnologies (CINT) at Los Alamos National Laboratory.

References

- [1] C. M. Lieber, "Nanoscale science and technology: building a big future from small things," *MRS Bulletin*, vol. 28, no. 7, pp. 486–491, 2003.
- [2] S. Jin, D. Whang, M. C. McAlpine, R. S. Friedman, Y. Wu, and C. M. Lieber, "Scalable interconnection and integration of nanowire devices without registration," *Nano Letters*, vol. 4, no. 5, pp. 915–919, 2004.
- [3] Y. N. Xia, P. D. Yang, Y. G. Sun, et al., "One-dimensional nanostructures: synthesis, characterization, and applications," *Advanced Materials*, vol. 15, no. 5, pp. 353–389, 2003.
- [4] C. R. Martin, "Nanomaterials: a membrane-based synthetic approach," *Science*, vol. 266, no. 5193, pp. 1961–1966, 1994.
- [5] Y. Lu, "Surfactant-templated mesoporous materials: from inorganic to hybrid to organic," *Angewandte Chemie International Edition*, vol. 45, no. 46, pp. 7664–7667, 2006.
- [6] C. J. Brinker and D. R. Dunphy, "Morphological control of surfactant-templated metal oxide films," *Current Opinion in Colloid & Interface Science*, vol. 11, no. 2–3, pp. 126–132, 2006.
- [7] Y. Lu, R. Ganguli, C. A. Drewien, et al., "Continuous formation of supported cubic and hexagonal mesoporous films by sol-gel dip-coating," *Nature*, vol. 389, no. 6649, pp. 364–368, 1997.
- [8] K.-S. Choi, H. C. Lichtenegger, G. D. Stucky, and E. W. McFarland, "Electrochemical synthesis of nanostructured ZnO films utilizing self-assembly of surfactant molecules at solid-liquid interfaces," *Journal of the American Chemical Society*, vol. 124, no. 42, pp. 12402–12403, 2002.
- [9] Z. Yang, Z. Niu, X. Cao, et al., "Template synthesis of uniform 1D mesostructured silica materials and their arrays in anodic alumina membranes," *Angewandte Chemie International Edition*, vol. 42, no. 35, pp. 4201–4203, 2003.
- [10] A. Yamaguchi, F. Uejo, T. Yoda, et al., "Self-assembly of a silica-surfactant nanocomposite in a porous alumina membrane," *Nature Materials*, vol. 3, no. 5, pp. 337–341, 2004.
- [11] Y. Wu, G. Cheng, K. Katsov, et al., "Composite mesostructures by nano-confinement," *Nature Materials*, vol. 3, no. 11, pp. 816–822, 2004.
- [12] J. Wang, C.-K. Tsung, W. Hong, Y. Wu, J. Tang, and G. D. Stucky, "Synthesis of mesoporous silica nanofibers with controlled pore architectures," *Chemistry of Materials*, vol. 16, no. 24, pp. 5169–5181, 2004.
- [13] J. F. Wang, C.-K. Tsung, R. C. Hayward, Y. Wu, and G. D. Stucky, "Single-crystal mesoporous silica ribbons," *Angewandte Chemie International Edition*, vol. 44, no. 2, pp. 332–336, 2004.
- [14] Q. Y. Lu, F. Gao, S. Komarneni, and T. E. Mallouk, "Ordered SBA-15 nanorod arrays inside a porous alumina membrane," *Journal of the American Chemical Society*, vol. 126, no. 28, pp. 8650–8651, 2004.
- [15] Z. Liang and A. S. Susha, "Mesostructured silica tubes and rods by templating porous membranes," *Chemistry: A European Journal*, vol. 10, no. 19, pp. 4910–4914, 2004.
- [16] B. D. Yao, D. Fleming, M. A. Morris, and S. E. Lawrence, "Structural control of mesoporous silica nanowire arrays in porous alumina membranes," *Chemistry of Materials*, vol. 16, no. 24, pp. 4851–4855, 2004.
- [17] K. W. Jin, B. Yao, and N. Wang, "Structural characterization of mesoporous silica nanowire arrays grown in porous alumina templates," *Chemical Physics Letters*, vol. 409, no. 4–6, pp. 172–176, 2005.
- [18] D. Wang, R. Kou, Z. Yang, J. He, Z. Yang, and Y. Lu, "Hierarchical mesoporous silica wires by confined assembly," *Chemical Communications*, no. 2, pp. 166–167, 2005.
- [19] A. Y. Ku, S. T. Taylor, and S. M. Loureiro, "Mesoporous silica composites containing multiple regions with distinct pore size and complex pore organization," *Journal of the American Chemical Society*, vol. 127, no. 19, pp. 6934–6935, 2005.
- [20] W. P. Zhu, Y. C. Han, and L. J. An, "Synthesis of ordered mesostructured silica nanotubular arrays," *Microporous and Mesoporous Materials*, vol. 84, no. 1–3, pp. 69–74, 2005.
- [21] B. Platschek, N. Petkov, and T. Bein, "Tuning the structure and orientation of hexagonally ordered mesoporous channels

- in anodic alumina membrane hosts: a 2D small-angle X-ray scattering study,” *Angewandte Chemie International Edition*, vol. 45, no. 7, pp. 1134–1138, 2006.
- [22] Y. Wu, T. Livneh, Y. X. Zhang, et al., “Templated synthesis of highly ordered mesostructured nanowires and nanowire arrays,” *Nano Letters*, vol. 4, no. 12, pp. 2337–2342, 2004.
- [23] N. Petkov, B. Platschek, M. A. Morris, J. D. Holmes, and T. Bein, “Oriented growth of metal and semiconductor nanostructures within aligned mesoporous channels,” *Chemistry of Materials*, vol. 19, no. 6, pp. 1376–1381, 2007.
- [24] W. H. Lai, J. Shieh, L. G. Teoh, and M. H. Hon, “Fabrication of one-dimensional mesoporous tungsten oxide,” *Nanotechnology*, vol. 17, no. 1, pp. 110–115, 2006.
- [25] S. Ezhilvalavan and T. Y. Tseng, “Preparation and properties of tantalum pentoxide (Ta_2O_5) thin films for ultra large scale integrated circuits (ULSIs) application: a review,” *Journal of Materials Science: Materials in Electronics*, vol. 10, no. 1, pp. 9–31, 1999.
- [26] Y. Zhu, F. Yu, Y. Man, Q. Tian, Y. He, and N. Wu, “Preparation and performances of nanosized Ta_2O_5 powder photocatalyst,” *Journal of Solid State Chemistry*, vol. 178, no. 1, pp. 224–229, 2005.
- [27] Y.-L. Chueh, L.-J. Chou, and Z. L. Wang, “ $\text{SiO}_2/\text{Ta}_2\text{O}_5$ core-shell nanowires and nanotubes,” *Angewandte Chemie International Edition*, vol. 45, no. 46, pp. 7773–7778, 2006.
- [28] Z. B. Wang, H. T. Wang, A. Mitra, L. M. Huang, and Y. S. Yan, “Pure-silica zeolite low-k dielectric thin films,” *Advanced Materials*, vol. 13, no. 10, pp. 746–749, 2001.
- [29] S. Li, Z. Li, D. Medina, C. Lew, and Y. Yan, “Organic-functionalized pure-silica-zeolite MFI low-k films,” *Chemistry of Materials*, vol. 17, no. 7, pp. 1851–1854, 2005.
- [30] S. Ivanova, B. Louis, M.-J. Ledoux, and C. Pham-Huu, “Autoassembly of nanofibrous zeolite crystals via silicon carbide substrate self-transformation,” *Journal of the American Chemical Society*, vol. 129, no. 11, pp. 3383–3391, 2007.
- [31] P. X. Gao, Y. Ding, W. Mai, W. L. Hughes, C. S. Lao, and Z. L. Wang, “Materials science: conversion of zinc oxide nanobelts into superlattice-structured nanohelices,” *Science*, vol. 309, no. 5741, pp. 1700–1704, 2005.
- [32] Z. L. Wang and J. Song, “Piezoelectric nanogenerators based on zinc oxide nanowire arrays,” *Science*, vol. 312, no. 5771, pp. 242–246, 2006.
- [33] X. Wang, C. J. Summers, and Z. L. Wang, “Mesoporous single-crystal ZnO nanowires epitaxially sheathed with Zn_2SiO_4 ,” *Advanced Materials*, vol. 16, no. 14, pp. 1215–1218, 2004.
- [34] P. D. Yang, D. Y. Zhao, D. I. Margolese, B. F. Chmelka, and G. D. Stucky, “Block copolymer templating syntheses of mesoporous metal oxides with large ordering lengths and semicrystalline framework,” *Chemistry of Materials*, vol. 11, no. 10, pp. 2813–2826, 1999.

Research Article

Suppression of Proinflammatory Cytokines in Functionalized Fullerene-Exposed Dermal Keratinocytes

Jun Gao,¹ Hsing-Lin Wang,² and Rashi Iyer¹

¹Biosciences Division, Los Alamos National Laboratory, M888, TA 43, HRL-2, Los Alamos, NM 87545, USA

²Chemistry Division, Los Alamos National Laboratory, J567, TA 46, Los Alamos, NM 87545, USA

Correspondence should be addressed to Rashi Iyer, rashi@lanl.gov

Received 1 October 2009; Accepted 24 November 2009

Academic Editor: Huisheng Peng

Copyright © 2010 Jun Gao et al. This is an open access article distributed under the Creative Commons Attribution License, which permits unrestricted use, distribution, and reproduction in any medium, provided the original work is properly cited.

Initial experiments using differentially functionalized fullerenes, CD-C₆₀, hexa-C₆₀, and tris-C₆₀, suggested a properties dependent effect on cytotoxic and proliferative responses in human skin keratinocytes. In the present study we investigated the cytokine secretion profile of dermal epithelial cells exposed to functionalized fullerenes. Keratinocyte-derived cytokines affect homing and trafficking of normal and malignant epidermal immune as well as nonimmune cells in vivo. These cytokines are critical for regulating activation, proliferation, and differentiation of epidermal cells. Our results indicate that tris-C₆₀ (size range <100 nm) significantly reduces inflammatory cytokine release in a dose- and time-dependent manner. In contrast CD-C₆₀ demonstrated a relatively pro-inflammatory cytokine response, while hexa-C₆₀ did not significantly perturb cytokine responses. Physical and chemical characterizations of these engineered nanomaterials suggest that the disparate biological responses observed may potentially be a function of the aggregation properties of these fullerenes.

1. Introduction

Engineered nanomaterials have been widely used for diagnostic therapy and drug delivery based on their unique properties, such as size and charge [1, 2]. C₆₀-derived fullerenes are carbon allotropes whose physical and chemical properties are easily manipulatable making them attractive targets for clinical and industrial applications [3, 4]. However, unmodified fullerenes tend to form large aggregates due to their high aspect ratio and the strong van der Waals attraction between them, resulting in limited solubility in aqueous media thus restricting their applications. Consequently, drug development platforms as well as other commercial uses (e.g., for composites) have focused on derivatizing native C₆₀ fullerene molecules rendering it soluble. This not only broadens the scope of applications but also makes fullerenes more available to and interactive with biological systems, raising concerns about the potential toxicity of these materials. Also, the claimed mass production of fullerenes by Frontier Carbon Corporation makes it a possible workplace hazard.

In the current study we used three hydrophilic fullerenes derivatives, hexa-dicarboxyl fullerene, tris-dicarboxyl fullerene, and gamma (γ)-cyclodextrin caged C₆₀. Encapsulation of C₆₀ by γ -cyclodextrin enhances the solubility of C₆₀ without impacting the physicochemical properties of native C₆₀, thus serving as an appropriate control [5]. While chemical functionalization of C₆₀ by the addition of carboxyl groups on the surface renders normally insoluble fullerenes soluble in aqueous media it also alters the electronic and physical properties of fullerenes. The physicochemical properties of the fullerene influence its interactions with cells and biological molecules. Studies have shown that nanomaterials can penetrate through skin and induce localized or even systemic biological responses [6]. In the present study human epidermal keratinocyte (HEK) cells were utilized to simulate the primary route of occupational dermal exposure and potential topical applications of fullerene derivatives. Skin epidermis is a first line of defense against pathogens and other environmental insults. Keratinocytes are the major cell type in human epidermis and are the primary responders to exogenous

insults generating a variety of different cytokines greatly influencing the inflammatory dermal response [7–9]. In a previous study (manuscript submitted), we performed a suite of cellular endpoint analysis to determine the response of epidermal keratinocyte (HEK) to these distinctly derivatized fullerenes. A comparative analysis of the cellular responses elicited by these functionalized fullerenes indicated that tris- C_{60} induced a differential response in HEK cells relative to either CD- C_{60} or hexa C_{60} fullerenes. Furthermore, the results presented herein suggest that engineered fullerene derivatives can dramatically alter the apoptotic and proliferative responses of HEK cells. Since cytokines influence viability, proliferation and differentiation of keratinocytes *in vivo* and are pivotal in the recruitment of immune cells [10] and the ensuing inflammatory response, we further evaluate the cytokine response of human epidermal keratinocyte (HEK) cells to modified fullerenes.

2. Materials and Methods

2.1. Chemicals and Reagents. All reagents used in the study were special grade commercial products purchased from Invitrogen (Carlsbad, CA) and Sigma-Aldrich (Saint Louis, MO), unless otherwise stated. The cytokine kits were purchased from BD Biosciences (San Diego, CA) and Antigenix America (Huntington Sta., NY). The cytokine array kit was obtained from RayBiotech (Norcross, GA).

2.2. Preparation of Fullerene and Its Derivatives. The water-soluble carboxyfullerenes C_{60} substituted with a total of 12 (hexa- C_{60}) or 6 (tris- C_{60}) carboxyl groups (see Supplement 1 available at doi: 10.1155/2010/41640) and γ -cyclodextrin- C_{60} fullerene molecule (referred to as CD- C_{60}) were synthesized for this study as described in [11].

Preparation of fullerene derivative working solutions: tris or hexa- C_{60} fullerene was added to sterilized distilled water and pH adjusted to 7.0 to create a stock solution of 2 mg/mL. The stock solutions were stored at 4°C until use. Before the experiment, the stock solutions were vortexed for 3 minutes, then sonicated for 10 minutes to break up aggregates and form a uniform suspension. From this stock, serial dilutions of 25, 50, and 100 $\mu\text{g/mL}$ in cell growth media were prepared and used to treat the cells.

2.3. Cell Culture. Human epidermal keratinocyte (HEK) cells (ATCC CRL-2404) were grown in defined keratinocyte serum free medium (SFM) (Cat No. 10785, Invitrogen, Carlsbad, CA) supplemented with 1 mL Defined Keratinocyte-SFM growth supplement (Cat No. 10784, Invitrogen) in a 37°C incubator with a humidified atmosphere and 5% CO_2 . HEK cells were either cultured in flat-bottom 96-well (1.5×10^4 cells/well) or 6-well (2.0×10^5 cells/well) cell culture plates depending on the end-point to be assayed. Cells were treated with caged- C_{60} or carboxyfullerenes at concentrations of 25 $\mu\text{g/mL}$, 50 $\mu\text{g/mL}$, and 100 $\mu\text{g/mL}$ in warm media for various time points. A control sample of untreated cells was cultured, washed, and incubated for

the same time points for each experiment. The cells were incubated at 37°C with a humidified atmosphere and 5% CO_2 during exposure.

2.4. Apoptosis Assay. Apoptotic cell death was analyzed by photometric enzyme-immunoassay kit (Cat. No. 11774425001, Roche Applied Science, Mannheim, Germany). Briefly, HEK cells were plated at a population of approximately 1.0×10^5 cells/well in 6-well cell culture plates. The cells were exposed to caged- C_{60} and carboxyfullerenes for 24 hours. Camptothecin (CAM, 1 μM) (Cat. No. 1039-1, BioVision) was used as a positive control for apoptosis induction. After treatment the cell culture plates were centrifuged for 10 minutes at $200 \times g$. At the end of each time point the cells were analyzed for apoptosis. The sample absorbance was measured with an ELISA plate reader Synergy 2 multimode microplate reader (BioTek Instruments, Inc., Winooski, VT) at 405 nm and 490 nm. To confirm the ELISA results, treated cells were dual labeled with acridine orange/ethidium bromide (AO/EB) dyes to visualize apoptotic cells. Equal volumes of 100 $\mu\text{g/mL}$ AO and EB in DPBS were mixed to stain the treated cells. Stained cells were immediately analyzed using a fluorescence microscope with 20 \times objective (Zeiss Axiophot, Carl Zeiss, Germany) and image-Pro Plus software (Ver. 6.2, Media Cybernetics, Silver Spring, MD). Apoptotic cells were delineated with orange nuclei, and live cells appear uniformly green.

2.5. Cell Proliferation Assay. The cell proliferation reagent WST-1 (a tetrazolium salt cleaved in viable cells) (Cat. No. MK400, TaKaRa BIO Inc., Madison, WI) was used to quantify cell proliferative activity. Briefly, HEK cells were seeded at 5×10^4 cells per well in 96-well plates and allowed to reattach for 24 hours prior to exposure to fullerenes. After 24 hours, cells were washed twice. 10 μL WST-1 and 100 μL fresh warm media were added to each well and incubated for an additional 2 hours. Cell proliferation was assessed by measuring the absorbance at 450 nm and 600 nm using a microplate reader.

2.6. Cytokine Antibody Array. The levels of cytokines released into cell culture media by functionalized fullerenes were measured using RayBio Human Cytokine Antibody Array III (Cat. No. AAH-CYT-3, RayBiotech). This antibody array matrix can simultaneously detect 44 cytokines, chemokines and growth factors (Figure 3). The samples were analyzed according to the manufacturer's instructions. Briefly, cell culture medium from control and fullerene (50 $\mu\text{g/mL}$) treated groups was collected after 4, 8, 12, and 24 hours. The antibody array membranes were blocked using 2 mL of 1 \times blocking buffer at room temperature for 30 minutes in an 8-well tray. Subsequently, 1 mL of cell culture medium was added to each well, and then incubated at room temperature for 2 hours. After incubation, the membrane was washed three times with washing buffer I for 5 minutes each, and then washed twice using washing buffer II for 5 minutes each. The membranes were incubated with biotin-conjugated

anticytokine antibodies for 2 hours, followed by HRP-labeled streptavidin incubation for 2 hours at room temperature. Cytokines were detected with supersignal west dura extended duration substrate (Cat. No. 34–75, Thermo Scientific Pierce, Rockford, IL) and visualized with ChemiDoc imaging system (BioRad, Hercules, CA). The intensity level of each spot was determined using Quality One Software (BioRad). The positive controls on membrane were used to normalize the signal intensity of individual cytokines.

2.7. Individual Cytokine Detection. HEK cells were seeded in 6-well plates at a concentration of 2×10^4 cells/well and treated with various concentrations of fullerene derivatives for 2, 4, 8, 12, 24, and 48 hours. At the end of each time point, cell supernatants were harvested for cytokine release analysis. The concentration of human IL-1 β , IL-6, IL-8, tumor necrosis factor β (TNF- β), MCP-1 (Cat. No. 557953, 555220, 555244, 550995, and 555179, BD biosciences), GRO- β , GRO- γ , and RANTES (Cat. No. RHF810CK, RHF820CK and RHF520CKC, Antigenix America) levels in the media were assessed by cytokine Enzyme-Linked Immunosorbent Assay (ELISA) kits according to the manufacturer's instructions. Briefly, the 96-well plates (Nunc) were coated overnight at 4°C with capture antibody diluted in coating buffer (BD OptEIA reagent set B, Cat. No. 550534). Plates were washed with freshly made wash buffer (PBS with 0.05% Tween-20), and blocked with 200 μ L assay dilute for 1 hour. Subsequently wells were washed 3 times standard cytokines and test samples were added to each well in triplicate (100 μ L/well) and incubated for 2 hours at room temperature. Bound cytokines were detected after 1 hour with working detector (100 μ L, detection antibody + horseradish peroxidase conjugated streptavidin). Finally, color was developed using substrate solution and stopping reagents. Absorbance was measured at 450 nm, and the background noise was read at 570 nm. Cytokine concentrations were determined using the standard curve in the same plate.

2.8. Statistical Analysis. Data were analyzed by Sigma Stat software (Jandel Science, San Rafael, CA). The statistical differences among groups were determined by one-way analysis of variance (ANOVA) and/or Student's *t*-test. A Dunnett correction was used for multiple comparisons. The values were expressed as mean \pm SEM. A *P*-value < .05 was considered a statistically significant difference.

3. Results and Discussion

3.1. Physicochemical Properties of Fullerenes. The physicochemical characteristics of engineered nanomaterials greatly impact their properties eventually influencing their ability to interact with biological systems. As we have shown in the current study CD-C₆₀, hexa-C₆₀ and tris-C₆₀ can induce diametrically opposite cellular and molecular responses. Using electrochemical characterization, UV-Vis spectra, dynamic light scattering, and atomic force microscopy, we obtained the following information about the physical and chemical properties of these fullerenes: (1) reduction potential of

CD-C₆₀, hexa-C₆₀, and tris-C₆₀ versus Ag/AgCl is -0.98 , -1.25 , and -1.12 V, respectively, (2) both the hexa-C₆₀ and CD-C₆₀ were highly polydisperse with a range of particles from 20 nm to micron sized, and (3) tris-C₆₀ is relatively monodisperse with particle size from 100 to 160 nm. The chemical modifications of fullerenes appeared to impact the redox properties and aggregation properties of the fullerenes.

3.2. Functionalized Fullerene-Induced Apoptosis. The previous studies in our laboratory have shown that fullerenes can regulate apoptosis in macrophage-like THP1 cells [11]. We therefore examined the ability of these fullerenes to induce cellular apoptosis in HEK cells. Programmed cell death was quantified after treatment with CD-C₆₀, hexa-C₆₀ and tris-C₆₀ (25, 50, and 100 μ g/mL) for 6 and 24 hours. Cells were treated with camptothecin (CAM) as a positive control. Using an ELISA assay, the amount of cytoplasmic nucleosomes, an indicator of apoptosis, was measured in each sample. Though all three fullerenes appeared to inhibit basal apoptotic cell death, tris-C₆₀ caused over a 50% decrease in the number of apoptotic cells at all concentration tested (Figure 1(a)). Moreover, unlike CD-C₆₀, and hexa-C₆₀, tris-C₆₀ protected the cells from camptothecin-induced apoptotic cell death in a dose dependent manner, and completely inhibiting apoptosis at 100 μ g/mL (Figure 1(b)). These results were confirmed morphologically using AO/EB fluorescent staining (data not shown). Apoptosis plays a critical role in the development and maintenance of homeostasis and in the maturation of organ systems [12]. Perturbation of this naturally occurring physiological process has been observed in several disease states. Dysregulation or failure of normal apoptosis contributes to the transformation of cells and provides a growth advantage to cancer cells [13]. The observed antiapoptotic function of CD-C₆₀ and hexa-C₆₀, and the ability of tris-C₆₀ to inhibit apoptosis by extraneous agents raise concerns about their safety. Conversely, tris-C₆₀ could potentially be used to prevent premature neuronal degeneration caused by apoptotic cell death as has been previously suggested in [14].

3.3. Effect of Functionalized Fullerene on HEK Cell Proliferation. Further we examined the proliferative response of cells on exposure to fullerenes. Cellular proliferation in HEK cells was quantified using a nonradioactive WST-1 assay. This tetrazolium salt is cleaved to a soluble formazan dye by the succinate-tetrazolium reductase which is active only in viable cells. The quantity of formazan dye is related directly to the number of metabolically active cells. While no significant changes were observed in the proliferation capacity of cells treated with CD-C₆₀ and hexa-C₆₀, there was a significant decrease in the percentage of proliferating cells in the tris-C₆₀ treated cells (Figure 2). These results indicate that not only can tris-C₆₀ perturb apoptotic mechanisms but it may also inhibit cell cycle progression, preventing cell division. Since cellular senescence is defined by the inability of cells to proliferate and occasionally to be resistant to apoptosis one can speculate that tris-C₆₀ may potentially induce senescence in HEK cells. Studies are ongoing to examine this response.

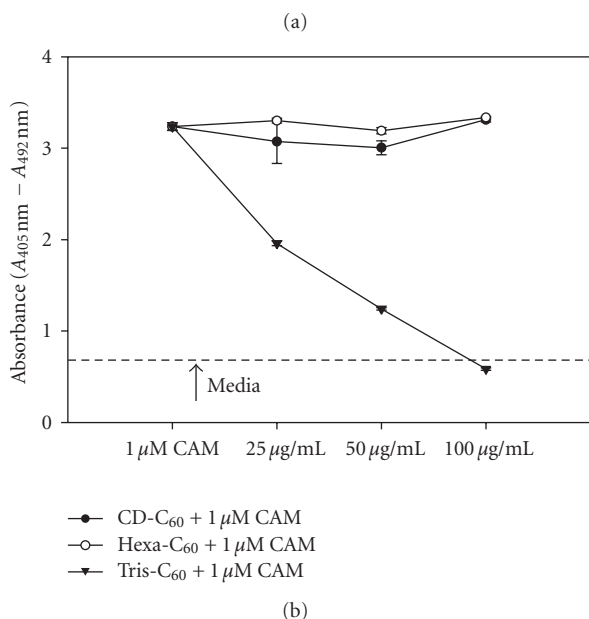
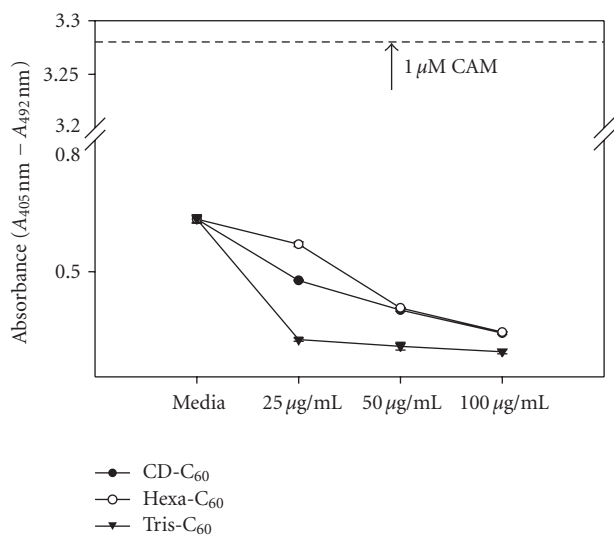


FIGURE 1: Evaluation of apoptotic response in HEK cells. (a) Cells were treated with fullerene and its derivatives for 24 hours. Apoptotic cell death was quantified by photometric enzyme-immunoassay. Media and 1 μM camptothecin (dash line) were used as negative and positive controls, respectively. (b) Cells were pretreated with fullerene and its derivatives for 2 hours, then cotreated with 1 μM camptothecin for 24 hours. Relative change in apoptosis was compared to untreated cells (Media, dash line), and camptothecin (CAM). Values are presented as means \pm SEM of triplicate cultures from two individual samples in each treatment group.

3.4. Fullerene-Mediated Cytokine Response. Insult mediated release of immunoregulatory molecules or cytokines primarily produced by keratinocytes are capable of initiating an immune response in the epidermis [15]. IL-1, which is constitutively produced and stored by keratinocytes, is released on damage to these cells and in turn stimulates the production of other cytokines such as, IL-6, IL-8, GM-CSF,

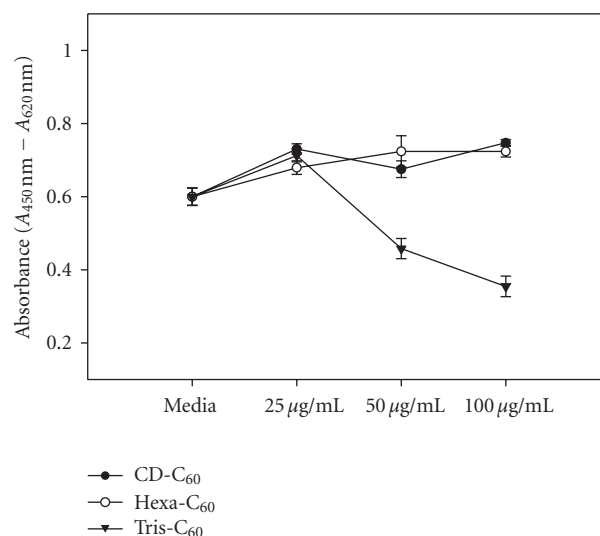


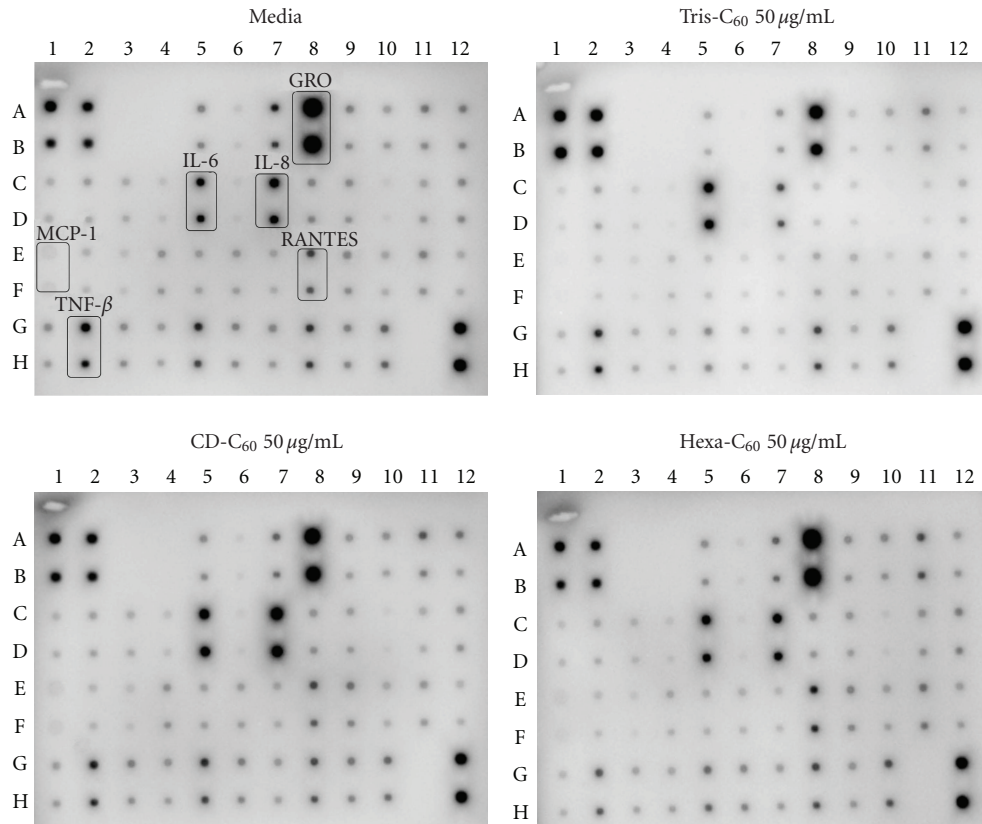
FIGURE 2: Detection of HEK cell proliferation. Proliferation was determined using the WST-1 proliferation assay. HEK cells were treated with fullerene derivatives for 24 hours; cells cultured with medium were used as control. Data are means \pm SEM. of quadruplicate cultures in each treatment group. Independent experiments were performed in triplicate.

and TNF- α amongst others [16]. Therefore, keratinocytes play a major role in the skin immune response. Moreover, physiological responses including apoptosis and proliferation are mediated by these very cytokines and play a deterministic role in the evolution and the integrity of the epidermal layer. We examined the secretion profile of cytokines in HEK cells exposed to the three different fullerenes using a cytokine antibody array to measure 44 different cytokines (Figure 3). HEK cells were treated with 50 $\mu\text{g/mL}$ fullerenes for 4, 8, 12 and 24 hours. Interestingly, tris-C₆₀ significantly suppressed the major proinflammatory cytokines IL-6 and IL-8 and reduced TNF- β , RANTES, and GRO release as well. However, a notable increase in IL-1 β levels was observed in a time-dependent manner. In contrast, CD-C₆₀ caused a significant increase in IL-6 and IL-8 release, but reduced TNF- β levels. Unexpectedly, the cytokine profiles for hexa-C₆₀ treated groups were similar to medium control.

3.5. Fullerene Derivatives Alter IL-1 β , IL-6, and IL-8 Release in HEK Cells. To determine the kinetics of the observed cytokine response and to confirm the array results we utilized single cytokine ELISA kits to assess extracellular cytokine levels from 2 to 48 hours. The cytokine array results indicate that functionalized fullerenes induce IL-1 β release, but not IL-1 α . We quantified IL-1 β levels after cells were treated with fullerenes for 24 hours. A dose dependent induction of IL-1 β release was observed in tris-C₆₀ treated cells. No significant difference was noted in the CD-C₆₀ and hexa-C₆₀ treated cells compared to medium control (Figure 4). It has been well demonstrated that normal human epidermal cells can produce interleukin-1 (IL-1) and TNF [17, 18]. Both these

	1	2	3	4	5	6	7	8	9	10	11	12
A	Pos	Pos	Neg	Neg	ENA-78	GCSF	GM-CSF	GRO	GRO- α	1-309	IL-1 α	IL-1 β
B	Pos	Pos	Neg	Neg	ENA-78	GCSF	GM-CSF	GRO	GRO- α	1-309	IL-1 α	IL-1 β
C	IL-2	IL-3	IL-4	IL-5	IL-6	IL-7	IL-8	IL-10	IL-12	IL-13	IL-15	IFN- γ
D	IL-2	IL-3	IL-4	IL-5	IL-6	IL-7	IL-8	IL-10	IL-12	IL-13	IL-15	IFN- γ
E	MCP-1	MPC-2	MCP-3	MCSF	MDC	MIG	MIP-1 δ	RANTES	SCF	SDF-1	TARC	TGF- β 1
F	MCP-1	MPC-2	MCP-3	MCSF	MDC	MIG	MIP-1 δ	RANTES	SCF	SDF-1	TARC	TGF- β 1
G	TNF- α	TNF- β	EGF	IGF-1	Angiagenin	Onco. M	Throm.	VEGF	PDGF BB	Leptin	Neg	Pos
H	TNF- α	TNF- β	EGF	IGF-1	Angiagenin	Onco. M	Throm.	VEGF	PDGF BB	Leptin	Neg	Pos

(a)



(b)

FIGURE 3: Cytokine array analysis in HEK cells treated with functionalized fullerene. (a) Antibody spotting map on the antibody array membrane. Each cytokine is represented by duplicate spots. Pos: positive control; Neg: negative control. (b) Detection of cytokines on membrane antibody array by chemiluminescence. HEK cells were treated with 50 $\mu\text{g}/\text{mL}$ fullerenes for 4, 8, 12, and 24 hours. Images represent cytokine array from 24 hours fullerene treated HEK cell culture media.

cytokines act synergistically to orchestrate inflammatory responses and can also induce endothelial adhesion molecule (ICAM) expression critical for the adhesion of immune cells to the endothelial surface [14, 19]. In addition, these keratinocyte-derived cytokines may enhance accumulation of diverse cytotoxic effector cells for the destruction of keratinocytes. Release of IL-1 by damaged keratinocytes induces the production of proinflammatory cytokines, IL-6 and IL-8. IL-6 is produced by keratinocytes in response to skin injuries and can play a dominant role in dermal inflammatory diseases [20]. IL-8 is a major neutrophil chemoattractant and an important mediator of cutaneous inflammatory events,

involved in lymphocyte migration and infiltration in human skin [21]. Conflictingly, in our array results, we observed a decrease in both IL-6 and IL-8 in tris-C₆₀ exposed cells. These results were further confirmed by cytokine-specific ELISAs, wherein, we saw a sharp decrease in the IL-6 levels as early as 2 hours, continuing to decrease to 48 hours in tris-C₆₀ treated cells. In contrast, IL-6 release was significantly increased in a dose dependent manner after 8 hours of CD-C₆₀ treatment in HEK cells. No significant differences occurred between hexa-C₆₀ treated and untreated media control group (Figure 5(a)). Similar IL-8 responses were noted (Figure 5(b)), where CD-C₆₀ upregulates IL-8 release

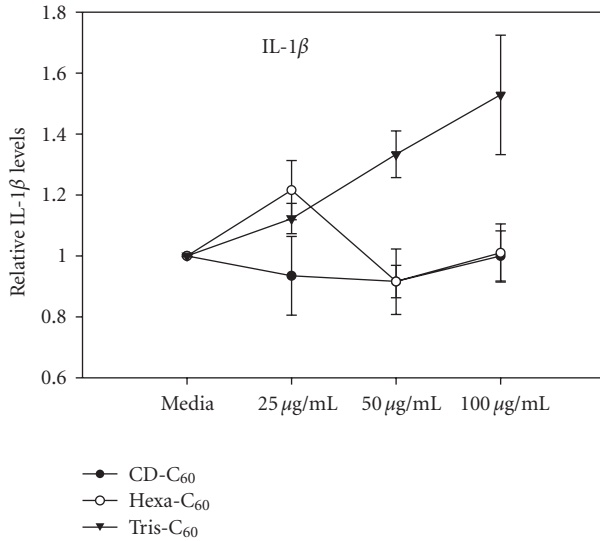
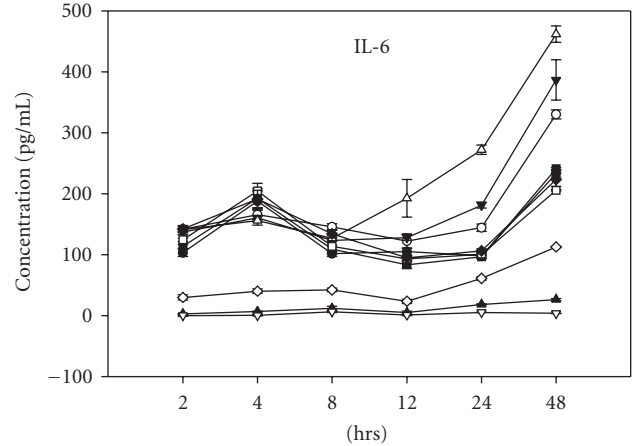


FIGURE 4: Effect of fullerene derivatives on IL-1 β release in HEK cells. HEK cells were treated with the different doses of fullerene derivatives for 24 hours. Cytokine ELISA detection kits were used to evaluate IL-1 β cytokines. The concentration of released cytokines was calculated by cytokine standard curve in the same measuring plate. Data are means \pm SEM. of quadruplicate cultures in each treatment group.

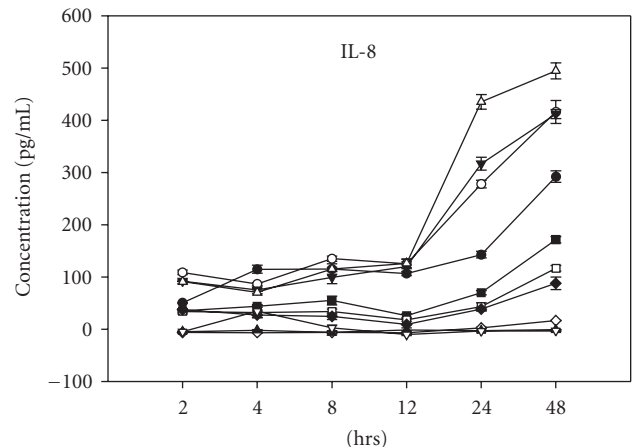
and tris-C₆₀ suppresses IL-8 release. Interestingly, release of IL-8 was significantly decreased in a dose-dependent manner after 2 hours of hexa-C₆₀ treatment. CD-C₆₀ induction of proinflammatory cytokines IL-6 and IL-8 suggests that CD-C₆₀ may potentially induce an inflammatory response in HEK cells [10, 22].

Interestingly, studies with mouse embryonic fibroblasts undergoing senescence demonstrated an increase in the expression and secretion of IL-1 β and the involvement of the IL-1 β signaling pathway in activation of p38 linked cellular senescence [23] implicating a role for IL-1 β in this phenomena. As discussed earlier, senescent cells are often characterized by their resistance to apoptosis and their inability to proliferate. Both of these responses were observed in tris-C₆₀ treated cells, accompanied with a simultaneous enhancement in IL-1 β levels. These responses were noted in a background of attenuated levels of proinflammatory cytokines IL-6 and IL-8, suggesting that tris-C₆₀ may be inducing senescence in these cells.

3.6. Fullerene Derivatives Alter TNF- β , GRO β , and RANTES Release in HEK Cells. In the cytokine array study, TNF- α was not affected by fullerene treatment. Interestingly, TNF- β (lymphotoxin alpha) was inhibited on exposure to tris, hexa and CD-C₆₀, and this result was confirmed by a TNF- β ELISA assay (Figure 6(a)). TNF- β is a potent mediator of inflammatory and immune responses. Like TNF- α , TNF- β is involved in the regulation of various biological processes including cell proliferation, differentiation, apoptosis, lipid metabolism, coagulation, and antiviral responses.



(a)



(b)

FIGURE 5: Effect of fullerene derivatives on IL-6 and IL-8 release in HEK cells. Cells were treated with fullerene derivatives for 2, 4, 8, 12, 24, and 48 hours. Cytokine ELISA detection kits were used to evaluate cytokines in culture media. IL-6 (a) and IL-8 (b) releases were significantly altered by fullerene derivatives. Data are means \pm SEM. of quadruplicate cultures in each treatment group.

GRO, also referred to as MGSA for melanoma growth-stimulatory activity, stimulates keratinocyte proliferation and migration, and angiogenesis in cutaneous wound healing [24]. Members of the GRO family, GRO α , GRO β and GRO γ , exhibit some functional redundancy. A decrease in total GRO levels was observed in tris-C₆₀ treated cells by the cytokine antibody array assay, but not GRO α . We further evaluated GRO β and GRO γ levels using the ELISA

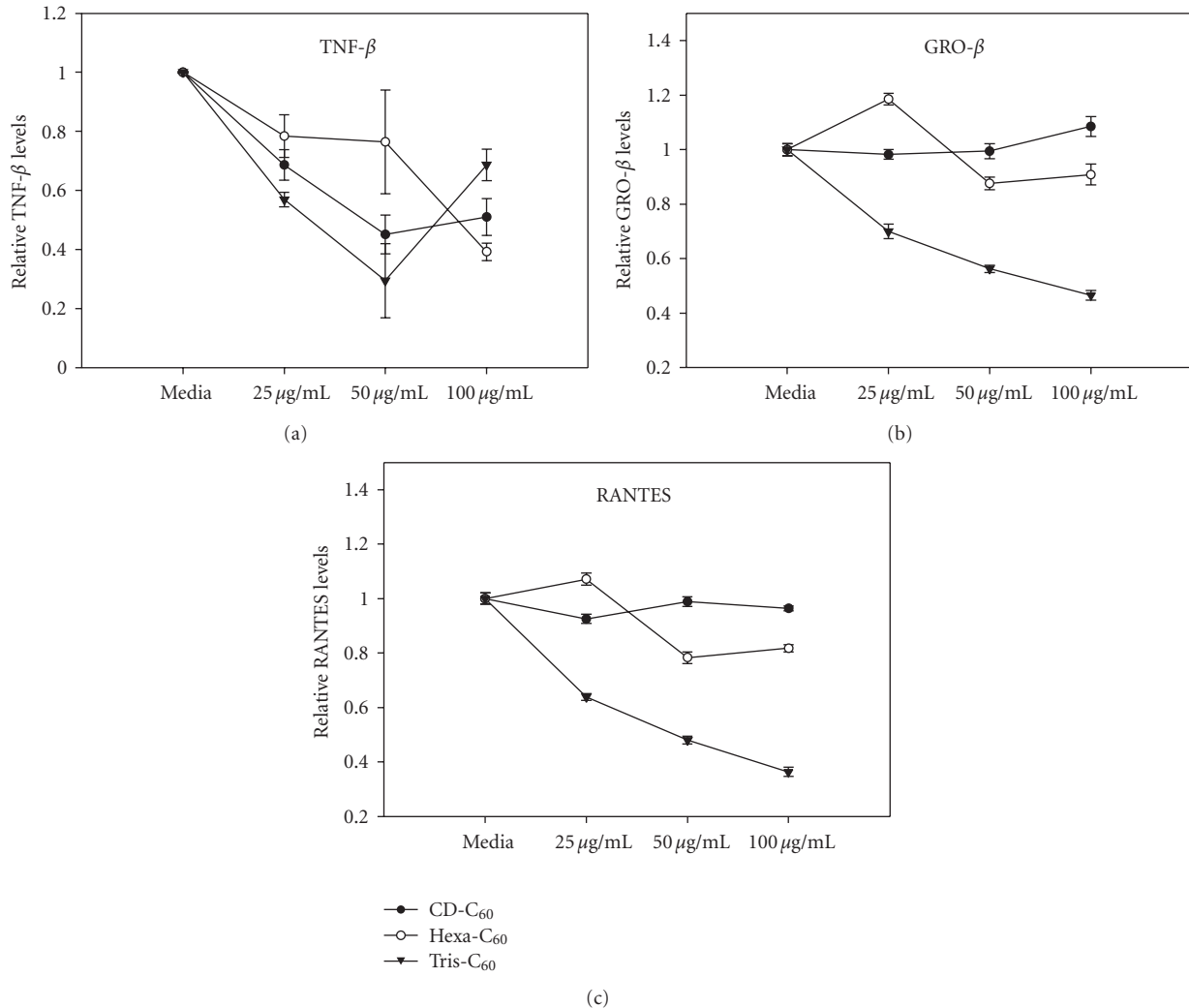


FIGURE 6: Effect of fullerene derivatives on TNF- β , GRO β and RANTES release in HEK cells. Cells were treated with fullerene derivatives for 24 hours. Cytokine ELISA detection kits were used to evaluate cytokines. TNF- β (a), GRO β (b) and RANTES (c) release were significantly altered by fullerene derivatives. Data are means \pm SEM. of quadruplicate cultures in each treatment group.

construction kit. No changes in GRO γ were noted with either of the functionalized fullerenes (data not shown). However, GRO β was suppressed by tris-C₆₀ treatment (Figure 6(b)). CD-C₆₀ and hexa-C₆₀ did not significantly affect GRO β secretion.

RANTES, or Regulated on Activation Normal T Cell Expressed and Secreted also called CCL5, is one of the chemokines produced by epidermal keratinocytes that might play an important role in the pathogenesis of cutaneous inflammatory disorders [25, 26]. It is predominantly chemotactic for T cells and is involved in the recruitment of T lymphocytes, eosinophils, basophils, and leukocytes to inflammatory sites [27]. Here again secretion of RANTES was significantly downregulated by tris-C₆₀ but was unaltered in CD-C₆₀ and hexa-C₆₀ treated cells suggesting that CD-C₆₀ and hexa-C₆₀ do not induce an inflammatory response (Figure 6(c)). However, tris-C₆₀ appears to decrease

the basal levels of RANTES secretion in HEK cells suggesting a downregulation of normal inflammatory responses and potentially an immunosuppressive function.

3.7. Fullerene Derivatives Did Not Affect MCP-1 Release in HEK Cells. Monocyte chemoattractant protein-1 (MCP-1) is a chemoattractant for monocytes, macrophages, and basophils, but not neutrophils [28]. MCP-1 has been implicated in regulating the expression of adhesion molecules and of some cytokines [29]. It is an important mediator in allergic inflammation [30]. The role of MCP-1 in both inflammatory diseases and normal tissue homeostasis is not clear. MCP-1 stimulates both chemotaxis of monocytes and several cellular events associated with chemotaxis, including Ca⁺⁺ flux and expression of integrins [31–33]. As shown in Figure 7, functionalized fullerenes did not alter MCP-1 levels even after 24 hours treatment.

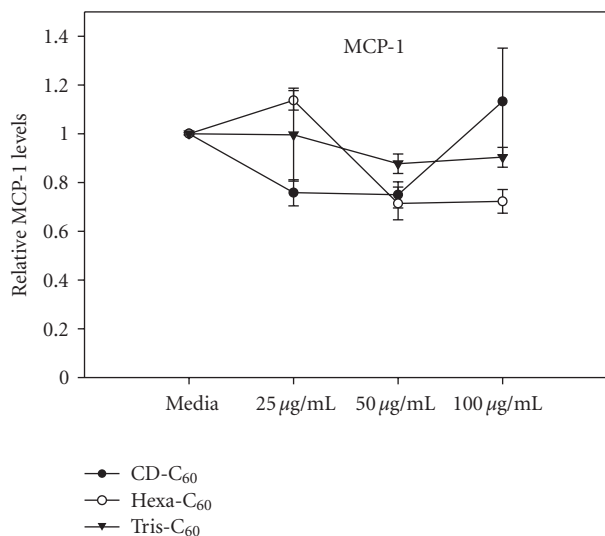


FIGURE 7: Effect of fullerene derivatives on MCP-1 release in HEK cells. Cells were treated with fullerene derivatives for 24 hours. Cytokine ELISA detection kits were used to evaluate cytokines. Data are means \pm SEM. of quadruplicate cultures in each treatment group.

4. Conclusions

The results of the cellular endpoint studies indicate that tris-C₆₀ can significantly reduce basal cell death and proliferation. Since apoptosis plays a critical role in maintaining cellular homeostasis, perturbation of this physiological response may potentially impact cell population dynamics and consequently organ-level responses [34]. A tris-C₆₀ induced cell resting state may potentially explain the overall unaltered or reduction of inflammatory cytokine release such as, IL-6, IL-8, GRO, TNF- β , RANTES, and MCP1. Our results demonstrate that CD-C₆₀, hexa-C₆₀, and tris-C₆₀ treatments elicit differential cytokine responses in HEK cells suggestive of a proinflammatory response by CD-C₆₀ (enhances IL-6 and IL-8 levels) and an antiinflammatory response by tris-C₆₀ (decreases all the inflammatory cytokines analyzed), while hexa-C₆₀ did not induce any significant changes in cytokine levels except a reduction in IL-8. Collectively, the antiapoptotic and antiproliferative function, the decrease of key inflammatory and growth promoting cytokines combined with the increase in senescent-inducing IL-1 β levels supports a prosenescent role for tris-C₆₀. Keratinocytes constitute about 95% of the epidermis and play a pivotal role in the response of the dermal tissue to environmental insults. Functional dysregulation of these cells or even partial abolition of this population could have significant ramifications in the response of the skin tissue to injuries and microbial infections.

In summary, tris-C₆₀ elicited different cellular responses when compared to either CD-C₆₀ or hexa-C₆₀. In contrast, CD-C₆₀ and hexa-C₆₀ induced relatively similar cellular responses. The observed difference in the biological responses of HEK cells to the three fullerenes could be tentatively attributed to the aggregation size of these particles.

Acknowledgments

This work was supported by Los Alamos National Laboratory, LDRD-DR program. This work was performed, in part, at the Center for Integrated Nanotechnologies, a U.S. Department of Energy, Office of Basic Energy Sciences user facility, Los Alamos National Laboratory (Contract DE-AC52-06NA25396), and Sandia National Laboratory (Contract DE-AC04-94AL85000). The authors thank Gabriel A. Montañó and Jennifer Martinez for their assistance with the physical characterization of the fullerenes.

References

- [1] S. Bosi, T. Da Ros, G. Spalluto, and M. Prato, "Fullerene derivatives: an attractive tool for biological applications," *European Journal of Medicinal Chemistry*, vol. 38, no. 11-12, pp. 913-923, 2003.
- [2] T. Da Ros, G. Spalluto, and M. Prato, "Biological applications of fullerene derivatives: a brief overview," *Croatica Chemica Acta*, vol. 74, no. 4, pp. 743-755, 2001.
- [3] S. H. Friedman, P. S. Ganapathi, Y. Rubin, and G. L. Kenyon, "Optimizing the binding of fullerene inhibitors of the HIV-1 protease through predicted increases in hydrophobic desolvation," *Journal of Medicinal Chemistry*, vol. 41, no. 13, pp. 2424-2429, 1998.
- [4] Z. Zhu, D. I. Schuster, and M. E. Tuckerman, "Molecular dynamics study of the connection between flap closing and binding of fullerene-based inhibitors of the HIV-1 protease," *Biochemistry*, vol. 42, no. 5, pp. 1326-1333, 2003.
- [5] T. Andersson, K. Nilsson, M. Sundahl, G. Westman, and O. Wennerström, "C₆₀ embedded in γ -cyclodextrin: a water-soluble fullerene," *Journal of the Chemical Society, Chemical Communications*, no. 8, pp. 604-606, 1992.
- [6] L. W. Zhang, W. W. Yu, V. L. Colvin, and N. A. Monteiro-Riviere, "Biological interactions of quantum dot nanoparticles in skin and in human epidermal keratinocytes," *Toxicology and Applied Pharmacology*, vol. 228, no. 2, pp. 200-211, 2008.
- [7] K. Arai, F. Lee, A. Miyajima, S. Miyatake, N. Arai, and T. Yokota, "Cytokines: coordinators of immune and inflammatory responses," *Annual Review of Biochemistry*, vol. 59, pp. 783-836, 1990.
- [8] J. Ye, A. Garg, C. Calhoun, K. R. Feingold, P. M. Elias, and R. Ghadially, "Alterations in cytokine regulation in aged epidermis: implications for permeability barrier homeostasis and inflammation. IL-1 gene family," *Experimental Dermatology*, vol. 11, no. 3, pp. 209-216, 2002.
- [9] R. C. McKenzie and D. N. Sauder, "The role of keratinocyte cytokines in inflammation and immunity," *Journal of Investigative Dermatology*, vol. 95, supplement 6, pp. 105S-107S, 1990.
- [10] A. Gröne, "Keratinocytes and cytokines," *Veterinary Immunology and Immunopathology*, vol. 88, no. 1-2, pp. 1-12, 2002.
- [11] M. Rebecca, W. Hsing-Lin, G. Jun, et al., "Impact of physico-chemical properties of engineered fullerenes on key biological responses," *Toxicology and Applied Pharmacology*, vol. 234, no. 1, pp. 58-67, 2009.
- [12] K. Nose, "Role of reactive oxygen species in the regulation of physiological functions," *Biological and Pharmaceutical Bulletin*, vol. 23, no. 8, pp. 897-903, 2000.
- [13] C. B. Thompson, "Apoptosis in the pathogenesis and treatment of disease," *Science*, vol. 267, no. 5203, pp. 1456-1462, 1995.

- [14] M. Bisaglia, B. Natalini, R. Pellicciari, et al., "C3-fullerol-tris-methanodicarboxylic acid protects cerebellar granule cells from apoptosis," *Journal of Neurochemistry*, vol. 74, no. 3, pp. 1197–1204, 2000.
- [15] D. N. Sauder, "The role of epidermal cytokines in inflammatory skin diseases," *Journal of Investigative Dermatology*, vol. 95, no. 5, pp. 27S–28S, 1990.
- [16] C. A. Dinarello, "Proinflammatory cytokines," *Chest*, vol. 118, no. 2, pp. 503–508, 2000.
- [17] S. Lisby and C. Hauser, "Transcriptional regulation of tumor necrosis factor- α in keratinocytes mediated by interleukin-1 β and tumor necrosis factor- α ," *Experimental Dermatology*, vol. 11, no. 6, pp. 592–598, 2002.
- [18] C. Ibsch, P. Bourdeau, C. Cadiot, J. Viac, and H. Gatto, "Upregulation of TNF- α production by IFN- γ and LPS in cultured canine keratinocytes: application to monosaccharides effects," *Veterinary Research Communications*, vol. 31, no. 7, pp. 835–846, 2007.
- [19] D. A. Norris, "Cytokine modulation of adhesion molecules in the regulation of immunologic cytotoxicity of epidermal targets," *Journal of Investigative Dermatology*, vol. 95, supplement 6, pp. 111S–120S, 1990.
- [20] M. Chabot-Fletcher, J. Breton, J. Lee, P. Young, and D. E. Griswold, "Interleukin-8 production is regulated by protein kinase C in human keratinocytes," *Journal of Investigative Dermatology*, vol. 103, no. 4, pp. 509–515, 1994.
- [21] J. M. Schröder, "Chemotactic cytokines in the epidermis," *Experimental Dermatology*, vol. 1, no. 1, pp. 12–19, 1992.
- [22] E. Corsini and C. L. Galli, "Cytokines and irritant contact dermatitis," *Toxicology Letters*, vol. 102–103, pp. 277–282, 1998.
- [23] N. Uekawa, A. Nishikimi, K.-I. Isobe, Y. Iwakura, and M. Maruyama, "Involvement of IL-1 family proteins in p38 linked cellular senescence of mouse embryonic fibroblasts," *FEBS Letters*, vol. 575, no. 1–3, pp. 30–34, 2004.
- [24] A. Richmond and H. G. Thomas, "Melanoma growth stimulatory activity: isolation from human melanoma tumors and characterization of tissue distribution," *Journal of Cellular Biochemistry*, vol. 36, no. 2, pp. 185–198, 1988.
- [25] M. Fukuoka, Y. Ogino, H. Sato, et al., "RANTES expression in psoriatic skin, and regulation of rantes and IL-8 production in cultured epidermal keratinocytes by active vitamin D₃ (tacalcitol)," *British Journal of Dermatology*, vol. 138, no. 1, pp. 63–70, 1998.
- [26] T. J. Schall, "Biology of the RANTES/SIS cytokine family," *Cytokine*, vol. 3, no. 3, pp. 165–183, 1991.
- [27] T. J. Schall, K. Bacon, K. J. Toy, and D. V. Goeddel, "Selective attraction of monocytes and T lymphocytes of the memory phenotype by cytokine RANTES," *Nature*, vol. 347, no. 6294, pp. 669–671, 1990.
- [28] T. Yoshimura and E. J. Leonard, "Human monocyte chemoattractant protein-1: structure and function," *Cytokines*, vol. 4, pp. 131–152, 1992.
- [29] Y. Jiang, D. I. Beller, G. Frendl, and D. T. Graves, "Monocyte chemoattractant protein-1 regulates adhesion molecule expression and cytokine production in human monocytes," *Journal of Immunology*, vol. 148, no. 8, pp. 2423–2428, 1992.
- [30] M. Baggiolini and C. A. Dahinden, "CC chemokines in allergic inflammation," *Immunology Today*, vol. 15, no. 3, pp. 127–133, 1994.
- [31] A. J. Valente, D. T. Graves, C. E. Vialle-Valentin, R. Delgado, and C. J. Schwartz, "Purification of a monocyte chemotactic factor secreted by nonhuman primate vascular cells in culture," *Biochemistry*, vol. 27, no. 11, pp. 4162–4168, 1988.
- [32] B. J. Rollins, A. Walz, and M. Baggiolini, "Recombinant human MCP-1/JE induces chemotaxis, calcium flux, and the respiratory burst in human monocytes," *Blood*, vol. 78, no. 4, pp. 1112–1116, 1991.
- [33] S. R. Williams, Y. Jiang, D. Cochran, G. Dorsam, and D. T. Graves, "Regulated expression of monocyte chemoattractant protein-1 in normal human osteoblastic cells," *American Journal of Physiology*, vol. 263, no. 1, pp. C194–C199, 1992.
- [34] R. Paus, T. Rosenbach, N. Haas, and B. M. Czarnetzki, "Patterns of cell death: the significance of apoptosis for dermatology," *Experimental Dermatology*, vol. 2, no. 1, pp. 3–11, 1993.

Research Article

Nanoprodugs of NSAIDs Inhibit the Growth of U87-MG Glioma Cells

Bong-Seop Lee, Xiangpeng Yuan, Qijin Xu, Minhee K. Ko, Aruna K. Nalla, Ilana Frankiel, Talia Shear, Keith L. Black, and John S. Yu

Department of Neurosurgery, Cedars-Sinai Medical Center, 8631 W. Third Street, Suite 800 East, Los Angeles, CA 90048, USA

Correspondence should be addressed to John S. Yu, john.yu@cshs.org

Received 2 October 2009; Accepted 4 January 2010

Academic Editor: Chao Lin

Copyright © 2010 Bong-Seop Lee et al. This is an open access article distributed under the Creative Commons Attribution License, which permits unrestricted use, distribution, and reproduction in any medium, provided the original work is properly cited.

Several recent reports have demonstrated that nonsteroidal anti-inflammatory drugs (NSAIDs) inhibit the growth of various malignant cells suggesting their application as anticancer agents. In this study, we prepared six nanometer-sized produgs (nanoprodugs) of NSAIDs, ibuprofen, indomethacin, and naproxen through the spontaneous emulsification mechanism using monomeric and dimeric derivatives of the NSAIDs. We evaluated their effect on the proliferation of U87-MG glioma cells by cell counting, WST-1 cell proliferation reagent, and propidium iodide incorporation. The two ibuprofen nanoprodugs inhibited the cell growth more potently than the indomethacin nanoprodugs, whereas the naproxen nanoprodugs did not show any significant effect. Remarkably, ibuprofen did not show any effect at an equimolar concentration. Approximately, 4.4% of the ibuprofen nanoprodugs was found in the cell, whereas no ibuprofen could be detected suggesting that the superior effect of the nanoprodugs can be attributed to the efficient cellular uptake of the nanoprodugs.

1. Introduction

Nonsteroidal anti-inflammatory drugs (NSAIDs) are widely used in the treatment of pain, fever, and inflammation. The major mechanism by which NSAIDs exert their anti-inflammatory activity is the inhibition of cyclooxygenase (COX)-derived prostaglandin synthesis. COX is the first enzyme in the formation of prostaglandin (PG) and thromboxane (TX) from arachidonic acid at the site of inflammation or after infection [1]. There are two types of COX enzymes, namely COX-1 and COX-2. COX-1 is expressed constitutively in many tissues, whereas COX-2 is expressed only at the site of inflammation [2]. Recent studies have shown that high COX-2 expression has been detected in various cancers, including colorectal, lung, breast, liver, head and neck and brain tumors, whereas COX-1 expression was unaffected [3–5].

Human glioblastoma multiforme (GBM) is one of the most common tumors of the central nervous system with poor prognosis and high rate of recurrence. It is a highly aggressive and recalcitrant brain tumor, and despite intensive multimodal therapeutic interventions, only modest progress

has been achieved over the last several decades in improving the treatment of patients with GBM [6]. Although the molecular mechanisms involved in the development of GBM are not yet fully understood, intensive studies have revealed some important molecular events correlated to the progress of malignant gliomas. The studies revealed that COX-2 have been expressed in brain tumors [7–9] and high COX-2 expression in gliomas is associated with poor prognosis [10].

A number of studies, clinical trials, and animal studies have demonstrated that NSAIDs may be effective in the prevention and treatment of certain types of cancers [11–14]. The molecular mechanisms by which NSAIDs exhibit antineoplastic effects are poorly understood and under intensive investigation. The chemopreventive and antitumorigenic effects of NSAIDs are partially attributed to the induction of apoptosis followed by inhibition of COX-2 [15–18]. Various studies have suggested that a COX-2-independent mechanism may also be involved because apoptosis induction by NSAIDs does not always correlate with their ability to inhibit COX-2 [19–22].

Indomethacin, ibuprofen and naproxen belong to the acidic NSAIDs which are widely used for the treatment

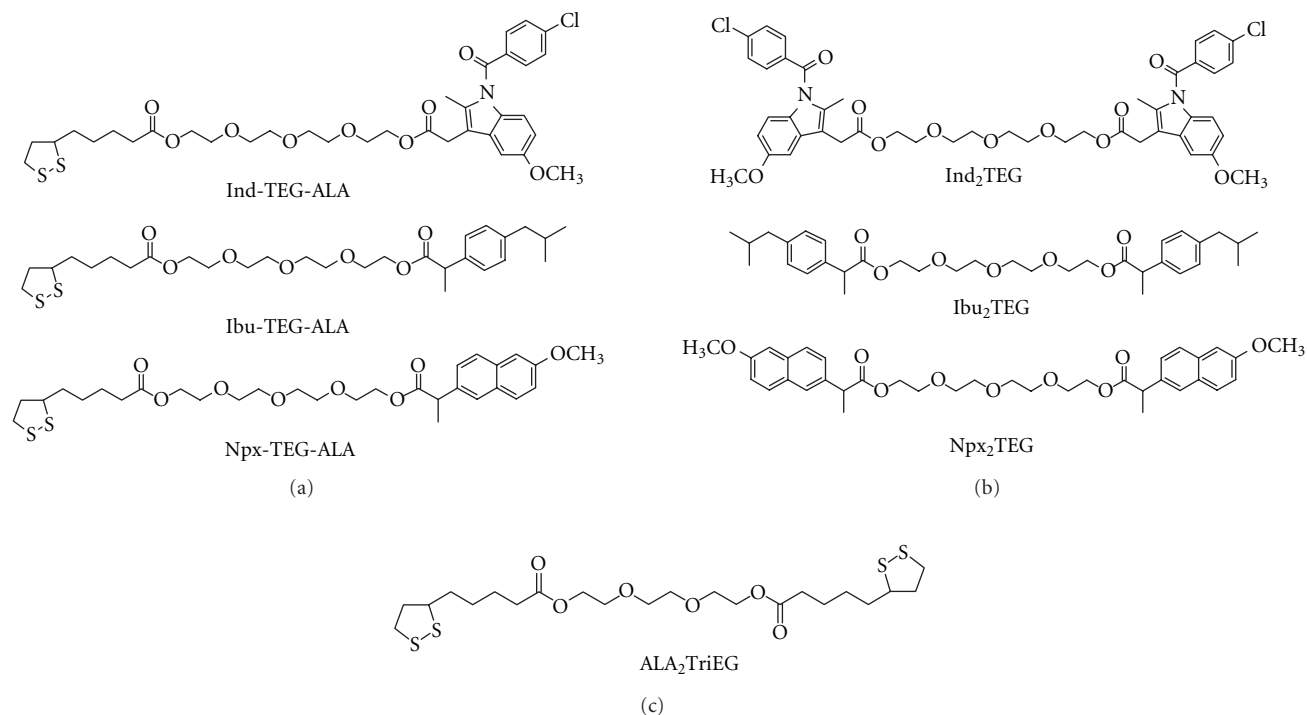


FIGURE 1: Derivatives of NSAIDs and ALA. ALA: α -lipoic acid; Ind: indomethacin; Ibu: ibuprofen; Npx: naproxen; TEG: tetraethylene glycol; TriEG: triethylene glycol.

of chronic inflammatory conditions. Ibuprofen is a potent COX-1 and COX-2 inhibitor. Besides its widespread use in the treatment of pain, fever, and inflammation, it has been shown that ibuprofen may be effective in the treatment of many cancers including prostate cancer [23], colon cancer [24, 25], and bladder cancer [26].

The inhibition of COX-derived prostaglandin synthesis, which is the major mechanism by which NSAIDs exert their anti-inflammatory activity, is also responsible for the adverse side effects, such as irritation and ulceration of the gastrointestinal (GI) mucosa [27]. These side effects are ascribed to the combined effect of the irritation caused by the free carboxylic groups in NSAIDs and blockage of prostaglandin biosynthesis in the GI tract [28]. In addition, the acidic moiety of these NSAIDs also contributes to the gastrointestinal side effect observed in response to these drugs [29]. Therefore, various prodrugs have been developed which attempt to alleviate the NSAID's adverse side effects as well as to improve their bioavailability by masking the carboxylic acid groups through the formation of bioreversible bonds [30–33].

In recent years, nanostructured biomaterials have received significant attention from the pharmaceutical industry, mainly because of their highly potential applicability as drug delivery vehicles. One of the most remarkable properties of nanostructured biomaterials is their improved bioavailability which can be ascribed to the generation of an enlarged surface area by transformation of bulk materials into the nanometer-sized structures [34, 35]. The surface-to-volume ratio increases with decreasing size of the nanostructures, which improves the bioavailability and enhances the

biological efficacy of the materials [36]. The other advantage of nanostructures is that water-insoluble therapeutics can be transported more efficiently in the aqueous physiological environment when formed into stable nanostructures [37].

In an effort to combine the two concepts of nanomeric biomaterials and prodrugs we have developed nanomeric prodrugs (nanoprodrugs) of NSAIDs by spontaneous emulsification of hydrophobic derivatives of NSAIDs and demonstrated their antioxidant activity, oxidant responsiveness and enzymatic prodrug activation [38]. Despite the highly hydrophobic nature of the derivatives, NSAIDs were readily hydrolyzed enzymatically from the nanoprodrugs, which is a prerequisite condition for the nanoprodrugs to be used as a prodrug. Thus, the nanoprodrugs may have potential as an anti-inflammatory prodrug and also as a biodegradable anti-inflammatory drug delivery vehicle.

In this study, we demonstrated the anti-proliferative effect of NSAID nanoprodrugs on U87GM glioma cells.

2. Materials and Methods

2.1. Preparation of NSAID Nanoprodrugs. The synthesis and characterization of the monomeric NSAID derivatives (Figure 1(a)) and the dimeric NSAID derivatives (Figure 1(b)) were performed as described [38]. Nanoprodrugs were prepared according to the method using spontaneous emulsification as described [38] with modifications. Briefly, 25 mg of the NSAID derivatives and 5 mg of α -tocopherol were dissolved in acetone (5 mL) containing polysorbate 80 (0.1% w/v). The organic solution was poured under moderate stirring on a magnetic plate into an aqueous

phase prepared by dissolving 25 mg of Pluronic F68 in 10 mL distilled water (0.25% w/v). Following 15 minutes of magnetic stirring, the acetone was removed under reduced pressure at room temperature. The suspensions were filtered through 0.8 μm hydrophilic syringe filter (Corning, Part no. 431221, Fisher Scientific Co., Pittsburgh, PA, USA), dialyzed in cellulose membrane tube (Sigma, code D9777) overnight in distilled water and stored at 4°C. As control, nanospheres were prepared with 25 mg of α -tocopherol or 25 mg of ALA₂TriEG (Figure 1(a)) in the absence of NSAID derivatives using the same procedure as described above. The α -lipopic acid-containing compound ALA₂TriEG was synthesized and characterized as described previously [39].

2.2. Size Measurements. The hydrodynamic size measurement and size distribution of the nanoprodugs were performed by the dynamic light scattering (DLS) using a Coulter N4-Plus Submicron Particle Sizer (Coulter Corporation, Miami, FL, USA) as described [38, 39]. For each preparation mean diameter and mean polydispersity index (P.I.) of three determinations were calculated. The error bar (S.D.) was calculated from triplicate determinations.

2.3. Stability of NSAID Nanoprodugs during Long Term Storage. The stability of the nanoprodugs was assessed by measuring the size and concentrations of prodrug molecules of NSAIDs after a 3-month storage at 4°C. The size of the nanoprodugs was measured as described above (Section 2.2) and the changes were calculated as follows:

$$\text{Size \% of control} = \left(\frac{\text{Size}_{t=0}}{\text{Size}_{t=3\text{ mo}}} \right) \times 100, \quad (1)$$

where $\text{Size}_{t=0}$ is the nanoprodug size immediately after dialysis and $\text{Size}_{t=3\text{ mo}}$ is the size after 3-month storage at 4°C. The amount of intact NSAIDs prodrugs was assessed by RP-HPLC as follows: the suspensions of nanoprodugs (100 μL) were added to acetonitrile (400 μL) and analyzed using RP-HPLC as described [38]. The recovery yield was calculated as follows:

$$\begin{aligned} \text{Recovery yield (\%)} \\ = \frac{\text{Amount of prodrugs after incubation}}{\text{Amount of prodrugs before incubation}} \\ \times 100. \end{aligned} \quad (2)$$

The error bar (S.D.) was calculated from triplicate determinations.

2.4. Enzymatic Hydrolysis of NSAID Nanoprodugs. The nanoprodugs were suspended in phosphate buffered saline (PBS, pH 7.4) to give the final concentration of 500 μM NSAID derivatives. Esterase (porcine liver, Sigma, code E3019) was added to the final concentration of 5 U/mL and the mixture was incubated for 1 hour in a water bath at 37°C.

To determine the amount of enzymatically hydrolyzed NSAIDs, samples were centrifuged for 10 minutes at 20,000

$\times \text{g}$ and the supernatants were analyzed by RP-HPLC using a C₁₈ reversed phase column as described [38].

The error bar (S.D.) was calculated from triplicate determinations.

2.5. Maintenance of Cell Line. The U87-MG human glioma cell line was obtained from American Type Culture Collection (ATCC, Bethesda, MD, USA). The cells were grown and maintained in Minimum Essential Medium (MEM, Invitrogen) containing antibiotics penicillin (100 U/mL) and streptomycin (100 $\mu\text{g}/\text{mL}$) and supplemented with 10% fetal bovine serum (FBS, Invitrogen). Cells were grown at 37°C at an atmosphere of 5% CO₂ in humidified air.

2.6. Cell Counting. The glioma cells were seeded at 10⁵ cells per well in 6-well plates and grown for 24 hours. The cells were treated with NSAID nanoprodugs for 3 days. After treatment, the culture medium was removed and cells were washed with PBS. 0.5 mL of 0.25% Trypsin/EDTA was added to each well and the detached cells were counted immediately in a hemocytometer. The antiproliferative effect of the nanoprodugs was presented as a cell number % of control, which was calculated as follows:

$$\text{Cell number \% of control} = \left(\frac{\text{Cell number}_{\text{treated}}}{\text{Cell number}_{\text{control}}} \right) \times 100, \quad (3)$$

where $\text{Cell number}_{\text{treated}}$ is the number of cells after treatment with nanoprodugs and $\text{Cell number}_{\text{control}}$ is the number of cells of control culture which was incubated with culture medium only. The cells were also treated with nanospheres prepared from α -tocopherol or ALA₂TriEG only. The error bar (S.D.) was calculated from triplicate determinations.

2.7. Assessment of Cell Viability Using Regent WST-1. The effect of the nanoprodugs on the cell proliferation was quantified using the cell proliferation reagent WST-1 (water-soluble tetrazolium salt) colorimetric assay (Boehringer Mannheim) according to the manufacturer's instructions. Nanoprodugs were prepared from the monomeric derivative Ibu₂TEG or dimeric derivative Ibu-TEG-ALA (Figure 1). Ibuprofen was prepared as a 100 mM solution in DMSO. The human glioma cells were seeded on a 96-well microtiter plate at 2×10^3 cells/well for 24 hours. The cells were treated with drugs at a final concentration ranging from 10 to 100 μM for nanoprodugs and 50 to 400 μM for ibuprofen. After 72 hours of treatment, culture medium containing the drugs was removed, cells were washed with 200 μL of PBS, and 90 μL of culture medium and 10 μL of WST-1 solution were added to each well. Cells were incubated at 37°C for 1–4 hours, and the absorbance was read by an ELISA plate reader at 450 nm. The cell viability was calculated as follows:

$$\text{Cell viability (\%)} = \left(\frac{\text{Abs}_s}{\text{Abs}_c} \right) \times 100, \quad (4)$$

where Abs_s is the absorbance of cells treated with drugs and Abs_c is the absorbance of control cells incubated with

TABLE 1: Size and polydispersity index (P.I.) of the nanoprodrugs ($n = 3, \pm S.D.$).

NSAIDs derivatives	Size (nm)	P.I.
ALA-TEG-Ind	$149 \pm 1 (253 \pm 25)^*$	0.12 ± 0.02
ALA-TEG-Ibu	$149 \pm 15 (251 \pm 13)^*$	0.09 ± 0.04
ALA-TEG-Npx	$147 \pm 6 (298 \pm 6)^*$	0.11 ± 0.02
Ind ₂ TEG	$140 \pm 8 (159 \pm 10)^*$	0.11 ± 0.04
Ibu ₂ TEG	$141 \pm 11 (186 \pm 11)^*$	0.10 ± 0.02
Npx ₂ TEG	$148 \pm 1 (259 \pm 9)^*$	0.06 ± 0.02

*Size of the nanoprodrugs in the absence of α -tocopherol [38]. ALA: α -lipoic acid; Ind: indomethacin; Ibu: ibuprofen; Npx: naproxen; TEG: tetraethylene glycol.

cell culture medium only. The cells were also treated with nanospheres prepared from α -tocopherol or ALA₂TriEG only. The error bar (S.D.) was calculated from triplicate determinations.

2.8. Propidium Iodide Assay. The glioma cells were treated with ibuprofen nanoprodrugs for 3 days. The cells were also treated with free ibuprofen and nanospheres prepared from α -tocopherol or ALA₂TriEG only. After treatment, the cells were incubated with $5 \mu\text{M}$ of propidium iodide (PI) (Sigma) for 1 hour. PI fluorescence was excited at 515–600 nm using an inverted microscope fitted with a standard rhodamine filter. Images were taken using a digital camera connected to the microscope.

2.9. Uptake of Ibu₂TEG Nanoprodrug and Ibuprofen by Glioma Cells. The glioma cells were plated in 75 cm^2 culture flasks containing 20 mL cell culture medium and grown up to approximate 70% confluent density. Cells were treated with $100 \mu\text{M}$ of Ibu₂TEG nanoprodrug suspension or ibuprofen dissolved in DMSO for 24 hours. Treated cells were washed three times with PBS to remove the drugs, and adherent cells were trypsinized. The cells were collected by centrifugation at $1,500 \times g$ and the recovered pellets were washed three times with PBS by repeated resuspending and centrifugation. In order to determine the content of ibuprofen, cells were disrupted in 0.5 mL of lysis buffer (1% of Triton X-100, 10 mM Tris-HCl, pH 4.7) and cell debris was removed by centrifugation for 10 minutes at $10,000 \times g$ and 25°C . The resulting supernatant was collected and frozen at -20°C . In order to determine the content of nanoprodrugs, 2 mL of acetonitrile was added to the cell lysates and the cell debris was removed by centrifugation for 10 minutes at $10,000 \times g$ and 25°C . The supernatant was collected for analysis. The content of Ibu₂TEG nanoprodrug and ibuprofen was determined from the supernatants as described previously using RP-HPLC [38].

2.10. Statistical Analysis. The results were analyzed and expressed as mean \pm standard deviation (S.D.). Statistical analysis of the results was carried out using Student's t -test. For all tests, differences with a $P < .05$ were considered to be significant.

3. Results and Discussion

3.1. Preparation of Nanoprodrugs of NSAIDs. In order to combine the concept of NSAIDs prodrug and nanostructured drug/drug delivery system, we have developed nanometer-sized prodrugs (nanoprodrugs) of NSAIDs [38]. Many favorable properties of nanostructured biomaterials have been characterized in respect to their applicability as a drug carrier. One of the most remarkable properties is their improved bioavailability which is attributed to an enlarged surface area by transformation of bulk materials into the nanometer-sized structures, leading to an enhanced biological efficacy of the materials [34, 40]. These properties of nanostructured biomaterials have been especially crucial for the development of nanoprodrugs based on the formation of nanostructures using the spontaneous emulsification method. This is because only water-insoluble hydrophobic prodrug molecules can be formed into nanometer-sized structures which is stable for a prolonged period of time in an aqueous biological environment, and in the other hand, the enzymatic activation of the hydrophobic prodrugs would be otherwise impossible due to the insolubility of the prodrugs in aqueous media.

Thus, the formation into the nanoprodrugs with an increased surface-to-volume ratio may improve the bioavailability and biological efficacy of the hydrophobic prodrug molecules by facilitating the interaction between hydrolytic enzymes and prodrugs [34, 40].

The hydrophobic derivatives of NSAIDs (Figure 1(a) and 1(b)) in organic solvents spontaneously formed into nanoprodrugs upon the addition into an aqueous solution containing hydrophilic surfactants by a spontaneous emulsification process [41–43].

The size and stability of nanoprodrugs depends on multiple factors, such as the nature and concentration of the compounds, the surfactants, and the ratio of organic solvent to water [42–44]. In this study, formulation parameters were kept the same as described [38] except for the addition of α -tocopherol (Section 2.1).

The hydrodynamic size was within the range of 140 and 150 nm and highly reproducible (Table 1). The size of the nanoprodrugs was significantly smaller when compared with the size of nanoprodrugs prepared without the addition of α -tocopherol [38].

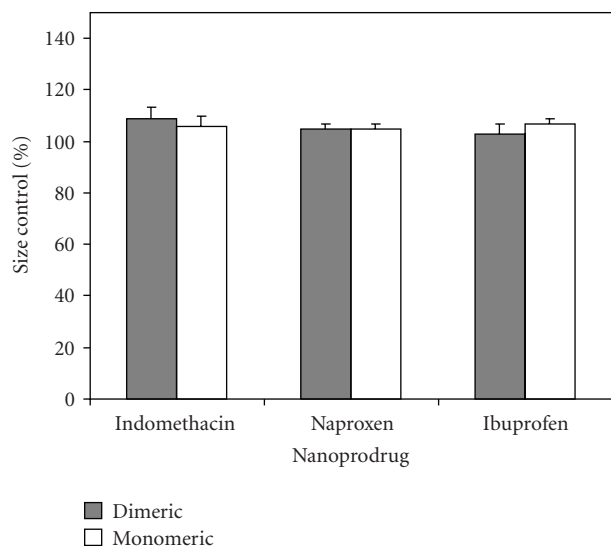


FIGURE 2: Long term stability of nanoprodrugs. Dimeric nanoprodrugs: Ind₂TEG, Npx₂TEG and Ibu₂TEG; Monomeric nanoprodrugs: Ind-TEG-ALA, Npx-TEG-ALA, and Ibu-TEG-ALA.

Moreover, practically no differences in the size were observed between the nanoprodrugs of different NSAIDs when supplemented with α -tocopherol. This is especially important when the therapeutic efficiency of different nanoprodrugs are compared. When the compositions of the nanoprodrugs are the same except for the active drug compounds and the size varies within a close range, the observed differences in the efficacy can be attributed directly to the different prodrug molecules involved.

The stability of the nanoprodrugs was assessed by measuring the size and contents of the intact prodrug molecules of NSAIDs after a 3-month storage at 4°C. In this study, the size of all the nanoprodrugs remained almost unchanged (Figure 2) and also no decreases were observed in the amount of the available prodrug molecules after the 3-month storage (data not shown). The observed chemical and physical stability of the nanoprodrugs may be ascribed to the strong assembly of the hydrophobic prodrug molecules and α -tocopherol which further reduces the interaction with water and increases the structural integrity of the nanoprodrugs.

3.2. Enzymatic Hydrolysis of Nanoprodrugs. In order to assess the differences in the rates of prodrug activation from the NSAID nanoprodrugs, the rate of enzymatic reconversion of the prodrugs into the parent drugs was investigated in vitro with porcine liver esterase. According to the molecular design based on ester bonds, the NSAID prodrug molecules were expected to be degraded by enzymatic ester hydrolysis. As shown in our previous investigation at room temperature [38], a different rate of enzymatic hydrolysis were observed, which was attributed to the different structures of the prodrug molecules. It has been shown that the indomethacin nanoprodrugs were more stable compared with the naproxen and ibuprofen nanoprodrugs, and the nanoprodrugs from dimeric Ind₂TEG, Npx₂TEG and Ibu₂TEG were more stable when compared with the

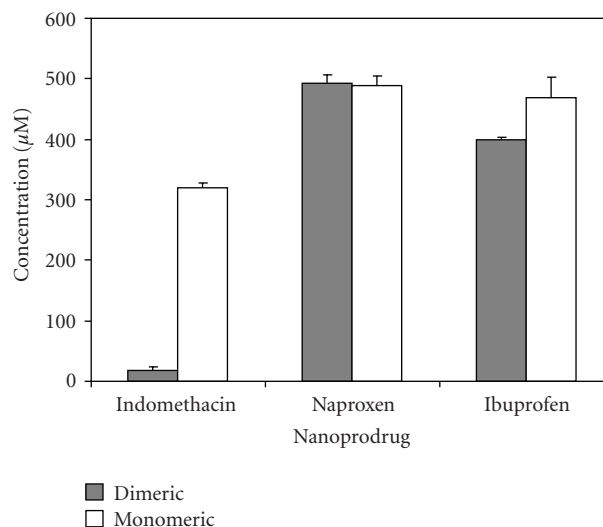


FIGURE 3: Enzymatic hydrolysis of NSAID nanoprodrugs at 37°C.

nanoprodrugs from monomeric Ind-TEG-ALA, Npx-TEG-ALA and Ibu-TEG-ALA. As shown in Figure 3, at an elevated temperature of 37°C, the differences in the hydrolysis rates between the monomeric and dimeric nanoprodrugs were completely disappeared (naproxen), drastically diminished (ibuprofen) or retained (indomethacin). Notably, after a 1 hour incubation at 37°C, approximately 65% of drug was released from the nanoprodrug of Ind-TEG-ALA compared with 39% at room temperature [38], whereas only 6% was released from the nanoprodrug of Ind₂TEG, presumably due to the effect of the bulkier indomethacin and the replacement of one indomethacin with ALA on the enzymatic hydrolysis rate [38].

3.3. Effect of NSAID Nanoprodrugs on Growth of Glioma Cells. In order to evaluate the effect of NSAID nanoprodrugs on tumor cell growth, we studied the effect of the NSAID nanoprodrugs on the cell growth of U87-MG glioma cells. Glioma cells were treated with six nanoprodrugs (10, 25, 50 and 100 µM) for three days (Section 2.6). Cells were also treated with nanospheres prepared from α -tocopherol or ALA₂TriEG only by exposing to an equimolar concentration of α -tocopherol or ALA unit.

As shown in Figure 4, the nanoprodrugs of ibuprofen were more potent at reducing the cell proliferation in comparison with the nanoprodrugs of indomethacin or naproxen. The concentration of 25 and 50 µM nanoprodrugs of Ibu₂TEG and Ibu-TEG-ALA, respectively, were sufficient to inhibit growth of the glioma cells. In addition, comparing the two ibuprofen nanoprodrugs, the nanoprodrug of dimeric Ibu₂TEG was more potent (Figure 4(a)). In Section 3.2, we showed that more than 80% of prodrugs were hydrolyzed from the nanoprodrugs of Ibu₂TEG and Ibu-TEG-ALA (Figure 3), suggesting that the observed difference may not be due to the slightly different rate of enzymatic prodrug activation. On the other hand, the indomethacin nanoprodrugs were able to cause a significant effect only in the concentration of 100 µM or higher (Figure 4(c)). The

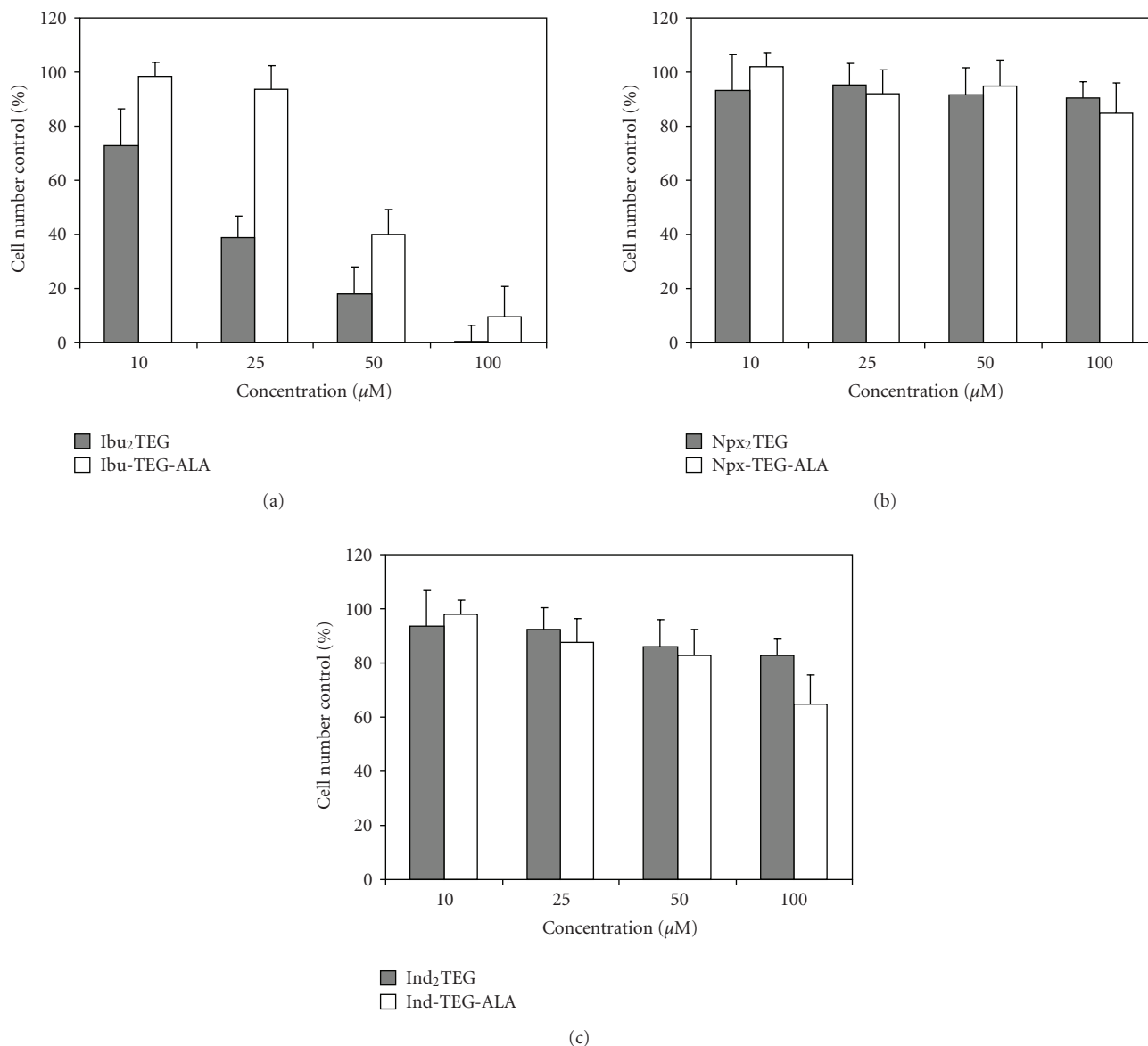


FIGURE 4: Effect of NSAID nanoprodrugs on glioma cell proliferation.

treatment with naproxen nanoprodrugs did not show any significant effect on cell proliferation (Figure 4(b)).

It is interesting to note that the nanoprodrug of the monomeric Ind-TEG-ALA was more potent than the nanoprodrug of dimeric Ind₂TEG ($P < .05$ at $100 \mu\text{M}$ each) (Figure 4(c)), which is in contrast to the ibuprofen nanoprodrugs. Considering the rate of the enzymatic hydrolysis of Ind-TEG-ALA and Ind₂TEG (Section 3.2), the more potent antiproliferative effect of the nanoprodrug Ind-TEG-ALA can be attributed to the more efficient prodrug activation. The treatment with control nanoprodrugs prepared from α -tocopherol or ALA₂TriEG only did not show any effect on the cell proliferation (data not shown).

3.4. Effect of Ibuprofen Nanoprodrug on Cell Viability. The WST-1 assay is based on the formation a water-soluble formazan crystal, which directly correlates to the number

of viable cells with active mitochondrial dehydrogenases. In order to evaluate the effect of ibuprofen nanoprodrugs on tumor cell viability, U87-MG glioma cells were treated with the ibuprofen nanoprodrugs ($10, 25, 50,$ and $100 \mu\text{M}$) for three days (Section 2.7). Cells were also treated with nanospheres prepared from α -tocopherol or ALA₂TriEG only by exposing to an equimolar concentration of α -tocopherol or ALA unit. Similar to the results from Section 3.3, the nanoprodrug from the dimeric Ibu₂TEG were more potent than the nanoprodrug from Ibu-TEG-ALA (Figure 5(a)). The IC₅₀ values were 25 and $47 \mu\text{M}$ for the Ibu₂TEG and Ibu-TEG-ALA nanoprodrugs, respectively. In Section 3.2, we showed that more than 80% of prodrugs were hydrolyzed from the nanoprodrugs of Ibu₂TEG and Ibu-TEG-ALA after 1 hour incubation at 37°C , suggesting that the observed difference may not be due to the slightly different rate of enzymatic prodrug activation.

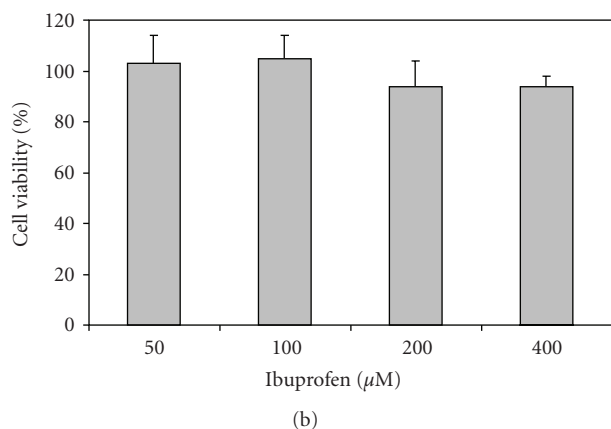
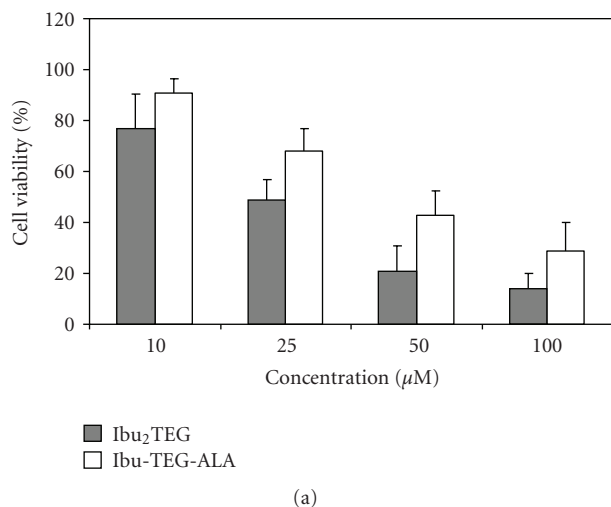


FIGURE 5: Effect of ibuprofen nanoprodugs (a) and ibuprofen (b) on the viability of glioma cells.

Obviously, the more potent effect of the dimeric nanoprodug can be ascribed to the higher parent drug concentration wherein the total amount of ibuprofen available from the nanoprodug of Ibu₂TEG is twice as much as that available from the Ibu-TEG-ALA nanoprodug. Again, the nanoprodugs prepared from α -tocopherol or ALA₂TriEG only did not show any effect on the cell viability (data not shown). More notably, the treatment with free ibuprofen did not show any significant effect on the cell proliferation even with a higher concentration of 400 μ M (Figure 5(b)).

3.5. Cytotoxic Effect of Ibuprofen Nanoprodug on Glioma Cells.

In order to demonstrate that the NSAID nanoprodugs induce cell death, glioma cells were treated for three days with ibuprofen nanoprodugs which were found to have a potent effect on growth inhibition (Sections 3.3 and 3.4) and incubated with propidium iodide (PI). PI incorporated into the dead cells, binds to DNA and becomes fluorescent [45]. Figure 6 shows representative images of U87-MG glioma cells treated with 50 μ M (c) and 100 μ M (d) of Ibu₂TEG nanoprodugs, 100 μ M of Ibu-TEG-ALA nanoprodugs and 200 μ M of ibuprofen (f). The treatment of the glioma cells with the nanoprodugs resulted in a

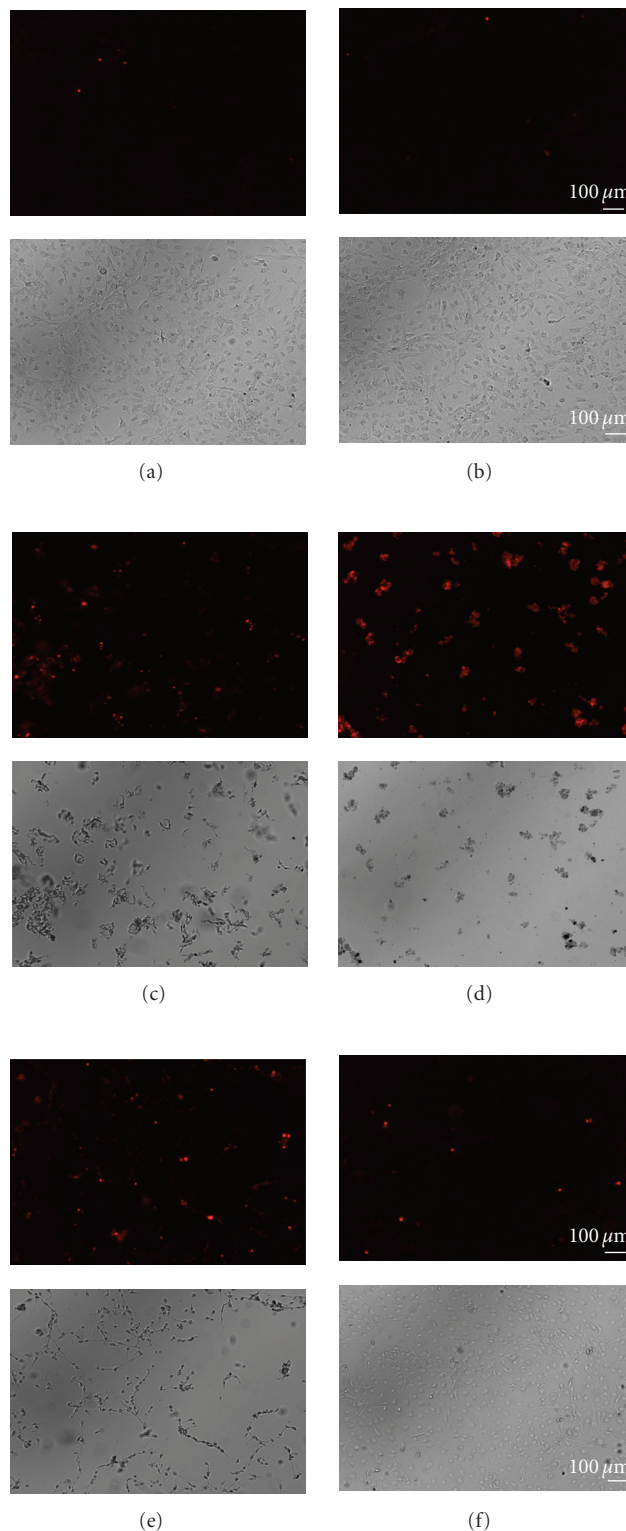


FIGURE 6: Effect of nanoprodugs on cell death in U87-MG glioma cells by propidium iodide incorporation. Representative pictures of: control cultures (a); cells treated with control nanoprodug from α -tocopherol (b); cells treated with 50 μ M (c) and 100 μ M (d) nanoprodug from Ibu₂TEG; cells treated with 100 μ M nanoprodug from Ibu-TEG-ALA (e); cells treated with 200 μ M ibuprofen (f). Panels above (a), (b), (c), (d), (e), and (f) are correspondent contrast phase photomicrographs.

significant reduction in the cell number and induced cell death with significant PI incorporation, whereas ibuprofen did not show any effect.

3.6. Cellular Accumulation of Ibu_2TEG Nanoprodrug. In order to investigate the relationship between the cytotoxicity and the drug concentration in cell, the cellular uptake of Ibu_2TEG nanoprodrug and free ibuprofen were determined in U87-MG glioma cells after a 24-hour exposure to equimolar concentration of ibuprofen and Ibu_2TEG nanoprodrug (100 μM) corresponding to a total amount of 2 μmol of ibuprofen or Ibu_2TEG nanoprodrug per flask containing 20 mL of cell culture medium (Section 2.9). Cell lysate was prepared from the cells harvested from one 75 cm^2 -flask which contained 5×10^6 – 6×10^6 cells/flask. The content of Ibu_2TEG found in the cell lysate was 88 nmol approximately corresponding to 4.4% of the initially added nanoprodrugs. No ibuprofen was detected in the cell lysates. These findings confirmed the previous assumption that the availability of parent drugs may be the crucial factor for the efficacy of the nanoprodrugs. The higher intracellular parent drug concentration can be achieved by a combination of efficient cellular uptake of the nanoprodrugs and prodrugs activation from the nanoprodrugs. The underlying mechanisms of the cellular uptake of the nanoprodrugs are under investigation.

As demonstrated in this study, water-insoluble drug compounds can be transformed into stable nanostructures obviating the need to dissolve the compounds in excessive amount of cosolvents and thus eliminating the interference of toxic side effects caused by cosolvents [46, 47]. The formation into the compact nanostructures confers an additional advantage of higher drug loading per volume, which is of crucial importance when high dosing is required. Probably, the most important advantage of the nanostructures in anticancer therapy is their increased accumulation within the tumor tissues, which is attributed to a phenomenon characterized as the enhanced permeability and retention (EPR) effect. The EPR effect was first described by Matsumura and Maeda [48] as a result of differences in tumor neovasculature compared to that of normal tissues. This includes leaky blood vessels and poor lymphatic drainage system. The leaky blood vessels allow the nanostructures penetrate more easily into the tumor tissues than into the normal tissues. Because of the dysfunctional lymphatic drainage system, the penetrated nanostructures are retained and accumulated in tumors, which allows them to diffuse into the vicinity of the tumor cells. Studies have shown that particles with diameters <200 nm are more effectively accumulated in the tumor tissues [49–52]. In this study, we showed that the NSAID nanoprodrugs could be prepared reproducibly in the size range of <150 nm and accumulated in the glioma cells to the amount sufficient to inhibit cell growth and elicit cell death.

4. Conclusion

In this study, nanoprodrugs of NSAIDs were prepared by spontaneous emulsification of hydrophobic prodrugs of NSAIDs and their antiproliferative effect was demonstrated

using U87-MG glioma cells. Among the tested three NSAIDs, the nanoprodrugs of ibuprofen inhibited the cell growth most significantly and induced cell death. In contrast to the ibuprofen nanoprodrugs, free ibuprofen did not show any effect on cell growth and viability. In addition, no accumulated ibuprofen was found in the cells, whereas approximately 4.4% of ibuprofen nanoprodrug was recovered from the treated glioma cells suggesting that the superior antiproliferative effect of the nanoprodrugs can be attributed to the enhanced uptake by the cells. We are further investigating the mechanisms of the cellular uptake and the molecular events underlying the antiproliferative effect of the ibuprofen nanoprodrugs.

References

- [1] J. A. Mitchell and T. D. Warner, "Cyclo-oxygenase-2: pharmacology, physiology, biochemistry and relevance to NSAID therapy," *British Journal of Pharmacology*, vol. 128, no. 6, pp. 1121–1132, 1999.
- [2] S. Kargman, S. Charleson, M. Cartwright, et al., "Characterization of prostaglandin G/H synthase 1 and 2 in rat, dog, monkey, and human gastrointestinal tracts," *Gastroenterology*, vol. 111, no. 2, pp. 445–454, 1996.
- [3] W. Dempke, C. Rie, A. Grothey, and H.-J. Schmoll, "Cyclooxygenase-2: a novel target for cancer chemotherapy?" *Journal of Cancer Research and Clinical Oncology*, vol. 127, no. 7, pp. 411–417, 2001.
- [4] D. B. Fournier and G. B. Gordon, "COX-2 and colon cancer: potential targets for chemoprevention," *Journal of Cellular Biochemistry*, vol. 34, supplement, pp. 97–102, 2000.
- [5] E. Fosslien, "Molecular pathology of cyclooxygenase-2 in neoplasia," *Annals of Clinical & Laboratory Science*, vol. 30, no. 1, pp. 3–21, 2000.
- [6] D. C. Shrieve, E. Alexander III, P. M. Black, et al., "Treatment of patients with primary glioblastoma multiforme with standard postoperative radiotherapy and radiosurgical boost: prognostic factors and longterm outcome," *Journal of Neurosurgery*, vol. 90, no. 1, pp. 72–77, 1999.
- [7] M. H. Deininger, M. Weller, J. Streffer, M. Mittelbronn, and R. Meyermann, "Patterns of cyclooxygenase-1 and -2 expression in human gliomas in vivo," *Acta Neuropathologica*, vol. 98, no. 3, pp. 240–244, 1999.
- [8] T. Joki, O. Heese, D. C. Nikas, et al., "Expression of cyclooxygenase 2 (COX-2) in human glioma and in vitro inhibition by a specific COX-2 inhibitor, NS-398," *Cancer Research*, vol. 60, no. 17, pp. 4926–4931, 2000.
- [9] R. Patti, K. Gumired, P. Reddanna, L. N. Sutton, P. C. Phillips, and C. D. Reddy, "Overexpression of cyclooxygenase-2 (COX-2) in human primitive neuroectodermal tumors: effect of celecoxib and rofecoxib," *Cancer Letters*, vol. 180, no. 1, pp. 13–21, 2002.
- [10] T. Shono, P. J. Tofilon, J. M. Bruner, O. Owolabi, and F. F. Lang, "Cyclooxygenase-2 expression in human gliomas: prognostic significance and molecular correlations," *Cancer Research*, vol. 61, no. 11, pp. 4375–4381, 2001.
- [11] J. J. Keller and F. M. Giardiello, "Chemoprevention strategies using NSAIDs and COX-2 inhibitors," *Cancer Biology & Therapy*, vol. 2, no. 4, supplement 1, pp. S140–S149, 2003.
- [12] R. A. Gupta and R. N. DuBois, "Colorectal cancer prevention and treatment by inhibition of cyclooxygenase-2," *Nature Reviews Cancer*, vol. 1, no. 1, pp. 11–21, 2001.

- [13] A. Umar, J. L. Viner, W. F. Anderson, and E. T. Hawk, "Development of COX inhibitors in cancer prevention and therapy," *American Journal of Clinical Oncology*, vol. 26, no. 4, supplement 2, pp. S48–S57, 2003.
- [14] R. E. Harris, J. Beebe-Donk, H. Doss, and D. Burr Doss, "Aspirin, ibuprofen, and other non-steroidal anti-inflammatory drugs in cancer prevention: a critical review of non-selective COX-2 blockade (review)," *Oncology Reports*, vol. 13, no. 4, pp. 559–583, 2005.
- [15] D. W. Lin and P. S. Nelson, "The role of cyclooxygenase-2 inhibition for the prevention and treatment of prostate carcinoma," *Clinical Prostate Cancer*, vol. 2, no. 2, pp. 119–126, 2003.
- [16] J. R. Mann and R. N. DuBois, "Cyclooxygenase-2 and gastrointestinal cancer," *Cancer Journal*, vol. 10, no. 3, pp. 145–152, 2004.
- [17] J. W. Basler and G. A. Piazza, "Nonsteroidal anti-inflammatory drugs and cyclooxygenase-2 selective inhibitors for prostate cancer chemoprevention," *The Journal of Urology*, vol. 171, no. 2, pp. S59–S63, 2004.
- [18] A. L. Sabichi and S. M. Lippman, "COX-2 inhibitors and other nonsteroidal anti-inflammatory drugs in genitourinary cancer," *Seminars in Oncology*, vol. 31, no. 21, supplement 7, pp. 36–44, 2004.
- [19] H.-C. Chuang, A. Kardosh, K. J. Gaffney, N. A. Petasis, and A. H. Schönthal, "COX-2 inhibition is neither necessary nor sufficient for celecoxib to suppress tumor cell proliferation and focus formation in vitro," *Molecular Cancer*, vol. 7, article 38, 2008.
- [20] J. Marx, "Anti-inflammatories inhibit cancer growth—but how?" *Science*, vol. 291, no. 5504, pp. 581–582, 2001.
- [21] D. J. Elder, D. E. Halton, A. Hague, and C. Paraskeva, "Induction of apoptotic cell death in human colorectal carcinoma cell lines by a cyclooxygenase-2 (COX-2)-selective nonsteroidal anti-inflammatory drug: independence from COX-2 protein expression," *Clinical Cancer Research*, vol. 3, no. 10, pp. 1679–1683, 1997.
- [22] H. Jiang, J. J. Lin, Z.-Z. Su, N. I. Goldstein, and P. B. Fisher, "Subtraction hybridization identifies a novel melanoma differentiation associated gene, mda-7, modulated during human melanoma differentiation, growth and progression," *Oncogene*, vol. 11, no. 12, pp. 2477–2486, 1995.
- [23] J. Andrews, D. Djakiew, S. Krygier, and P. Andrews, "Superior effectiveness of ibuprofen compared with other NSAIDs for reducing the survival of human prostate cancer cells," *Cancer Chemotherapy and Pharmacology*, vol. 50, no. 4, pp. 277–284, 2002.
- [24] M. Yao, W. Zhou, S. Sangha, et al., "Effects of nonselective cyclooxygenase inhibition with low-dose ibuprofen on tumor growth, angiogenesis, metastasis, and survival in a mouse model of colorectal cancer," *Clinical Cancer Research*, vol. 11, no. 4, pp. 1618–1628, 2005.
- [25] A. Janssen, T. J. Maier, S. Schiffmann, et al., "Evidence of COX-2 independent induction of apoptosis and cell cycle block in human colon carcinoma cells after S- or R-ibuprofen treatment," *European Journal of Pharmacology*, vol. 540, no. 1–3, pp. 24–33, 2006.
- [26] F. Khwaja, J. Allen, J. Lynch, P. Andrews, and D. Djakiew, "Ibuprofen inhibits survival of bladder cancer cells by induced expression of the p75^{NTR} tumor suppressor protein," *Cancer Research*, vol. 64, no. 17, pp. 6207–6213, 2004.
- [27] B. J. R. Whittle, "Gastrointestinal effects of nonsteroidal anti-inflammatory drugs," *Fundamental & Clinical Pharmacology*, vol. 17, no. 3, pp. 301–313, 2003.
- [28] G. Dannhardt and W. Kiefer, "Cyclooxygenase inhibitors—current status and future prospects," *European Journal of Medicinal Chemistry*, vol. 36, no. 2, pp. 109–126, 2001.
- [29] V. K. Tammara, M. M. Narurkar, A. M. Crider, and M. A. Khan, "Synthesis and evaluation of morpholinoalkyl ester prodrugs of indomethacin and naproxen," *Pharmaceutical Research*, vol. 10, no. 8, pp. 1191–1199, 1993.
- [30] F. P. Bonina, C. Puglia, T. Barbuzzi, et al., "In vitro and in vivo evaluation of polyoxyethylene esters as dermal prodrugs of ketoprofen, naproxen and diclofenac," *European Journal of Pharmaceutical Sciences*, vol. 14, no. 2, pp. 123–134, 2001.
- [31] S. Chandrasekaran, A. M. Al-Ghananeem, R. M. Riggs, and P. A. Crooks, "Synthesis and stability of two indomethacin prodrugs," *Bioorganic & Medicinal Chemistry Letters*, vol. 16, no. 7, pp. 1874–1879, 2006.
- [32] I. C. Siskou, E. A. Rekkas, A. P. Kourounakis, M. C. Chrysselis, K. Tsiakitzis, and P. N. Kourounakis, "Design and study of some novel ibuprofen derivatives with potential nootropic and neuroprotective properties," *Bioorganic & Medicinal Chemistry*, vol. 15, no. 2, pp. 951–961, 2007.
- [33] C. A. Velázquez, P. N. Praveen Rao, M. L. Citro, L. K. Keefer, and E. E. Knaus, "O²-acetoxymethyl-protected diazeniumdiolate-based NSAIDs (NONO-NSAIDs): synthesis, nitric oxide release, and biological evaluation studies," *Bioorganic & Medicinal Chemistry*, vol. 15, no. 14, pp. 4767–4774, 2007.
- [34] B. Huang, J. Zhang, J. Hou, and C. Chen, "Free radical scavenging efficiency of Nano-Se in vitro," *Free Radical Biology & Medicine*, vol. 35, no. 7, pp. 805–813, 2003.
- [35] J. N. Cheong, C. P. Tan, Y. B. C. Man, and M. Misran, "α-tocopherol nanodispersions: preparation, characterization and stability evaluation," *Journal of Food Engineering*, vol. 89, no. 2, pp. 204–209, 2008.
- [36] S. Shafiq, F. Shakeel, S. Talegaonkar, F. J. Ahmad, R. K. Khar, and M. Ali, "Development and bioavailability assessment of ramipril nanoemulsion formulation," *European Journal of Pharmaceutics and Biopharmaceutics*, vol. 66, no. 2, pp. 227–243, 2007.
- [37] F. Kuo, B. Subramanian, T. Kotyla, T. A. Wilson, S. Yoganathan, and R. J. Nicolosi, "Nanoemulsions of an antioxidant synergy formulation containing gamma tocopherol have enhanced bioavailability and anti-inflammatory properties," *International Journal of Pharmaceutics*, vol. 363, no. 1–2, pp. 206–213, 2008.
- [38] B.-S. Lee, X. Yuan, Q. Xu, et al., "Stimuli-responsive antioxidant nanoprodrugs of NSAIDs," *International Journal of Pharmaceutics*, vol. 372, no. 1–2, pp. 112–124, 2009.
- [39] B. S. Lee, X. Yuan, Q. Xu, et al., "Preparation and characterization of antioxidant nanospheres from multiple α-lipoic acid-containing compounds," *Bioorganic & Medicinal Chemistry Letters*, vol. 19, no. 6, pp. 1678–1681, 2009.
- [40] E. G. Heckert, A. S. Karakoti, S. Seal, and W. T. Self, "The role of cerium redox state in the SOD mimetic activity of nanoceria," *Biomaterials*, vol. 29, no. 18, pp. 2705–2709, 2008.
- [41] K. Bouchemal, S. Briançon, E. Perrier, H. Fessi, I. Bonnet, and N. Zydowicz, "Synthesis and characterization of polyurethane and poly(ether urethane) nanocapsules using a new technique of interfacial polycondensation combined to spontaneous emulsification," *International Journal of Pharmaceutics*, vol. 269, no. 1, pp. 89–100, 2004.
- [42] K. Bouchemal, S. Briançon, E. Perrier, and H. Fessi, "Nanoemulsion formulation using spontaneous emulsification: solvent, oil and surfactant optimisation," *International Journal of Pharmaceutics*, vol. 280, no. 1–2, pp. 241–251, 2004.

- [43] F. Chouinard, F. W. K. Kan, J.-C. Leroux, C. Foucher, and V. Lenaerts, "Preparation and purification of polyisohexylcyanoacrylate nanocapsules," *International Journal of Pharmaceutics*, vol. 72, no. 3, pp. 211–217, 1991.
- [44] H. Fessi, F. Piusieux, J. Ph. Devissaguet, N. Ammoury, and S. Benita, "Nanocapsule formation by interfacial polymer deposition following solvent displacement," *International Journal of Pharmaceutics*, vol. 55, no. 1, pp. R1–R4, 1989.
- [45] J. D. Macklis and R. D. Madison, "Progressive incorporation of propidium iodide in cultured mouse neurons correlates with declining electrophysiological status: a fluorescence scale of membrane integrity," *Journal of Neuroscience Methods*, vol. 31, no. 1, pp. 43–46, 1990.
- [46] M. Weiner and I. L. Bernstein, *Adverse Reactions to Drug Formulation Agents*, Marcel Dekker, New York, NY, USA, 1989.
- [47] S. C. Gad, *Drug Safety Evaluation*, chapter 13.8, John Wiley & Sons, New York, NY, USA, 2002.
- [48] Y. Matsumura and H. Maeda, "A new concept for macromolecular therapeutics in cancer chemotherapy: mechanism of tumorotropic accumulation of proteins and the antitumor agent smancs," *Cancer Research*, vol. 46, no. 12, pp. 6387–6392, 1986.
- [49] P. Couvreur and C. Vauthier, "Nanotechnology: intelligent design to treat complex disease," *Pharmaceutical Research*, vol. 23, no. 7, pp. 1417–1450, 2006.
- [50] F. Yuan, M. Dellian, D. Fukumura, et al., "Vascular permeability in a human tumor xenograft: molecular size dependence and cutoff size," *Cancer Research*, vol. 55, no. 17, pp. 3752–3756, 1995.
- [51] V. P. Torchilin, "Recent advances with liposomes as pharmaceutical carriers," *Nature Reviews Drug Discovery*, vol. 4, no. 2, pp. 145–160, 2005.
- [52] S. K. Hobbs, W. L. Monsky, F. Yuan, et al., "Regulation of transport pathways in tumor vessels: role of tumor type and microenvironment," *Proceedings of the National Academy of Sciences of the United States of America*, vol. 95, no. 8, pp. 4607–4612, 1998.

Research Article

Nanoconjugate Platforms Development Based in Poly(β ,L-Malic Acid) Methyl Esters for Tumor Drug Delivery

José Portilla-Arias,¹ Rameshwar Patil,¹ Jinwei Hu,¹ Hui Ding,¹
Keith L. Black,¹ Montserrat García-Alvarez,² Sebastián Muñoz-Guerra,²
Julia Y. Ljubimova,¹ and Eggehard Holler^{1,3}

¹ Department of Neurosurgery, Maxine Dunitz Neurosurgical Institute, Cedars-Sinai Medical Center, 8631 W. Third Street, Suite 800E, Los Angeles, CA 90048, USA

² Departament d'Enginyeria Química, Universitat Politècnica de Catalunya, ETSEIB, Diagonal 647, 08028 Barcelona, Spain

³ Institut für Biophysik und Physikalische Biochemie, Universität Regensburg, D-93040 Regensburg, Germany

Correspondence should be addressed to José Portilla-Arias, portillaj@cshs.org

Received 29 October 2009; Accepted 21 January 2010

Academic Editor: Chao Lin

Copyright © 2010 José Portilla-Arias et al. This is an open access article distributed under the Creative Commons Attribution License, which permits unrestricted use, distribution, and reproduction in any medium, provided the original work is properly cited.

New copolyesters derived from poly(β ,L-malic acid) have been designed to serve as nanoconjugate platforms in drug delivery. 25% and 50% methylated derivatives (coPMLA-Me₂₅H₇₅ and coPMLA-Me₅₀H₅₀) with absolute molecular weights of 32 600 Da and 33 100 Da, hydrodynamic diameters of 3.0 nm and 5.2 nm and zeta potential of -15 mV and -8.25 mV, respectively, were found to destabilize membranes of liposomes at pH 5.0 and pH 7.5 at concentrations above 0.05 mg/mL. The copolymers were soluble in PBS (half life of 40 hours) and in human plasma (half life of 15 hours) but they showed tendency to aggregate at high levels of methylation. Fluorescence-labeled copolymers were internalized into MDA-MB-231 breast cancer cells with increased efficiency for the higher methylated copolymer. Viability of cultured brain and breast cancer cell lines indicated moderate toxicity that increased with methylation. The conclusion of the present work is that partially methylated poly(β ,L-malic acid) copolyesters are suitable as nanoconjugate platforms for drug delivery.

1. Introduction

Biodegradable polymers are suitable materials for the manufacture of various devices which, because of their biocompatibility, are widely applied in medicine and pharmacology. Examples are poly(lactic acid) and (PLA), poly(glycolic acid) and their copolymers, with a successful 30 years history in surgical settings [1].

The relatively new biopolymer, poly (β ,L-malic acid) (PMLA), is a carboxylic-functionalized polyester that can be produced by either chemical synthesis or biological fermentation from the slime mold *Physarum polycephalum*. Both α - and β -structures, either racemic or optically pure, may be obtained by chemical methods whereas microorganisms exclusively generate PMLA of extremely high optical purity [2, and references therein]. The attractive properties in nanobiotechnology and biomedicine are the lack of in vitro

and in vivo toxicity and non-immunogenicity. PMLA is a completely biodegradable polymer that is metabolized to water and carbon dioxide in the citric acid cycle. It is biocompatible with regard to its limited stability in the bloodstream thus prohibiting physiologically adverse host responses after injection. It is chemically convenient to handle due to its solubility in water and certain organic solvents and to the reactivity of its pendant carboxylic groups [2–9].

So far, the most advanced application reported for PMLA, is the development of “Polycefin”, a nanoconjugate prototype vehicle for the cellular delivery of antisense oligonucleotides. It consists of PMLA that harbors antisense morpholino oligonucleotides and several biochemically functional units which are chemically conjugated with the carboxyl groups. These functional units are tumor-specific antibodies that promote receptor-mediated endosomal

uptake by the tumor cells, a unit that allows the vehicle to escape from the endosomal vesicles into the cytoplasm and another unit that, after cleavage, releases free oligonucleotides. This nanoconjugate can carry several antisense oligonucleotides or other drugs at the same time and also simultaneously several antibodies, which can bind specifically to cell surface antigens during drug delivery [5–9].

Both synthetic and biosynthetic polymeric acids are spontaneously or enzymatically degraded in aqueous environment (see review [2]). Regardless of chirality, degradation is moderate at physiological pH and proceeds rapidly in acidic (pH < 5) and basic (pH > 9) solutions [2] by random scission of the main chain ester bonds to yield malic acid as the final degradation product [10]. By chemical blocking of the pendant carboxylic groups, the properties of PMLA could be changed to slow down its hydrolysis rate. Methylation with diazomethane has proven to be an efficient method that produced poly(α -methyl β ,L-malic acid) (PMLA-Me) without significant cleavage of the polyester backbone [11, 12]. While low degrees of methylation resulted in water soluble products, 75% methylation of pendant carboxyl groups allowed formulation of stable, water insoluble nanoparticles that could be loaded with proteins for delivery applications [13].

The soluble PMLA methyl esters containing 25% and 50% of methylated carboxylic side groups (coPMLA-Me₂₅H₇₅ and coPMLA-Me₅₀H₅₀) are characterized here by investigating their light scattering properties, their degradation in human plasma and their cytotoxicity for several human cancer cell lines to be used as nanoplatfoms for drug delivery.

2. Materials and Methods

2.1. PMLA Production. PMLA of microbial origin was used in this work. It was obtained by cultivation of *Physarum polycephalum* and subsequent purification as described in detail elsewhere [14]. The polyacid of NMR purity had a $M_w = 34\,300$ Da and a polydispersity $M_w/M_n = 1.1$. All chemicals of highest purity, including human plasma, were bought from Merck (Germany) and Sigma-Aldrich (Germany). Organic solvents were of analytical grade and used without further purification. Water used for buffer preparation was double distilled and deionized in a “Milli-Q” system.

2.2. Esterification. Partial esterification of PMLA was performed as described recently by Portilla-Arias et al. [11]. In brief, a solution of diazomethane in ether (12.5 meq) was added to a solution of PMLA in dry acetone (4.3 meq with regard to malic acid units) in different ratios according to the esterification degree to be obtained, and the mixture was left under stirring at room temperature for 1 hour. The reaction mixture was then evaporated under vacuum and the residue was dissolved in a small amount of *N*-methyl-2-pyrrolidone and precipitated with cold diethyl ether. The copolymer was recovered by filtration as a white powder. Yields for coPMLA-Me₂₅H₇₅ and coPMLA-Me₅₀H₅₀

were 97% and 92%, respectively. The ¹H NMR analysis in deuterated water revealed that the conversion actually attained in the copolyesters was 20.2, 46.5, which are pretty close to the nominal values.

2.3. Absolute Molecular Weight, Hydrodynamic Diameter and Zeta Potential Measurements. The copolymers were characterized with respect to their absolute molecular weight (M_w), size and ζ potential using a Malvern Zetasizer Nano (Malvern Instruments, UK). Absolute weight average molecular weight was calculated with a modification of the Rayleigh equation that can be used to generate a Debye plot, which is a linear fit of Kc/R_θ versus concentration according to the equation $Kc/R_\theta = 1/M_w + 2A_2cR_\theta$ is the Rayleigh ratio of scattered to incident light intensity, K is a constant defined by the solvent and analyte dependent refractive index increment ($dn/dc = 0.169$ mL/g for PMLA), Avogadro's number and the solvent refractive index. c is the particle concentration and A_2 is the second virial coefficient [15]. The intercept obtained from the Debye plot is equal to the inverse of the molecular weight and the slope is twice the second virial coefficient.

The size was calculated on the basis of noninvasive backscattering (NIBS) measurements using the Stokes-Einstein equation, $d(H) = kT/3\pi\eta D$. $d(H)$ is the hydrodynamic diameter, D the translational diffusion coefficient, k Boltzmann's constant, T absolute temperature and η the viscosity. The diameter that is measured in DLS (Dynamic Light Scattering) refers to the particle diffusion within a fluid and is referred to as the hydrodynamic diameter corresponding to the diameter of a sphere that has the same translational diffusion coefficient as the particle [16]. The ζ potential was calculated from the electrophoretic mobility based on the Helmholtz-Smoluchowski formula, using electrophoresis M3-PALS. All calculations were carried out by the Zetasizer 6.0 software. For the molecular weight determination, 5 solutions of the copolymers in phosphate buffered saline (PBS, pH 7.4) were generated by serial dilution starting with 4 mg/mL. For the measurement of the ζ potential, the concentration of the sample was 2 mg/mL dissolved in water containing 10 mM NaCl, and the voltage applied was 150 V. For the particle size measurements, the solutions were prepared in PBS at a concentration of 2 mg/mL, filtered through a 0.2 μ m pore membrane. All the copolymer solutions were prepared immediately before analysis at 25°C. Data represent the mean \pm standard deviation obtained for three measurements.

2.4. Copolyesters Stability in PBS and Human Plasma. The degradation essays in human plasma were carried out at 37°C with a polymer concentration of 1 mg/mL. The sample vials were sealed to avoid evaporation and stored at 37°C in an incubator. For the isolation from the plasma, aliquots of 1 mL were extracted with 5 mL of chloroform/ethyl acetate (1:1 v/v). The copolyester contained in the organic phase was dried and redissolved in PBS and the M_w measured by sec-HPLC (Calibrated with polystyrene sulphonate-sodium salt standards). Sample preparation with the polymers of known M_w verified that the isolation had no effect on

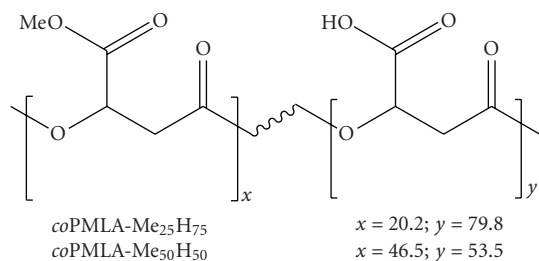


FIGURE 1: Chemical structure of copolyesters studied in the present work with indication of their contents in methylated and free-carboxyl malic units.

molecular weights. For comparison, the degradation study was performed in PBS (pH 7.4) at a concentration of 1 mg/mL for each copolymer. Chromatography was performed on a Hitachi analytical Elite LaChrom HPLC-UV system and size exclusion column BioSep-SEC-S 3000 column (300 × 7.80 mm) following the elution at 220 nm wavelength. Molecular weights $M_w(t)$ were plotted as a function of degradation time with reference to $M_w(t = 0)$ at zero incubation time.

2.5. Cell Lines and Culture Conditions. Primary glioma cell lines—U-87 MG and T98G—and invasive breast carcinoma cell lines—MDA-MB-231 and MDA-MB-468—were obtained from American Type Culture Collection (ATCC) USA. U-87 MG and T98G cells were cultured in MEM supplemented with the following ingredients (final concentrations): 10% fetal bovine serum, 1% MEM NEAA, 1 mM sodium pyruvate and 2 mM L-glutamine. For MDA-MB-231 and MDA-MB-468, Leibovitz's L-15 medium with 10% final concentration fetal bovine serum was used. Cells were seeded at 10,000 cells per well (0.1 mL) in 96-well flat-bottomed plates and incubated overnight at 37°C in humid atmosphere with 5% CO₂ (breast cancer cell lines MDA-MB-231 and MDA-MB-468 were incubated without CO₂).

2.6. Cytotoxicity Test. The copolymers (1 mg/mL and serial dilutions) were dissolved in culture media and incubated with cells for 24 hours. Cell viability was measured using the CellTiter 96 Aqueous One Solution Cell Proliferation Assay kit (Promega Corporation, Cat. No.PR-G3580). Yellow [3-(4,5-dimethylthiazol-2-yl)-5-(3-carboxymethoxyphenyl)-2-(4-sulfophenyl)-2H-tetrazolium, inner salt] (MTS) is bioreduced by cells into formazan that is soluble in the tissue culture medium. The absorbance reading at 490 nm from the 96-well plates was directly proportional to the number of living cells [17]. The viability of the untreated cells was referenced as 100%. The results shown are the means and deviations standard of three independent measurements, calculated with the statistical software GraphPad PRISM 3.0.

2.7. Liposome Leakage Assay. The capability of the copolymers to escape from endosome was measured by the liposome leakage assay. This method generally assumed to represent main features of the endosome membrane and

TABLE 1: Physical properties of copolymers.

	coPMLA-Me ₂₅	coPMLA-Me ₅₀
	H ₇₅	H ₅₀
Methylation ^(a) (%)	20.2	46.5
M_w ^(b)	32,600	33,100
M_n ^(b)	26,100	24,300
T_m ^(c) (°C)	174	172
T_d ^(d) (°C)	186	198
Microstructure ^(e)		
Contiguous patches n^f Me	3.9	11.8
Contiguous patches n^g COOH	11.5	14.5
R	0.3	0.2

^(a)Copolymer composition determined by ¹H NMR; ^(b)Weight- and number-average molecular weight measured by sec-HPLC; ^(c)Melting temperature measured by differential scanning calorimetry; ^(d)Onset decomposition temperature measured at 5% of loss of initial weight; ^(e) n^f and n^g refer to averaged numbers of methylated and free carboxyl group within homogeneous sequences, respectively, and (R) refers the randomness determined by ¹³C NMR analysis [11].

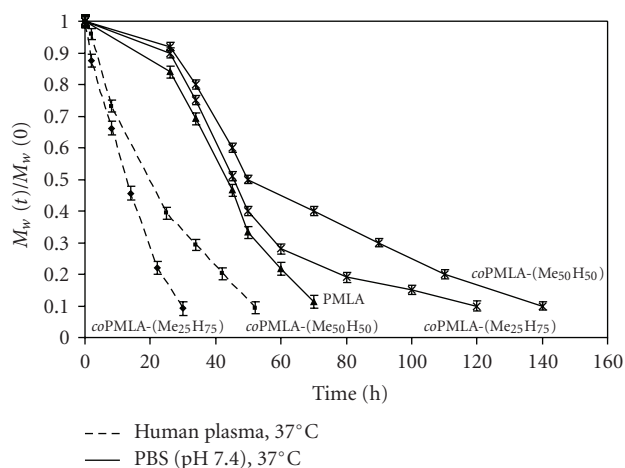


FIGURE 2: Degradation at 37°C in PBS (pH 7.4) and human plasma for PMLA and the copolyesters.

gives similar results as the red blood cell lysis method, because it is less biased by adverse effects of proteins contained in erythrocytes/membranes. Liposome suspensions were prepared by the extrusion method. Briefly, the mixture of egg phosphatidylcholine and cholesterol (molar ratio 2 : 1) dissolved in CHCl₃/MeOH (v/v, 2 : 1) was dried under a stream of nitrogen. The lipid mixture was hydrated with HBS buffer (5 mM HEPES, 150 mM NaCl, pH 7.4) containing 90 mM calcein, followed by 19 extrusions through 0.1 μm polycarbonate membrane using mini-extruder (Avanti Polar Lipids). Serial dilutions were carried out using 95 μL of two buffers of different pH, 137 mM HEPES buffer pH 7.4 and 137 mM citrate buffer pH 5.0. Liposome 5 μL (lipid concentration 200 μM) was added to each sample and the plate was incubated at room temperature for 1 hour. Complete leakage of calcein (100% reference) was achieved with the addition of 0.25% (v/v) Triton-X100 solution of respective buffers.

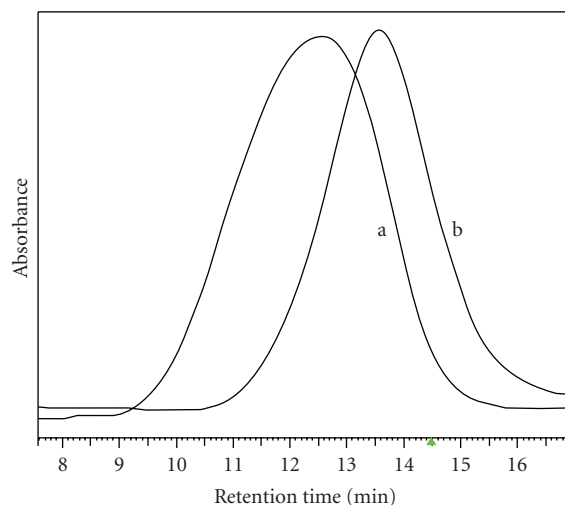


FIGURE 3: Elution profiles obtained by sec-HPLC for *coPMLA-Me₅₀H₅₀* at time zero (a) and after 24 hours of incubation (b) in human plasma at 37°C. Samples were extracted with chloroform/ethylacetate before chromatography (see Section 2).

Fluorescence of released calcein release was measured using excitation wavelength 488 nm and an emission wavelength 535 nm. The results shown are the means and deviations standard of three independent measurements, calculated with the statistical software GraphPad PRISM 3.0.

2.8. Method of Fluorescence Labeling. The copolymers were fluorescence labeled with rhodamine as follows: Pendant carboxyl groups of copolymer (1 mmol methyl residues) in 1 mL of dimethyl formamide (DMF) were activated with a mixture of *N*-hydroxysuccinimide (NHS, 1 mmol) and dicyclohexylcarbodiimide (DCC, 1 mmol) dissolved in 2 mL of DMF at room temperature for 3–4 hours under vigorous stirring. 2-Mercapto-1-ethylamine (0.1 mmol) and 0.1 mmol of dithiothreitol (DTT), were added and the reaction was completed in 30–40 minutes. After 30 minutes of stirring in 6 mL of water at room temperature, the mixture was centrifuged and the clear supernatant passed over Sephadex G10 columns in water. The product containing fractions were freeze dried yielding a white powder. Rhodamine Red C₂ maleimide (40 μ L of 1 mg/mL solution in DMF) was added to 2 mg of activated copolymer dissolved in 2 mL of PBS of pH 5.5 and stirred for 3 hours at room temperature. The fluorescent polymers were purified over Sephadex PD-10 columns pre-equilibrated with PBS (pH 7.4).

2.9. Fluorescence Microscopy. MDA-MB-231 cells were seeded into the microscopic chamber slide. For fluorescence microscopy study, cells were incubated with rhodamine-labeled-polymer (1 mg/mL) in fetal bovine serum (FBS) free medium for 3 hours. The stained cells were washed with PBS and fixed in 4% paraformaldehyde (PFA) for 15 minutes. Then the cells were counterstaining with DAPI to visualize the nuclei and observed under a DM6000 Leica fluorescence microscope (Wetzlar, Germany). The amount of polymer

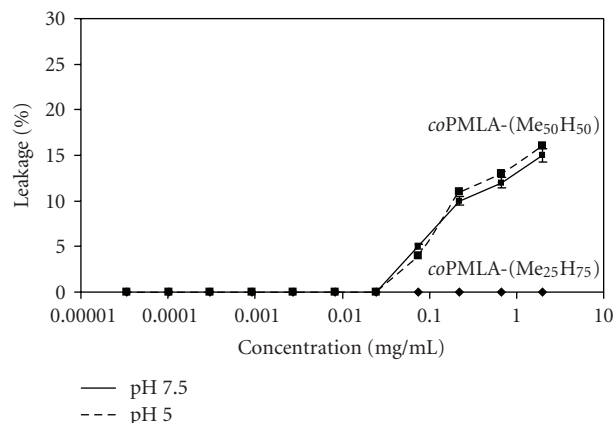


FIGURE 4: Liposome leakage at pH 5.0 and 7.5 and 37°C. 100% leakage is obtained after the addition of 0.25% Triton X100.

uptake was calculated from the rhodamine fluorescence intensity, with subtracted background and divided by the area of the cell under study using the Image J1.43c software from NIH (values averaged over >50 cells). The experiment was done by triplicate, with three independent preparations of cells. Mean and deviation standard were calculated with the statistical software GraphPad PRISM 3.0.

3. Results and Discussion

3.1. Chemical Characterization. Partially methylated poly(β -L-malic acid) copolymers were synthesized in high yield and purity by the diazomethane in acetone method. The two products are denoted as *coPMLA-Me₂₅H₇₅* and *coPMLA-Me₅₀H₅₀*, their chemical formulae are depicted in Figure 1 and their properties are shown in Table 1. The degree of methylation attained in the two cases (20.2 and 46.5%) in the reaction was close to the input ratio of diazomethane to total carboxylic acid (25 and 50%). Molecular weights of M_w (weight-average) = 32,600 Da and 33,100 Da with polydispersity indexes (M_w/M_n) of 1.3 and 1.1, respectively, were determined by sec-HPLC for the two copolyesters which are values comparable to those measured for the original polymalic acid ($M_w = 34\,300$, $M_w/M_n = 1.1$). The slightly decrease in M_w and increase in polydispersity observed after methylation suggest partial cleavage during the chemical synthesis. The ¹³C-NMR analysis revealed that the distribution of methyl groups along the copolyesters chain is not random. The average number of contiguous methylated carboxylic groups indicated hydrophobic patches as opposed to regions with contiguous free carboxyl groups and interdispersed free/methylated carboxyl groups. As expected, the length of hydrophobic sequences was larger for the polymer with the higher degree of methylation.

3.2. Absolute Molecular Weight, Hydrodynamic Diameter and Zeta Potential. The values for absolute weight averaged molecular weight, particle size and zeta potential of the resulting copolyesters together with PMLA are shown in Table 2. The values of molecular weight and polydispersity

TABLE 2: Light scattering and zeta potential measurements.

	PMLA	<i>co</i> PMLA-Me ₂₅ H ₇₅	<i>co</i> PMLA-Me ₅₀ H ₅₀
Molecular weight (Da)	34,200	30,100	31,900
Polydispersity index	1.1	1.22	1.41
2nd virial coefficient A_2 (mL · mol/g ²)	6.50E-05	2.85E-05	3.50E-08
Hydrodynamic diameter (nm)	3.4 (±0.1)	3.0 (±0.1)	5.2 (±0.1)
Zeta potential (mV)	-22.9 (±1.7)	-15 (±1.1)	-8.25 (±1.3)

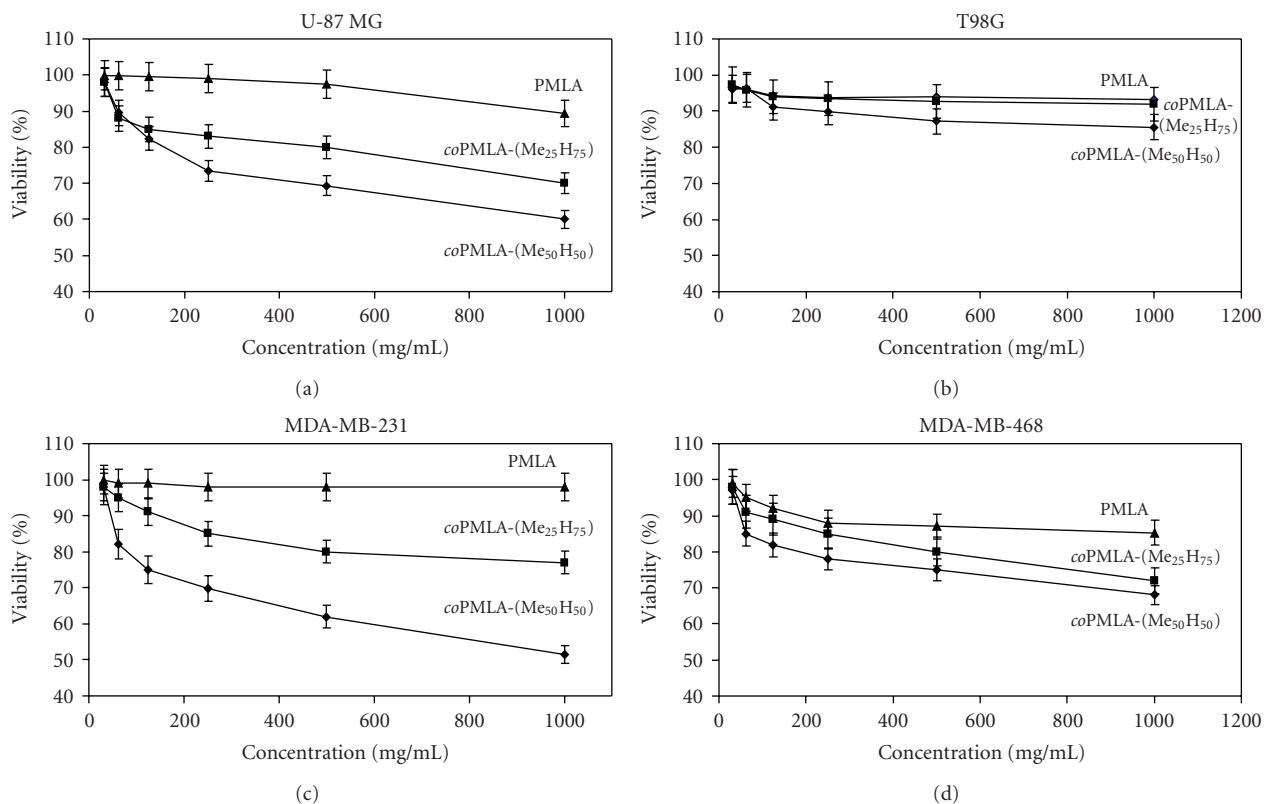


FIGURE 5: Cell viability of cultured cells after 24 hours incubation at 37°C for different cell lines in the presence of the indicated polyesters.

found by DLS are similar to those obtained by GPC (see Table 1) and corroborate the notion that some cleavage occurred during synthesis. While the hydrodynamic diameter does not follow a clear trend upon methylation, the second virial coefficient A_2 and the ζ -potential correlate well with the degree of methylation. The second virial coefficient is a parameter describing the interaction strength between the molecule and the solvent [16]. The relatively high values obtained for PMLA and *co*PMLA-Me₂₅H₇₅ indicate the ability of these polymers to stay in solution, whereas the much lower value obtained for *co*PMLA-Me₅₀H₅₀ indicates that this copolymer has some tendency for aggregation. The conclusion is corroborated by the progressive decrease of negative ζ -potential observed for increasing methylation, that is, less repulsion and thus higher tendency for aggregation.

The effects of esterification on solubility are both an increase in hydrophobicity and a decrease in electrostatic mutual repulsion between polymers at higher degrees of

methylation. The blocky microstructure of the copolymer harboring highly hydrophobic domains of contiguously methylated units could contribute to aggregation by favoring intermolecular hydrophobic contacts. The polyacid is highly soluble in water and acetone, *co*PMLA-Me₅₀H₅₀ is less soluble in water than *co*PMLA-Me₂₅H₇₅, and *co*PMLA-Me₇₅H₂₅ (not studied here) has been reported to be water insoluble [11].

3.3. Copolyesters Degradation in PBS and Human Plasma.

Copolyester degradation was followed by measuring molecular weights M_w by sec-HPLC as a function of incubation time (Figure 2). During incubation in PBS (pH 7.4) at 37°C the polymers were slowly degraded as indicated by an increase in the retention time [11]. The measurements for degradation in serum at 37°C were complicated by the presence of proteins which co-eluted and interfered with the polymers in sec-HPLC, rendering polymer detection impossible. The degraded polyesters except PMLA could be separated from

proteins by extraction of the plasma mixture with chloroform/ethyl acetate. As an example the chromatograms of *coPMLA-Me₅₀H₅₀* incubated in serum at time zero (a) and after incubation (b) are compared in Figure 3. This case once more demonstrates the degradability of PMLA and its derivatives in physiological conditions. Specific PMLA hydrolases have been reported for microorganisms [18, 19]. As in the case of degradation in PBS (not shown), the elution profile indicated a single peak. This suggested cleavage from the ends and not fragmentation at internal cleavage sites.

Comparison of kinetics in Figure 2 revealed that (i) degradation in human plasma was faster than in PBS with half lives of 13 h in plasma for *coPMLA-Me₂₅H₇₅* and 20 hours for *coPMLA-Me₅₀H₅₀* compared with 45 hours and 50 hours in PBS, respectively and (ii) Half life was lowest for PMLA and increased with higher levels of methylation in agreement with the notion that alkylation of the α -carboxyl group stabilized the main chain ester bond. Hydrolysis was significantly enhanced by constituents of human plasma, either by general catalysis or by hydrolytic enzymes, most likely esterases, such as plasma lipases or cholinesterases [20].

3.4. Membrane Disruption. The membrane disruption activity of *coPMLA-Me₂₅H₇₅* and *coPMLA-Me₅₀H₅₀* was measured by the phosphatidylcholine liposome leakage assay. The liposomes are filled with calcein, which leaks out if the liposome becomes destabilized or disrupted. Leakage was measured at pH 7.5, resembling physiological pH, and at pH 5.0, resembling pH of late endosomes/lysosomes. While *coPMLA-Me₂₅H₇₅* did not show leakage activity, *coPMLA-Me₅₀H₅₀* was active at concentrations above 0.1 mg/mL and the activity was pH independent (Figure 4). The finding suggested that membrane leakage was inferred by methylation of pendant carboxyl groups that increased hydrophobicity and neutralized negative charges (decrease in ζ -potential, Table 2). The absence of effect of pH change indicated that the carboxylic groups of the methylated PMLA did not protonate in this pH range, or if they did, they had no effect on the leakage activity.

The role of hydrophobicity together with charge neutralization has been considered in drug delivery to be the mechanism for membrane disruption by a variety of molecular devices [21–25]. In the case of our methylated PMLA we think that the methylation dependent leakage refers mainly to the formation of the contiguous, electrically neutral hydrophobic patches (Table 2) which are prone to intrude into the lipid bilayer and cause the membrane damage. The membrane disruption activity especially *coPMLA-Me₅₀H₅₀* is thought to be useful in the design of nanoconjugates that can deliver drugs to intracellular targets.

3.5. Cytotoxicity. Partially methylated PMLA contains carboxylic groups that can be conjugated to several prodrugs and in addition to a variety of biologically active units such as antibodies for targeting or PEG for protection against enzymatic degradation and resorption by the reticuloendothelial system (RES). The pro-drug is activated within the targeted

cell compartment and only then unfolds its cytotoxic or any other activity.

It is desirable to know whether methylated PMLA as the platform is itself not toxic. To this end, the in vitro toxicity of the copolymers was tested. Figure 5 shows the viability of cultured brain and breast cancer cells: T98G, U-87 MG, MDA-MB-231 and MDA-MB-468 cells after 24 hours of incubation as a function of copolymer concentrations.

While PMLA only marginally decreased cell viability, the copolymers showed toxicity that increased with the degree of methylation, but the decrease in percentage cell viability was moderate and above 50% at concentrations ≤ 1 mg/mL. Effects on cell viability depended also on the type of cell line, glioma U-87 MG cells, and breast cancer MDA-MB-231 cells being more affected than glioma T98G cells and breast cancer MDA-MB-468 cells.

There are two main toxicity mechanisms commonly considered: (i) toxicity due to physical damage such as destabilization of membranes and (ii) toxicity resulting from the degradation products after intracellular uptake. The possibility of physical damage due to membrane disruption of the kind as seen by the liposome leakage assay (Figure 5) may not be significant since the effect of copolymers on cell viability is not manifested in the time scale of minutes or a few hours (results not shown). It is highly likely that toxicity was the result of methanol formation during degradation. It is known that degradation in pure deuterated water generates as main products methanol and L-malic acid [11]. While L-malic acid is converted into water and carbon dioxide in the tricarboxylic acid cycle, methanol is known to be toxic for living cells. In the same line it has been reported that benzylesters of PMLA were toxic due to release of free benzylalcohol during degradation [26]. However, for consideration of the copolymer application in drug delivery, the short residence times of only a few hours before complete clearance through the renal system relates their toxicity in vivo.

3.6. Cellular Uptake Study. Since we have found that the copolymers *coPMLA-Me₂₅H₇₅* and *coPMLA-Me₅₀H₅₀* contained hydrophobic patches that could be active in membrane disruption, it was important to test whether the polymers could enter cells in vitro. Rhodamine labeled copolymers were incubated with MDA-MB-231 cells for 3 hours. The cell's uptake of the fluorescent polymers was seen under the fluorescence microscope (Figure 6). Rhodamine alone did not stain the cells (picture not shown). The distribution of copolymers-rhodamine in all cells, appeared to be homogeneous and probably involved nuclei. The fluorescence intensity was semi quantitatively measured by triplicate in >50 cells, and appeared to be 1.8 (Standard Deviation = ± 0.3) folds more intensive for *coPMLA-Me₅₀H₅₀* than for *coPMLA-Me₂₅H₇₅* accordingly to the Image J1.43c software, thus correlating with the higher degree of hydrophobicity of the higher methylated polymer. The results are evidences that the copolymers are highly versatile materials and suitable for various applications.

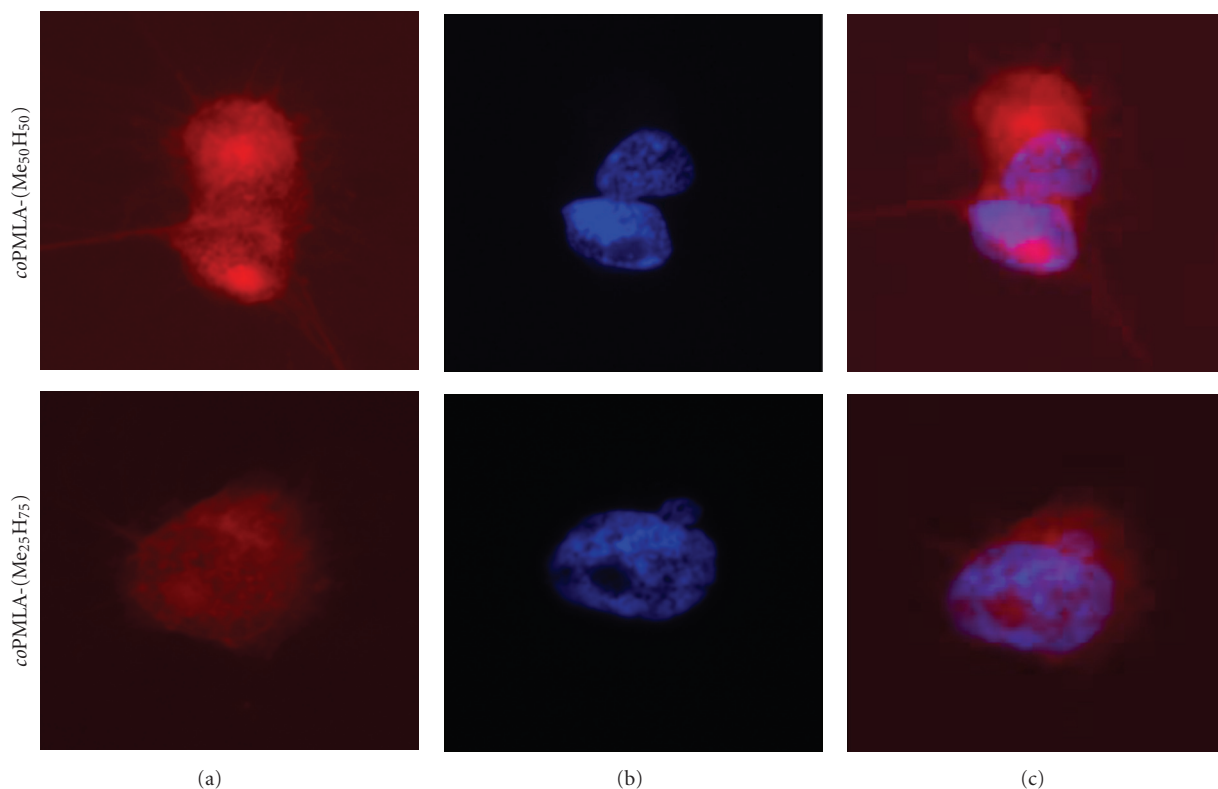


FIGURE 6: Localization of rhodamine tagged copolymers in MDA-MB-231 cells. Panels (a) and (b) separated copolymer-rhodamine uptake and DAPI staining. Panel (c) The copolymers are indicated by red fluorescence co-localizing with nuclei stained in blue with DAPI.

4. Conclusion

New designs of nanoconjugate drug delivery systems are introduced here. The systems involve a polymer platform containing pendant chemically reactive groups to be conjugated with molecular units that function in pro-drug attachment, cell recognition, membrane penetration and protection. The copolymers *coPMLA-Me₂₅H₇₅* and *coPMLA-Me₅₀H₅₀* are biodegradable and biocompatible and its half-life is limited, so they may minimize adverse host's responses and development of liver storage diseases. The copolymers are endowed with membrane disrupting/penetrating activities which allow them to deliver drugs directly to intracellular targets by passing the plasma membrane. By raising the degree of methylation above 50%, the copolymers become insoluble and can be used as drug delivering nanoparticles. These results support the fact that poly(β ,L-malic acid) is a highly versatile material and can be used for the design of a variety of nanoconjugate platforms for drug delivery systems.

Acknowledgments

The project was funded by grants from NIH/NCI R01 CA123495 to JYL; MAT2006-13209-C02-02 from CICYT (Comisión Interministerial de Ciencia y Tecnología) of Spain to SM and CONACYT-México (Concejo Nacional de Ciencia y Tecnología) for fellow granted to J. Portilla-Arias.

References

- [1] D. Peer, J. M. Karp, S. Hong, O. C. Farokhzad, R. Margalit, and R. Langer, "Nanocarriers as an emerging platform for cancer therapy," *Nature Nanotechnology*, vol. 2, no. 12, pp. 751–760, 2007.
- [2] B.-S. Lee, M. Vert, and E. Holler, "Water-soluble aliphatic polyesters: poly(malic acid)s," in *Biopolymers*, Y. Doi and A. Steinbüchel, Eds., pp. 75–103, Wiley-VCH, Weinheim, Germany, 2002.
- [3] B. Gasslmaier, C. M. Krell, D. Seebach, and E. Holler, "Synthetic substrates and inhibitors of β -poly(L-malate)-hydrolase (polymalataze)," *European Journal of Biochemistry*, vol. 267, no. 16, pp. 5101–5105, 2000.
- [4] B. Gasslmaier and E. Holler, "Specificity and direction of depolymerization of β -poly(L-malate) catalysed by polymalataze from *Physarum polycephalum*—fluorescence labeling at the carboxy-terminus of β -poly(L-malate)," *European Journal of Biochemistry*, vol. 250, no. 2, pp. 308–314, 1997.
- [5] B.-S. Lee, M. Fujita, N. M. Khazenzon, et al., "Polycefin, a new prototype of a multifunctional nanoconjugate based on poly(β -L-malic acid) for drug delivery," *Bioconjugate Chemistry*, vol. 17, no. 2, pp. 317–326, 2006.
- [6] M. Fujita, N. M. Khazenzon, A. V. Ljubimov, et al., "Inhibition of laminin-8 in vivo using a novel poly(malic acid)-based carrier reduces glioma angiogenesis," *Angiogenesis*, vol. 9, no. 4, pp. 183–191, 2006.
- [7] M. Fujita, B.-S. Lee, N. M. Khazenzon, et al., "Brain tumor tandem targeting using a combination of monoclonal antibodies attached to biopoly(β -L-malic acid)," *Journal of Controlled Release*, vol. 122, no. 3, pp. 356–363, 2007.

- [8] J. Y. Ljubimova, M. Fujita, N. M. Khazenzon, et al., "Nanoconjugate based on poly(malic acid) for tumor targeting," *Chemico-Biological Interactions*, vol. 171, no. 2, pp. 195–203, 2008.
- [9] J. Y. Ljubimova, M. Fujita, A. V. Ljubimov, V. P. Torchilin, K. L. Black, and E. Holler, "Poly(malic acid) nanoconjugates containing various antibodies and oligonucleotides for multi-targeting drug delivery," *Nanomedicine*, vol. 3, no. 2, pp. 247–265, 2008.
- [10] C. Braud and M. Vert, "Degradation of poly(β -malic acid)-monitoring of oligomers formation by aqueous SEC and HPCE," *Polymer Bulletin*, vol. 29, no. 1-2, pp. 177–183, 1992.
- [11] J. A. Portilla-Arias, M. García-Álvarez, A. M. de Ilarduya, E. Holler, J. A. Galbis, and S. Muñoz-Guerra, "Synthesis, degradability, and drug releasing properties of methyl esters of fungal poly(β , L-malic acid)," *Macromolecular Bioscience*, vol. 8, no. 6, pp. 540–550, 2008.
- [12] C. E. Fernandez, M. Mancera, E. Holler, J. J. Bou, J. A. Galbis, and S. Muñoz-Guerra, "Low-molecular-weight poly(α -methyl β ,L-malate) of microbial origin: synthesis and crystallization," *Macromolecular Bioscience*, vol. 5, no. 2, pp. 172–176, 2005.
- [13] J. A. Portilla-Arias, M. García-Álvarez, J. A. Galbis, and S. Muñoz-Guerra, "Biodegradable nanoparticles of partially methylated fungal poly(β -L-malic acid) as a novel protein delivery carrier," *Macromolecular Bioscience*, vol. 8, no. 6, pp. 551–559, 2008.
- [14] E. Holler, *Handbook of Engineering Polymeric Materials*, vol. 997, Marcel Dekker, New York, NY, USA, 1997.
- [15] P. C. Hiemenz, "Light scattering by polymer solutions," in *Polymer Chemistry: The Basic Concepts*, p. 659, Marcel Decker, New York, NY, USA, 1984.
- [16] (ISO), I. O. f. S., "Methods for Determination of Particle Size Distribution Part 8: Photon Correlation Spectroscopy," International Standard ISO13321, 1996.
- [17] T. Mosmann, "Rapid colorimetric assay for cellular growth and survival: application to proliferation and cytotoxicity assays," *Journal of Immunological Methods*, vol. 65, no. 1-2, pp. 55–63, 1983.
- [18] C. Korherr, M. Roth, and E. Holler, "Poly(β -L-malate) hydrolase from plasmodia of *Physarum polycephalum*," *Canadian Journal of Microbiology*, vol. 41, supplement 1, pp. 192–199, 1995.
- [19] K. Rathberger, H. Reisner, B. Willibald, H.-P. Molitoris, and E. Holler, "Comparative synthesis and hydrolytic degradation of poly (L-malate) by myxomycetes and fungi," *Mycological Research*, vol. 103, no. 5, pp. 513–520, 1999.
- [20] F. M. Williams, "Clinical significance of esterases in man," *Clinical Pharmacokinetics*, vol. 10, no. 5, pp. 392–403, 1985.
- [21] S. R. Tonge and B. J. Tighe, "Responsive hydrophobically associating polymers: a review of structure and properties," *Advanced Drug Delivery Reviews*, vol. 53, no. 1, pp. 109–122, 2001.
- [22] C. Kusunwiriawong, P. van de Wetering, J. A. Hubbell, H. P. Merkle, and E. Walter, "Evaluation of pH-dependent membrane-disruptive properties of poly(acrylic acid) derived polymers," *European Journal of Pharmaceutics and Biopharmaceutics*, vol. 56, no. 2, pp. 237–246, 2003.
- [23] M.-A. Yessine, M. Lafleur, C. Meier, H.-U. Petereit, and J.-C. Leroux, "Characterization of the membrane-destabilizing properties of different pH-sensitive methacrylic acid copolymers," *Biochimica et Biophysica Acta*, vol. 1613, no. 1-2, pp. 28–38, 2003.
- [24] M.-A. Yessine and J.-C. Leroux, "Membrane-destabilizing polyanions: interaction with lipid bilayers and endosomal escape of biomacromolecules," *Advanced Drug Delivery Reviews*, vol. 56, no. 7, pp. 999–1021, 2004.
- [25] R. Chen, S. Khormae, M. E. Eccleston, and N. K. H. Slater, "The role of hydrophobic amino acid grafts in the enhancement of membrane-disruptive activity of pH-responsive pseudo-peptides," *Biomaterials*, vol. 30, no. 10, pp. 1954–1961, 2009.
- [26] M. E. Martinez Barbosa, S. Cammas, M. Appel, and G. Ponchel, "Investigation of the degradation mechanisms of poly(malic acid) esters in vitro and their related cytotoxicities on J774 macrophages," *Biomacromolecules*, vol. 5, no. 1, pp. 137–143, 2004.

Research Article

Controlled Release of Doxorubicin from Doxorubicin/ γ -Polyglutamic Acid Ionic Complex

Bhavik Manocha and Argyrios Margaritis

Department of Chemical and Biochemical Engineering, The University of Western Ontario, London, ON, Canada N6A 5B9

Correspondence should be addressed to Argyrios Margaritis, amarg@uwo.ca

Received 6 November 2009; Accepted 19 February 2010

Academic Editor: Chao Lin

Copyright © 2010 B. Manocha and A. Margaritis. This is an open access article distributed under the Creative Commons Attribution License, which permits unrestricted use, distribution, and reproduction in any medium, provided the original work is properly cited.

Formation of drug/polymer complexes through ionic interactions has proven to be very effective for the controlled release of drugs. The stability of such drug/polymer ionic complexes can be greatly influenced by solution pH and ionic strength. The aim of the current work was to evaluate the potential of γ -polyglutamic acid (γ -PGA) as a carrier for the anticancer drug, Doxorubicin (DOX). We investigated the formation of ionic complexes between γ -PGA and DOX using scanning electron microscopy, spectroscopy, thermal analysis, and X-ray diffraction. Our studies demonstrate that DOX specifically interacts with γ -PGA forming random colloidal aggregates and results in almost 100% complexation efficiency. In vitro drug release studies illustrated that these complexes were relatively stable at neutral pH but dissociates slowly under acidic pH environments, facilitating a pH-triggered release of DOX from the complex. Hydrolytic degradation of γ -PGA and DOX/ γ -PGA complex was also evaluated in physiological buffer. In conclusion, these studies clearly showed the feasibility of γ -PGA to associate cationic drug such as DOX and that it may serve as a new drug carrier for the controlled release of DOX in malignant tissues.

1. Introduction

The efficacy of cancer chemotherapy is limited by its toxicity to healthy tissues. This is partially attributed to the lack of specificity of anticancer agents for cancerous tissues, and partially to the poor biopharmaceutical properties of the drug [1]. Both these factors together dictate the success of chemotherapy. Most of the anticancer agents are administered as intravenous injections/infusions which lead to an initial burst release and subsequent decay of drug concentrations, below therapeutic levels in blood. The success of controlled or sustained release drug formulations has proved that long-term exposure of ailing tissues to moderate drug concentrations is more beneficial than a pulsed supply of the drug at higher concentrations [1, 2]. The limitations associated with conventional anticancer drug formulations have led to numerous attempts in developing more effective formulations for chemotherapy [1–3].

Doxorubicin (DOX), an anthracycline antibiotic, is a widely used antineoplastic agent; however, its therapeutic efficacy is limited because of the dose-dependent cardiotoxi-

city, myelosuppression [4, 5], and development of multidrug resistance [6]. Such adverse side effects associated with conventional formulations of DOX have led researchers to investigate alternative forms of administering DOX, for example, prodrug approach or binding/encapsulation in particulate carriers [7–10].

DOX association to nanoparticulate carriers such as liposomes [11], nanoparticles [12], or micelles [13] has led to its controlled release over extended periods of time, thereby increasing its efficacy and reducing toxic side effects. The majority of attempts to associate DOX to polymeric nanoparticles have used either anionic or neutral polymers, such as polyacrylates [14] or pullulan [15], respectively. Anionic polymers exploit the charge interactions with cationic DOX to achieve high association or complexation efficiencies. Despite of such high association, the DOX-loaded nanoparticles exhibit negative zeta potential, which impedes their adhesion to cell membranes and hence their cell uptake. To overcome this limitation, the negatively charged nanoparticles are coated with a cationic polymer/lipid layer [16]. In an alternate approach, Janes et al.

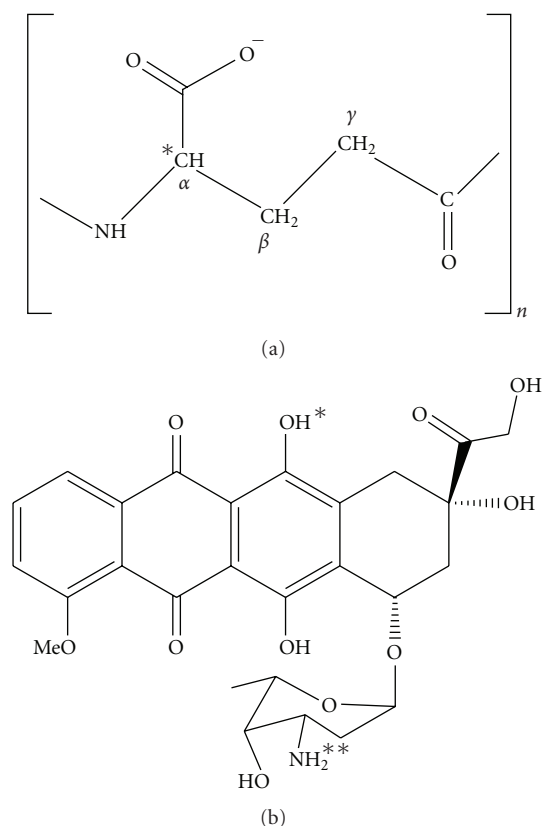


FIGURE 1: Chemical structures of (a) γ -Polyglutamic Acid and (b) Doxorubicin. In (b), *Deprotonable functional group, **Protonable functional group.

[7] illustrated the ionic complexation of DOX to a positively charged polymeric carrier, chitosan. Although DOX binding to chitosan was very low (1.4% w/w), the DOX-loaded chitosan nanoparticles entered the cell via endocytosis, releasing DOX intracellularly.

Carboxyl groups have the ability to form strong ionic interactions with desired drug candidates because they are excellent hydrogen bond donors [17]. Anionic polymers, owing to their high negative-charge density can bind substantial amounts of cationic drugs. Such an association based on ionic/electrostatic interactions is termed as polymer/drug complexation, and the complex formed is termed as polyelectrolyte complexes. The activity, solubility, cell permeability, and stability of drugs can be manipulated by using polymers with different chemical and physical properties. For instance, pH-induced degradation of basic drug procaine was markedly improved by ion pairing it with acidic polyelectrolyte, carbomer, thereby improving its aqueous chemical stability [18]. Guo et al. [19] demonstrated the controlled release of coenzyme A from pH-sensitive ionic complexes of chitosan/carboxymethyl chitosan. Recently, low molecular weight γ -PGA was used as an excipient to form complex with a bitter tasting drug, diphenhydramine. The complex not only improved the drug stability and masked its bitter taste, but also facilitated its sustained drug release [20].

Gamma-polyglutamic acid (γ -PGA) is a homopolyamide of glutamic acid monomers, connected by amide linkages between α -amino and γ -carboxyl groups (Figure 1(a)). The presence of a free α -carboxylate anion per glutamic acid monomer imparts a high anionic character to γ -PGA, making it a potential candidate to achieve high association efficiencies with cationic drugs. These side-chain carboxyl groups also offer attachment points for the conjugation of chemotherapeutic agents to the polymeric carrier [21]. γ -PGA is produced as a capsular material or slime by several *Bacillus* species and is a water-soluble, biodegradable, and biocompatible polymer. γ -PGA is nontoxic and nonimmunogenic and can be easily assimilated in vivo, rendering it a potential biomaterial for various drug delivery applications, such as nanoparticulate drug/gene carriers, hydrogels, and tissue scaffolds [3, 22, 23].

The aim of this work was to investigate the use of carboxyl-group-containing polymer, γ -PGA, to form ionic complexes with a cationic anticancer drug, DOX. The specific interactions between γ -PGA and DOX to form stable ionic complexes were investigated. The pH-controlled release of DOX from DOX/ γ -PGA complex and hydrolytic degradation of polymer and drug/polymer complex were also investigated in vitro.

2. Materials and Methods

2.1. Materials. Gamma-polyglutamic acid (HM-form; 125 kDa by GPC) was a gift from Natto Biosciences (Montreal, Canada). Doxorubicin hydrochloride was obtained as a 2 mg/mL solution (pH 3.0) in 0.9% (w/v) sodium chloride from Novopharm (Toronto, Canada). Unless otherwise mentioned, all other chemicals were reagent grade and purchased from Sigma Aldrich (Toronto, Canada). All the glasswares used were pre-treated with SylonCT (5% dimethyldichlorosilane in toluene; Sigma Aldrich, Toronto, Canada).

2.2. Formation of DOX/ γ -PGA Complex. Predetermined amounts of DOX were added to aqueous solutions of γ -PGA (10 mg/mL; pH 7, nonbuffered) to obtain six different DOX: γ -PGA weight ratios (1:200, 1:100, 1:10, 1:1, 2:1, and 3:1). The DOX/ γ -PGA mixtures were left under magnetic stirring at room temperature for 24 hours, dialyzed against deionized water (500 mL) for 24 hours (Spectrapor membrane tubing; MWCO 6–8 kDa, Spectrum Labs, CA, USA), and then freeze-dried overnight. DOX/ γ -PGA complexes that showed instantaneous precipitation were collected by centrifugation (11,000 \times g for 10 minutes), washed twice with deionized water, and then freeze-dried.

All the procedures were performed in triplicates. Photodegradation of DOX was prevented by conducting all experiments in dark.

2.3. Evaluation of DOX Complexation with γ -PGA. DOX/ γ -PGA complexation efficiency was determined by analyzing the unbound DOX in the dialysate, supernatant, and sample washes using HPLC, as described previously [24].

The samples were eluted through Zorbax C18 (250 mm × 4.6 mm, 5 μm) column (Agilent Technologies, Missis-sauga ON), attached to fluorescence detector. The emission and excitation wavelengths were set at 480 and 560 nm, respectively. The mobile phase composition was 70:30 water/acetonitrile with 0.1% triethylamine; pH was adjusted to 3.0 with phosphoric acid. The samples were eluted under isocratic conditions at flow rate 1.2 mL/min and column temperature 35°C.

DOX/γ-PGA complexation efficiency was calculated as follows:

$$\begin{aligned} \text{Dox Encapsulation Efficiency (\%)} \\ = \frac{\text{Total DOX} - \text{Free DOX}}{\text{Total DOX}} \times 100. \end{aligned} \quad (1)$$

2.4. Physical Characterization of DOX/γ-PGA Complex

2.4.1. Spectrophotometric Analysis. Doxorubicin concentration was maintained constant at 40 μg/mL, and spectra of DOX in the absence and presence of γ-PGA were recorded from 190 to 600 nm using UV-Visible spectrophotometer (Cary 50 Conc, Varian, USA) with a 2 nm slit width and a 1 cm path length at intervals of 1 nm, using water as the baseline reference.

2.4.2. Size and Surface Characteristics of DOX/γ-PGA Complexes. The surface morphology of DOX/γ-PGA complexes was examined using a scanning electron microscope (SEM; Hitachi S-3400N, Toronto, ON). A current of 99 μA, voltage of 15 kV, and a working distance of 9.3 mm were applied. The samples were prepared by placing 5–10 μL of precipitates (diluted 50–100×) on formvar grids and allowed to air-dry overnight under vacuum. All samples were sputtered with Au/Pd (10–12 nm thickness) and consecutive magnifications (1500×, 2000×, and 5000×) were used to view the morphology of formed DOX/γ-PGA complexes.

Particle size and zeta potential measurements of the precipitates were performed by photon correlation spectroscopy (90Plus/BI-MAS) and ZetaPALS Zeta potential analyzer (Brookhaven Instruments, NY), respectively. For size measurements, samples were diluted in MiliQ water and measured for at least 120 seconds. For zeta potential measurements, samples were diluted in 10 mM KNO₃. All the measurements were performed in triplicate.

2.4.3. Thermal Analysis. The differential scanning calorimetry (DSC) thermogram of DOX/γ-PGA complex was recorded using DSC 822e (Mettler Toledo, Columbus, OH) and compared with the thermograms of pure DOX and γ-PGA. The scanning rate was controlled at 10°C/min; the starting and ending temperature were 25 and 500°C, respectively. Thermogravimetric analysis (TGA) was performed using TGA/SDTA 851e (Mettler Toledo, Columbus, OH) with a starting and ending temperatures of 25 and 500°C, respectively.

2.4.4. X-Ray Diffraction Crystallography. The X-ray crystallographic patterns of DOX, γ-PGA, and DOX/γ-PGA complexes were studied using an X-ray diffractometer (Rigaku, Tokyo, Japan). Samples were pressed into circular form on a quartz sample holder, and scanned from 0 to 60°. A Bragg angle of 2θ was recorded at a scan rate of 1.0°/min.

2.4.5. Evaluation of In Vitro DOX Release from DOX/γ-PGA Complex. Effect of ionic strength and pH on drug release was studied in different buffers. DOX/γ-PGA complex (1:1 w/w) was placed in dialysis membrane (Spectrapor membrane tubing; MWCO 6–8 kDa, Spectrum Labs, CA, USA) and immersed in 100 mL of different buffers of varying pHs (154 mM sodium chloride, pH 2.2; 100 mM acetate buffers pH 4.0 and 6.0; 100 mM phosphate buffer saline, pH 7.4), and ionic strengths (77, 154 and 308 mM phosphate buffered saline, pH 7.4). All flasks were incubated at room temperature under mild agitation. Samples were collected at different time intervals. Buffers in all the flasks were replaced every 24 hour. The free DOX released into the dialysate was estimated using fluorescence HPLC and plotted as a function of time to determine drug release kinetics.

2.4.6. Hydrolytic Degradation Studies. A predetermined amounts of γ-PGA and DOX/γ-PGA ionic complex (1:10 w/w) were dissolved in 154 mM phosphate buffer saline, pH 7.4. At specified time intervals, samples were collected and molecular weights were measured by gel permeation chromatography (GPC). The GPC system comprised of Agilent 1200 HPLC system, equipped with two Waters Ultrahydrogel Linear columns in series, a refractive index detector, a UV detector (210 nm), and a column thermostat maintained at 30°C. Phosphate buffer (100 mM, pH 7.4) was used as a mobile phase at a flow rate of 0.8 mL/min. The injection volume of all the samples was maintained constant at 25 μL. Molecular weight calibration was performed with polyethylene glycol/poly (ethylene oxide) standard kit (M_p 500–2,740,000) from Sigma-Aldrich, Canada.

The weight average molecular weight (M_w) of polymer was plotted as a function of time to estimate the polymer degradation kinetics.

3. Results and Discussion

The main aim of this work was to develop γ-PGA-based colloidal carrier for anticancer drug, DOX. Because of high negative charge density of γ-PGA, we expected a fairly high association of DOX owing to electrostatic attraction between the polymer and drug.

DOX is predominantly positively charged amphoteric drug, containing protonable amino group in the sugar moiety and two deprotonable phenolic groups in the aglycone part of the molecule (Figure 1(b)). To begin, we tested the extent of DOX:γ-PGA association by incubating DOX and γ-PGA aqueous solutions in different drug/polymer weight ratios, then dialyzing the drug/polymer solution to remove

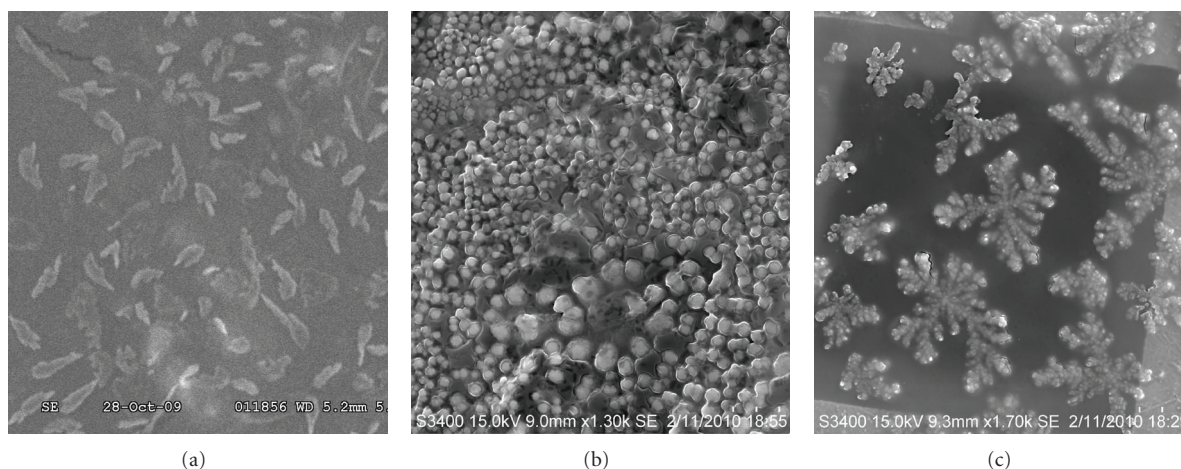


FIGURE 2: SEM images of DOX/ γ -PGA complexes at different DOX:PGA weight ratios: (a) 1:100 w/w (12000 \times); (b) 1:10 w/w (7000 \times); (c) 1:1 w/w (10000 \times).

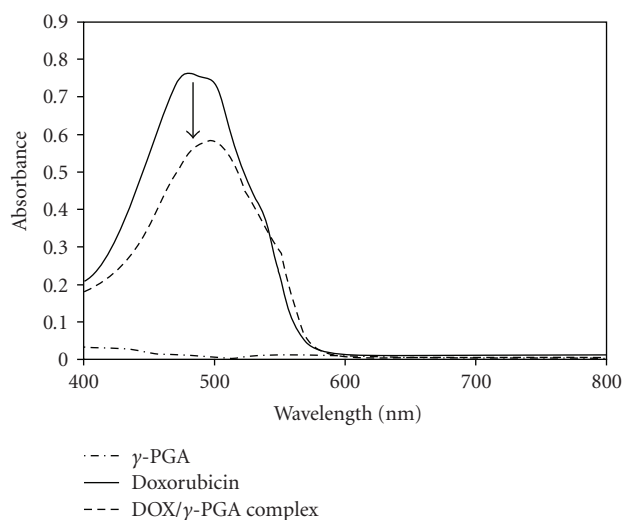


FIGURE 3: Visible spectra of DOX solution, γ -PGA solution, and DOX/ γ -PGA complex.

nonassociated DOX, and lyophilizing to promote polymer-drug interactions. For all the DOX: γ -PGA weight ratios tested, all of the DOX that was added formed complex with γ -PGA, giving the complexation efficiency of almost 100% (Table 1). However, a marked difference in the aqueous solubility of various DOX/ γ -PGA complexes was observed. At lower DOX: γ -PGA weight ratios, no precipitation was observed during the 24-hour reaction time, and the freeze-dried complex was easily dissolved in water. For DOX: γ -PGA 1:1, mild precipitation was observed at the beginning of the reaction; after 24 hours, the complex was collected as a precipitate. The freeze dried 1:1 complex was soluble in water after stirring overnight. In case of 2:1 and 3:1 DOX/ γ -PGA complexes, water insoluble precipitates were formed.

TABLE 1: Complexation efficiencies for DOX/ γ -PGA complexes formed by mixing DOX and PGA in different weight ratios ($n = 3$).

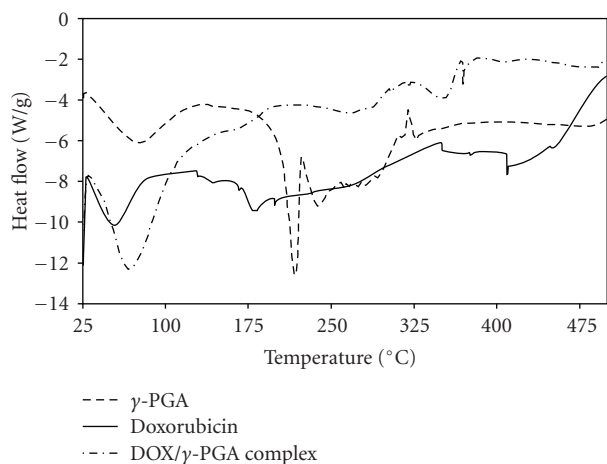
DOX: γ -PGA ratio (w/w)	Complexation efficiency (%)	Aqueous solubility
1:100	99 \pm 0.89	Soluble
1:50	99.3 \pm 1.2	Soluble
1:10	99.7 \pm 2.65	Soluble
1:1	99.1 \pm 0.6	Precipitate
2:1	95.4 \pm 4.1	Precipitate
3:1	96 \pm 6.5	Precipitate

3.1. Size and Surface Characteristics of DOX/ γ -PGA Complexes. SEM micrographs revealed that the formed complexes are submicron-sized random-shaped structures, ranging from elongated needles (Figure 2(a)) to colloidal aggregates (Figures 2(b) and 2(c)). Table 2 shows the size and surface characteristics of various DOX/ γ -PGA complexes, as measured by particle size and zeta potential analyzer. The average particle size of the precipitates was found to be $\sim 80 \mu\text{m}$. Various DOX/ γ -PGA ionic complexes exhibited significantly high negative zeta potential values, and zeta potential of complex decreased with the increase in DOX ratio w.r.t. γ -PGA. As mentioned above, previous studies have shown that nanoparticles with negative zeta potential are most likely rejected by cells owing to charge repulsions between negatively charged cell membranes and particles with negative surface charges. We would like to clarify that DOX/ γ -PGA complexes are not our final intended formulation.

More studies are underway to overcome the negative zeta potential by formulating the DOX/ γ -PGA ionic complexes into polymeric nanoparticles of 100–200 nm diameter.

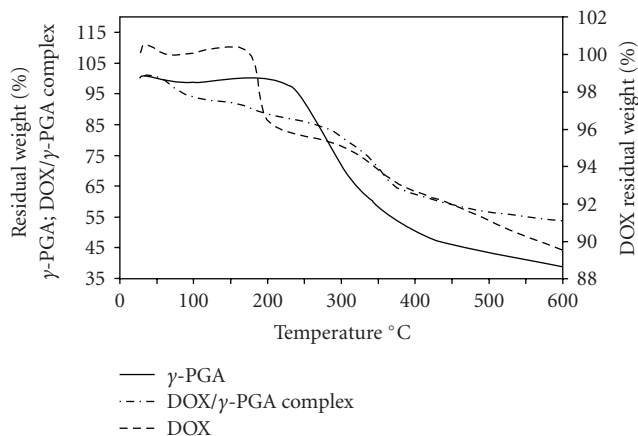
TABLE 2: Size and surface characteristics of different DOX/ γ -PGA ionic complexes ($n = 3$).

DOX : γ -PGA ratio (w/w)	Particle size (μm)	Polydispersity	Zeta potential (mV)
1 : 200	83 ± 14	0.45 ± 0.13	-30.6 ± 3.1
1 : 100	82.5 ± 28	0.45 ± 0.14	-39 ± 3.5
1 : 10	81 ± 11	0.39 ± 0.1	-47.7 ± 2.8
1 : 1	80 ± 37	0.53 ± 0.14	-53.7 ± 1.1

FIGURE 4: DSC thermograms of freeze dried Doxorubicin, γ -PGA and DOX/ γ -PGA (1 : 1 w/w) complex.

3.2. Specific Interaction between DOX and γ -PGA. The interaction of DOX with γ -PGA was investigated spectrophotometrically by comparing the visible spectra of DOX/ γ -PGA complex with that of pure γ -PGA and pure DOX. As shown in Figure 3, DOX has a characteristic λ_{max} at 480 nm; no detectable absorbance was noted for γ -PGA over the chosen wavelength range at the concentrations tested. In case of DOX/ γ -PGA complex, spectral changes in DOX peak maxima were observed. The λ_{max} of complex appeared at 495 nm, suggesting that addition of γ -PGA to DOX induces red-shift of 15 nm. Moreover, the intensity of DOX peak at 480 nm was reduced by $\sim 23\%$ which suggest that a complex was formed between γ -PGA and DOX. No significant difference in pH was observed upon mixing γ -PGA and DOX solutions.

As stated above, γ -PGA exhibits high negative character because of the presence of one carboxylate anion per monomer (Figure 1(a)). The pK_a of γ -PGA is 2.6 (as calculated by acid-base titration), thus in slightly acidic to neutral environment, the α -carboxyl groups remain unprotonated. Doxorubicin is an amphoteric drug containing protonable amino group and deprotonable phenolic groups; thus a continuous equilibrium exists between the positively charged, negatively charged, neutral and zwitter ionic species of DOX. In the pH range of 0–6, the amine group in DOX is protonated and exists in the form of NH_3^+ . Thus, it is most likely that the electrostatic interactions between negatively charged γ -PGA and positively charged DOX lead

FIGURE 5: TGA thermograms of DOX, γ -PGA, and DOX/ γ -PGA (1 : 1 w/w) complex.

to the formation of DOX/ γ -PGA complex. In a similar study, Agresti et al. [20] reported the formation of an ionic complex between PGA and diphenhydramine (DPH) under acidic conditions (pH 3.0). The DPH/PGA complex was formed by pH-induced transition in PGA conformation from random coil to α -helix. DPH was released from the complex under weakly acidic or neutral conditions, resulting in the reversal of PGA conformation from α -helix to random coil. In the present work, when aqueous γ -PGA (pH 7, nonbuffered; random coil conformation) was mixed with DOX (pH 3.0, as supplied), the pH of the mixture was ~ 6 . As expected, we did not observe any change in γ -PGA conformation as confirmed by CD spectral analysis of γ -PGA and DOX/ γ -PGA complex at pH 6 and 7 (data not shown). Hence, it can be concluded that electrostatic interaction is the predominant force between DOX and γ -PGA. However, one cannot rule out the possibility of other factors such as hydrophilic/hydrophobic interactions, resonance effect, and so forth, which might play a role in DOX complexation with γ -PGA. To further elucidate the type of interaction between DOX and γ -PGA, DOX/ γ -PGA complexes were characterized by thermal analysis and X-ray powder diffraction.

3.3. Characterization of DOX/ γ -PGA Complexes

3.3.1. Differential Scanning Calorimetry (DSC). DSC measurements were done to (a) exclude the possibility of pure DOX being precipitated during DOX/ γ -PGA complexation and (b) to confirm the specific interactions between DOX and γ -PGA to form stable complexes. The DSC thermograms were plotted simultaneously to compare the thermal properties of newly formed DOX/ γ -PGA complexes with those of pure DOX and pure γ -PGA. As illustrated in Figure 4, γ -PGA exhibited two endothermic peaks at 82 and 218°C, and an exothermic peak at 320°C. γ -PGA obtained from different sources has a varying molecular weight and associated physico-chemical properties such as viscosity, thermal characteristics, and so forth. Very few reports are

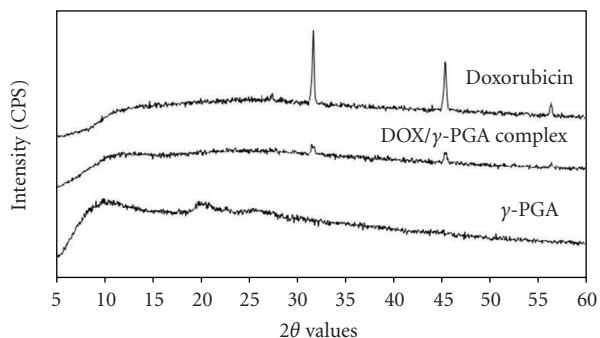


FIGURE 6: Wide angle X-ray diffraction (WAXS) patterns of DOX, γ -PGA, and DOX/ γ -PGA (1 : 1 w/w) complex.

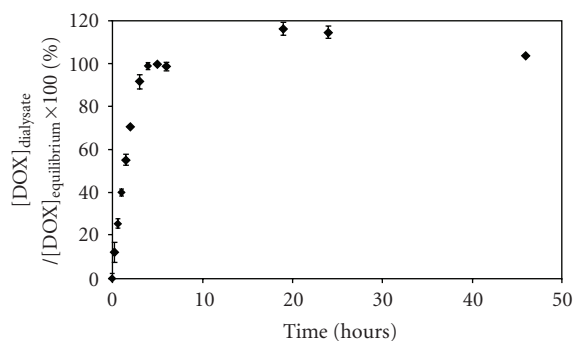


FIGURE 7: Control equilibration study of free DOX through the dialysis membrane (MWCO: 6–8 kDa) used in in vitro release studies. The equilibration is complete after 5 hours. Mean and S.D. are shown ($n = 3$).

available on the glass transition (T_g) and melting (T_m), or decomposition (T_d) temperatures of γ -PGA. Khachatoorian et al. [25] reported the T_g and T_m of γ -PGA to be around 110°C and 397°C; however, the source and molecular weight of γ -PGA used in their study was not mentioned. Ho et al. [26] reported the thermal decomposition of γ -PGA H-form (M.W.: 2×10^6 Da) obtained from *B. subtilis* (natto): T_m (206°C) and T_d (209.8°C) [26]. Since γ -PGA used in this study was obtained from natto gum (M.W.: ~ 127 kDa, GPC), thus the first endothermic peak at 82°C most likely corresponds to the T_g of γ -PGA, while the sharp endothermic peak at 218°C is the melting endotherm (T_m or T_d) of γ -PGA.

For DSC of pure drug, DOX from the injection vial was first freeze-dried to obtain a dry powder. Three endotherm peaks appeared at 54, 195, and 355°C. The sharp endothermic peak at 54°C is most likely because of residual moisture left after freeze drying. The peak at 195°C corresponds to the melting endotherm of DOX ($T_m = 218^\circ\text{C}$) [12].

In case of DOX/ γ -PGA complex, a broad endotherm peak appeared at 68°C which could possibly be the T_g of the complex, since association with DOX may have altered the T_g of pure γ -PGA. The absence of a characteristic melting peak of DOX between 150 and 260°C confirms that no pure DOX was precipitated during DOX/ γ -PGA complexation and that the entire added drug was bound to the polymer.

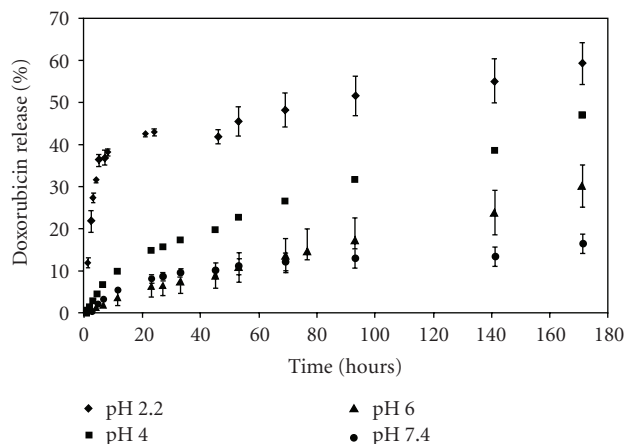


FIGURE 8: In vitro release of bound DOX from DOX/ γ -PGA complexes (1 : 1 w/w) from dialysis membrane in buffered aqueous solutions at different pHs.

This also strongly indicates the formation of stable DOX/ γ -PGA complex. An endothermic peak at 360°C most likely represents the decomposition of DOX/ γ -PGA complex.

3.3.2. Thermogravimetric Analysis (TGA). To further evaluate the stability of DOX/ γ -PGA complex, pure polymer, pure drug, and the polymer/drug complex were analyzed by thermogravimetry. As shown in Figure 5, a total of 10% weight loss of pure DOX was observed in the tested temperature range from 25 to 600°C, suggesting that most of the DOX did not decompose to vapor state, and was collected as char in the crucible. The temperature range of 175–220°C accounted for up to 4% loss in DOX weight. This thermal decomposition range matches with the DOX melting peak at 195°C, as determined by DSC. Thermal degradation of pure γ -PGA started at 210°C, which is the T_m of γ -PGA as noted from DSC. Around 60% of γ -PGA were decomposed as the temperature reached up to 600°C. In case of DOX/ γ -PGA complex, around 60% of the complex remained undecomposed when heated from 25 to 600°C, suggesting that DOX is strongly associated to γ -PGA. The observed weight loss in DOX/ γ -PGA complex is most likely attributed to thermal decomposition of γ -PGA. The TGA curve of DOX/ γ -PGA complex reflects the heterogeneous nature of the interaction between DOX and γ -PGA. Therefore, it might be suggested that in addition to the possible electrostatic interactions between the amino group of DOX and the carboxyl groups in γ -PGA, the anthracycline ring of DOX might also be participating in DOX/ γ -PGA complexation by interacting with the hydrophobic domains on γ -PGA backbone.

3.3.3. X-Ray Powder Diffraction Analysis. To further elucidate the interaction between DOX and γ -PGA, the crystal characteristics of the DOX/ γ -PGA complex were examined using wide angle X-ray powder diffraction (Figure 6). For DOX, clear peaks are visible in the diffractogram indicating the presence of crystalline phase in the native form, whereas

γ -PGA showed a typical amorphous pattern. The appearance of identical peaks in the diffractogram of DOX/ γ -PGA complex confirms the association of DOX with γ -PGA and that the formed complexes are crystalline in nature.

3.3.4. Drug Release from DOX/ γ -PGA Complexes. Of all the water-soluble DOX/ γ -PGA complexes that were formed, the one with maximum DOX amount (1:1 w/w DOX: γ -PGA) was chosen for drug release studies. We simulated “sink” conditions by placing the DOX/ γ -PGA complex in a dialysis bag (MWCO: 6–8 kDa), and regularly replacing the dialysate buffer every 24 hour. A control experiment with free DOX (Figure 7) confirmed that the high MWCO (6–8 kDa) of dialysis membrane selected ensured unrestricted diffusion of the released drug; the time interval between dialysate replacement was in excess for reaching the complete equilibration of DOX solutions on either sides of dialysis membrane (5 hours). The highest concentration of drug in the dialysate was $1.2 \mu\text{g/mL}$; a value much below 10% of drug’s aqueous solubility, which is a requirement for the fulfillment of “sink” conditions.

Because of predominantly ionic nature of DOX/ γ -PGA complex, it was expected that changing the pH and/or ionic strength of the release medium may cause dissociation of DOX/ γ -PGA complex.

Effect of Ionic Strength on DOX Release from DOX/ γ -PGA Ionic Complexes. The in vitro DOX release profiles from ionic complex (1:1 w/w) suspended in phosphate buffered saline (pH 7.4) at different ionic strengths namely; 77 mM, 154 mM, and 308 mM are presented in Figure 8. Increasing the ionic strength of the release medium did not have a significant effect on the DOX release rate. At higher ionic strength (308 mM PBS), a maximum of 14% of total DOX was dissociated from the complex over 10-hour period, then DOX concentration decreases, probably due to its degradation in presence of high salt concentration. In case of low ionic strength buffer, only 8% of total drug were dissociated; however, under physiological buffer conditions (154 mM PBS, pH 7.4), DOX release was linear, releasing upto 15% of total DOX over 30-hour period. Since the initial binding of drug to the polymer is predominantly based on electrostatic complementarity, increased ionic strength, to some extent, helps in mitigating the electrostatic attraction, resulting in less effective binding and hence relatively faster dissociation of drug from drug/polymer complex.

3.4. pH-Triggered Release of DOX from DOX/ γ -PGA Ionic Complexes. The in vitro DOX release from DOX/ γ -PGA complex at varying pH is shown in Figure 9. At pH 2.2, burst release of DOX was observed, releasing 40% of drug in the first 8 hours, followed by slow release over a week. No such burst release was observed at pH higher than 2.2. There could be several reasons for such a burst release of DOX in low pH environment. One possibility is that at pH 2.2, most of the carboxyl groups in γ -PGA ($\text{pK}_a = 2.6$) are protonated, and so is the amine group in DOX (NH_3^+). Thus, the interaction between γ -PGA and DOX is weakened

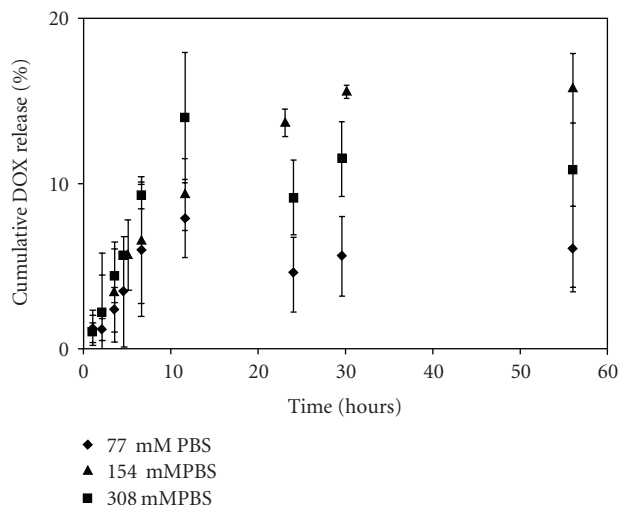


FIGURE 9: Effect of ionic strength on release of DOX from DOX/PGA ionic complex (1:1 w/w) in phosphate buffered saline, pH 7.4 at different ionic strengths.

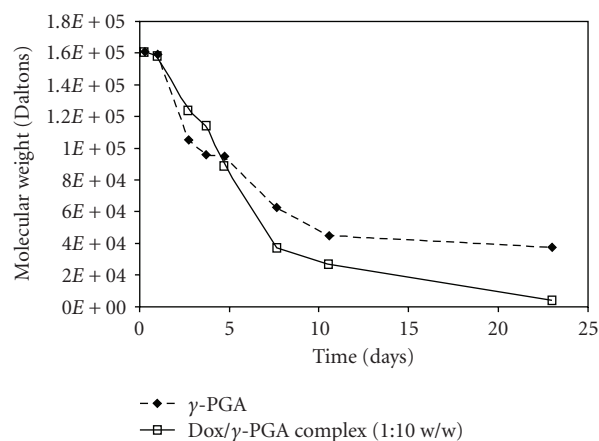


FIGURE 10: Degradation of γ -PGA and DOX/ γ -PGA ionic complex (1:10 w/w) in 154 mM phosphate buffered saline, pH 7.4 at 37°C .

because of electrostatic repulsion between both the positively charged drug and the polymer, thereby dissociating the drug.

Another possible reason could be the precipitation of γ -PGA under acidic conditions. At pH 2.2, a small fraction of γ -PGA precipitates out of the complex (visual observation), leaving behind the dissociated DOX in the dialysis bag, which then rapidly diffuses out into the release medium.

Based on these observations, one might assume a 100% release of DOX at pH 2.2; however, DOX dissociation slows down after several hours. The possible explanation of such a phenomenon could be derived from thermal analysis of the complex. The DSC and TGA thermograms show that DOX association with γ -PGA is quite strong, which suggests the involvement of additional interactions between DOX and γ -PGA, apart from electrostatic forces. As a result, only a part of DOX/ γ -PGA ionic complex responded to pH change, leaving the rest of the complex undissociated, which dissociates at a much slower rate.

On the other hand, at higher pHs (4 to 7.4), γ -PGA remains soluble, thus the only possible way that DOX can be released is by pH-induced dissociation, thus no burst release effect is observed at any of the higher pHs studied. Nevertheless, in the pH range of 4–7.4, the carboxyl groups in γ -PGA are unprotonated; thus higher the pH, more the number of un-protonated carboxyl groups, and stronger the polymer/drug interaction. Therefore, increasing the medium pH reduced the DOX dissociation, hence release rate. Up to 15% of total drug were released at the physiological pH as opposed to 50% and 30% at pH 4 and 6, respectively. From clinical perspective, it is desirable to achieve slow or minimal drug release from targeted drug delivery system at physiological pH in blood circulation thus reducing the drug loss until the intended target is reached. In all cases, the drug release from the complex was linear as observed over a week. It is thus concluded that pH-triggered DOX/ γ -PGA complexes facilitate sustained release of DOX over a long period of time.

3.5. Degradation of DOX/ γ -PGA Ionic Complex. The biodegradability of γ -PGA and DOX/ γ -PGA complex was estimated following hydrolysis under physiological condition. As illustrated in Figure 10, the molecular weight of both γ -PGA and DOX/ γ -PGA ionic complex decreased exponentially from 170 kDa to 40 and \sim 10 kDa, respectively, over a period of 3 weeks. Since the molecular weight cut off of kidney is \sim 70 kDa, thus both, the DOX-free γ -PGA and the undissociated DOX/ γ -PGA complex, can be excreted out by kidney within 2-3 weeks. However, detailed in vivo studies need to be performed to confirm the polymer degradation and renal clearance.

4. Conclusions

In this paper, we describe the feasibility of using γ -PGA as a carrier for the delivery of small, cationic anthracycline drug, DOX. We have demonstrated that DOX can interact with γ -PGA to form stable complexes with almost 100% complexation of DOX with γ -PGA. The polymer/drug complexation approach binds the drug tightly to the polymer; as a result, the formed complexes demonstrated pH-dependent slow release of Doxorubicin, in vitro. More studies need to be done to prove the exact mechanism of interaction between DOX and γ -PGA. A detailed in vitro cytotoxicity studies are ongoing to determine the bioactivity of release of DOX and the effect of plasma proteins on DOX release from the ionic complex.

Acknowledgments

The authors sincerely thank their colleague and department's lab supervisor Mr. Brian Dennis for his technical assistance and discussion. This research was supported by the Natural Sciences and Engineering Research Council of Canada through Discovery Grant no. 4388 awarded to Dr. A. Margaritis.

References

- [1] S. Feng and S. Chien, "Chemotherapeutic engineering: application and further development of chemical engineering principles for chemotherapy of cancer and other diseases," *Chemical Engineering Science*, vol. 58, pp. 4087–4114, 2003.
- [2] S. M. Moghimi, A. C. Hunter, and J. C. Murray, "Long-circulating and target-specific nanoparticles: theory to practice," *Pharmacological Reviews*, vol. 53, pp. 283–318, 2001.
- [3] B. Manocha and A. Margaritis, "Production and characterization of γ -polyglutamic acid nanoparticles for controlled anticancer drug release," *Critical Reviews in Biotechnology*, vol. 28, pp. 83–99, 2008.
- [4] D. D. Von Hoff, M. Rozenzweig, and M. Piccart, "The cardiotoxicity of anticancer agents," *Seminars in Oncology*, vol. 9, pp. 23–33, 1982.
- [5] P. Singal, N. Iliskovic, T. Li, and D. Kumar, "Adriamycin cardiomyopathy: pathophysiology and prevention," *FASEB Journal*, vol. 11, pp. 931–936, 1997.
- [6] L. J. Goldstein, H. Galski, A. Fojo, et al., "Expression of a multidrug resistance gene in human cancers," *Journal of the National Cancer Institute*, vol. 81, pp. 116–124, 1989.
- [7] K. A. Janes, M. P. Fresneau, A. Marazuela, A. Fabra, and M. J. Alonso, "Chitosan nanoparticles as delivery systems for doxorubicin," *Journal of Controlled Release*, vol. 73, pp. 255–267, 2001.
- [8] D. Kalaria, G. Sharma, V. Beniwal, and M. Ravi Kumar, "Design of biodegradable nanoparticles for oral delivery of doxorubicin: in vivo pharmacokinetics and toxicity studies in rats," *Pharmaceutical Research*, vol. 26, pp. 492–501, 2009.
- [9] A. Papagiannaros, S. Hatziantoniou, K. Dimas, G. T. Papaioannou, and C. Demetzos, "A liposomal formulation of Doxorubicin, composed of hexadecylphosphocholine (HePC): physicochemical characterization and cytotoxic activity against human cancer cell lines," *Biomedicine & Pharmacotherapy*, vol. 60, pp. 36–42, 2006.
- [10] S. Dreis, F. Rothweiler, M. Michaelis, J. Cinatl Jr., J. Kreuter, and K. Langer, "Preparation, characterisation and maintenance of drug efficacy of doxorubicin-loaded human serum albumin (HSA) nanoparticles," *International Journal of Pharmaceutics*, vol. 341, pp. 207–214, 2007.
- [11] A. Gabizon, R. Shiota, and D. Papahadjopoulos, "Pharmacokinetics and tissue distribution of doxorubicin encapsulated in stable liposomes with long circulation times," *Journal of the National Cancer Institute*, vol. 81, pp. 1484–1488, 1989.
- [12] D. Missirlis, R. Kawamura, N. Tirelli, and J. A. Hubbell, "Doxorubicin encapsulation and diffusional release from stable, polymeric, hydrogel nanoparticles," *European Journal of Pharmaceutical Sciences*, vol. 29, pp. 120–129, 2006.
- [13] G. S. Kwon, M. Naito, M. Yokoyama, T. Okano, Y. Sakurai, and K. Kataoka, "Physical entrapment of adriamycin in AB block copolymer micelles," *Pharmaceutical Research*, vol. 12, pp. 192–195, 1995.
- [14] P. Couvreur, B. Kante, L. Grislain, M. Roland, and P. Speiser, "Toxicity of polyalkylcyanoacrylate nanoparticles. II: doxorubicin-loaded nanoparticles," *Journal of Pharmaceutical Sciences*, vol. 71, pp. 790–792, 1982.
- [15] K. Akiyoshi, I. Taniguchi, H. Fukui, and J. Sunamoto, "Hydrogel nanoparticle formed by self-assembly of hydrophobized polysaccharide. Stabilization of adriamycin by complexation," *European Journal of Pharmaceutics and Biopharmaceutics*, vol. 42, pp. 286–290, 1996.

- [16] X. R. Teng, D. G. Shchukin, and H. Möhwald, "A novel drug carrier: lipophilic drug-loaded polyglutamate/ polyelectrolyte nanocontainers," *Langmuir*, vol. 24, pp. 383–389, 2008.
- [17] P. Vishweshwar, J. A. McMahon, J. A. Bis, and M. J. Zawortko, "Pharmaceutical co-crystals," *Journal of Pharmaceutical Sciences*, vol. 95, pp. 499–516, 2006.
- [18] A. Jimenez-Kairuz, D. A. Allemanni, and R. H. Manzo, "The improvement of aqueous chemical stability of a model basic drug by ion pairing with acid groups of polyelectrolytes," *International Journal of Pharmaceutics*, vol. 269, pp. 149–156, 2004.
- [19] B. Guo, J. Yuan, and Q. Gao, "pH and ionic sensitive chitosan/carboxymethyl chitosan IPN complex films for the controlled release of coenzyme A," *Colloid and Polymer Science*, vol. 286, pp. 175–181, 2008.
- [20] C. Agresti, Z. Tu, C. Ng, Y. Yang, and J. F. Liang, "Specific interactions between diphenhydramine and α -helical poly(glutamic acid)—a new ion-pairing complex for taste masking and pH-controlled diphenhydramine release," *European Journal of Pharmaceutics and Biopharmaceutics*, vol. 70, pp. 226–233, 2008.
- [21] C. Li, "Poly(L-glutamic acid)—anticancer drug conjugates," *Advanced Drug Delivery Reviews*, vol. 54, pp. 695–713, 2002.
- [22] J. M. Buescher and A. Margaritis, "Microbial biosynthesis of polyglutamic acid biopolymer and applications in the biopharmaceutical, biomedical and food industries," *Critical Reviews in Biotechnology*, vol. 27, pp. 1–19, 2007.
- [23] B. Manocha and A. Margaritis, "A novel method for the selective recovery and purification of γ -polyglutamic acid from *Bacillus licheniformis* fermentation broth," *Biotechnology Progress*, vol. 26, no. 3, 2010.
- [24] S. R. Urva, B. S. Shin, V. C. Yang, and J. P. Balthasar, "Sensitive high performance liquid chromatographic assay for assessment of doxorubicin pharmacokinetics in mouse plasma and tissues," *Journal of Chromatography B*, vol. 877, pp. 837–841, 2009.
- [25] R. Khachatourian, I. G. Petrisor, and T. F. Yen, "Prediction of plugging effect of biopolymers using their glass transition temperatures," *Journal of Petroleum Science and Engineering*, vol. 41, pp. 243–251, 2004.
- [26] G. Ho, T. Ho, K. Hsieh, et al., " γ -Polyglutamic acid produced by *Bacillus subtilis* (natto): structural characteristics, chemical properties and biological functionalities," *Journal of the Chinese Chemical Society*, vol. 53, pp. 1363–1384, 2006.

Research Article

Preparation, Mechanical, and Thermal Properties of Biodegradable Polyesters/Poly(Lactic Acid) Blends

Peng Zhao,^{1,2} Wanqiang Liu,³ Qingsheng Wu,^{1,2} and Jie Ren^{1,3,4}

¹The Institute for Advanced Materials and Nano Biomedicine, Tongji University, Shanghai 200092, China

²Department of Chemistry, Tongji University, Shanghai 200092, China

³Institute of Nano and Bio-Polymeric Materials, School of Material Science and Engineering, Tongji University, Shanghai 200092, China

⁴Key Laboratory Advanced Civil Engineering Materials, Tongji University, Ministry of Education, Shanghai 200092, China

Correspondence should be addressed to Jie Ren, renjie.tongji@gmail.com

Received 30 September 2009; Accepted 27 November 2009

Academic Editor: Huisheng Peng

Copyright © 2010 Peng Zhao et al. This is an open access article distributed under the Creative Commons Attribution License, which permits unrestricted use, distribution, and reproduction in any medium, provided the original work is properly cited.

Series of biodegradable polyesters poly(butylene adipate) (PBA), poly(butylene succinate) (PBS), and poly(butylene adipate-co-butylene terephthalate) (PBAT) were synthesized successfully by melt polycondensation. The polyesters were characterized by Fourier transform infrared spectroscopy (FTIR), ¹H-NMR, differential scanning calorimetry (DSC), and gel permeation chromatography (GPC), respectively. The blends of poly(lactic acid) (PLA) and biodegradable polyester were prepared using a twin screw extruder. PBAT, PBS, or PBA can be homogeneously dispersed in PLA matrix at a low content (5–20 wt%), yielding the blends with much higher elongation at break than homo-PLA. DSC analysis shows that the isothermal and nonisothermal crystallizabilities of PLA component are promoted in the presence of a small amount of PBAT.

1. Introduction

In recent years, considerable interest has been focused on biodegradable polymers due to their obvious environment-friendly property comparing to conventional nondegradable or slowly degradable synthetic petrochemical-based polymeric materials [1, 2]. Biodegradable polymers degrade in a physiological environment by macromolecular chain scission into smaller fragments, and ultimately into simple stable end-products [3]. The degradation may occur via different pathway, such as catalysis of aerobic or anaerobic microorganisms, biologically active processes (e.g., enzyme reactions), and hydrolytic cleavage [4]. Poly(lactic acid) (PLA) is the most important plastic derived from renewable resources [5]. PLA-based products (e.g., NatureWork) have been extensively used for their application in biomedical field [6]. However, disadvantages of PLA are inherent brittleness and low toughness despite high tensile modulus and strength [7]. The flexibility, toughness and melt stability of PLA can be improved by some approaches, such as copolymerization [8, 9], blending [10], and plasticizers addition [11, 12]. Generally, blending is a relatively simple and easy way compared

to other approaches. Therefore, in recent years the blends of PLA and biocompatible and biodegradable polymers, such as poly(ϵ -caprolactone) (PCL) [13], poly(ethylene glycol) (PEG) [14, 15], poly(hydroxy butyrate) (PHB) [16], starch [17], poly(propylene carbonate) (PPC) [18], collagen [19], and PBS [20], have been widely studied for application in drug delivery and tissue engineering. PLA is approved for human use by the US Food and Drug Administration. Biodegradable polymeric nanoparticles (NPs) can be formulated to encapsulate various types of therapeutic agents including low-molecular-weight drugs, and macromolecules such as proteins or plasmid DNA. The NPs not only target the drug to its site of action but also maintain the drug concentrations at therapeutically relevant levels for a sustained period of time [21–23].

In this study, series of biodegradable polyesters, that is aliphatic homopolyesters PBA, PBS, and aliphatic-aromatic copolyester PBAT were synthesized by melt polycondensation. The blends of PLA and these biodegradable polyesters were prepared using a twin screw extruder. The mechanical and thermal properties of the blends were investigated.

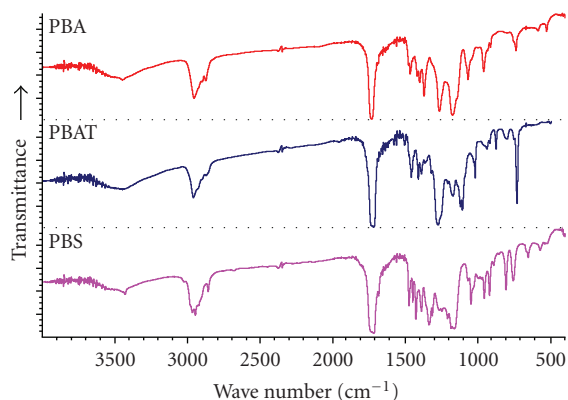


FIGURE 1: FTIR spectra of PBS, PBAT, and PBA.

2. Experimental

2.1. Materials. 1,4-butanediol, adipic acid and succinic acid (BASF, Germany), dimethyl-terephthalate (DMT, Merck), and tetrabutylorthotitanate (TBOT, Aldrich) were used without further purification. Pellets of PLA ($M_w = 130,000$ g/mol) were purchased from Tongjieliang Biomaterials Co., Ltd., Shanghai, China. Other solvents used were purchased from the Shanghai Chemical Reagent Company, China Medicine (Group).

2.2. Synthesis of Biodegradable Polyesters. The homo- and copolyesters were synthesized by melt polycondensation of 1,4-butanediol, adipic acid and succinic acid, and DMT with TBOT as the catalyst.

The homopolyesters were prepared via a two-step process, that is, esterification first and subsequent polycondensation. Amount of adipic acid or succinic acid and 1,4-butanediol with designed mole ratio (1 : 1.2) were added into a 36 L stainless steel reactor under N_2 atmosphere. The temperature of reactants was raised to $160^\circ C$ with stirring, and the water formed during this reaction was removed by distillation. After reaction for 1–2 hours, a certain amount of TBOT was added to the reaction mixture under N_2 atmosphere. Then the reaction temperature was raised from $160^\circ C$ to $230^\circ C$ within 5 hours under vacuum. After distillation of excess 1,4-butanediol, the reaction was carried out for another 20 hours under high vacuum (<50 Pa).

The procedure of synthesis of copolyester PBAT was as follows: amount of adipic acid and 1,4-butanediol with designed mole ratio (1 : 1.2) were added into a 36 L stainless steel reactor under N_2 atmosphere. The temperature of reactants was raised to $160^\circ C$ with stirring, and the water formed during this reaction was removed by distillation. After reaction for 1–2 hours, TBOT was added to the reaction mixture under N_2 atmosphere. The reaction temperature was raised to $180^\circ C$ for 4 hours under vacuum. DMT, 1,4-butanediol, and TBOT with designed mole ratio (1 : 1.2) were added to the reaction mixture under N_2 atmosphere. The reaction temperature was maintained at $180^\circ C$ for 2 hours, and was then raised to $230^\circ C$ within 4 hours under

vacuum. The reaction carried out for another 20 hours under high vacuum (<50 Pa).

2.3. Preparation of Polyesters/PLA Blends. PLA and PBAT (PBS or PBA) were dried under a vacuum at $45^\circ C$ for 12 hours to ensure that they were moisture free before being used. Blending of PLA and PBAT/PBS/PBA was performed using a corotating twin screw extruder (Leistritz ZSE-18) equipped with a volumetric feeder and a strand pelletizer. A screw with diameter of 27 mm and an L/D ratio of 40 were employed. The two polymers were weighed, manually tumbled to premix the pellets, and then fed into the extruder for melt blending. The extrusion temperature was independently controlled in eight zones along the extruder barrel and a strand die to achieve a temperature profile ranging from $150^\circ C$ to $180^\circ C$. A 150 rpm screw speed was used for all extrusions. The blends obtained were cut into small pieces and dried at $60^\circ C$ for 12 hours under vacuum before injection molding. The weight ratios of PLA/PBAT (PBS or PBA) were 95/5, 90/10, 85/15, 80/20, and 75/25.

2.4. Characterization. 1H NMR spectra were recorded on a Varian MERCURYPLUS400 Spectrometer with a $CDCl_3$ signal as a standard. The thermal properties of the polymers were measured with a TA MDSC-Q100 differential scanning calorimeter with a heating rate of $10^\circ C$ /minute. FTIR spectra in the range of 4000 – 400 cm^{-1} were recorded on KBr pellet samples, with a Nicolet NEXUS-912A Spectrometer with a resolution of 1 cm^{-1} . The molecular weight and the distribution of the polymers were measured by GPC (Waters150C). Tetrahydrofuran (THF) is used as the mobile phase at a flow rate of 1.0 mL/minute. Calibration is performed with polystyrene standards to determine the weight-average and number-average molecular weights (M_w and M_n). Field emission-scanning electronic microscopy (FE-SEM) images of the multiblock copolymer samples were recorded on a FEI Quanta 200 FEG at an accelerated voltage of 15 kV. The samples were sputter coated with a thin layer of gold before observation.

Tensile tests and flexural tests were performed using an autograph tensile testing apparatus DXLL-5000 (Jiedeng Co., Ltd., China). The dumbbell-shaped specimens for tensile tests were prepared from compression molded samples according to the standard method for testing the tensile properties of rigid plastics (GB/T1040-1992). Span length was 50 mm, and the testing speed was 5 mm/minute. Specimens for flexural tests were also prepared from compression molded samples according to the standard of plastics (GB/T 9341-2000). Izod impact tests were carried out according to GB/T 16420-1996 standard, with a standard impact tester X CJ-50 (Chende Co., Ltd, China). Five composite specimens were tested for each sample, and the mean values and standard deviation were calculated.

3. Results and Discussion

3.1. FTIR, 1H NMR and GPC. Figure 1 shows FTIR spectra of PBS, PBAT, and PBA. The spectra show characteristic

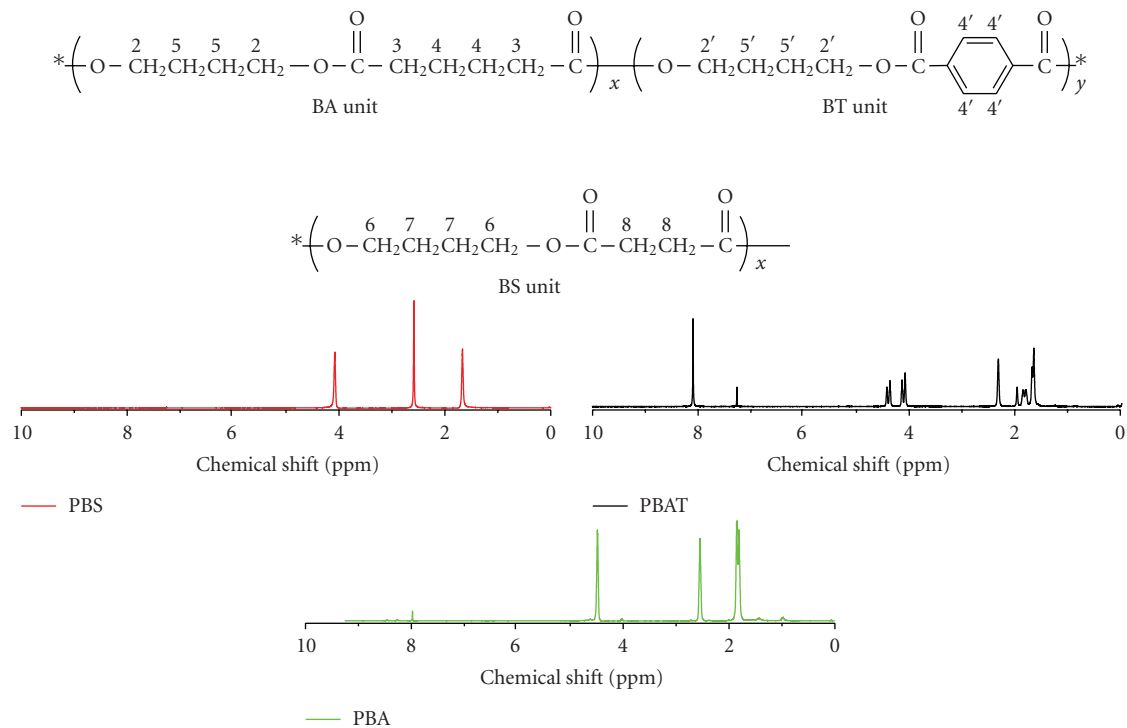


FIGURE 2: ^1H NMR spectra of synthesized polyester.

ester absorption peaks at 1690 , 1670 , and 1725 cm^{-1} for the stretching vibration of the $-\text{COO}-$ and at $1100 \sim 1300\text{ cm}^{-1}$ for the stretching vibration of the C-O-C . In the FTIR spectrum of PBAT, the absorption bands at 1018 , 1456 , 1495.65 , and 1573.91 cm^{-1} are characteristic group stretching of phenylene group. The red shift of ester absorption peak in PBAT is caused by conjugative effect between phenylene and carboxyl group.

Figure 2 shows ^1H NMR spectra of these polyesters and corresponding proton resonance signals, respectively. The signals occurring at 4.077 , 2.314 , 1.682 , and 1.643 ppm can be assigned to the methylene protons H_2 , H_3 , H_5 , and H_4 . The ratio of integrated peak area of $\text{H}_2 : \text{H}_3 : (\text{H}_5 + \text{H}_4)$ is $1 : 1 : 2$, corresponding to those of BA unit in equimolar ratio. No COOH resonance signal can be detected due to instrumental detection limit. These data indicate that synthesized linear PBA chains are terminated by hydroxyl functional end groups. In ^1H NMR spectrum of PBAT, the signal of aromatic protons appearing at 8.10 ppm (H_4) indicates phenylene structure in the polymer's chain. The signal of CH_2 proton groups of BA unit appears at δ 4.149 4.091 ppm , and 2.239 ppm (H_2 , H_3) as a multiple peak; the ratio of the integrated peak intensities of $\text{H}_2 : \text{H}_3$ is $1 : 1$ corresponding to the molar ratio of hydrogen atoms ($4 : 4$). The chemical shifts at δ 4.436 , 4.379 ppm for $-\text{OCH}_2-(\text{H}'_2)$, and δ 8.097 ppm for proton adjacent to aromatic carbon (H'_4) are attributed to those of BT unit. The ratio of the integrated peak intensities of H_3 protons and H'_4 protons is $1.34 : 1$, indicating that the content of BA unit is $57.3\text{ mol}\%$. The ^1H NMR data are consistent with the proposed molecular structure of the polyesters. ^1H NMR

TABLE 1: GPC and thermal characteristics of synthesized PBAT, PBS, and PBA.

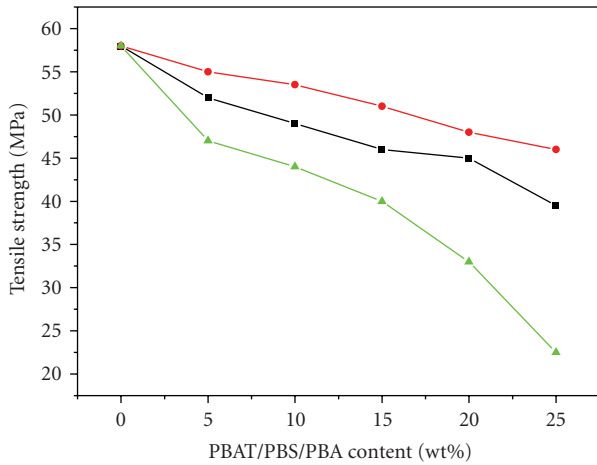
Sample	M_w	M_n	PI	T_g ($^{\circ}\text{C}$)	T_m ($^{\circ}\text{C}$)
PBAT	135000	59730	2.26	-28	114
PBS	98240	54270	1.81	-36	114
PBA	105000	57600	1.82	-68	55

spectrum of PBS shows three proton signals of BS unit, that is δ 4.077 for the proton of H_6 , δ 1.673 ppm for H_7 , δ 2.583 ppm for H_8 . The molar ratio of structures $\text{H}_6 : \text{H}_7 : \text{H}_8$ is approximately equal to $1 : 1 : 1$. All above data indicate that biodegradable polyesters of PBS, PBAT and PBA were synthesized successfully.

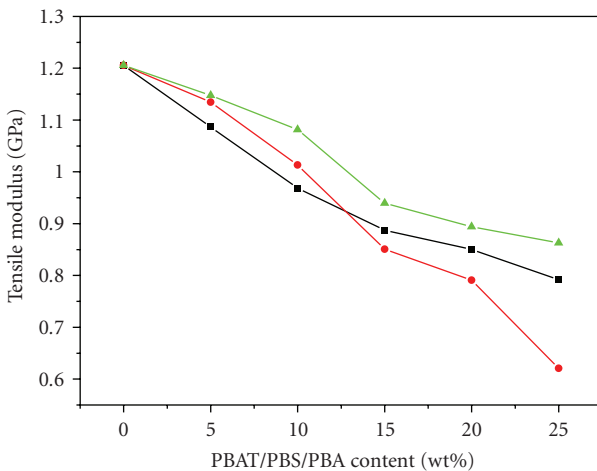
GPC results and thermal characteristics of PBAT, PBS and PBA are summarized in Table 1. M_w of PBAT, PBS and PBA are 135000 , 98240 and 105000 , respectively, and M_n of PBAT, PBS and PBA are 59730 , 54270 and 57600 , respectively. PDI are in the range of $1.81\text{--}2.26$.

3.2. Mechanical Properties

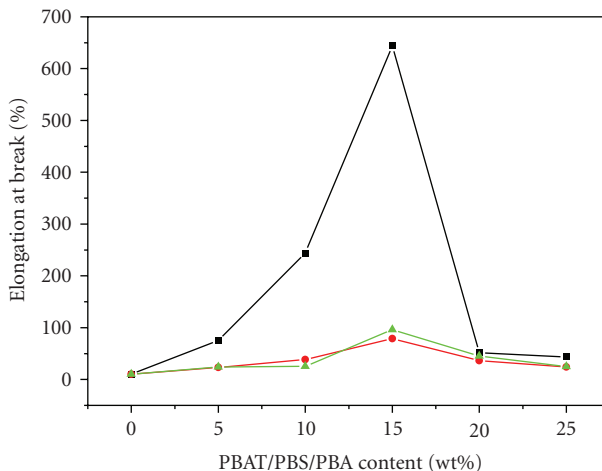
3.2.1. Tensile Properties. The tensile properties of PLA/PBS and PLA/PBA as well as PLA/PBAT blends are shown in Figure 3. The tensile strength and tensile modulus of PLA/PBAT (PBS, PBA) blends follow approximately the rule of mixtures over the whole composition range. Moreover, the PLA/PBAT blends showed much higher elongation at break than those of pure PLA and PLA/PBS and PLA/PBA blends over the whole composition range. Tensile strength



(a)



(b)



(c)

FIGURE 3: Tensile properties of PLA/PBAT and PLA/PBS, PLA/PBA blends: (a) tensile strength, (b) tensile modulus, and (c) elongation at break.

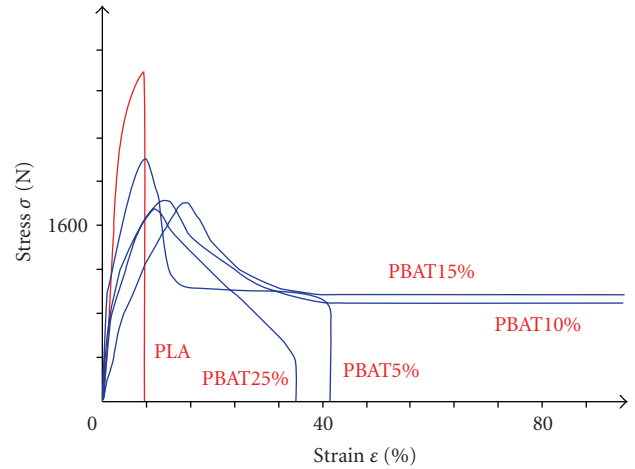


FIGURE 4: Stress-strain curves for PLA/PBAT 95/5, 90/10, 85/15, and 75/25 blends.

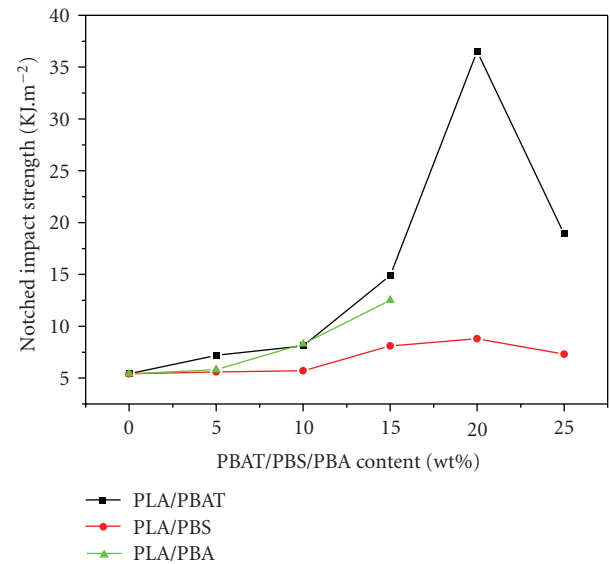


FIGURE 5: Notched impact properties of PLA/PBAT and PLA/PBS, PLA/PBA blends.

and Young's modulus of blends decreased with increasing polyester content, but elongation at break showed the peak values at 15 wt% of polyester content. Elongation at break (Figure 3(c)) increased with the increasing polyester content as expected. Small amount of polyester significantly alters the elongation. This is consistent with the tensile strength results. Addition of polyester to the PLA system resulted in a decrease in tensile strength and an increase in the elongation at break. The tensile strength of the blend did not significantly change with PBAT (PBS or PBA) content in the range from 5% to 15% but decreased rapidly when PBAT (PBS or PBA) content was increased to more than 25%. The elongation at break (Figure 3(c)) increased at higher polyester contents with the maximum value (>600%) occurring at a PBAT content of 15%. Interestingly, there is no dramatic decrease of tensile strength and modulus of the blends when polyester content

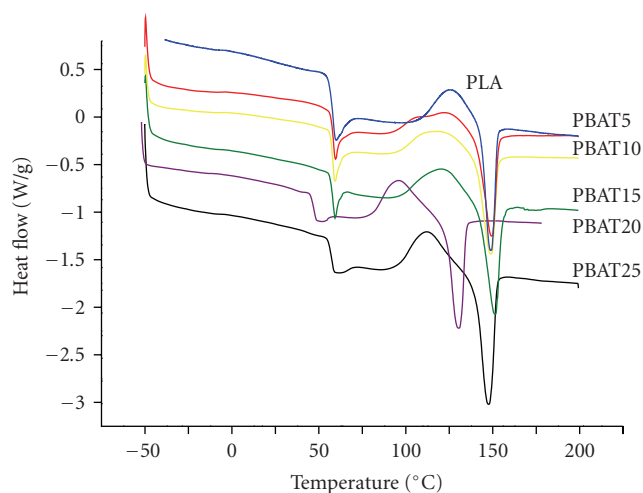


FIGURE 6: The DSC traces of PLA/PBAT blends.

was decreased to less than 20%. An increase of the polyester content to 15% does not lead to a significant decrease of the tensile strength and tensile modulus of the PLA/PBS (PBAT) blends. A decrease by 30% was observed for the PLA/PBA system.

It can be concluded from above analysis that the PLA/PBAT blends have the most outstanding properties. So the PLA/PBAT system was used for further investigation.

Figure 4 shows typical stress-strain curves for pure PLA and PLA/PBAT blends with different PBAT content. After a yield point, necking was observed. The necking continued until failure. Besides, strain hardening occurred after the yield point, and continued until failure. Fracture behavior of the specimen in the tensile tests changes from brittle fracture of plain PLA to ductile fracture of the blends. This is demonstrated in the tensile stress-extension curves as shown in Figure 4. Plain PLA shows a distinct break point before yielding and its strain at break is only about 7.7%. On the contrary, all the blends show distinct yielding and stable necking in cold drawing. Notably, when 5% PBAT was added, the elongation of the blend is tremendously increased by 200%.

3.2.2. Impact Property. The correlation between the notched impact strength and the composition of the PLA/PBAT, PLA/PBS and PLA/PBA blends are shown in Figure 5. Figure 5 shows that notched impact strength of plain PLA is 5.1 KJ/m² but increased to 15.3 KJ/m² when the content of PBAT is 15 wt%, and the notched impact strength can be 37.3 KJ/m² when the content of PBAT is 20 wt%. Therefore, it can be concluded that the addition of PBAT into PLA can remarkably improve the toughness of PLA. It can also be seen from Figure 4 that there is a sharp increase in the toughness of PLA/PBAT blends when the content of PBAT is up to 20 wt%, which is a sign of brittle-to-tough transition. Impact toughness is also increased from 5.1 KJ/m² for pure PLA to 12.6 KJ/m² for PLA-15%PBA as shown in Figure 4. Moreover, the notched impact strength of PLA/PBA blends

is too high to break when the content of PBA is higher than 20 wt%. Notched impact strength of PLA/PBS blends has similar trends as PLA/PBAT blends with a little difference.

3.2.3. Toughening Mechanism. SEM micrographs of tensile section and impact section are shown in Figures 7 and 8. Neat PLA which had no necking in the tensile test showed a smooth longitudinal fracture surface without visible plastic deformation. PLA/PBAT (15%) blend had the highest elongation at break, and its matrix underwent tremendous plastic deformation in the stress direction (Figure 7(d)). In the two-phase system, PBAT evenly dispersed in PLA matrix (Figure 8(b)). Normally, debonding of the round PBAT particles from the PLA matrix under tensile stress may cause oval cavities and these cavities were formed at the interface between the PLA matrix and PBAT inclusions during tension when the stress was higher than the bonding strength. PBAT debonded from the PLA matrix at the interface, so cavities arose. Since PBAT has different elastic properties compared to PLA matrix, its particles served as stress concentrators under tensile stress. The voids caused by debonding altered the stress state in the PLA matrix surrounding the voids, and triaxial tension was locally released and shear yielding was allowed. In the debonding progress, PLA matrix strands between PBAT particles deformed more easily to achieve the shear yielding. This toughening mechanism is consistent with other systems [24, 25].

3.3. Thermal Properties of PLA /PBAT Blends. The thermal properties of PLA/PBAT blends were investigated by DSC. The second heating curves for melt-quenched samples were chosen in order to remove previous thermal history and to make T_g more clear and obvious. The determined data are listed in Table 2 and the typical DSC curves are shown in Figure 6. At the same time, T_g and T_m of the blends with different compositions were observed. There are glass transition platforms at 50–60 °C corresponding to T_g of PLA component on all the curves. (DSC traces are not presented for T_g of PBAT component at -40 °C, because the exothermic heat flow is too slow to be detected during the test process.) Additionally, T_g of blends did not change with PBAT contents in blends. This trend suggests that the PLA and PBAT are not thermodynamic compatible, especially with higher PBAT content. If they are compatible, both T_g s of PLA and PBAT will move to combine with each other, and T_g peaks should be weaker and wider after they are extruded.

As shown in Figure 6, the addition of PBAT to the PLA matrix resulted in weaker and wider crystallization peak (about 110 °C), which was present at a lower temperature. This suggests that blending of PBAT with PLA has an influence on crystallizability of PLA. Moreover, T_m s of blends (about 150 °C) are same with T_m of pure PLA, indicating that addition of PBAT into PLA has no effect on T_m of PLA.

With the increase of PBAT content in blends, ΔH_c and ΔH_m of blends increase firstly, reach the highest value when the PBAT content is 15 wt%, and then decrease. It has been frequently practiced that the degree of crystallinity of thermoplastic is determined by dividing an observed heat of

TABLE 2: Composition and thermal characteristics of the samples.

Sample	PLA/PBAT ^a (wt%)	T_g^b (°C)	T_c^b (°C)	T_m^b (°C)	ΔH_c^b (Jg ⁻¹)	ΔH_m^b (Jg ⁻¹)	X_c^c (%)
PLA	100/0	58.36	124.70	148.64	10.337	11.00	12.76
PBAT5	95/5	58.40	122.65	149.46	11.28	13.12	13.92
PBAT10	90/10	58.27	116.19	149.79	11.83	15.10	14.61
PBAT15	85/15	58.07	120.73	151.39	14.42	18.67	17.80
PBAT20	80/20	58.60	110.02	147.59	12.09	17.36	14.93
PBAT25	75/25	58.00	111.88	147.39	10.24	16.74	12.64

^aWeight ratio of the blends.

^bThe glass transition temperatures (T_g), the crystallization temperatures (T_c), the melting temperatures (T_m), crystallization enthalpies (ΔH_c), melting enthalpies (ΔH_m) were registered by DSC at a heating/cooling rate of 10 °C/min.

^cThe degree of relative crystallinity (X_c) was calculated by dividing the observed ΔH_m from the first heating trace by the theoretical value (81 Jg⁻¹) for a 100% crystalline PLA. $X_c = \Delta H_c / \Delta H_c^* \Delta H_m^* = 81 \text{ J} \cdot \text{g}^{-1}$.

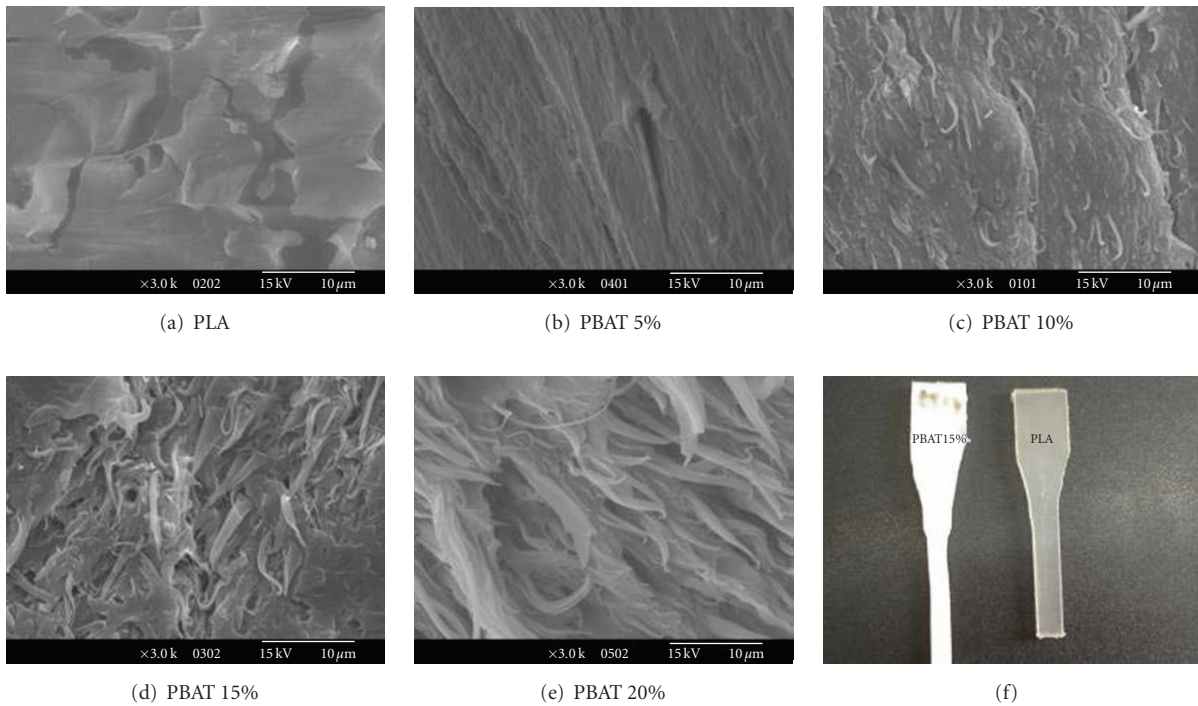


FIGURE 7: Tensile section SEM images of PLA/PBAT blends.

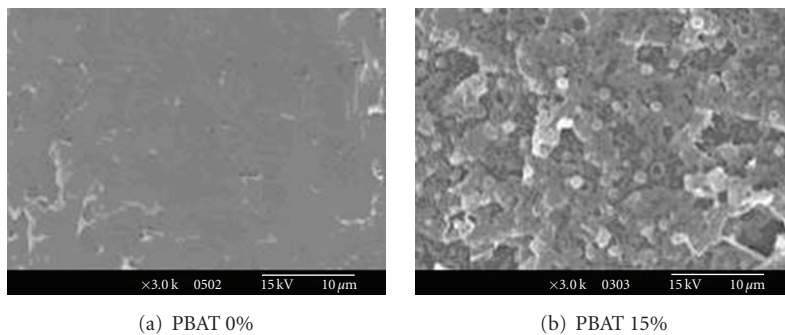


FIGURE 8: Impact section SEM images of PLA/PBAT blends.

fusion from the first heating trace by the theoretical value for a 100% crystalline polymer [26]. The theoretical ΔH_m value for PLA was 81 Jg^{-1} . The data of X_c are listed in Table 2. The trend of X_c with the increase of PBAT content is the same as that of ΔH_m . Therefore, the thermal properties of PLA, especially T_g and T_m , are slightly affected by the addition of PBAT. However, the addition of tough polyester to PLA matrix can influence the crystallizability of PLA matrix evidently.

4. Conclusion

Biodegradable polyesters, that is, poly(butylene adipate) (PBA), poly(butylene succinate) (PBS), and poly(butylene adipate-co-butylene terephthalate) (PBAT), were successfully synthesized by melt polycondensation. These polyesters/PLA blends show considerably higher elongation at break than pure PLA with an acceptable loss of strength. The elongation at break increases at the higher polyester contents with the maximum value (>600%) occurring at a PBAT content of 15%. Addition of PBAT into PLA may improve the toughness of PLA. Moreover, the crystallizability of PLA component of blends can be increased by the addition of a small amount of PBAT.

Acknowledgments

The work is sponsored by the 863 High Technology Research and Development Program Plan of China (2006AA02Z248), the Program of Shanghai Subject Chief Scientist (07XD14029), the fund of Shanghai International co-operation of Science and Technology (no. 075207046) and the Shanghai Nano Special fund (0952nm04800).

References

- [1] E. Chiellini and R. Solaro, "Biodegradable polymeric materials," *Advanced Materials*, vol. 8, no. 4, pp. 305–313, 1996.
- [2] A. C. Albertsson and S. Karlsson, "Degradable polymers for the future," *Acta Polymerica*, vol. 46, no. 2, pp. 114–123, 1995.
- [3] D. J. Mooney, K. Sano, M. P. Kaufmann, et al., "Long-term engraftment of hepatocytes transplanted on biodegradable polymer sponges," *Journal of Biomedical Materials Research*, vol. 37, no. 3, pp. 413–420, 1997.
- [4] D. Satyanarayana and P. R. Chatterji, "Biodegradable polymers: challenges and strategies," *Journal of Macromolecular Science*, vol. C33, no. 3, pp. 349–368, 1993.
- [5] A. Torres, S. M. Li, S. Roussos, and M. Vert, "Poly(lactic acid) degradation in soil or under controlled conditions," *Journal of Applied Polymer Science*, vol. 62, no. 13, pp. 2295–2302, 1996.
- [6] E. T. H. Vink, K. R. Rábago, D. A. Glassner, and P. R. Gruber, "Applications of life cycle assessment to NatureWorks™ polylactide (PLA) production," *Polymer Degradation and Stability*, vol. 80, no. 3, pp. 403–419, 2003.
- [7] Y. Li and H. Shimizu, "Toughening of polylactide by melt blending with a biodegradable poly(ether)urethane elastomer," *Macromolecular Bioscience*, vol. 7, no. 7, pp. 921–928, 2007.
- [8] T. Ouchi and Y. Ohya, "Design of lactide copolymers as biomaterials," *Journal of Polymer Science A*, vol. 42, no. 3, pp. 453–462, 2004.
- [9] C. Nouvel, P. Dubois, E. Dellacherie, and J.-L. Six, "Controlled synthesis of amphiphilic biodegradable polylactide-grafted dextran copolymers," *Journal of Polymer Science A*, vol. 42, no. 11, pp. 2577–2588, 2004.
- [10] S.-Y. Gu, K. Zhang, J. Ren, and H. Zhan, "Melt rheology of polylactide/poly(butylene adipate-co-terephthalate) blends," *Carbohydrate Polymers*, vol. 74, no. 1, pp. 79–85, 2008.
- [11] M. Baiardo, G. Frisoni, M. Scandola, et al., "Thermal and mechanical properties of plasticized poly(L-lactic acid)," *Journal of Applied Polymer Science*, vol. 90, no. 7, pp. 1731–1738, 2003.
- [12] N. Ljungberg and B. Wesslen, "The effects of plasticizers on the dynamic mechanical and thermal properties of poly(lactic acid)," *Journal of Applied Polymer Science*, vol. 86, no. 5, pp. 1227–1234, 2002.
- [13] L. Wang, W. Ma, R. A. Gross, and S. P. McCarthy, "Reactive compatibilization of biodegradable blends of poly(lactic acid) and poly(ϵ -caprolactone)," *Polymer Degradation and Stability*, vol. 59, no. 1–3, pp. 161–168, 1998.
- [14] S. Tanoue, A. Hasook, Y. Iemoto, and T. Unryu, "Preparation of poly(lactic acid)/poly(ethylene glycol)/ organoclay nanocomposites by melt compounding," *Polymer Composites*, vol. 27, no. 3, pp. 256–263, 2006.
- [15] M. Sheth, R. A. Kumar, V. Davé, R. A. Gross, and S. P. McCarthy, "Biodegradable polymer blends of poly(lactic acid) and poly(ethylene glycol)," *Journal of Applied Polymer Science*, vol. 66, no. 8, pp. 1495–1505, 1997.
- [16] L. L. Zhang, C. D. Xiong, and X. M. Deng, "Biodegradable polyester blends for biomedical application," *Journal of Applied Polymer Science*, vol. 56, no. 1, pp. 103–112, 1995.
- [17] J.-F. Zhang and X. Z. Sun, "Mechanical and thermal properties of polydactic acid/ starch blends with dioctyl maleate," *Journal of Applied Polymer Science*, vol. 94, no. 4, pp. 1697–1704, 2004.
- [18] X. F. Ma, J. G. Yu, and N. Wang, "Compatibility characterization of poly(lactic acid)/ poly(propylene carbonate) blends," *Journal of Polymer Science B*, vol. 44, no. 1, pp. 94–101, 2006.
- [19] X. Q. Yang, M. L. Yuan, W. Li, and G. Y. Zhang, "Synthesis and properties of collagen/polylactic acid blends," *Journal of Applied Polymer Science*, vol. 94, no. 4, pp. 1670–1675, 2004.
- [20] W. P. Jun and I. Seung, "Phase behavior and morphology in blends of poly(L-lactic acid) and poly(butylene succinate)," *Journal of Applied Polymer Science*, vol. 86, pp. 647–655, 2002.
- [21] O. Zelphati, Y. Wang, S. Kitada, J. C. Reed, P. L. Felgner, and J. Corbeil, "Intracellular delivery of proteins with a new lipid-mediated delivery system," *Journal of Biological Chemistry*, vol. 276, no. 37, pp. 35103–35110, 2001.
- [22] J. Panyam and V. Labhasetwar, "Sustained cytoplasmic delivery of drugs with intracellular receptors using biodegradable nanoparticles," *Molecular Pharmacology*, vol. 1, no. 1, pp. 77–84, 2004.
- [23] S. Prabha and V. Labhasetwar, "Nanoparticle-mediated wild-type p53 gene delivery results in sustained antiproliferative activity in breast cancer cells," *Molecular Pharmacology*, vol. 1, no. 3, pp. 211–219, 2004.
- [24] G.-M. Kim and G. H. Michler, "Micromechanical deformation processes in toughened and particle filled semicrystalline polymers—part 2: model representation for micromechanical deformation processes," *Polymer*, vol. 39, no. 23, pp. 5699–5703, 1998.

- [25] K. Wang, J. S. Wu, L. Ye, and H. M. Zeng, "Mechanical properties and toughening mechanisms of polypropylene/barium sulfate composites," *Composites A*, vol. 34, no. 12, pp. 1199–1205, 2003.
- [26] Y. Yoo, M.-S. Ko, S.-I. Han, T.-Y. Kim, S. Im, and D.-K. Kim, "Degradation and physical properties of aliphatic copolyesters derived from mixed diols," *Polymer Journal*, vol. 30, no. 7, pp. 538–545, 1998.

Research Article

Electrospun Poly(L-Lactide-co- ϵ -Caprolactone)/Polyethylene Oxide/Hydroxyapatite Nanofibrous Membrane for Guided Bone Regeneration

Gang Wang,¹ Tianbin Ren,¹ Chunhong Cao,¹ Weizhong Yuan,¹ Ying Song,¹ and Jiansheng Su²

¹ Institute of Nano and Bio-Polymeric Material, School of Material Science and Engineering, Tongji University, Shanghai, 200092, China

² School of Stomatology, Tongji University, Shanghai, 200092, China

Correspondence should be addressed to Tianbin Ren, rtb002@163.com and Jiansheng Su, ts1967118@yahoo.com.cn

Received 28 September 2009; Revised 22 November 2009; Accepted 5 March 2010

Academic Editor: Huisheng Peng

Copyright © 2010 Gang Wang et al. This is an open access article distributed under the Creative Commons Attribution License, which permits unrestricted use, distribution, and reproduction in any medium, provided the original work is properly cited.

A series of poly(L-lactide-co- ϵ -caprolactone)/polyethylene oxide/hydroxyapatite (PLCL/PEO/HA) composite fibrous membranes were prepared by electrospinning technology for guided bone regeneration. The morphology, water permeability and mechanical properties of the membranes were investigated. The HA nanocrystals can be well distributed in the PLCL/PEO matrix. And the diameter of composite nanofiber is larger than that of pure PLCL. The fibers with uniform size and large diameter were obtained when the contents of PEO and HA were 0.4% and 0.03%, respectively. In this condition, the obtained membrane presents the best water permeability. Furthermore, the nanofibrous membrane with largest tensile strength was obtained when the contents of PEO and HA were 0.5% and 0.03%, respectively.

1. Introduction

Guided bone regeneration membranes (GBRMs) are able to promote bone repair for their physical barrier function, separating defects with surrounding tissues and creating necessary growth spaces to bone. Therefore, considerable attention has been paid on GBRMs for the applications in biomedical field [1–3]. The common materials of GBRMs are non-bioabsorbable materials such as expanded-polytetrafluoroethylene [4, 5], and bioabsorbable materials such as collagen [6–10]. However, the non-bioabsorbable GBRMs have to be removed by secondary surgical procedures after new bone regeneration. In contrast, the bioabsorbable GBRMs are more and more widely researched and applied for avoiding secondary surgery to alleviate patients' sufferings and limit risks of tissue infection [11–14]. However, the natural bioabsorbable GBRMs are usually lack excellent mechanical performance and degraded rapidly which hinder bone recovery. Therefore, developing of new GBRMs composed of synthetic

polymeric materials, such as polyester, or their composites with inorganic materials which have good osteoconductivity, is attracting more and more attention [15–18].

Different methods also have been developed to prepare GBRMs [19–21]. And the main technologies are solvent-casting, phase inversion, and electrospinning [22–25]. Among them, nanofibrous membranes prepared by electrospinning have large specific surface area and porosity to mimic natural extracellular matrix (ECM). The thickness and pore size also can be adjusted by the control of electrospinning parameter [26–28].

In this paper, PLCL/PEO/HA composites were used to fabricate nanofibrous GBRMs by electrospinning because of their proper biodegradation rate, good biocompatibility, mechanical performance, and hydrophilic properties. The morphology, porosity, water permeability, and mechanical properties of the membranes were investigated by SEM, contact angle measurement system, and tensile tester.

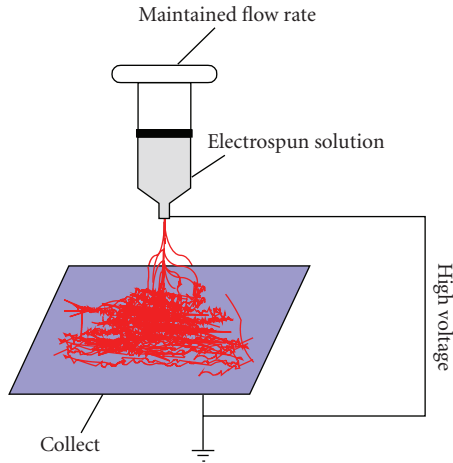


FIGURE 1: Schematic of the general electrospinning setup.

2. Materials and Methods

2.1. Materials. ϵ -Caprolactone (CL) was obtained from Acros Organics. L-Lactide (L-LA) was purified by recrystallization with ethyl acetate. PEO was used as received (Changchun Dadi Fine Chemical Co., Ltd, P. R. China). Nano-HA [29] and random copolymer of PLCL [30] [L-LA/ ϵ -CL=6:4 (mol/mol)] ($M_w = 240,000$ g/mol) were produced by ourselves. Dichloromethane, chloroform, and N, N-dimethylformamide were used without further purification.

2.2. Solvents and Electrospinning. PLCL solutions were prepared by dissolving 1.2 g of PLCL in 20 mL of chloroform/dichloromethane/DMF (5/3/2, v/v/v) mixed solvent and stirred for 6 hours. Then typically 0.08 g of PEO and 0.006 g of HA were mixed into PLCL solution sequentially. The mixed solutions were stirred for additional 12 hours and finally vibrated by supersonic oscillator for 10 minutes. The 20 mL of solution were loaded into a 20 mL syringe (the needle diameter was 0.9 mm) and injected into the Al collector under a high field strength (12 kV/18 cm) at an injection rate of 3 mL/h. The schematic of the general electrospinning setup was shown in Figure 1.

2.3. Composite Nanofiber Morphology. The morphology of PLCL/PEO/HA fibers was observed with an S-2360N scanning electron microscope (SEM) (Hitachi, Japan) at an accelerating voltage of 20 kV and H-600 TEM (Hitachi, Japan) at an accelerating voltage of 75 kV. Electrospun fibers were sputter-coated with gold prior to SEM analysis. TEM samples were loaded on copper grids. The average diameter of electrospun fibers was determined by measuring the diameters of nanofibers at 70 different points.

2.4. Surface Tension of the Solution and Surface Contact Angle of Membrane. Surface tension of the solution and surface contact angle of the membrane were measured by a contact angle measurement system (OCA, Dataphysics,

TABLE 1: The contents of PLCL, PEO, and HA in electrospun solutions, respectively, and the surface tension of these solutions and the average diameter of composite fiber.

Sample	PLCL/PEO/HA concentration (% , g/mL)	Average fiber diameter (μm)*	Surface tension (mN/m)**
1	6/0/0	0.90 ± 0.25	32.42 ± 0.50
2	6/0.2/0.03	1.28 ± 0.29	31.75 ± 0.75
3	6/0.3/0.03	1.35 ± 0.43	31.52 ± 0.38
4	6/0.4/0.03	2.09 ± 0.28	31.47 ± 0.45
5	6/0.5/0.03	1.45 ± 0.71	31.46 ± 0.50
6	6/0.6/0.03	1.46 ± 0.22	26.55 ± 0.71
7	6/0.4/0.01	1.19 ± 0.22	—
8	6/0.4/0.05	1.04 ± 0.14	—
9	6/0.4/0.07	0.85 ± 0.19	—
10	6/0.4/0.1	1.53 ± 0.22	—

*The data are representative of seventy samples and expressed as mean \pm SD ($n = 70$).

**The data are representative of five samples and expressed as mean \pm SD ($n = 5$).

Germany). A single drop of distilled water was dropped on the membrane samples.

2.5. Mechanical Properties of Membrane. Mechanical properties of electrospun PLCL/PEO/HA membranes were measured using a CMT6104 tensile tester (TUV, Germany) at a cross-head speed of 10 mm/min at room temperature. All samples were 80×10 mm² with a thickness of 50–120 μm . The tensile strength and elongation at break were both averaged over three samples.

3. Results and Discussion

3.1. Morphology of Composite Nanofibers. A series of PLCL/PEO/HA composite fibrous membranes were prepared by electrospinning technology for investigating the effects of PEO and HA contents on the performance of the composite membrane. The concentrations of PEO or HA are shown in Table 1. The morphology of nanofibers is shown by SEM images in Figures 2 and 3. And the inserted images show the diameter distributions of composite fiber. Continuous nanofibers were successfully obtained when the PEO content was varied from 0.2 to 0.6% and the contents of PLCL and HA were 6% and 0.03%, respectively. The fibers containing 0.4% of PEO were more uniform than other fibers. The average fiber diameter was 2.09 ± 0.28 μm (Table 1 and Figure 4(a)). It is known that fiber morphology was influenced by solution properties [31, 32] such as viscosity, surface tension and conductivity, and electrospinning parameters. In this investigation, the conductivity of solution would not change largely because of the nonconducting solution and the electrospinning parameters were the same. So this is due to the variety of viscosity and surface tension of electrospun solution with different PEO concentration. The surface tension also

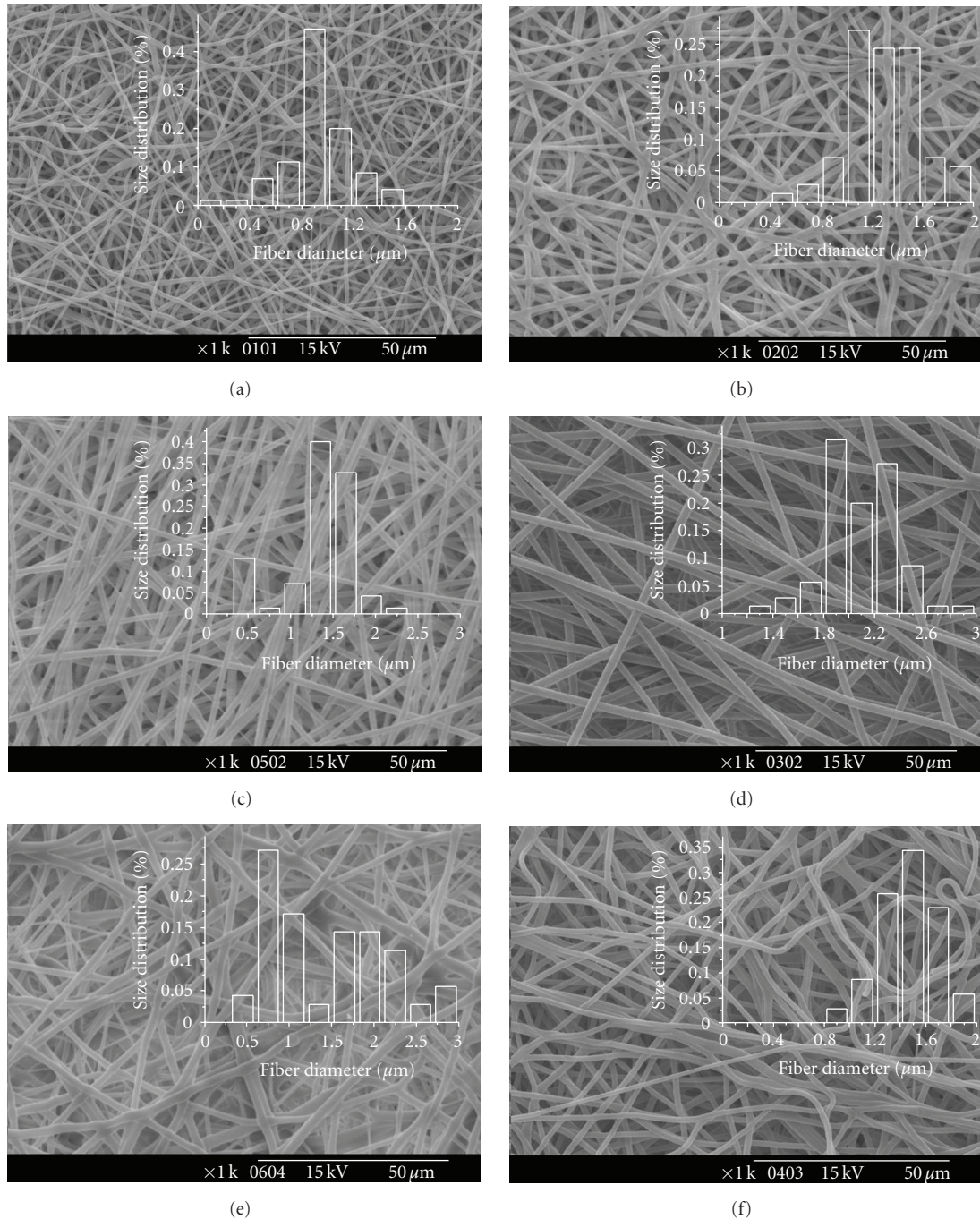


FIGURE 2: SEM images of PLCL/PEO/HA nanofibers: (a) pure PLCL; (b)–(f) PLCL and HA contents were fixed at 6% and 0.03%, respectively, (b) 0.2% PEO; (c) 0.3% PEO; (d) 0.4% PEO; (e) 0.5% PEO; (f) 0.6% PEO. The insets show the fiber size distributions

changed slightly (Table 1) while viscosity increased obviously with the increase of PEO concentration. Generally, proper PEO can improve the spinnability [33]. However, excess PEO may result in the excessive entanglement of PLCL and PEO which has negative effect on forming fibers. Obviously, the optimal concentrations of PLCL and PEO are 6% and 0.4%, respectively, in the range of this investigation.

So the contents of PLCL and PEO were fixed at 6% and 0.4%, respectively, while the HA content was varied

from 0.01 to 0.1%. These fibers were all uniform (Figure 3). HA with nanoscale (0.01–0.1%) did not have obvious an effect on fiber diameter (Figure 4 (b)) and morphology of membrane. With the decrease of HA and PEO contents, the dispersion of HA was improved as shown in Figure 5 (the dark areas). Low HA content can reduce the aggregation of HA nanoparticles and less PEO content can reduce the viscosity of the solution which are both beneficial for the dispersion of HA.

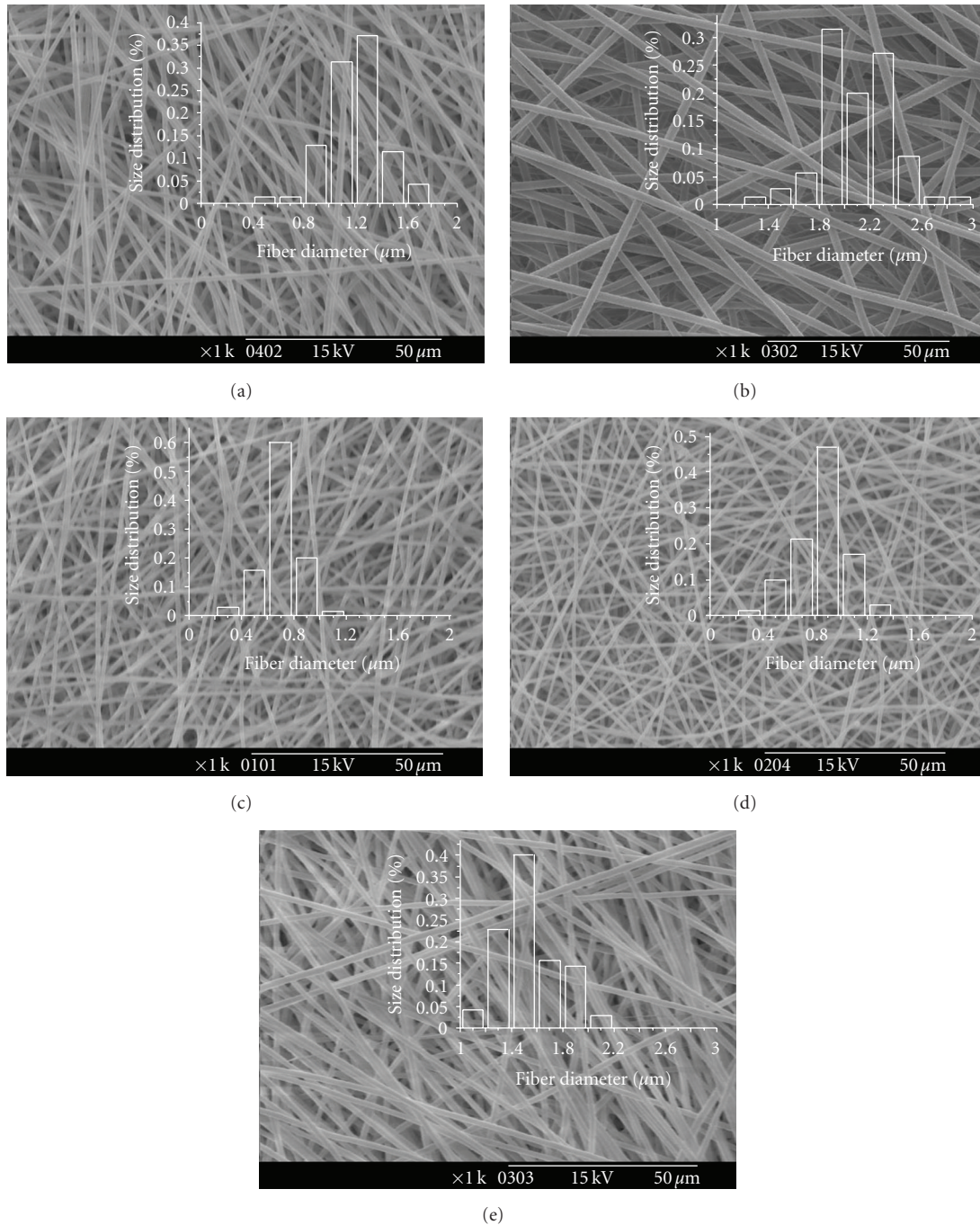


FIGURE 3: SEM images of PLCL/PEO/HA nanofibers: (a)–(e) PLCL and PEO contents were fixed at 6% and 0.4%, respectively, (a) 0.01% HA; (b) 0.03% HA; (c) 0.05% HA; (d) 0.07% HA; (e) 0.1% HA. The insets show the fiber size distributions.

3.2. Water Permeability. Good hydrophilicity is beneficial for the biocompatibility and flowing of nutrition liquid in vivo. PEO is a kind of hydrophilic polymer, so the membranes containing PEO exhibit better hydrophilicity than pure PLCL membrane (Table 2 and Figure 6). Generally, larger fibers result in larger pore size membrane. So a membrane with 0.4% PEO and 0.03% HA has the better water permeability than others because of its larger and more uniform fibers.

3.3. Mechanical Properties. The relationship between tensile properties and PEO or HA content in PLCL/PEO/HA nanofibrous membranes is shown in Table 2, Figures 7 and 8. The elongation at break increased below 0.3% of PEO content, which may be attributed to the good toughness of PEO, and decreased afterwards, which may be because the excess PEO has negative effects on fiber arrangement and bonding as shown in Figure 2. So the toughness of nanofibrous membranes is reduced with excess

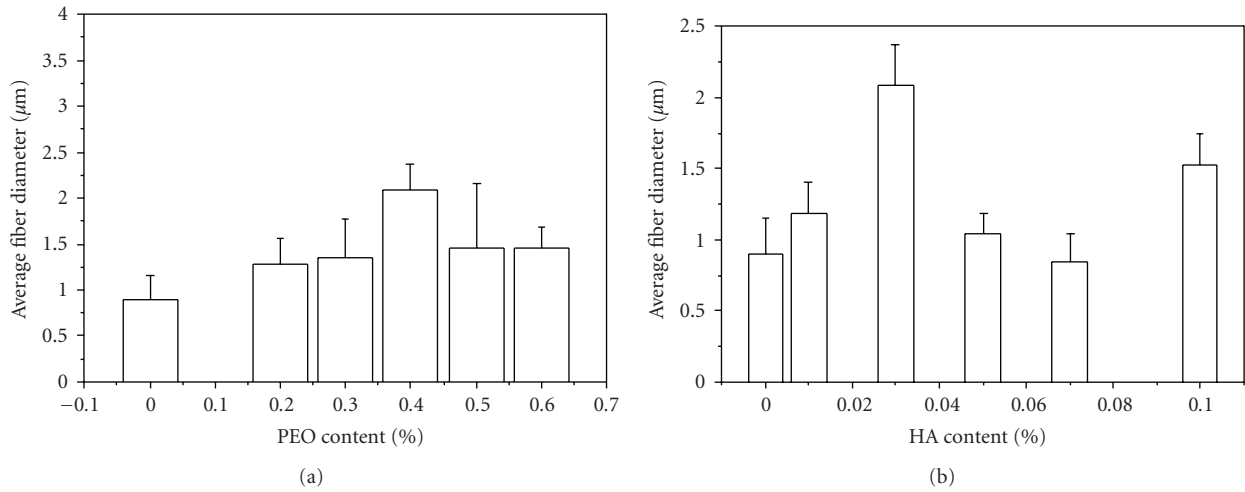


FIGURE 4: The effect of PEO and HA contents on average fiber diameter. (a) The effect of PEO content on average fiber diameter; (b) the effect of HA content on average fiber diameter.

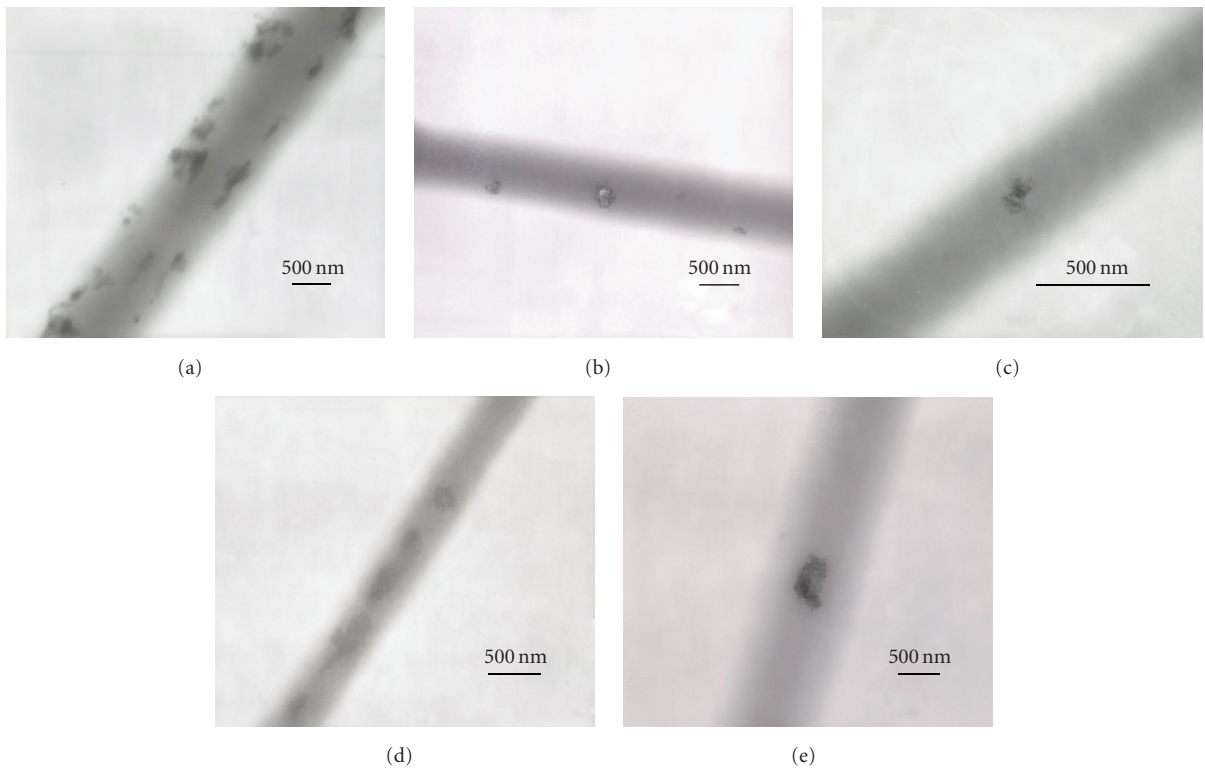


FIGURE 5: TEM images of the electrospun PLCL/PEO/HA nanocomposite fibers. (a) PLCL/PEO/HA: 6/0.4/0.01; (b) PLCL/PEO/HA: 6/0.4/0.03; (c) PLCL/PEO/HA: 6/0.4/0.07; (d) PLCL/PEO/HA: 6/0.2/0.03; (e) PLCL/PEO/HA: 6/0.6/0.03.



FIGURE 6: The change of contact angles of the PLCL/PEO/HA (6/0.4/0.03) composite fibrous.

TABLE 2: Mechanical properties and contact angles of the PLCL/PEO/HA composite fibrous membranes.

Materails and their concentration (g/mL)	Tensile strength (MPa)*	Elongation at break (%)*	Contact angle in 5 minutes (°C)	Contact angle in 5 seconds (°C)
PLCL (6)	9.88 ± 0.64	1.85 ± 0.43	130.0	—
PLCL/PEO/HA (6/0.3/0.03)	10.64 ± 0.38	3.53 ± 0.35	60.9	—
PLCL/PEO/HA (6/0.4/0.03)	13.97 ± 0.74	2.61 ± 0.12	0	0
PLCL/PEO/HA (6/0.5/0.03)	17.19 ± 0.32	2.79 ± 1.20	0	73.5
PLCL/PEO/HA (6/0.6/0.03)	10.47 ± 1.24	2.21 ± 0.46	32.9	—
PLCL/PEO/HA (6/0.4/0.01)	8.83 ± 0.28	2.08 ± 0.02	0	37.5
PLCL/PEO/HA (6/0.4/0.03)	13.97 ± 0.74	2.61 ± 0.12	0	0
PLCL/PEO/HA (6/0.4/0.05)	12.50 ± 1.03	2.00 ± 0.15	0	109.1
PLCL/PEO/HA (6/0.4/0.1)	8.22 ± 1.01	2.24 ± 0.22	129.2	—

*The data are representative of three samples and expressed as mean ± SD ($n = 3$).

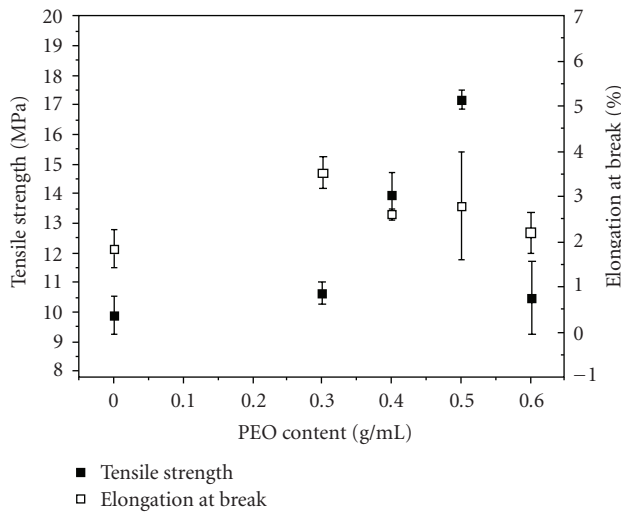


FIGURE 7: The effect of PEO content on mechanical properties of composite fibrous membranes.

PEO. Moreover, the tensile strength increases when the content of HA is below 0.03% and increased afterwards. Obviously, the presence of HA with suitable content can improve the mechanical properties of the membrane. However, excess HA hinders the formation of fibers because of their agglomerate in some extent and produce defects in fibers which lead to the decrease of tensile strength (Figure 5).

4. Conclusion

PLCL/PEO/HA nanofibrous membranes were prepared by electrospinning. Addition of PEO and HA with suitable content to PLCL solution can improve the GBRMS's hydrophilic

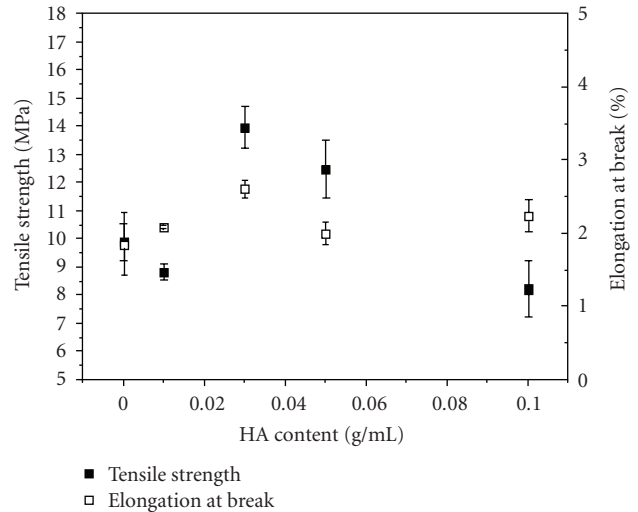


FIGURE 8: The effect of HA content on mechanical properties of composite fibrous membranes.

and mechanical properties effectively. According to the SEM images, more uniform fibers and larger average fiber diameter were obtained when the contents of PEO and HA were 0.4% and 0.03%, respectively. So the composite membrane in this constitute had the best water permeability. Furthermore, the mechanical properties of membrane were improved by adding HA nanocrystals. And the largest tensile strength of nanofibrous membrane can be obtained with 0.5% content of PEO and 0.03% content of HA.

Acknowledgments

This work was supported by National Natural Science Foundation of China (project number: 30800230/C100202)

and the project of Nano Science and Technology of Shanghai, China. (project number: 0852nm03600).

References

- [1] N. P. Lang, C. H. Hämmerle, U. Brägger, B. Lehmann, and S. R. Nyman, "Guided tissue regeneration in jawbone defects prior to implant placement," *Clinical Oral Implants Research*, vol. 5, no. 2, pp. 92–97, 1994.
- [2] C. Tinti, G. Vincenzi, P. Cortellini, G. Pini Prato, and C. Clauser, "Guided tissue regeneration in the treatment of human facial recession. A 12-case report," *Journal of Periodontology*, vol. 63, no. 6, pp. 554–560, 1992.
- [3] H. M. Powell and S. T. Boyce, "Fiber density of electrospun gelatin scaffolds regulates morphogenesis of dermal-epidermal skin substitutes," *Journal of Biomedical Materials Research Part A*, vol. 84, no. 4, pp. 1078–1086, 2007.
- [4] T. Takata, H.-L. Wang, and M. Miyauchi, "Attachment, proliferation and differentiation of periodontal ligament cells on various guided tissue regeneration membranes," *Journal of Periodontal Research*, vol. 36, no. 5, pp. 322–327, 2001.
- [5] R. G. Caffesse, C. E. Nasjleti, E. C. Morrison, and R. Sanchez, "Guided tissue regeneration: comparison of bioabsorbable and non-bioabsorbable membranes. Histologic and histometric study in dogs," *Journal of Periodontology*, vol. 65, no. 6, pp. 583–591, 1994.
- [6] A. K. Schlegel, H. Möhler, F. Busch, and A. Mehl, "Preclinical and clinical studies of a collagen membrane (Bio-Gide®)," *Biomaterials*, vol. 18, no. 7, pp. 535–538, 1997.
- [7] A. Stavropoulos, A. Sculean, and T. Karring, "GTR treatment of intrabony defects with PLA/PGA copolymer or collagen bioresorbable membranes in combination with deproteinized bovine bone (Bio-Oss)," *Clinical Oral Investigations*, vol. 8, no. 4, pp. 226–232, 2004.
- [8] J.-H. Song, H.-E. Kim, and H.-W. Kim, "Production of electrospun gelatin nanofiber by water-based co-solvent approach," *Journal of Materials Science: Materials in Medicine*, vol. 19, no. 1, pp. 95–102, 2008.
- [9] P. Pellen-Mussi, P. Fravalto, M. Guigand, and M. Bonnaure-Mallet, "Evaluation of cellular proliferation on collagenous membranes," *Journal of Biomedical Materials Research*, vol. 36, no. 3, pp. 331–336, 1997.
- [10] S. M. Kuo, S. J. Chang, T. W. Chen, and T. C. Kuan, "Guided tissue regeneration for using a chitosan membrane: an experimental study in rats," *Journal of Biomedical Materials Research Part A*, vol. 76, no. 2, pp. 408–415, 2006.
- [11] U. S. Sajeev, K. A. Anand, D. Menon, and S. Nair, "Control of nanostructures in PVA, PVA/chitosan blends and PCL through electrospinning," *Bulletin of Materials Science*, vol. 31, no. 3, pp. 343–351, 2008.
- [12] H. W. Kim, J. H. Song, and H. E. Kim, "Nanofiber generation of gelation-hydroxyapatite biomimetics for guided tissue regeneration," *Advanced Functional Materials*, vol. 15, pp. 1988–1994, 2005.
- [13] E. Milella, G. Barra, P. A. Ramires, G. Leo, P. Aversa, and A. Romito, "Poly(L-lactide)acid/alginate composite membranes for guided tissue regeneration," *Journal of Biomedical Materials Research*, vol. 57, no. 2, pp. 248–257, 2001.
- [14] Z.-M. Huang, Y. Zhang, and S. Ramakrishna, "Double-layered composite nanofibers and their mechanical performance," *Journal of Polymer Science, Part B*, vol. 43, no. 20, pp. 2852–2861, 2005.
- [15] K. Fujihara, M. Kotaki, and S. Ramakrishna, "Guided bone regeneration membrane made of polycaprolactone/calcium carbonate composite nano-fibers," *Biomaterials*, vol. 26, no. 19, pp. 4139–4147, 2005.
- [16] X. Xu, X. Chen, A. Liu, Z. Hong, and X. Jing, "Electrospun poly(l-lactide)-grafted hydroxyapatite/poly(l-lactide) nanocomposite fibers," *European Polymer Journal*, vol. 43, no. 8, pp. 3187–3196, 2007.
- [17] I. K. Kwon and T. Matsuda, "Co-electrospun nanofiber fabrics of poly(L-lactide-co- ϵ -caprolactone) with type I collagen or heparin," *Biomacromolecules*, vol. 6, pp. 2096–2105, 2005.
- [18] J. H. Kim, P.-H. Choung, I. Y. Kim, et al., "Electrospun nanofibers composed of poly(ϵ -caprolactone) and polyethylenimine for tissue engineering applications," *Materials Science and Engineering C*, vol. 29, no. 5, pp. 1725–1731, 2009.
- [19] Y. Ueyama, K. Ishikawa, T. Mano, et al., "Usefulness as guided bone regeneration membrane of the alginate membrane," *Biomaterials*, vol. 23, no. 9, pp. 2027–2033, 2002.
- [20] G. R. H. Owen, J. Jackson, B. Chehroudi, H. Burt, and D. M. Brunette, "A PLGA membrane controlling cell behaviour for promoting tissue regeneration," *Biomaterials*, vol. 26, no. 35, pp. 7447–7456, 2005.
- [21] M. Kikuchi, Y. Koyama, T. Yamada, et al., "Development of guided bone regeneration membrane composed of β -tricalcium phosphate and poly(L-lactide-co-glycolide-co- ϵ -caprolactone) composites," *Biomaterials*, vol. 25, no. 28, pp. 5979–5986, 2004.
- [22] S. Liao, W. Wang, M. Uo, et al., "A three-layered nanocarbonated hydroxyapatite/collagen/PLGA composite membrane for guided tissue regeneration," *Biomaterials*, vol. 26, no. 36, pp. 7564–7571, 2005.
- [23] Y. J. Park, K. H. Nam, S. J. Ha, C. M. Pai, C. P. Chung, and S. J. Lee, "Porous poly(L-lactide) membranes for guided tissue regeneration and controlled drug delivery: membrane fabrication and characterization," *Journal of Controlled Release*, vol. 43, no. 2-3, pp. 151–160, 1997.
- [24] K. S. Tiaw, S. H. Teoh, R. Chen, and M. H. Hong, "Processing methods of ultrathin poly(ϵ -caprolactone) films for tissue engineering applications," *Biomacromolecules*, vol. 8, no. 3, pp. 807–816, 2007.
- [25] J. Lannutti, D. Reneker, T. Ma, D. Tomasko, and D. Farson, "Electrospinning for tissue engineering scaffolds," *Materials Science and Engineering C*, vol. 27, no. 3, pp. 504–509, 2007.
- [26] Q. P. Pham, U. Sharma, and A. G. Mikos, "Electrospun poly(ϵ -caprolactone) microfiber and multilayer nanofiber/microfiber scaffolds: characterization of scaffolds and measurement of cellular infiltration," *Biomacromolecules*, vol. 7, no. 10, pp. 2796–2805, 2006.
- [27] K. Fujihara, M. Kotaki, and S. Ramakrishna, "Guided bone regeneration membrane made of polycaprolactone/calcium carbonate composite nano-fibers," *Biomaterials*, vol. 26, no. 19, pp. 4139–4147, 2005.
- [28] H.-W. Kim, H.-H. Lee, and J. C. Knowles, "Electrospinning biomedical nanocomposite fibers of hydroxyapatite/poly(lactic acid) for bone regeneration," *Journal of Biomedical Materials Research, Part A*, vol. 79, no. 3, pp. 643–649, 2006.
- [29] G. Shuying, Z. Hui, R. Jie, and Z. Xinyu, "Sol-gel synthesis and characterisation of nano-sized hydroxyapatite powders and hydroxyapatite/ poly(D,L-lactide-co-glycolide) composite scaffolds," *Polymers & Polymer Composites*, vol. 15, no. 2, pp. 137–144, 2007.

- [30] K. Garkhal, S. Verma, S. Jonnalagadda, and N. Kumar, "Fast degradable poly(L-lactide-co- ϵ -caprolactone) microspheres for tissue engineering: synthesis, characterization, and degradation behavior," *Journal of Polymer Science, Part A*, vol. 45, no. 13, pp. 2755–2764, 2007.
- [31] S. L. Shenoy, W. D. Bates, H. L. Frisch, and G. E. Wnek, "Role of chain entanglements on fiber formation during electrospinning of polymer solutions: good solvent, non-specific polymer-polymer interaction limit," *Polymer*, vol. 46, no. 10, pp. 3372–3384, 2005.
- [32] J. H. Yu, S. V. Fridrikh, and G. C. Rutledge, "The role of elasticity in the formation of electrospun fibers," *Polymer*, vol. 47, no. 13, pp. 4789–4797, 2006.
- [33] B. Duan, C. Dong, X. Yuan, and K. Yao, "Electrospinning of chitosan solutions in acetic acid with poly(ethylene oxide)," *Journal of Biomaterials Science, Polymer Edition*, vol. 15, no. 6, pp. 797–811, 2004.

Research Article

Uptake and Cytotoxicity of Ce(IV) Doped TiO₂ Nanoparticles in Human Hepatocyte Cell Line L02

Jian Mao,¹ Long Wang,^{1,2} Zhiyong Qian,³ and Mingjing Tu¹

¹ College of Material Science and Engineering, Sichuan University, Chengdu, 610064 Sichuan, China

² Institute of Zhongshan Opto-electronics, Zhongshan Torch Polytechnic, Zhongshan Torch Polytechnic, Zhongshan 528436, Guangdong, China

³ State Key Laboratory of Biotherapy, West China Hospital, Sichuan University, Chengdu, 610041 Sichuan, China

Correspondence should be addressed to Jian Mao, maojianemail@163.com and Zhiyong Qian, anderson-qian@163.com

Received 4 September 2009; Revised 29 November 2009; Accepted 8 March 2010

Academic Editor: Huisheng Peng

Copyright © 2010 Jian Mao et al. This is an open access article distributed under the Creative Commons Attribution License, which permits unrestricted use, distribution, and reproduction in any medium, provided the original work is properly cited.

Ce(IV) doped anatase TiO₂ nanoparticles (CDTs) were prepared and the underlying mechanism by which CDT nanoparticle enters into cell and its cytotoxicity were investigated in a human hepatocellular line L02 cell. The results showed that CDTs can enter into cytoplasm of L02 cell via endocytosis and nonendocytic ways. Large aggregation of CDTs went into cell by endocytosis and finally formed an endocytic vesicle with membrane boundary. Tiny aggregation of CDTs entered into cell cytoplasm via channels similar to that for lung-blood substance exchange in the alveolar-airway barrier. In addition, tiny aggregation of CDTs was observed in nucleus, and maybe CDTs could pass through the nucleus envelope via the channels provided by nuclear pore complexes (NPCs). Results from MTT assay, fluorescence microscope, and TEM observations showed that the cell viability, cell morphology, cell growth, and cell division periods could not be obviously impaired when cells were exposed to CDTs of different concentration from 30 to 150 $\mu\text{g mL}^{-1}$ without UV irradiation. However, large vacuoles containing CDTs were found in cytoplasm, some structure changes were observed in mitochondria, and smooth envelope around the nucleus was shrank and deformed.

1. Introduction

TiO₂ was previously classified as biologically inert and has been widely used in the cosmetics, pharmaceutical, paint, and paper industries. However, the cytotoxicity of nanosized TiO₂ has caused wide concerns by scientists and engineers in the last decades.

Several studies [1–4] have shown that the cytotoxicity of nanosized TiO₂ was very low or negligible as compared with other nanoparticles. The size was not the effective factor of cytotoxicity [4]. Without UV irradiation, nanosized TiO₂ showed no inflammatory effect or genotoxicity in rats [5] and induced no DNA damages in human cells [6]. In contrast, several studies [7–16] showed the cell cytotoxicity of nano-TiO₂ in vitro. For example, Oberdörster et al. [7] reported that chronic pulmonary inflammation in the rat could be induced by nanosized TiO₂ required the presence of alveolar macrophages. De Virgilio et al. [8] concluded that the presence of TiO₂ nanoparticle in the

cell surroundings could lead to cytotoxic effects, which are dependent on the chemical composition, the concentration of the nanoparticles, the exposure time, and the type of treated cell. Rahman et al. [9] reported that in human and rat alveolar macrophages, the level of reactive oxygen species increased after exposure to nanosized TiO₂. The results of Jin et al. [10] showed that the weakly aggregated anatase TiO₂ nanoparticles in solution could induce significant cytotoxicity in L929 cells. In Syrian hamster embryo fibroblasts, ultrafine TiO₂ alone resulted in micronuclei formation and apoptosis [11]. Lai et al. [12] found that TiO₂ micro- and nanoparticles induced cell death on both human astrocytes-like astrocytoma U87 cell and normal human fibroblasts in a concentration-related manner. Nanosized TiO₂ was also reported to affect gene expressions including an apoptosis-related gene [13], especially the following several latest reports supported the genotoxicity of nanosized TiO₂. Wang et al. [14] reported that ultrafine TiO₂ can cause genotoxicity and cytotoxicity in cultured human cells. Reeves et al. [15]

reported that nanosized TiO₂ (0.1–1000 µg mL⁻¹) with UVA irradiation (0.5–2.0 kJ m⁻²) could cause a significant cell viability decrease on gold fish skin cell and further increase in DNA damages. Vevers and Jha [16] also reported the similar results; without UVA irradiation, there is little oxidative DNA damage of RTG-2 cells of fish exposure to TiO₂-engineered nanoparticles, whereas a significantly increased level of DNA strand break breaks was observed in combination with UVA irradiation (3 kJ m⁻²).

Anatase TiO₂ has a wide band gap about 3.2 eV, and doping with impurities has been widely used to modify the photocatalysis of TiO₂ by introduction of new states in its electronic structure [17, 18]. In particular, for the unique 4f electron configuration, lanthanide metal ions are ideal dopants to promote a higher producing rate of reactive electron/hole pairs [19–21]. But as a kind of engineering application nanoparticle, the cell cytotoxicity of lanthanide ion doped nano-TiO₂ should be evaluated.

In this paper, Ce (IV) doped TiO₂ nanoparticles (CDTs) were prepared by impregnation method, the cell viability, cell morphology, and cell ultrastructure of L02 cells after exposure to CDTs were examined, and the pathways by which CDTs enter into L02 cells also were investigated.

2. Materials and Methods

2.1. Preparation and Characterization of CDT Nanoparticles. The CDTs were prepared by impregnation technique. A required amount of nanosized anatase TiO₂ was added into milli-Q water, sonication for 15 minutes, then the cerium sulphate [Ce(SO₄)₂] aqueous solution was slowly dropped into it under stirring at 60°C for 2 hours; the mixture was filtered, dried at 120°C for 2 hours, and finally calcined at 500°C for 3 hours. The CDTs were characterized by high resolution transmission electron microscopy (HRTEM, JEOL JEM 2010, Cs = 0.5 mm, point resolution = 0.19 nm) with a beryllium window energy-dispersive (EDS) detector. The crystallization of CDTs was analyzed by X-ray diffraction (XRD, Rigaku D/max2500).

2.2. Preparation of CDTs Suspension. Firstly, the CDTs were sterilized by autoclaving at 121°C for 30 minutes, then the CDT powder was weighed and resuspended into milli-Q purified water by ultrasonic dispersion method; the suspension was deposited for 30 minutes, then we took the upper of suspension for the next cytotoxicity experiments because of its better dispersibility compared to the lower of suspension. The particle concentration is determined by the following method. After taking away the upper finely dispersed suspension, the weight of CDTs in the remained suspension can be gained through boiling off the water of the suspension, so the weight of CDTs in the finely dispersed suspension can be calculated and the suspension's concentration is also gained. Finally we diluted the gained finely dispersed suspension with Dulbecco's modified Eagle's medium (DMEM, Gibco) for appropriate concentration for the latter using.

2.3. Cell Culture. The Human hepatocyte cell line (L02, provided by State Key Laboratory of Biotherapy, Sichuan university, China) was cultured in DMEM medium containing 10% (v/v) fetal calf serum (FCS), 50 units mL⁻¹ penicillin, 50 µg mL⁻¹ streptomycin, and 1% (v/v) 0.2 M L-glutamine at 37°C in a 5% (v/v) of CO₂-humidified atmosphere.

A total of 2 × 10⁵ L02 cells per well were inoculated in 6-wells plates overnight, then medium was replaced with a freshly prepared DMEM/CDTs suspension, with the final concentrations of CDTs 150, 120, 75, and 30 µg mL⁻¹. Culture media without CDT nanoparticles served as the control group in each experiment.

2.4. Cytotoxicity. Cytotoxicity of CDTs on L02 cells was determined by 1-(4,5-dimethylthiazol-2-yl)-3,5-diphenylformazan (MTT, Sigma) assay. The cells were seeded in 96-well plates at a density of 1 × 10⁴ cells per well; L02 cells were cultured in the prepared DMEM/CDTs suspension containing different concentrations of CDT nanoparticles for 24, 48, and 72 hours, respectively, then 20 µL of MTT (5 mg mL⁻¹ in phosphate buffer with pH value equal to 7.4) was added to each well and incubated for 4 hours. Afterward, supernatant was discarded and 50 µL Dimethyl Sulphoxide (DMSO) was added to each well. 15 minutes later, the absorbance of each well was measured at 570 nm with Spectra Max M5 (USA), and the relative cell viability (%) was calculated by the equation [A]test/[A]control × 100%, where [A]test is the absorbance of the treated sample, and [A]control is the absorbance of control sample.

All experiments were repeated 6 times to ensure reproducibility. Experiment data were analyzed by using two-tailed paired *t*-test statistical analysis method.

2.5. Cell Morphology. Cell morphology was investigated by fluorescence microscope and transmission electron microscopy (TEM). For fluorescence microscope observations, after culturing in different media, L02 cells were gently washed with phosphate-buffered saline (PBS) and then fixed in cold ethanol for 15 minutes; after thorough drying; they were stained with Hoechst-33258 (Sigma, 2.5 mg mL⁻¹) for 5 minutes. Fluorescence microscopic observations were performed by using Olympus BX60 which was equipped with Olympus DP50 digital camera.

For TEM observations, L02 cells were seeded in 75 cm² glass culture flask with 10 mL DMEM media for overnight, then the cells were cultured with the DMEM medium containing 150 µg mL⁻¹ concentration of CDTs. In control experiments, medium without CDTs was used. L02 cells were gently washed with PBS and fixed with 0.5%, 3.0% glutaraldehyde in PBS at 4°C for 1 hour, respectively, then postfixed in the media containing 1% osmium tetroxide and 1.5% potassium ferrocyanide for about 1 hour. After thorough washing with PBS, the cells were sequentially dehydrated for 10 minutes each in 50%, 70%, 95%, and 100% ethanol. Finally, the fixed samples were embedded in araldite resin. Serial ultrathin sections (approximately 60 nm in thickness) were gained by ultramicrotome and were stained with uranyl acetate and lead citrate. The

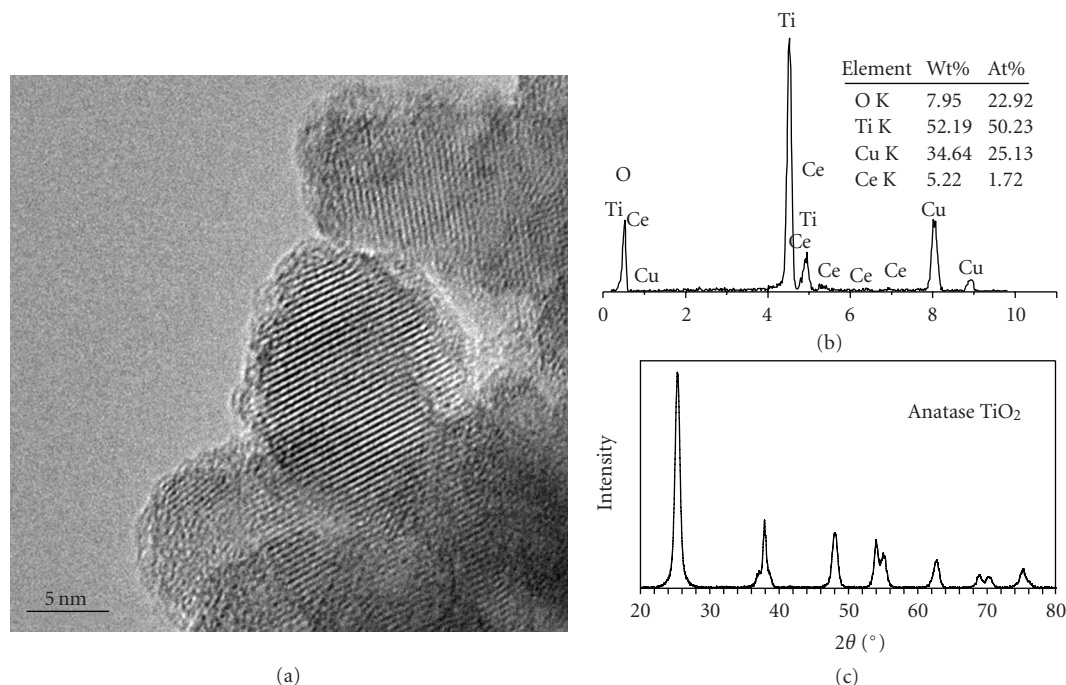


FIGURE 1: HRTEM image (a), EDS (b), and XRD pattern (c) of CDT nanoparticles.

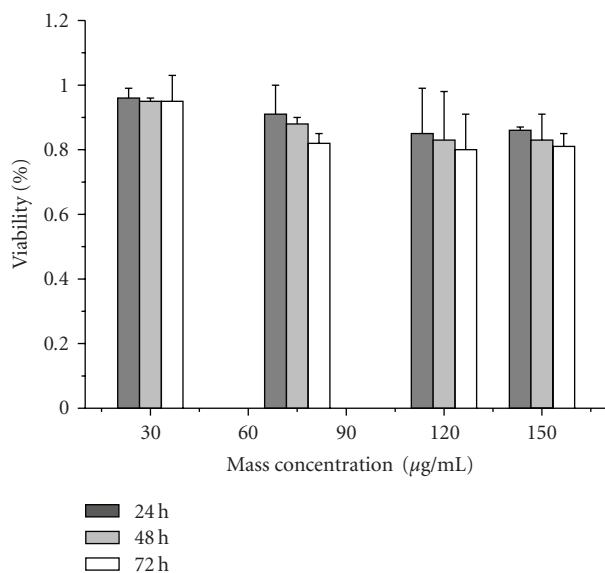


FIGURE 2: Cell viability of L02 cells exposure to CDT nanoparticles. Cells treated with different concentrations of CDTs for 24, 48, and 72 hours, respectively.

microstructure of cells was examined by TEM (JEOL JEM-1200 EX electron microscope, Tokyo, Japan).

3. Results and Discussions

3.1. Characterization of CDTs. The average particle size of CDTs can be estimated as about 15 nm in the HRTEM measurement (Figure 1(a)). EDS result was shown in

Figure 1(b), which indicated that the sample consisted of Ce, Ti, and O elements (Cu element was from the copper grid support). XRD pattern of CDTs in Figure 1(c) showed that the crystalline structure of CDTs was still anatase phase and no rutile TiO_2 or cerium dioxide phase was found, which meant that cerium doping made no change on the anatase structure of original TiO_2 nanoparticles.

3.2. Cytotoxicity of CDTs. The results of MTT assay were shown in Figure 2. The results showed that the cell viability was above 80% when cells were exposed to CDT nanoparticles of different dose from 30 to 150 $\mu\text{g mL}^{-1}$ for 24, 48, and 72 hours, respectively. There is only a slightly decrease in relative growth rate as dose increases from 30 to 120 $\mu\text{g mL}^{-1}$. The latest investigations [15, 16] strongly supported that nanosized TiO_2 could cause a significant cell viability decrease with UVA irradiation. In our experiments, the cell viability cannot be significantly impaired when L02 cells are exposed to CDT nanoparticles; lack of UV irradiation may be the main reason.

3.3. Morphology and Ultrastructure of L02 Cells. Hoechst 33258 can enter into living cells or dead cells and will emit bright blue fluorescence with UV irradiation. A uniform dispersive blue fluorescence can be found in living cells, whereas, a hyperchromic blocky fluorescence can be observed within the nucleus or cytoplasm of apoptosis cells. Fluorescence micrographs of L02 cells stained with Hoechst 33258 are shown in Figure 3. Cell morphology of treated group and control group was shown in Figures 3(a) and 3(b), respectively, Figures 3(c) and 3(d) were the enlarged view of Figures 3(a) and 3(b), respectively.

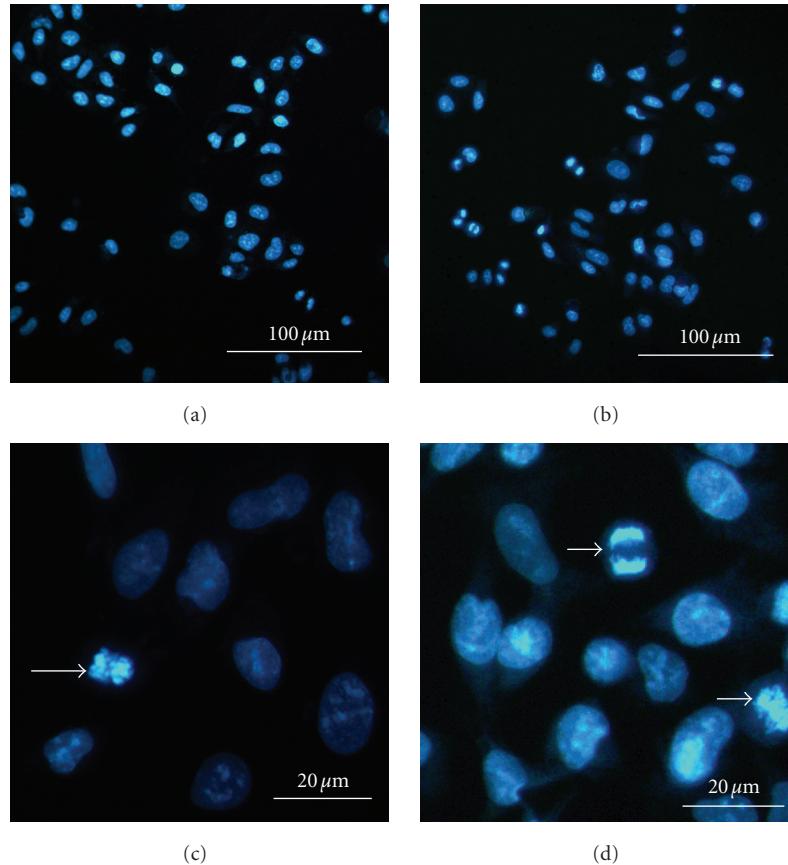


FIGURE 3: Fluorescence micrographs of L02 cells treated with $150 \mu\text{g mL}^{-1}$ CDTs for 48 hours. ((a) and (c)) and those of control cells ((b) and (d)). Magnification upper: $400\times$, lower: $1000\times$.

Figure 3(a) showed that cells distributed in groups, and the hyperchromic condition of the cells indicated that they were in the S period. Most of the cells exhibited the tight waist shape in the enlarged view (Figure 3(c)), and the cell indicated by arrow in Figure 3(c) was in the middle and later periods of cell division. Figure 3(b) showed that cells in the control group were in normal growing conditions. In Figure 3(d), the cell indicated by the upper arrow was in the later periods of cell division, and the cell indicated by the lower arrow was in the middle periods of cell division. The above analysis showed that, both in treated group and control group, most of the cells appeared with the similar morphology and only the proliferation period was different. Which meant the cell morphology and cell growth could not be obviously influenced when L02 cells were exposed to CDTs; the result is the same as that of MTT assay.

Figure 4 showed the TEM images at different cell division periods of L02 cells exposure to CDT nanoparticles. The cells were in primary, middle and later periods of cell division in Figures 4(a), 4(b), and 4(c), respectively. The normal cell division procedures were observed from Figure 4(a) to Figure 4(c). It seems that there is little influence on the cell division when CDT nanoparticles are in the cell cytoplasm or nucleus.

Ultrastructure of L02 Cells exposed to CDT nanoparticles had shown some differences with that of control cells (Figure 5). The appearance of normal L02 cell is oval shaped and the size is about $12 \mu\text{m}$; its ultrastructure was shown in Figure 5(a). The cell nucleus was round with smooth envelope, rough endoplasmic reticulum (RER) and numerous free ribosomes and polysomes were distributed in the cell cytoplasm, meanwhile, round or elongated mitochondria (indicated by the arrows in Figure 5(a)) also scattered in the cytoplasm; distinct cristae could be found in the inner membrane of mitochondria. However, in the ultrastructure of treated cell (Figure 5(b)), some large vacuoles in which there were aggregations of CDTs were found in cytoplasm; some membrane boundaries of these vacuoles became illegible and some membrane boundaries were broken, which led to leaking out of CDT nanoparticles. In addition, it seemed that microstructure of mitochondria was influenced by these CDTs, and the shape of mitochondria (indicated by the arrows in Figure 5(b)) was changed, in which the cristae became short or disappeared. Furthermore, In Figure 5(c), it was shown that the smooth envelope around the nucleus was shrank and deformed when the cells were exposed to CDT nanoparticles. Cellular necrosis also was found in treated group (Figure 5(d)).

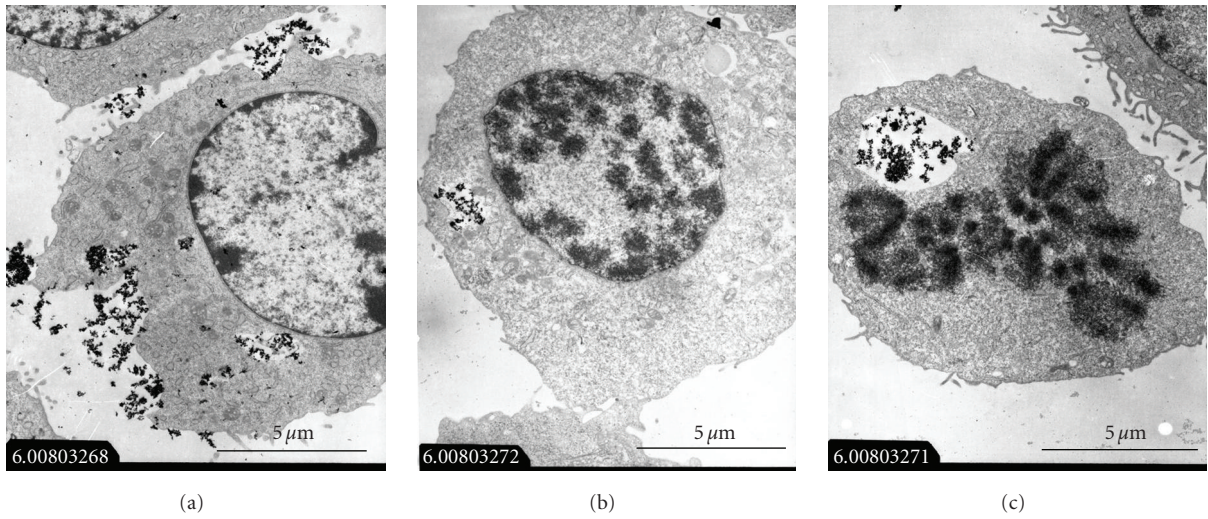


FIGURE 4: TEM image of L02 cells treated with 150 mg mL^{-1} CDTs for 48 hours. The cells were at different cell division periods: (a), primary periods, (b), middle periods, and (c), later periods.

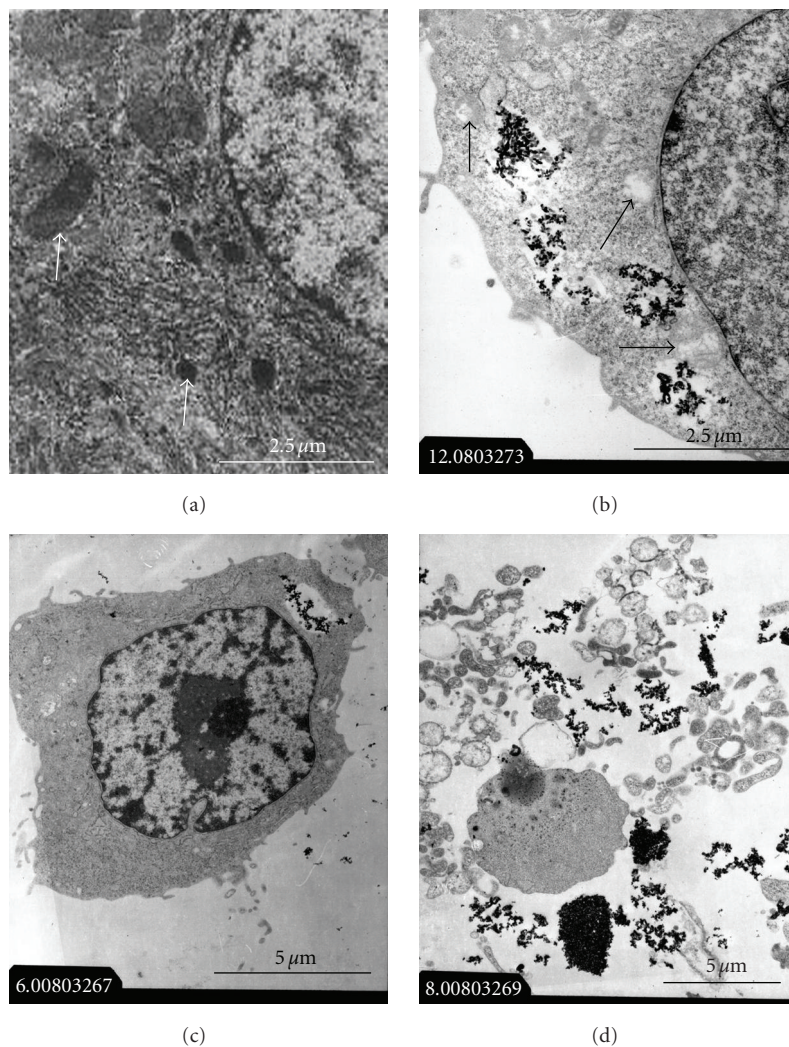


FIGURE 5: Ultrastructure of L02 cells in control group ((a), $12\,000\times$) and in treated group with $150 \mu\text{g mL}^{-1}$ CDTs for 48 hours ((b), (c), and (d)). Magnification of (b), (c), and (d) is $12\,000\times$, $6\,000\times$, and $8\,000\times$, respectively.

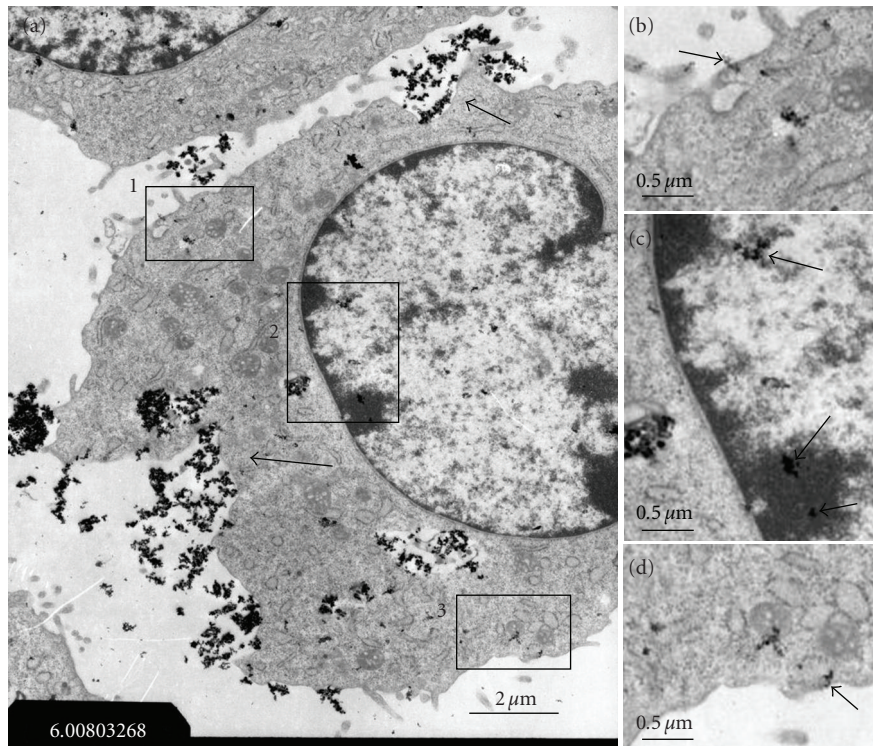


FIGURE 6: TEM feature of L02 cell after exposure to $150 \mu\text{g mL}^{-1}$ CDTs for 48 hours. (a) is full view ($6,000\times$). (b), (c) and (d) are the clear magnification of rectangle region 1, 2 and 3 in (a), respectively.

3.4. Uptake Pathway of CDTs in L02 Cells. From the above results of TEM, we found that CDT nanoparticles could enter into L02 cells. It is difficult to gain the living observations of nanoparticles going into cells, so the possible pathways by which CDT nanoparticles went into L02 cells were discussed by analyzing the TEM images.

We found that several CDT nanoparticles could easily gather into a finely ground particle (FGP), and the average size of FGP estimated from the TEM images is about 200 ± 50 nm. And the finely ground particles (FGPs) normally appeared as large aggregations or tiny aggregations in the cells (Figures 4 and 5). We can deduce that these large undispersed nanoparticles got into cells by endocytosis of cell membrane, the regions pointed by the arrows in Figure 6(a) showed that the endocytosis action was happening, and then an endocytic vesicle with membrane-bound was formed in cytoplasm. By the way, these large gathering CDTs were found only in cytoplasm not in nucleus.

Clear magnifications of rectangle regions 1, 2, and 3 were shown in Figures 6(b), 6(c), and 6(d), respectively. Single FGP and tiny aggregations of several FGPs were found in the cell cytoplasm (Figures 6(b) and 6(d)) and nucleus (Figure 6(c), which is indicated by the arrows) without membrane. One part of FGPs in cytoplasm might come from the leakage of nanoparticles from vacuoles, and the other might come from the outside of cells, which suggested that a single CDT or tiny agglomerates of several CDTs can enter into cells by other ways different from endocytosis. We surprisingly found that a tiny aggregation of FGPs pointed by the arrow

in Figure 6(b) just inserted in cytoplasm membrane and the cell membrane still kept smooth without deformation. Another tiny aggregation of FGPs indicated by the arrow in Figure 6(d) happened to complete the access procedure. All of these proved that a tiny aggregation of FGPs can directly cross the cell plasma membrane. The way it adopted might be transporting via the channels of substance exchange between the cell and external environment, which was like those for lung-blood substance exchange in the alveolar-airway barrier. The investigations of Conhaim et al. [22] showed that the alveolar-airway barrier consisted not only of tight intercellular junctions that allowed passage of only water and electrolytes but also of a smaller number of large leaks that allowed passage of particles up to nearly 400 nm in radius, maybe similar channel can exist in L02 cells. The shape of tiny aggregation of FGPs pointed by the arrow in Figure 6(b) is like a chain, of which the length is about 220 nm and the width is about 75 nm, so the tiny aggregation of FGPs could carry out the transmembrane action via pores. This kind of passive uptake, not triggered by receptor-ligand interactions, might be activated by electrostatic, Van de Waals, or steric interactions, which were subsumed under “adhesive interactions” by Rimai et al. [23].

The FGPs found in nucleus might be attributed to that the CDT nanoparticle passed through the envelope via the channels provided by nuclear pore complexes (NPCs). Although the channel provided by NPCs is about 9 nm in diameter [24], Panté and Kann reported [25] that ultrafine gold particles coated with cargo-receptor complexes of

up to 39 nm in diameter could pass through the NPCs by signal-mediated transport in xenopus oocytes. In our investigations, the particle size of CDTs is about 15 nm, so it had the ability to pass through the pores. But passing through NPCs needs a signal-mediated mechanism; the mechanism for CDT nanoparticles is not clear and needs further investigation.

In sum, it is very likely that CDT nanoparticles aggregated at cells surface, large aggregations were engulfed by L02 cells by endocytosis and tiny aggregations or even a single nanoparticle could carry out the transmembrane action directly via pores, then a single CDT nanoparticle could enter into nucleus through NPCs channels.

4. Conclusions

(1) Anatase CDTs of mean size about 15 nm were prepared by using impregnating method. Cell viability, cell morphology, cell growth, and cell division periods cannot be influenced when L02 cells are exposed to CDTs of different doses from 30 to 150 $\mu\text{g mL}^{-1}$ without UV irradiation for 24, 48, and 72 hours, respectively. But the ultrastructure of cells has been changed by exposure to CDTs, nucleus was shrank in size and nuclear envelope was deformed, large vacuoles containing CDTs were found in cytoplasm, and the shape of mitochondria was also changed, in which the cristae became short or disappeared.

(2) CDT nanoparticles aggregated at the surface of cells, several CDT nanoparticles easily gathered into a finely ground particle (FGP) with mean size about 200 ± 50 nm, large aggregations of FGPs entered into L02 cells by endocytosis, and tiny aggregations of FGPs or even a single CDT could cross the cell membrane directly through the channels for mass exchange between the cell and external environment; this action might be activated by adhesive interactions consisting of electrostatic, Van de Waals, or steric interactions, and so forth. Then single CDT nanoparticle could enter into nucleus through nuclear pore complexes (NPCs) channels.

Acknowledgments

This work was supported by National 863 Items of China (no. 2007AA021801, no. 2007AA021901), and the authors thank State Key Laboratory of Biotherapy (Sichuan University, P. R. China) for providing experimental material and apparatus.

References

- [1] Y.-M. Kwon, Z. Xia, S. Glyn-Jones, D. Beard, H. S. Gill, and D. W. Murray, "Dose-dependent cytotoxicity of clinically relevant cobalt nanoparticles and ions on macrophages in vitro," *Biomedical Materials*, vol. 4, no. 2, pp. 25018–25052, 2009.
- [2] K. Peters, R. E. Unger, C. J. Kirkpatrick, A. M. Gatti, and E. Monari, "Effects of nano-scaled particles on endothelial cell function in vitro: studies on viability, proliferation and inflammation," *Journal of Materials Science: Materials in Medicine*, vol. 15, no. 4, pp. 321–325, 2004.
- [3] A. Yamamoto, R. Honma, M. Sumita, and T. Hanawa, "Cytotoxicity evaluation of ceramic particles of different sizes and shapes," *Journal of Biomedical Materials Research*, vol. 68, no. 2, pp. 244–256, 2004.
- [4] Q. Zhang, Y. Kusaka, K. Sato, K. Nakakuki, N. Kohyama, and K. Donaldson, "Differences in the extent of inflammation caused by intratracheal exposure to three ultrafine metals: role of free radicals," *Journal of Toxicology and Environmental Health A*, vol. 53, no. 6, pp. 423–438, 1998.
- [5] B. Rehn, F. Seiler, S. Rehn, J. Bruch, and M. Maier, "Investigations on the inflammatory and genotoxic lung effects of two types of titanium dioxide: untreated and surface treated," *Toxicology and Applied Pharmacology*, vol. 189, no. 2, pp. 84–95, 2003.
- [6] R. Dunford, A. Salinaro, L. Cai, et al., "Chemical oxidation and DNA damage catalysed by inorganic sunscreen ingredients," *FEBS Letters*, vol. 418, no. 1-2, pp. 87–90, 1997.
- [7] G. Oberdörster, J. Ferin, R. Gelein, S. C. Soderholm, and J. Finkelstein, "Role of the alveolar macrophage in lung injury: studies with ultrafine particles," in *Environmental Health Perspectives*, vol. 97, pp. 193–199, 1992.
- [8] A. L. Di Virgilio, M. Reigosa, and M. F. de Mele, "Response of UMR 106 cells exposed to titanium oxide and aluminum oxide nanoparticles," *Journal of Biomedical Materials Research A*, vol. 92, no. 1, Article ID 19165783, pp. 80–86, 2010.
- [9] Q. Rahman, J. Norwood, and G. Hatch, "Evidence that exposure of particulate air pollutants to human and rat alveolar macrophages leads to differential oxidative response," *Biochemical and Biophysical Research Communications*, vol. 240, no. 3, pp. 669–672, 1997.
- [10] C.-Y. Jin, B.-S. Zhu, X.-F. Wang, and Q. H. Lu, "Cytotoxicity of titanium dioxide nanoparticles in mouse fibroblast cells," *Chemical Research in Toxicology*, vol. 21, no. 9, pp. 1871–1877, 2008.
- [11] Q. Rahman, M. Lohani, E. Dopp, et al., "Evidence that ultrafine titanium dioxide induces micronuclei and apoptosis in syrian hamster embryo fibroblasts," *Environmental Health Perspectives*, vol. 110, no. 8, pp. 797–800, 2002.
- [12] J. C. K. Lai, M. B. Lai, S. Jandhyam, et al., "Exposure to titanium dioxide and other metallic oxide nanoparticles induces cytotoxicity on human neural cells and fibroblasts," *International Journal of Nanomedicine*, vol. 3, no. 4, pp. 533–545, 2008.
- [13] F. Carinci, S. Volinia, F. Pezzetti, F. Francioso, L. Tosi, and A. Piattelli, "Titanium-cell interaction: analysis of gene expression profiling," *Journal of Biomedical Materials Research B*, vol. 66, no. 1, pp. 341–346, 2003.
- [14] J. J. Wang, B. J. S. Sanderson, and H. Wang, "Cytotoxicity of ultrafine TiO_2 particles in cultured human lymphoblastoid cells," *Mutation Research*, vol. 628, no. 2, pp. 99–106, 2007.
- [15] J. F. Reeves, S. J. Davies, N. J. F. Dodd, and A. N. Jha, "Hydroxyl radicals ($\cdot\text{OH}$) are associated with titanium dioxide (TiO_2) nanoparticle-induced cytotoxicity and oxidative DNA damage in fish cells," *Mutation Research—Fundamental and Molecular Mechanisms of Mutagenesis*, vol. 640, no. 1-2, pp. 113–122, 2008.
- [16] W. F. Vevers and A. N. Jha, "Genotoxic and cytotoxic potential of titanium dioxide (TiO_2) nanoparticles on fish cells in vitro," *Ecotoxicology*, vol. 17, no. 5, pp. 410–420, 2008.
- [17] W. Choi, A. Termin, and M. R. Hoffmann, "The role of metal ion dopants in quantum-sized TiO_2 : correlation between photoreactivity and charge carrier recombination dynamics,"

- Journal of Physical Chemistry*, vol. 98, no. 51, pp. 13669–13679, 1994.
- [18] U. Diebold, “The surface science of titanium dioxide,” *Surface Science Reports*, vol. 48, pp. 53–229, 2003.
- [19] M. Anpo and M. Takeuchi, “The design and development of highly reactive titanium oxide photocatalysts operating under visible light irradiation,” *Journal of Catalysis*, vol. 216, no. 1-2, pp. 505–516, 2003.
- [20] A.-W. Xu, Y. Gao, and H.-Q. Liu, “The preparation, characterization, and their photocatalytic activities of rare-earth-doped TiO₂ nanoparticles,” *Journal of Catalysis*, vol. 207, no. 2, pp. 151–157, 2002.
- [21] T. H. Hou, J. Mao, X. D. Zhu, and M. J. Tu, “STM and STS investigations of Ce-doped TiO₂ nanoparticles,” *Rare Metals*, vol. 25, no. 4, pp. 331–336, 2006.
- [22] R. L. Conhaim, A. Eaton, N. C. Staub, and T. D. Heath, “Equivalent pore estimate for the alveolar-airway barrier in isolated dog lung,” *Journal of Applied Physiology*, vol. 64, no. 3, pp. 1134–1142, 1988.
- [23] D. S. Rimai, D. J. Quesnel, and A. A. Busnaina, “The adhesion of dry particles in the nanometer to micrometer-size range,” *Colloids and Surfaces A: Physicochemical and Engineering Aspects*, vol. 165, no. 1–3, pp. 3–10, 2000.
- [24] P. L. Paine, L. C. Moore, and S. B. Horowitz, “Nuclear envelope permeability,” *Nature*, vol. 254, no. 5496, pp. 109–114, 1975.
- [25] N. Panté and M. Kann, “Nuclear pore complex is able to transport macromolecules with diameters of ~39 nm,” *Molecular Biology of the Cell*, vol. 13, no. 2, pp. 425–434, 2002.